Towards atom assembly on nanophotonic structures with optical tweezers

Thesis by
Xingsheng Luan

In Partial Fulfillment of the Requirements for the
Degree of
Doctor of Philosophy

CALIFORNIA INSTITUTE OF TECHNOLOGY
Pasadena, California

2020
Defended May 26, 2020

Xingsheng Luan
ORCID: 0000-0003-0649-2221

To my family.

ACKNOWLEDGEMENTS

First, my thanks go to my advisor Jeff Kimble, for his support and encouragement over the past 6 years. In the adventure to the atom-nanophotonic world, Jeff really amazed me with his great vision of the future, his passion on science and his incredible creativity in solving challenging problems. There are so many moments that I said things couldn't be done but later proved that I was usually wrong and Jeff was usually right! I feel so honored that I could be part of the journey and become his last PhD student in the end. I will always remember Jeff's saying "If you know what you are doing, don't do it!" which reminds me to always stay open-minded and fearless when exploring the unknowns in my future career.

I would also thank Oskar Painter for introducing me to Jeff and sponsoring me to work in Jeff's group in my second year at Caltech. Oskar's leading research in the field of cavity optomechanics was the main reason I came to Caltech. The first year in his group was very productive, with one publication and fifteen classes completed (i.e. five classes per quarter). "Contradictory" to Jeff's saying quoted above, Oskar taught me "You should know every detail of what you are doing", which is another limit I am still aiming to approach.

Within the Quantum Optics Group, I have been very fortune to have many group members always there willing to help and support me through my whole PhD study. My journey into the atom-nanophotonic world started in the summer of 2016 when Jeff formally took me as his student and allowed me to work in one of his labs, Lab 11. In Lab 11, I had a short overlap with Jon Hood, Su-Peng Yu and Mingwu Lu before Jon and I moved the setup in Lab 11 to JILA. Specifically, thanks to Jon, who taught me hand-on-hand on how to run the complex experimental setup in Lab 11 and later helped me to take it apart and move to JILA for rebuilding. Jon also kindly gave his beloved Camry to me when I promised to drive it from California to Colorado. To Su-Peng, who taught me the recipes in nanophotonic design and nano-fabrication. To Mingwu, who shared his knowledge and experience to me without reservation. Besides, I would also like to take this chance to thank Aki Goban and Chen-Lung Hung who built the original apparatus in Lab 11. Especially to Aki, who spent a lot time outside his own research helping me debug problems during my time in JILA. Outside Lab 11, crew members in Lab 2 were very helpful for their enlightening discussions. Thanks to Andrew McClung and Juan Muniz, who patiently taught me the basics of atomic physics and laser physics during my

initial transition into Jeff's group. To Alex Burgers, who was always very helpful to talk to. I was amazed that he could understand me even when I didn't express myself clearly. Besides, I would like to thank him for taking the lead on the tweezer project in Lab 11 after I returned from JILA in 2018. To Lucas Peng, who shared the same office with me and helped me solve many numerical simulation problems. On the theory side, I would like to thank Ana Asenjo-Garcia for her stimulating discussions and sharing her valuable notes/codes for me to play with. In the last two years at Caltech, I also worked closely with Zhongzhong Qin and Jean-Baptiste Béguin. Thanks to Zhongzhong, who helped me move the lab back to Caltech again and rebuild the laser and vacuum system from two empty tables in Lab 11 and Lab 9. To Jean-Baptiste, who solved many important experimental obstacles in the new apparatus with his innovations and critical thinking. To Prof. Julien Laurat, for his valuable suggestions during the time we built the new apparatus and his contributions in the superposed Laguerre-Gauss beam project. Finally, to Scott Curtis, our lab administrator, who helped me in both the lab management and also my personal life. He is the key person that ensures the whole lab running smoothly.

I would like to thank Cindy Regal for her host during my stay in JILA from 2016-2018. I had a wonderful time in JILA and was able to directly interact with many renowned scientists such as Jun Ye and Jan Hall. I would like to thank them for sharing their life experience and valuable advice. Thanks to my labmates in JILA, Tobias Thiele and Ting-Wei Hsu. To Tobias, with whom we rebuilt and recovered the previous Lab 11 setup in JILA within three months! To Ting-Wei, who managed to demonstrate several techniques for mounting the chip inside the glass cell. To Yiheng Lin, who always stay very humble despite having so many top-journal publications. To Prof. Shengwang Du from HKUST, for his care and support to me and my family during his visit in JILA.

I would also like to take this chance to express my appreciation to many friends at Caltech, especially the Caltech-NJUers. To Xiaolin Mao, who drove me to the supermarkets to buy food every week when we didn't have a car. To Junlong Kou, with whom we even dreamed to start up a company together. To Baoyi Chen and his wife Yingying Wu, who bought so many toys to my sons and I haven't got the chance to give back to their future baby. To Jingling Huang, who devoted much her time helping me prepare for job interviews. To many friends whom I couldn't list their names here due to space limitation, thank you all for your support in the past!

Finally, I would like to thank my family for their persistent love and support in my

life. 我要感谢我父母的养育之恩。在我成长的道路上，他们一直对我非常宽容，让我自由地去追求自己的选择。这篇博士论文要特别献给我的父亲。他年轻时因为医疗事故听力受损，在高考分数达到某一流高校录取线的情况下，却因为听力的原因没有获得入学资格，以致于他的才智没能得到进一步地施展。希望我现在的努力能够给他一丝欣慰。同时感谢我的母亲，虽然她年轻时没有机会接受高等教育，但她却一直非常开明富有远见，让我明白了很多人生的道理。同时我还要感谢我的爷爷奶奶、岳父岳母以及亲戚朋友们一直以来对我学业的关心。现在他们终于不需要再问我什么时候毕业了，哈哈。 Most importantly, thanks to my wife Mei, for her love and support over a decade. She could also have the chance to become a Doctor but later chose to sacrifice herself when we had our first baby. She deserves to earn half of my PhD degree. This thesis is also dedicated to my two little sons Cheng and Yu, who have been the main source of joy in our life and later the most important motivation for me to complete my PhD degree (so that I can be the first Doctor in my family, not them).

ABSTRACT

The integration of atomic physics and nanophotonics combines the best of two worlds. With atoms as the naturally existing qubits and nanophotonic devices as the engineered interaction medium, new frontiers can be explored for building novel quantum optical circuits for non-conventional quantum optics and exotic quantum many-body physics, as well as potentially serving as a fundamental building block for quantum computation and communication with neutral atoms. While important experimental milestones towards this goal have been reached, a grand challenge for experiments in this new field is the loading and trapping of atomic arrays with high fractional filling near complex nanophotonic structures. In this thesis, we have proposed a novel protocol for atom assembly on nanophotonic structures by integrating optical tweezer arrays and photonic crystal waveguides. This research is inspired by recent exciting progress in free-space atom assembly. However, unlike its free-space counterpart, our new proposal should enable subwavelength atom arrays with complex patterns defined by precision nanofabrication. To demonstrate the basic principles behind this new proposal, we have designed and built an advanced apparatus with a compact footprint that overcomes several significant experimental barriers in previous experiments. To achieve efficient atom delivery and assembly of arrays for more complex nanostructures, we have proposed a novel direct delivery scheme with optical tweezers by exploiting the rapid spatial variation of the Gouy phase of radial Laguerre-Gauss beams. With reduced dimension in the axial direction, the optical tweezer formed by supposed Laguerre-Gauss beams may find important applications in the communities of general atomic physics and super-resolution imaging. Finally, we have investigated the optomechanical properties of our nanophotonic devices for trapping atoms and evaluated potential heating mechanisms for trapped atoms. The studies presented in this thesis should provide important guidance to future atom-nanophotonic experiments.

PUBLISHED CONTENT AND CONTRIBUTIONS

X. Luan, J.-B. Béguin, A.P. Burgers, Z. Qin, S.-P. Yu, and H. J. Kimble, (2020). "The Integration of Photonic Crystal Waveguides with Atom Arrays in Optical Tweezers", In: *Advanced Quantum Technologies* DOI: 10.1002/qute.202000008.
X.L. designed and constructed the experiment apparatus, performed the experiments, analyzed the data and prepared the manuscript.

J.-B. Béguin, A. P. Burgers, X. Luan, Z. Qin, S.-P. Yu, and H. J. Kimble, (2020). "Advanced apparatus for the integration of nanophotonics and cold atoms," In: *Optica* 7, 1-2. DOI: 10.1364/OPTICA.384408.
X.L. designed and constructed the experiment apparatus, performed the experiments, analyzed the data and prepared the manuscript.

J.-B. Béguin, J. Laurat, X. Luan, A. P. Burgers, Z. Qin, H. J. Kimble, (2020). "Reduced volume and reflection for optical tweezers with radial Laguerre-Gauss beams", submitted for review. arXiv:2001.11498v2 [quant-ph].
X.L. performed the numerical simulations and prepared the manuscript.

K. Fang, M. Matheny, X. Luan, O. Painter, (2016). "Optical transduction and routing of microwave phonons in cavity-optomechanical circuits". In:*Nature Photonics* 10, 489–496. DOI: 10.1038/nphoton.2016.107.
X.L. performed the experiment and data analysis.

TABLE OF CONTENTS

LIST OF ILLUSTRATIONS

Number *Page*

Chapter 1

INTRODUCTION

1.1 The atom-light interactions

The interaction of atom and light lies at the heart of quantum optics. In the development of quantum optics, one of the central goals in experiment is to achieve strong interactions between atoms and photons at the quantum level [39, 42]. Efficient interactions between atoms and light constitute the key enabling mechanism for applications with atomic systems, ranging from quantum information processing to metrology to nonlinear optics [40, 110]. The figure of merit that characterizes the interaction strength between the atom and light is the Purcell factor P, which is defined as the ratio between the rate an excited atom decaying into the specific light field of interest (Γ_{int}) versus the rate decaying into other channels (Γ').

$$P = \frac{\Gamma_{\text{int}}}{\Gamma'}. \tag{1.1}$$

Perhaps the simplest way for increasing the atom-light interaction is to improve the spatial overlap between the light field and the atom. For example, the scattering cross-section for two-level atoms with transition wavelength λ_0 is defined as $\sigma_0 = 3\lambda_0^2/2\pi$. For achieving strong atom-light interaction, one can focus the light beam to dimensions comparable to the atomic scattering cross-section, as shown in Fig. 1.1 (a). However, the smallest area the light can be focused down in free-space is set by the diffraction limit, resulting in $A_{\text{eff,min}} \simeq \lambda^2$. As a result the Purcell factor P_f for the interaction of free-space focusing beam with a two-level atom is limited to [188]

$$P_{f,\text{max}} \propto \frac{\sigma_0}{A_{\text{eff,min}}} \simeq 0.5. \tag{1.2}$$

The tightly focused beam reduced the transverse dimension of the photon wavepacket. One can further increase the atom-light coupling strength by reducing the dimension of wavepacket in the propagation direction, leading to the confinement of photons. This can be achieved by an optical cavity formed by a pair of highly reflective mirrors, as shown in Fig. 1.1 (b). The approach to enhance atom-light interaction by confining both the atom and light field in a same cavity forms the field cavity QED. It first suggested by Purcell in 1940s [149] and the experiments are pioneered by Jeff Kimble in the optical domain [109] and Serge Haroche in the microwave domain [82]. Intuitively, the atom-light interaction strength inside a cavity is enhanced by

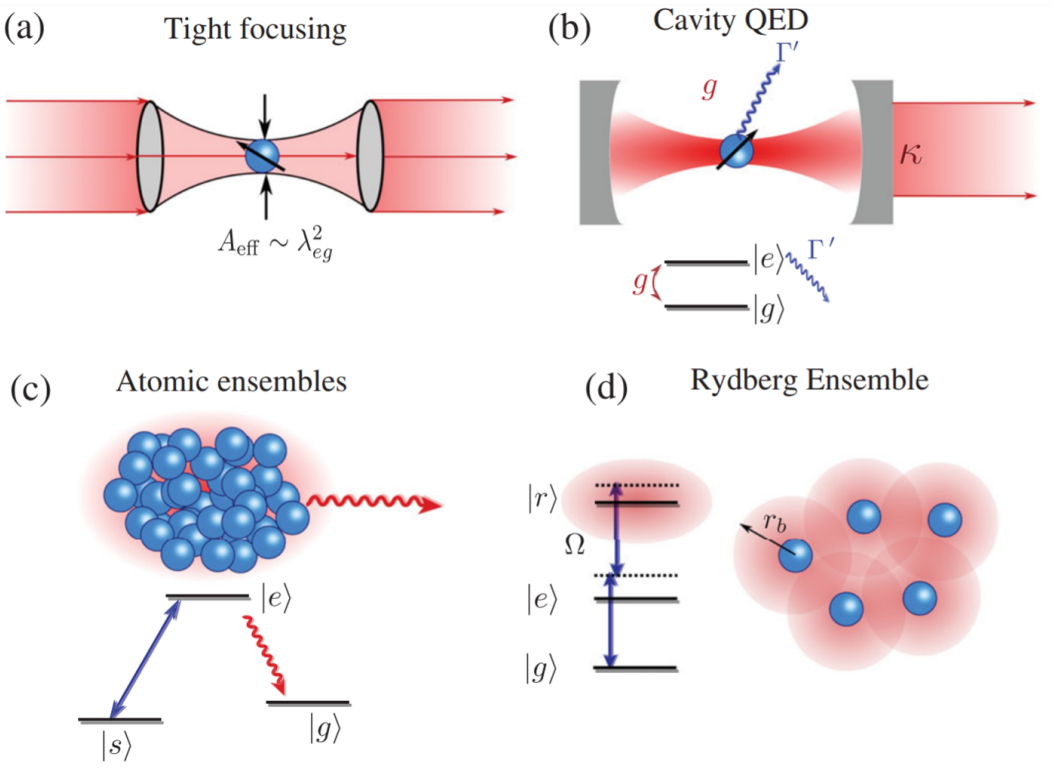

Figure 1.1: a) Diffraction-limited focusing of an optical beam onto a tightly trapped atom. b) Cavity QED where the interaction is enhanced by a large number of photon-round trips. c) Atomic ensemble, where a large atom number results in high probability of interaction with a single photon. d) atomic ensemble of Rydberg atoms. Figures adapted from Ref. [40] with permissions.

the number of round-trips that the photon makes across the atom due to the reflection off the mirrors, that is

$$P_{\text{cav}} \propto N_{\text{trips}} \frac{\sigma_0}{A_{\text{eff}}} \propto Q \frac{\lambda_0^3}{V_{\text{eff}}}. \tag{1.3}$$

Here we have used the relation of N_{trips} to the cavity length L and decay rate κ, $N_{\text{trip}} = c/\kappa L$, the definition of quality factor of the cavity $Q = \omega_c/\kappa$ and the volume of the cavity mode $V_{\text{eff}} = A_{\text{eff}} L$. From this expression, it is obvious that the strong atom-light interaction can be achieved by making a high quality-factor cavity with a small mode volume. Since the initial demonstration in conventional Fabry-Perot cavities [82, 155, 183], different types of cavities have been explored in experiment [7, 44, 184, 187] and a Purcell factor on the order 10~100 can be reached.

The cavity QED approach represents a state-of-the-art for achieving strong single atom-light interactions. One can further increase the overall atom-light interactions by making the photon interact with atom assembles of large atom numbers N_a, as

shown in Fig. 1.1 (c). Despite a relatively weak single atom-light coupling, this approach in itself has find many applications including quantum memories for light [41, 59], spin squeezing [117] and long distance quantum communications [53]. Furthermore, when the light propagation phase is negligible compared to the atom ensemble dimension, the light decayed from atoms in the ensemble will sum up coherently, leading to a collective decay rate proportional to atom number N_a. This effect is called Dicke superradiance as it is first realized by Dicke in 1954 [50]. It is worth mentioning that in an optical cavity, the resonant light forms a standing wave pattern without propagation phase. As a result, for N_a atoms inside the optical cavity with the cavity resonance matching the atomic transition, the N_a atoms will form a "super-atom" with collective decay rate $N\Gamma_{\text{cav}}$. The Purcell effect for the "super-atom" is

$$P_{\text{cav,super}} = N_a \frac{\Gamma_{\text{cav}}}{\Gamma'} \propto N_a N_{\text{trips}} \frac{\sigma_0}{A_{\text{eff}}} \propto N_a Q \frac{\lambda_0^3}{V_{\text{eff}}}. \tag{1.4}$$

In our previous discussion, the atom is simplified as a two-level atom with a fixed scattering cross-section σ_0. Strong single atom-light interactions are achieved by engineering the properties of the light field. As the atom-light interaction is proportional to the atomic dipole moment $|\mathbf{d}| = e|\mathbf{r}|$. For real atoms, an alternative approach to increase the atom-light interaction is by exciting the atom to the Rydberg state with high principle quantum number n (n is typically between 50∼100 [28]), as illustrated in Fig. 1.1 (d). As the Rydberg state dipole moment scales with n^2 and the lifetime scales with n^3, the Purcell factor for light interacting with Rydberg atoms scales with n^5. The strong interactions between atom-light and atom-atom within this Rydberg approach provide a remarkable platform for studying nonlinear quantum optics [39, 184] and many body physics [21, 28].

1.2 Atom-light interaction on nanophotonics devices

In the previous section, we have presented the conventional ways for achieving strong atom-light interaction, which are typically implemented in a macroscopic, free-space setup. Despite many experimental successes in achieving strong atom-light interaction in the conventional interfaces, there has also been an effort for over a decade to migrate from free-space to micro/nanophotonic platforms [3, 7, 66, 67, 182, 191] for a number of motivations. First, as suggested in Eq. 1.3, nanophotonic cavities can lead to strong atom-light interactions with an achievable mode volume on the order of λ^3 [187]. Besides, the photonic systems fabricated from the state-of-the-art lithographic techniques provide excellent robustness and

scalability beyond the conventional atom-light interfaces, which is promising for the realization of quantum internet with chip-scale quantum nodes [110]. While these original motivations are largely centered on improving upon free-space approaches, the integration of ultra-cold atoms with nanophotonic devices also creates new paradigms for atom-photon interactions [40, 124]. As we will show shortly, the complexity of fields and dispersions in nanophotonic systems give rise to a variety of unanticipated opportunities, namely the chiral interactions between atoms and light [124] and the atom-photonic bound state [101].

One of the basic nanophotonic structures is the unstructured waveguide, as illustrated in Fig. 1.2 (a). As the light propagates in the dielectric waveguide with group velocity $v_g < c$, the Purcell factor for an atom next to the unstructured waveguide is modified as

$$P_{\mathrm{wg}} = \frac{\Gamma_{1\mathrm{D}}}{\Gamma'} \propto \frac{c}{v_g} \frac{\sigma_0}{A_{\mathrm{eff}}}. \tag{1.5}$$

Here the A_{eff} is the optical effective mode area which is related to the design of the waveguide and the atom position. For example, for atom trapped in the gap center of a slot waveguide with dimensions described in Ref. [157], the mode area A_{eff} can be as small as $0.1\lambda^2$. However, for the enhancement from slow group velocity in the unstructured dielectric waveguide, it is typically limited by the material refractive index n_g which is of order unity.

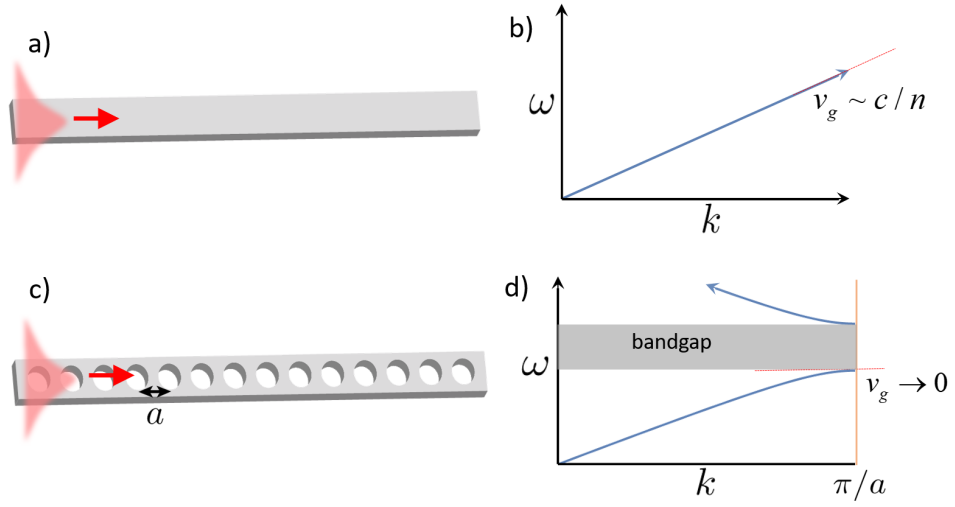

Figure 1.2: a) An illustration of unstructured waveguide b) The dispersion relation for unstructured waveguide c) Illustration photonic crystal waveguide. d) Dispersion relation for photonic crystal waveguide

Large reduction in group velocity can be achieved by artificial structures, namely the

photonic crystal waveguides. As illustrated in Fig. 1.2 (c), the periodic modulation of the waveguide creates a periodic lattice for the light, modifies the dispersion relation for light propagating on it. Similar to the electrons in solid state lattices, light propagating on photonic crystal waveguides leads to the formation of propagating band and band gap, as shown in Fig. 1.2 (d). The group velocity of light can be generally evaluated from $v_g = d\omega/dk$, corresponding to the slope of the dispersion relation in the band diagram. Near the band-edges, the group velocity is reduced and finally approaches to zero at the band-edge. This reduction of group velocity leads to the slow light enhancement of atom-light interaction. For example, for the alligator photonic crystal waveguide (APCW) reported in Ref. [200], a group index $n_g \sim 10$ is observed. For atom trapped in the gap of the APCW with a mode area $A_{\text{eff}} \simeq 0.3\lambda^2$, this leads to a single atom Purcell factor ~10. In a more recent design of the Slot Photonic Crystal Waveguide (SPCW) reported in Ref. [204], the group index can be further increased to ~ 40 and the estimated Purcell factor is of order ~100, which is comparable to the interaction strength in the state-of-the-art cavity QED. However, we emphasize that unlike the cavity QED case where strong atom-light coupling relies on small mode volume, the slow light enhancement in the photonic crystal waveguide is capable of mediating long-range atom-atom interactions by way of the guided mode.

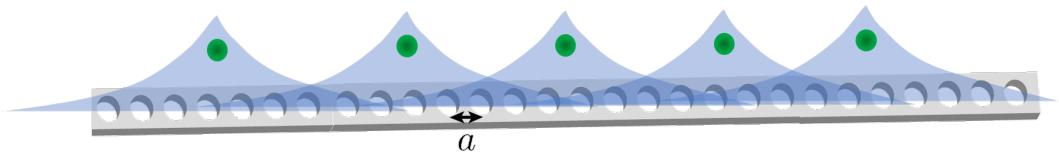

Figure 1.3: Atoms coupled to the bandgap of a photonic crystal waveguide. As light cannot propagate in photonic bandgap, the atoms and the emitted photons form atom-photon bound states

Apart from the slow-light enhancement near the photonic crystal band edge, what makes the photonic crystal waveguide most interesting for atom-light interactions is the physics inside the photonic bandgap. As indicated with gray area in Fig. 1.2 (d), the photonic bandgap is a region in frequency that light with frequencies within this range cannot propagate inside the photonic crystal waveguide. Imagine that an excited atom is coupled to the photonic crystal waveguide but with transition frequency within the bandgap, as shown in 1.3. The atom can still emit a photon into the structure, but the photon cannot propagate inside the photonic crystal waveguide due to the photonic bandgap. As a result, the photon will be localized near the atom

position with an exponential decay length L_d, forming an atom-photonic bound state [101]. When atoms are placed next to each other with spacings less than L_d, as illustrated in Fig. 1.3, the incoherent interaction between the field and the atoms is greatly suppressed while the coherent exchange between atoms along the device can still present. The physics of coherent excitation exchange within the atoms chains next to the photonic crystal waveguide can be directly mapped to a 1D spin chain [52]. Interestingly, the decay length L_d is a function of the detuning to band edge $\Delta_{\mathrm{BE}} = \omega - \omega_{\mathrm{BE}}$ and can vary from the length of a few unit cells (when ω in the center of bandgap) to infinite long (when $\omega = \omega_{\mathrm{BE}}$). This flexibility makes the photonic crystal waveguide a unique platform to explore many-body systems of photons and atoms with tunable interaction ranges.

Besides the tunable-range interactions in the photonic bandgap, the complexity in the fields within the nanostructures can be engineered to study the chiral quantum optics [124] where the coupling of atom and photons are taken place in a directionally dependent way, even if the system is nominally mirror symmetric. Furthermore, the guided mode of the nanophotonic structure can form stable lattice for trapping atoms with lattice geometry defined by nanostructure from precision nanofabrication. This provides a practical platform to achieving subwavelength atomic arrays with strong photon mediated atom-atom interaction for investigating novel quantum many-body matter [71].

In Chapter 2 and Chapter 3, we will give a more detailed and more formal description of atom-light interactions on nanophotonics. Specifically, Chapter 2 is dedicated to the basic theory of atom-light interactions with two-level atoms on quasi-1D structures while Chapter 3 provides a connection between the basic theory and the real world practices of atom-light interactions on nanophotonic devices.

1.3 Motivation of the thesis

While exciting theoretical opportunities of atoms coupled to nanophotonics have emerged, this research of integrating atoms and nanophotonics only moves forward in the laboratory by advancing nanophotonic device fabrication and by integrating these novel devices into the realm of ultracold atoms. However, in comparison to the rapidly expanding theoretical literature, to date experimental progress has been modest. Important experimental lab systems include optical nanofibers, where $\simeq 10^3$ atoms have been trapped $\simeq 220$ nm from fiber surfaces [66, 191], dispersion engineered photonic crystal cavities [164, 182, 184] and waveguides [33, 68, 86],

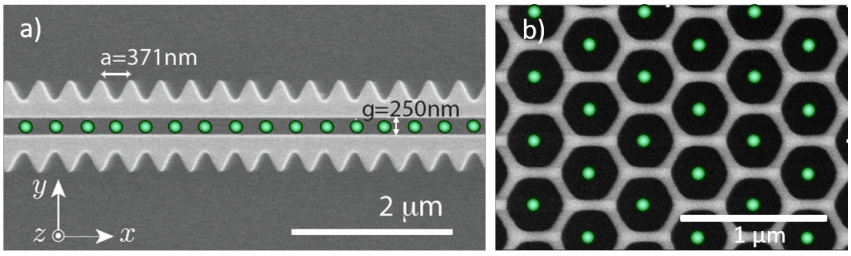

Figure 1.4: Schematic for building nanoscopic atomic arrays with one atom per unit cell in (a) 1-D alligator photonic crystal waveguide (APCW) [67, 200] and (b) 2-D honeycomb photonic crystal lattice [204], respectively. In both cases the silicon nitride structures (gray) are suspended above an underlying silicon substrate (dark background). Green spheres represent the yet to be achieved trapped single atoms.

where strong atom-photon coupling and collective atom-atom interactions have been observed, albeit with only a few atoms trapped $\simeq$ 150 nm from dielectric surfaces. A grand challenge for this emerging field is the laboratory attainment of one and two-dimensional atomic lattices with high filling fraction near or within the nanophotonic structures. This major experimental difficulty originates from the nature of fields confined in nanophotonic systems, such as their polarization and dispersion relation, which can be quite different than in free space. As a result, techniques from conventional atomic physics toolbox of loading, cooling, and trapping free-space atoms do not immediately apply when it comes to confining atoms within nanoscale regions of dielectric structures.

In this thesis, we propose a novel protocol for achieving high filling fraction atom arrays on nanophotonic structures by integrating optical tweezer arrays and nanophotonic devices, as illustrated in Fig. 1.5 (a) for 1D APCW and (b) for 2D photonic crystal slab. This research of atom assembly on nanophotonic structures is inspired

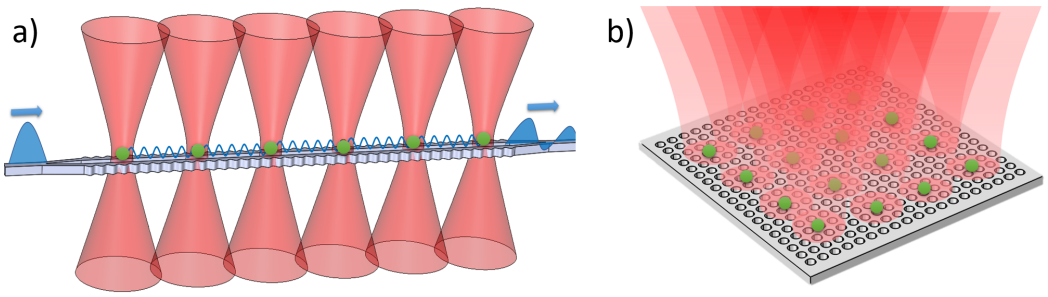

Figure 1.5: a) 1D atom array on the APCW b) 2D atom array on a square photonic crystal slab

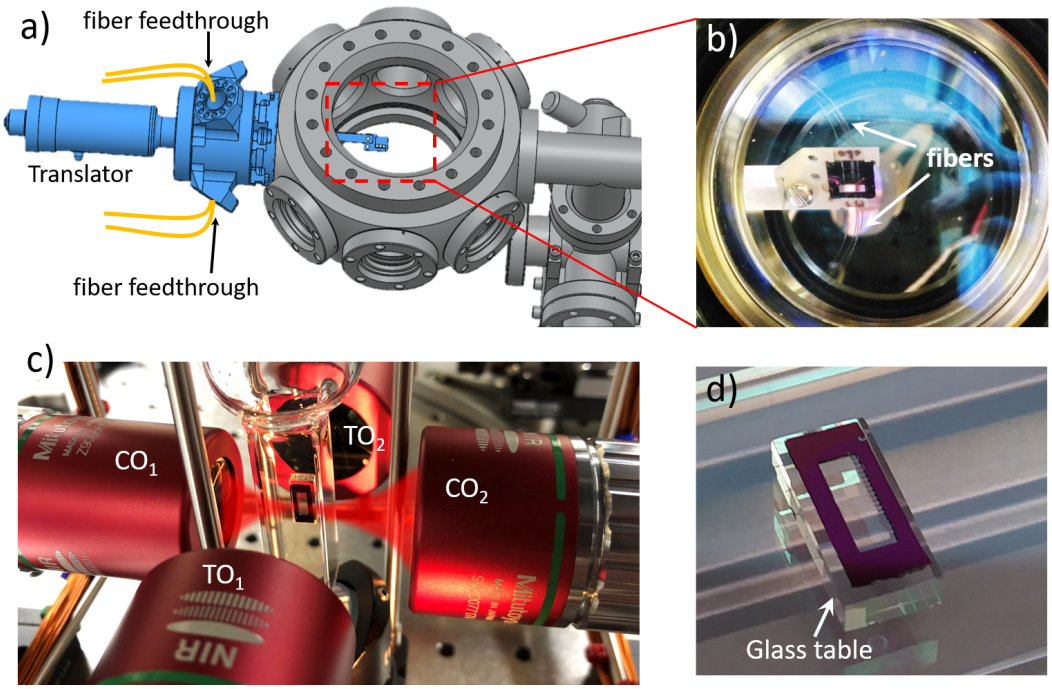

Figure 1.6: (a) The 'old' experimental setup consists of a 'bulky' metal chamber with fiber feedthroughs connecting to the photonic chip hold inside the chamber by a long mechanical arm. (b) A zoomed image of the chip inside the vacuum chamber, with the fibers indicated by white arrows. (c) The new advanced apparatus for integrating optical tweezers and free-space coupling. The chip is silicate bonded inside the glass cell with red focused beam indicating the free-space coupling. (d) A photograph of the assembled free-space coupling chip and its supporting glass table. Fig. (a) courtesy of Akihisa Goban, Fig. (c, d) adapted from Ref. [125] with modifications.

by recent exciting progress in free-space atom assembly [16, 17, 57]. However, as we will show in Chapter 4, direct atom assembly on the surface of nanostructure is rather challenging due to inefficient imaging tools and short trapping lifetime near the dielectric surfaces. Instead, we propose to circumvent these difficulties by first assembling the atom array in free-space and then transfer the atom array to the target positions on device. This method takes advantages of well-developed techniques in free-space atom assembly [16, 17, 57] but requires efficient transfer of atom arrays from free-space to nanophotonic devices. From a series of numerical Monte-Carlo simulations in Chapter 4, we show that the possibility of nearly deterministic transfer with the side-transfer technique [182] for a variety of nanostructures. Different from the free-space counterpart, our new proposal should enable subwavelength atom arrays with complex patterns defined by precision nanofabrication. The integration

of optical tweezers with nanophotonics could largely extend the ability of precise control of the position and state of the surface trapped atom. As we suggested in Chapter 4, a simple experiment with two atoms on the nanophotonic device could allow one to map the two-body Green's function of the structure which provides full information for describing atom-light interactions on nanostructure.

To demonstrate the basic principles behind this new proposal, we have designed and built an advanced apparatus with a compact footprint, as shown in Fig. 1.6. As a comparison, an illustration of the previous generation of experimental setup is shown in Fig. 1.6 (a, b). Through a series of technical innovations, namely 1) a vacuum-compatible silicate-bonding technique, 2) a free-space coupling with 'Y-couplers' and 3) efficient loading and transport of tweezer array with single atoms, our new apparatus overcame several significant experimental barriers in previous experiments, making a significant step towards atom assembly near nanophotonic structures. The details about the new advanced apparatus will be presented in Chapter 5.

In Chapter 6, we have proposed a novel atom direct delivery scheme with optical tweezers by exploiting the rapid spatial variation of the Gouy phase of radial Laguerre-Gauss beams. As illustrated in Fig. 1.7, optical tweezers of the super-

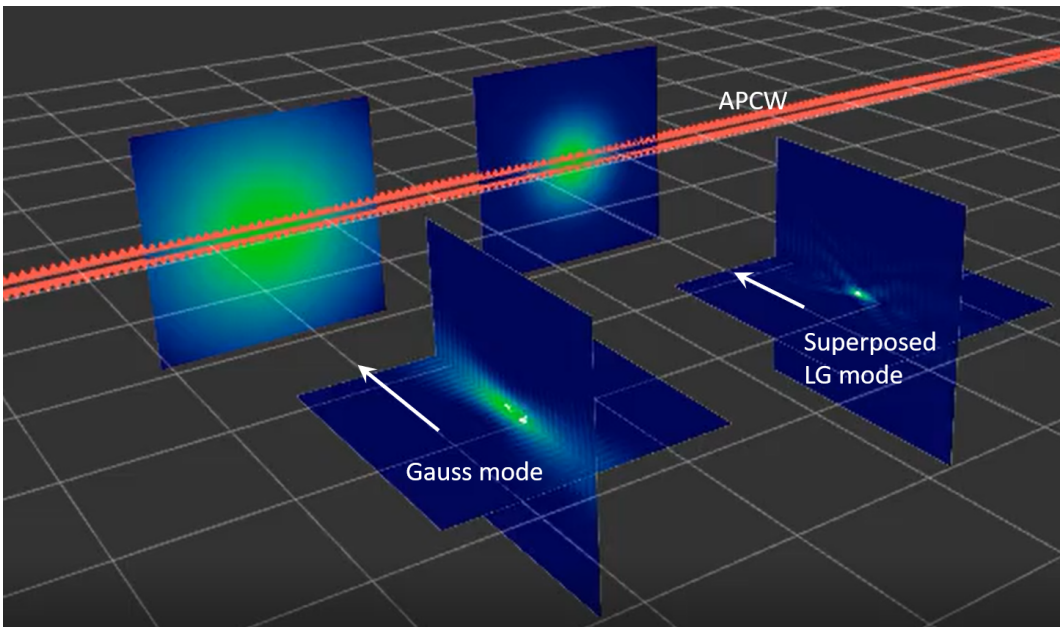

Figure 1.7: An Illustration of atom delivery to the APCW with *left*: Gauss beam and *right*: the superposed Laguerre-Gauss beam. The white arrows indicate the beam moving directions. Image courtesy of Jean-Baptiste Béguin .

posed Laguerre-Gauss beam lead to a significant reduction in the axial dimension as compared to the Gaussian beam. Such axial reduction can be applied to efficiently delivery atoms 'straightly' from free-space to complex nanostructures, such as 2D photonic crystal slabs. Besides, a more general discussion on the link between apodization and the smallest axial dimension of the focus is presented in Chapter 6. The optical tweezer formed by the superposed Laguerre-Gauss beams may find important applications in the communities of general atomic physics and super-resolution imaging.

Finally, in Chapter 7, we will investigate the optomechanical properties of the photonic crystal waveguides for the case of the APCW. We show that due to their unique dispersion relations, the optomechanical coupling in a photonic crystal waveguide cannot be simply described by the conventional cavity optomechanics framework or the unstructured waveguide optomechanics framework. This new degree of freedom in the atom-nanophotonic systems may provide opportunities to study the strong coupling of atoms, photons and phonons within a single photonic crystal waveguide.

Chapter 2

ATOM-LIGHT INTERACTIONS IN NANOSTRUCTURES: A SIMPLE STORY

2.1 Introduction

In this chapter, we will introduce the basic theory of atom-light interactions in nanostructures. To simplify our discussion, we restrict our discussion to two-level atoms on 1D or quasi-1D structures. The goal here is to capture the essential physics of atom-light interactions in nanostructures without distracting to complicated experimental details (which I will discuss in detail in Chapter 3). Two different approaches are presented here, namely the transfer matrix model and the Green's function approach. I will start with the simple transfer matrix model for a 1D photonic crystal waveguide. The goal there is to find the basic scaling laws for atom-light interaction with respect to device parameters and to understand the origin of enhancement for atom-light interactions. With a basic understanding of the scaling laws for atom-light interactions in the 1D photonic waveguides, we then turn to a more powerful Green's function approach. We will see how the complex optical properties of nanostructures are encoded in the atom-light interactions and how multiple atoms interact with each other in the presence of complex optical structure. After a general theory of atom-light interactions with the Green's function approach, we will give specific examples on quasi-1D nanostructures to understand the basic physics and differences behind them. This material presented in this chapter is largely based on previous published (mostly Ref. [11]) and unpublished works by Ana Asenjo-Garcia (who is now a professor at Columbia University) and Jonathon Hood (who is now a professor at Purdue University). Other main references for the Green's function approach are Ref. [30] and works from Welsh and his colleagues Refs. [31, 74].

2.2 Transfer matrix model of 1D photonic crystal waveguide

The transfer matrix method

For wave propagation in one dimensional structures, the electric field (here we consider a scalar field E for simplicity) can be decomposed into right-going and left-going field as $E = E^{+}e^{ikx} + E^{-}e^{-ikx}$, where $E^{+/-}$ denotes the amplitude of right/left-going field and k is the propagation wave-vector ($k = n_0\omega/c$ and n_0 is the refractive index which we will set to 1 in the rest of our discussion) as illustrated in

Fig. 2.1 (b). The transfer matrix $\mathcal{M}$ describes the relation between the field on the left hand side to the right hand side by

$$\begin{bmatrix} E_R^+ \\ E_R^- \end{bmatrix} = \mathcal{M}_\delta \begin{bmatrix} E_L^+ \\ E_L^- \end{bmatrix}. \tag{2.1}$$

While the transfer matrix method can apply to any potential in general, here, for

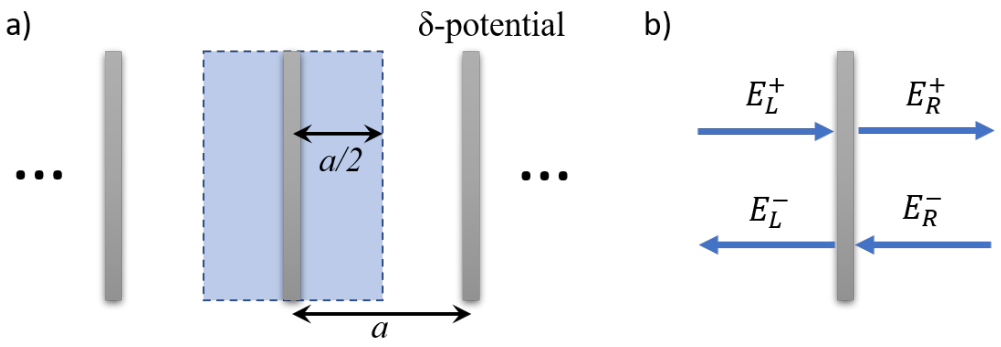

Figure 2.1: (a) Sketch of the system. The gray slabs depict δ-function potentials, characterized by reflection and transmission coefficients. We define a symmetric unit cell that consist of a barrier in the center and free propagation over distance $a/2$ on each side (blue shaded area). (b) Convention for left (-) and right (+) propagating electric fields at the left (L) and right (R) sides of a barrier.

simplicity, we choose a δ-function potential barrier as our basic element in the 1D structure. The δ-function barrier is characterized by reflection (r) and transmission (t) coefficients that are related by continuity of the electric field ($t = 1+r$). The field amplitude at right and left side of the barrier (as illustrated in 2.1b) can be further related by the continuity of the field

$$\begin{aligned} E_R^+ &= tE_L^+ + rE_R^-, \\ E_L^- &= rE_L^+ + tE_R^-. \end{aligned} \tag{2.2}$$

This leads to a transfer matrix for the δ-function barrier as

$$\mathcal{M}_\delta[\zeta] = \frac{1}{t}\begin{bmatrix} t^2 - r^2 & r \\ -r & 1 \end{bmatrix} = \begin{bmatrix} 1 + i\zeta & i\zeta \\ -i\zeta & 1 - i\zeta \end{bmatrix}, \tag{2.3}$$

with $\zeta \equiv -ir/t$. Note that transfer matrices in the form only require the continuity equation ($t = 1 + r$) and thus can be applied to any planar scatterer (either lossy or lossless). In this section, we consider only lossless scatterers for which energy conservation ($|r|^2 + |t|^2 = 1$), r has to be an imaginary number and as a result, ζ is a real number. For simplicity, we assume $\zeta > 0$ in our following discussion.

For free-space propagation, the transfer matrix for a propagation distance x is

$$\mathcal{L}[x] \equiv \begin{bmatrix} e^{ikx} & 0 \\ 0 & e^{-ikx} \end{bmatrix}. \tag{2.4}$$

With these two transfer matrix we can further construct the transfer matrix for a 1D Fabry-Perot cavity by a pair barriers separated by distance L, namely

$$\mathcal{M}_{\mathrm{FP}} = \mathcal{M}_{\delta}[\zeta_1]\mathcal{L}[L]\mathcal{M}_{\delta}[\zeta_2], \tag{2.5}$$

and construct the transfer matrix for 1D finite/infinite photonic crystal waveguides with array barriers with spacing a

$$\mathcal{M}_{\mathrm{pcw}} = \prod_i \mathcal{M}_{\delta}[\zeta_i]\mathcal{L}[a]. \tag{2.6}$$

It can be shown that for any lossless 1D structure, the transfer matrix $\mathcal{M}_{\mathrm{tot}}$ can be generally expressed in terms of the overall transmission (t_{tot}) and reflection (r_{tot}) coefficient as

$$\mathcal{M}_{\mathrm{tot}} = \begin{bmatrix} 1/t^*_{\mathrm{tot}} & r_{\mathrm{tot}}/t_{\mathrm{tot}} \\ r^*_{\mathrm{tot}}/t^*_{\mathrm{tot}} & 1/t_{\mathrm{tot}} \end{bmatrix}. \tag{2.7}$$

Thus, we can calculate the overall transmission and reflection coefficient from the elements of transfer matrix $\mathcal{M}_{\mathrm{tot}}$ as

$$t_{\mathrm{tot}} = 1/\mathcal{M}^{22}_{\mathrm{tot}}, \tag{2.8}$$

$$r_{\mathrm{tot}} = \mathcal{M}^{12}_{\mathrm{tot}}/\mathcal{M}^{22}_{\mathrm{tot}}. \tag{2.9}$$

The transfer matrix model of a 1D photonic crystal waveguide

In this section, we will present the transfer matrix model of a 1D photonic crystal waveguide (PCW). As illustrated in Fig. 2.1 (a), we model the PCW as infinite periodic system of δ-function potential barriers separated by a distance a. The transfer matrix for the unit cell (as indicated in the blue area in Fig. 2.1a) can then be written as

$$\mathcal{M}_{\mathrm{cell}} = \mathcal{L}[a/2]\mathcal{M}_{\delta}\mathcal{L}[a/2] = \begin{bmatrix} (1+i\zeta)e^{ika} & i\zeta \\ -i\zeta & (1-i\zeta)e^{-ika} \end{bmatrix}. \tag{2.10}$$

As $\det\mathcal{M}_{\mathrm{cell}} = 1$, the two eigenvalues of unit-cell transfer matrix take the form $\lambda_{\pm} = e^{\pm iqa}$ (as $\lambda_+\lambda_- = \det\mathcal{M}_{\mathrm{cell}} = 1$). From the Bloch's theorem that the eigenmodes of an infinite, periodic structure are Bloch modes with Bloch index q as quasi-momentum in the Bloch space. The dispersion relation of the 1D infinite array (the

relationship between ω and q) can be obtained from the trace of the unit-cell transfer matrix

$$\cos qa = \cos ka - \zeta \sin ka. \tag{2.11}$$

For non-zero ζ, this dispersion equation does not always have a real solution of q for any ω, as the left hand side (LHS) of Eq. 2.11 is bounded within $[-1, 1]$ while the right hand side (RHS) is bounded with $[-\sqrt{1+\zeta^2}, \sqrt{1+\zeta^2}]$. This suggests a bandgap is formed in the 1D photonic crystal waveguide, as illustrated in Fig. 2.2 (a) as an example. For frequencies lie in between the two band-edge frequencies ω_- and ω_+, light cannot propagate inside this 1D lattice. The band-edge frequencies ω_+ and ω_- can be determined by setting the RHS of Eq. 2.11 equal to 1

$$\begin{aligned} \omega_+ &= \frac{\pi c}{a} \\ \omega_- &= \frac{c}{a} \cos^{-1}\left(\frac{\zeta^2 - 1}{\zeta^2 + 1}\right). \end{aligned} \tag{2.12}$$

Here we restrict the solution within the Brillouin zone $q \in [-\pi/a, \pi/a]$. For small ζ ($\zeta \ll 1$), $\omega_- \simeq \frac{\pi c}{a}(1 - 2\zeta/pi)$ and the size of bandgap is

$$\delta\omega_{\mathrm{BG}} \equiv \omega_+ - \omega_- \simeq \frac{2\zeta c}{a}. \tag{2.13}$$

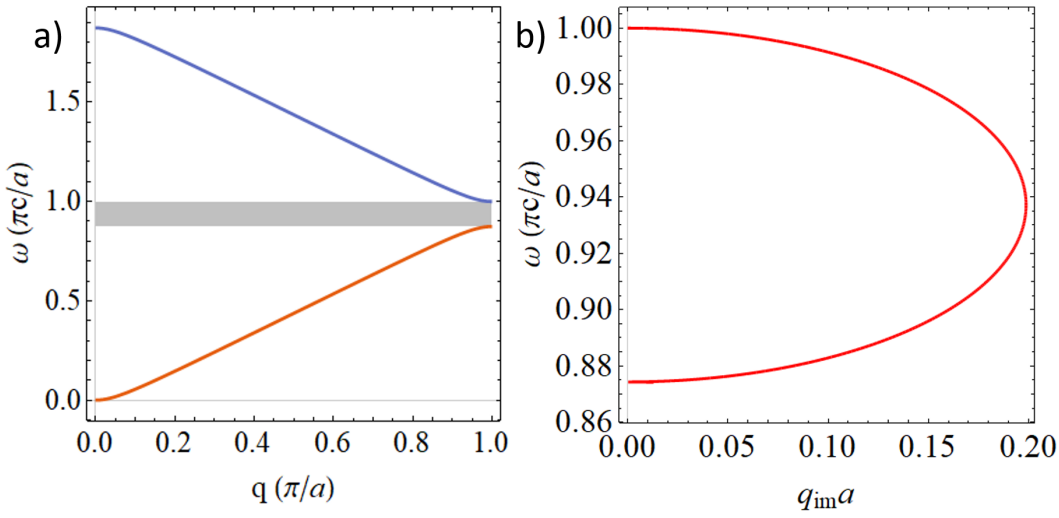

Figure 2.2: (a) Band diagram for $\zeta = 0.2$. The band gap is indicated with gray area. (b) Figure of the imaginary propagation constant q_{im} inside the bandgap as a function of ω, with $\zeta = 0.2$.

Intuitively, this suggests that the size of bandgap can be tuned by the scatter's reflectivity and larger reflectivity leads to larger bandgap. From these simple equations

(Eq. 2.12 and Eq. 2.13), we can have a quick estimation of a and ζ by aligning ω_- and ω_+ to Cs atom main transitions at D1 and D2 lines to find $a \simeq 426$ nm and $\zeta \simeq 0.064$. As a comparison, for real structures such as the APCW, we fitted $n_0 \sim 1.7$, $a = 370$ nm and $\zeta \sim 0.2$ (see Chapter 3 for detail).

To get insights inside the bandgap, we rewrite Eq. 2.11 with a complex propagation constant $q_{\text{gap}} = q_{\text{re}} + iq_{\text{im}}$

$$\cos q_{\text{re}}a \cosh q_{\text{im}}a + i \sin q_{\text{re}}a \sinh q_{\text{im}}a = \cos ka - \zeta \sin ka. \tag{2.14}$$

As the RHS of Eq. 2.14 is in a real domain, we require $\sin(q_{\text{re}}a) = 0$ to keep the LHS also in the real domain. This led to $q_{\text{re}} = \pi/a$ and

$$\cosh q_{\text{im}}a = -\cos ka + \zeta \sin ka. \tag{2.15}$$

For near the band-edge (but in the bandgap), we get

$$\begin{aligned} q_{\text{im}} &\simeq \sqrt{2(-\cos ka + \zeta \sin ka - 1)} \\ &\simeq \sqrt{2\zeta}\frac{|\delta\omega|a}{c}, \end{aligned} \tag{2.16}$$

with $\delta\omega = \omega - \omega_{\text{BE}}$. The maximum q_{im} is at the center of the gap and

$$q_{\text{im,max}} = \frac{\text{arccosh}\sqrt{1+\zeta^2}}{a}. \tag{2.17}$$

Fig. 2.2 (b) shows an example of the imaginary propagation constant q_{im} inside the bandgap for $\zeta = 0.2$. The maximum $q_{\text{im,max}}a \simeq 0.2$ which indicates the e^{-1} decay length is $\simeq 5a$.

As shown in Chapter 1, the group velocity v_g is an important figure of merit for slow-light-enhanced atom-light interactions. This can be derived from the dispersion relation (Eq. 2.11) as

$$v_g \equiv \frac{d\omega}{dq} = \frac{c \sin qa}{\sin ka + \zeta \cos ka}. \tag{2.18}$$

It worth noting that v_g is positive for lower band but negative for upper band. Typically, small group velocity is achieved near the band-edge. This can be shown by making an expansion near the band-edge ($\delta q \equiv \pi/a - q$). The dispersion relation (Eq. 2.11) and group velocity (Eq. 2.18) near the upper and lower band-edge can be approximated as

$$\omega \simeq \omega_\pm \pm \frac{ca}{2\zeta}\delta q^2 \tag{2.19}$$

$$v_g \simeq \mp\frac{ca}{\zeta}\delta q. \tag{2.20}$$

From Eq. 2.19, when ω tuned to the band-edge, the group velocity approaches to zero near band-edge and the group index $n_g \equiv c/v_g$ diverges, corresponding to a Van Hove singularity at the band-edge.

We can further calculate the field distribution from the eigenvectors of the unit-cell matrix which take the form

$$\begin{aligned} \mathbf{u}_q &= \frac{1}{\sqrt{1+f^2}} \begin{bmatrix} 1 \\ f \end{bmatrix}, \\ \mathbf{u}_{-q} &= \frac{1}{\sqrt{1+f^2}} \begin{bmatrix} f \\ 1 \end{bmatrix}, \end{aligned} \tag{2.21}$$

where f is defined as

$$f = -\frac{\sqrt{n_g^2 - 1}}{n_g + 1} = -\mathrm{sgn}(n_g)\sqrt{r_g}, \tag{2.22}$$

and $r_g = (n_g - 1)/(n_g + 1)$ is the Fresnel reflection coefficient between two interfaces $n_1 = 1$ and $n_2 = n_g$. At the band-edge ($q = \pi/a$), we have $|n_g| \to \infty$ and $r_g \to 1$ and $f = 1$ for upper band and $f = -1$ for lower band.

The electric field and intensity within one unit cell can be expressed as

$$E_q(x) = \frac{1}{\sqrt{1+f^2}}(e^{ikx} + fe^{-ikx}), \tag{2.23}$$

$$|E_q(x)|^2 = \frac{1}{1+f^2}(1 + f^2 + 2f\cos 2kx). \tag{2.24}$$

where $0 < x < a$ with $x = 0$ corresponding to the left edge of the unit cell as shown in Fig. 2.3. This equation suggests that the eigenmode with Bloch wavevector +q is a summation of right- and left-propagating field with ratio f. Thus, f can be interpreted as the reflection coefficient of an infinite lattice (for a plane wave e^{ikx} input).

For upper and lower band-edges, the electric field profiles take the form of a standing wave

$$E_{\mathrm{BE},+}(x) = \sqrt{2}\cos k_+ x = \sqrt{2}\cos\frac{\pi}{a}x, \tag{2.25}$$

$$E_{\mathrm{BE},-}(x) = -i\sqrt{2}\sin k_- x \simeq -i\sqrt{2}\sin\frac{\pi - 2\zeta}{a}x. \tag{2.26}$$

This also explains why the group velocity approaches to zero near the band-edge Eq. 2.19. As shown in Fig. 2.3, the intensity at the upper band band-edge (blue

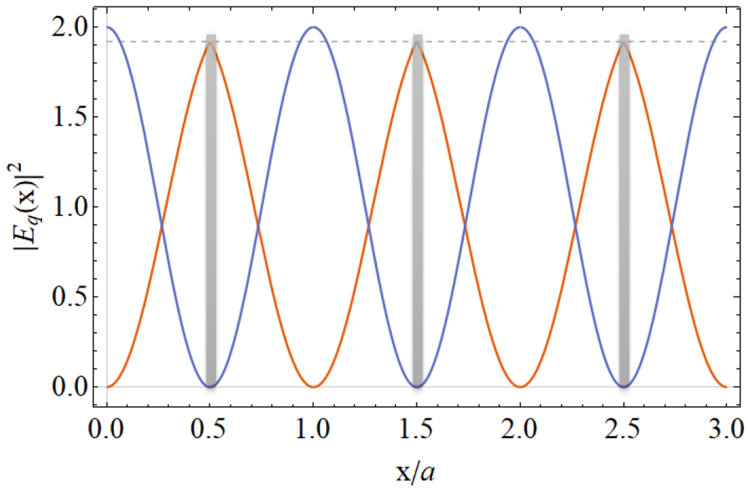

Figure 2.3: Bloch mode intensity at the band-edge for upper (blue curve) and lower (orange curve) with $\zeta = 0.2$. The scatterer positions are indicated with gray vertical bar.

curve) maximizes at the center between the scatters while the intensity at the lower band band-edge maximizes at the scatterer position. For this reason, the upper band is typically called as 'air band' as the intensity distribution concentrates more on the 'air' (lower index) part while the lower band is named as 'dielectric band' as the intensity distribution concentrates more on the 'dielectric' part (higher index, or here the scatter).

Additionally, the transformation $\mathcal{O}$ that diagonalizes the unit-cell matrix can be constructed from the eigenvectors:

$$\begin{aligned} \mathcal{O} &= \frac{1}{1-f^2}\begin{bmatrix} 1 & f \\ f & 1 \end{bmatrix}, \\ \mathcal{O}^{-1} &= \begin{bmatrix} 1 & -f \\ -f & 1 \end{bmatrix}. \end{aligned} \tag{2.27}$$

It is easy to check that

$$\mathcal{O}\mathcal{O}^{-1} = \mathcal{I} = \begin{bmatrix} 1 & 0 \\ 0 & 1 \end{bmatrix}, \tag{2.28}$$

and

$$\mathcal{O}\mathcal{M}_{\text{cell}}\mathcal{O}^{-1} = \Lambda = \begin{bmatrix} e^{iqa} & 0 \\ 0 & e^{-iqa} \end{bmatrix}. \tag{2.29}$$

These two equations will be useful later for simplifying the transfer matrix for a finite PCW.

Transfer matrix model of 1D finite scatterer array

In the previous section, we have discussed the properties of 1D infinite periodic structures. This corresponds to an ideal case, as there is no such infinite periodic structure in experiment. All PCWs we fabricated always have a finite size. Thus, it is important to understand the a finite photonic crystal waveguide with two boundaries. For a finite scatterer array with N unit cells, the total transfer matrix is written as

$$\mathcal{M}_N = \underbrace{\mathcal{M}_{\text{cell}}\mathcal{M}_{\text{cell}}...\mathcal{M}_{\text{cell}}}_{\text{N unit cell}} = \mathcal{M}_{\text{cell}}^N. \tag{2.30}$$

To simplify this expression, we insert the identity $OO^{-1} = \mathcal{I}$ into Eq. 2.30

$$\begin{aligned}\mathcal{M}_N &= OO^{-1}\mathcal{M}_{\text{cell}}OO^{-1}\mathcal{M}_{\text{cell}}...O^{-1}\mathcal{M}_{\text{cell}}OO^{-1} \\ &= O\Lambda^N O^{-1} = O\begin{bmatrix} e^{iNqa} & 0 \\ 0 & e^{-iNqa}\end{bmatrix}O^{-1} \\ &= \frac{1}{1-f^2}\begin{bmatrix} e^{iNqa} - f^2e^{-iNqa} & -2if\sin(Nqa) \\ 2if\sin(Nqa) & e^{-iNqa} - f^2e^{iNqa}\end{bmatrix}.\end{aligned} \tag{2.31}$$

This expression is particularly interesting as it suggests this 1D finite photonic crystal waveguide is equivalent to a Fabry-Perot cavity in the Bloch-space (as the propagation constant is q not k) with two 'mirrors' O and O^{-1} of reflectivity $r = f$. This reflectivity at the boundary can be intuitively understood as the mismatch of free-space k momentum and Bloch mode q quasi-momentum on the boundary.

The overall transmission (t_N) and reflection (r_N) coefficient can be calculated from the matrix element of $\mathcal{M}_N$ as

$$t_N = \frac{1}{\mathcal{M}_N^{22}} = \frac{1-f^2e^{iNqa}}{1-f^2e^{2iNqa}} = \frac{1}{\cos Nqa - in_g\sin Nqa}, \tag{2.32}$$

$$r_N = \frac{\mathcal{M}_N^{12}}{\mathcal{M}_N^{22}} = -\frac{2if\sin(Nqa)}{e^{-iNqa} - f^2e^{iNqa}}. \tag{2.33}$$

Fig. 2.4 shows the power transmission coefficient (or transmissivity) $T_N = |t_N|^2$ (red curves) and the power reflection coefficient (or reflectivity) $R_N = |r_N|^2$ (blue curves) for $\zeta = 0.2$, with two different unit-cell numbers, $N = 25$ in (a) and $N = 50$ in (b), respectively. One unique feature for the finite structure transmission compared with the infinite structure case is the formation of resonances near the band-edge. This agrees with previous observation of the equivalence to Fabry-Perot cavity in Bloch

q-space from the total transfer matrix (Eq. 2.31) and we expect the resonances near the band-edge are narrower due to larger group index mismatch and thus larger reflectivity at the boundary. Another interesting feature is the position and linewidth of the resonances are strongly related to the total number of unit cells, as comparing (a) and (b). As so, it will be interesting to see the resonance position and linewidth scaling with the total unit cell number N.

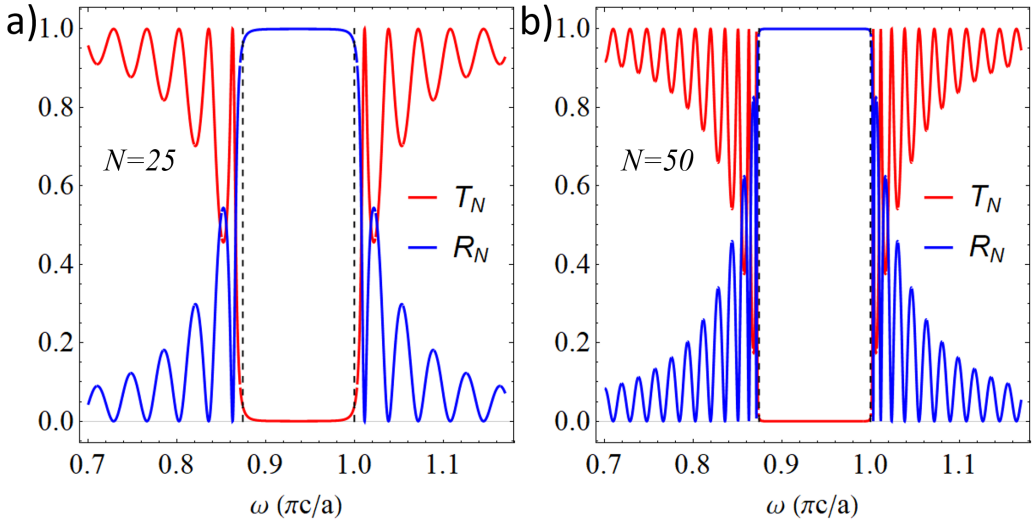

Figure 2.4: Power transmission and reflection spectrum for 1D finite periodic structure, with (a) $N = 25$ unit-cells and (b) $N = 50$ unit-cells. The solid curves (red for transmission and blue for reflection) are calculated from Eq. 2.32 with the two black dashed lines indicate the position of band-edge for infinite structure. $\zeta = 0.2$ for both (a) and (b).

The resonances' positions can be calculated from $r_N = 0$ or equivalently $\sin(Nqa) = 0$ as

$$q_m = (1 - \frac{m}{N})\frac{\pi}{a}, \tag{2.34}$$

where the resonance index m is counted from band-edge, for example, the first resonance ($m = 1$) from the band-edge has $q_1 = (1 - 1/N)\pi/a$. For resonances near the band-edge, the resonances' frequencies can be found approximately by using Eq. 2.19

$$\omega_{\pm,m} = \omega_{\pm} \pm \frac{\pi^2 c}{2\zeta a}\frac{m^2}{N^2}. \tag{2.35}$$

This equation can be used to infer the band-edge position from experimentally measured transmission spectrum (see Chapter 3 for details). One can further calculate

the group velocity at resonances near band-edge based on Eq. 2.19 and get

$$v_{g,m} = \pm \frac{\pi c}{\zeta} \frac{m}{N}. \tag{2.36}$$

It is worth noting that this group velocity alone may not fully characterize the interaction strength of atom-light for such 1D finite structure as it does not account for the cavity enhancement from the boundary reflections. This is different from the case in an infinite PCW.

For probe frequency ω close to resonance ω_m, we can approximate $\cos(Nqa) \simeq (-1)^{N-m} + O((q-q_m)^2)$, $\sin(Nqa) \simeq N(q-q_m)a + O((q-q_m)^2)$ and $q - q_m \simeq n_g(\omega - \omega_m)/c$, we get

$$t_N \simeq \frac{(-1)^{N-m}}{1 - i(-1)^{N-m} n_g^2 Na(\omega - \omega_m)/c}. \tag{2.37}$$

Comparing this expression to a Lorentzian

$$\mathcal{L}_m(\omega) = \frac{(-1)^{N-m}}{1 - 2i(-1)^{N-m}(\omega - \omega_m)/\kappa_m}. \tag{2.38}$$

We can extract the effective full-width at half-maximum (FWHM) linewidth κ_m as

$$\kappa_m \simeq \frac{2c}{n_g^2 Na}. \tag{2.39}$$

For near the band-edge, we have $n_g \gg 1$ and the identity $\zeta^2 = (n_g^2 - 1)\sin^2(qa) \simeq n_g^2 m^2 \pi^2 / N^2$, we can rewrite κ_m in Eq. 2.39 as

$$\kappa_m \sim \frac{2m^2\pi^2 c}{\zeta^2 N^3 a}. \tag{2.40}$$

Here, we replicated the linewidth scaling m^2/N^3 as shown in Ref. [12].

2.3 The transfer matrix model with atoms in the story

Singe atom transfer matrix

In the previous section, we have presented the transfer matrix model for 1D infinite and finite PCWs. In this section, we will incorporate atoms into the transfer matrix model. Here, we neglect the quantum nature of the atom but only treated it as a narrow band lossy scatterer. For this reason, the transfer matrix theory here will be only valid for the low saturation limit.

Under the low saturation limit, we approximate a single atom as an narrow-band delta-function scatterer. The transfer matrix is very similar to $\mathcal{M}_\delta$ and can be

expressed as

$$\mathcal{M}_a[\zeta_0] = \begin{bmatrix} 1+i\zeta_0 & i\zeta_0 \\ -i\zeta_0 & 1-i\zeta_0 \end{bmatrix}, \tag{2.41}$$

with $\zeta_0 \equiv -i\frac{r}{t}$. The reflection coefficient r for an atom is given in Ref. [38] as

$$r = -\frac{\gamma_{1D}}{\gamma_{1D}+\Gamma'}\frac{1}{1-2i\Delta_A/(\gamma_{1D}+\Gamma')}, \tag{2.42}$$

where $\Delta_A = \omega - \omega_A$, $\gamma_{1D} = \frac{\sigma_0}{2A_{\text{eff}}}\Gamma_0$ is the decay rate into the 1D unstructured waveguide mode (without slow-light or cavity enhancement) with A_{eff} being the effective mode area and $\sigma_0 = 3\lambda_0^2/2\pi$ being the atom's radiative cross-section. Here we use the lower case γ_{1D} to differentiate it from slow-light and cavity enhanced Γ_{1D}. Γ' represents the decay rate into all other channels. Together with the continuity equation $t = 1 + r$, ζ_0 can be written as

$$\zeta_0 = i\frac{\gamma_{1D}}{\Gamma'}\frac{1}{1-2i\Delta_A/\Gamma'}. \tag{2.43}$$

Recall that energy conservation requires ζ being a real number. The ζ_0 of an atom is a complex number suggests an atom is a lossy narrow-band scatterer centered at ω_A with a Lorentzian linewidth Γ'.

Singe atom inside 1D infinite scatterer array

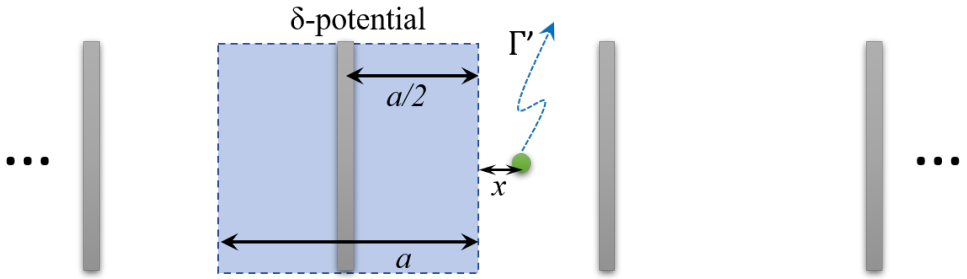

Figure 2.5: (a) Sketch of an infinite scatterer array with single atom (indicated with green dots) inside one unit cell. The distance x is measured from the edge of left-hand side unit cell ($x < 0$ if inside the left-hand side unit cell). Note that the atom is a 'lossy' scatterer with decay rate Γ' to all other channels.

For a single atom inside an infinite structure with position x in the cell ($-a/2 \leq x < a/2$) as illustrated in Fig. 2.5 (a), the total transfer matrix can be symbolically

written as

$$\begin{aligned} M_{\infty,\text{atom}} &= \underbrace{\ldots \mathcal{M}_{\text{cell}}}_{\infty \text{ unit cell}} \mathcal{L}[-x]\mathcal{M}_a[\zeta]\mathcal{L}[x] \underbrace{\mathcal{M}_{\text{cell}}\ldots}_{\infty \text{ unit cell}} \\ &= \underbrace{\ldots OO^{-1}\mathcal{M}_{\text{cell}}OO^{-1}}_{\infty \text{ unit cell}} \mathcal{L}[-x]\mathcal{M}_a[\zeta]\mathcal{L}[x] \underbrace{OO^{-1}\mathcal{M}_{\text{cell}}OO^{-1}\ldots}_{\infty \text{ unit cell}} \\ &= \Lambda^{\infty}O^{-1}\mathcal{L}[-x]\mathcal{M}_a[\zeta]\mathcal{L}[x]O\Lambda^{\infty}. \end{aligned} \tag{2.44}$$

From this expression, we see the atom inside the infinite PCW behaves like a 'dressed' atom in the Bloch q-space. The effective transfer matrix for the 'dressed' atom is

$$\begin{aligned} \mathcal{M}_{a,\text{eff}}[x] &= O^{-1}\mathcal{L}[-x]\mathcal{M}_{\text{a}}[\zeta]\mathcal{L}[x]O \\ &= \mathcal{L}[-l_{\text{eff}}(x)]\mathcal{M}_a[\zeta_{\text{eff}}(x)]\mathcal{L}[l_{\text{eff}}(x)], \end{aligned} \tag{2.45}$$

where we defined

$$\zeta_{\text{eff}}(x) = \zeta_0 \frac{1 + 2f\cos 2kx + f^2}{|1 - f^2|}, \tag{2.46}$$

$$l_{\text{eff}}(x) = x - \frac{1}{2k}\arg\left(\frac{1 + fe^{2ikx}}{1 + fe^{-2ikx}}\right). \tag{2.47}$$

Fig. 2.6 shows the plot of kl_{eff} for lower (a) and upper band (b). When atom is located near the Bloch mode intensity maximum, kl_{eff} can be well approximated as $kl_{\text{eff}} \sim 0$ for near upper band-edge and $\pi/2$ near the lower band-edge.

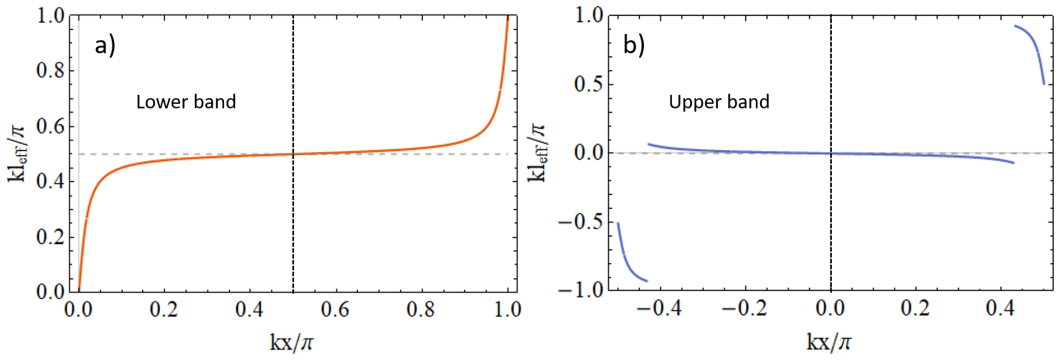

Figure 2.6: The effective length l_{eff} as a function of x for lower (a) and upper band (b). Here $k(l_{\text{eff}}/\pi$ is plotted vs. kx/π for $n_g = 10$ (or equivalently $f = -0.905$) for lower band and $n_g = -10$ (or equivalently $f = 0.905$) for upper band. The Bloch mode intensity maximum positions are indicated with gray vertical dashed lines.

To see the physics meaning of ζ_{eff}, we rewrite ζ_{eff} with Eq. 2.22 and Eq. 2.23 and we get

$$\frac{\zeta_{\text{eff}}(x)}{\zeta_0} = |n_g| \times |E_q(x)|^2 \tag{2.48}$$

This ratio can be absorbed into the definition of a spatial dependent enhanced coupling rate $\Gamma_{1D}(x)$

$$\boxed{\Gamma_{1D}(x) = \gamma_{1D} \times |n_g| \times |E_q(x)|^2} \tag{2.49}$$

This new expression for coupling rate is very intuitive and self-explained. It suggests the enhancement of coupling rate due to 1D infinite photonic crystal is the product of the group index and the normalized Bloch mode intensity at the position of atom. Typically, in the nano-fiber experiments[66, 191], $\gamma_{1D}/\Gamma' \sim 0.05$ when probing on resonance ($\Delta = 0$). In order to achieve $\Gamma_{1D}/\Gamma' \sim 1$ at the peak intensity of Bloch mode, the PCW group index n_g should be ~ 10.

We further calculate the transmission spectrum of the effective atom as

$$\begin{aligned} T(\Delta) &= \left|\frac{1}{1 - i\zeta_{\text{eff}}}\right|^2 = \frac{\Gamma'^2 + 4\Delta^2}{\Gamma_{\text{tot}}(x)^2 + 4\Delta^2} \\ &= 1 - \underbrace{\left(1 - \frac{\Gamma'^2}{\Gamma_{\text{tot}}(x)^2}\right)}_{\text{depth}} \underbrace{\frac{1}{1 + 4\Delta^2/\Gamma_{\text{tot}}(x)^2}}_{\text{width}}, \end{aligned} \tag{2.50}$$

where we defined the total decay rate $\Gamma_{\text{tot}}(x) = \Gamma_{1D}(x) + \Gamma'$.

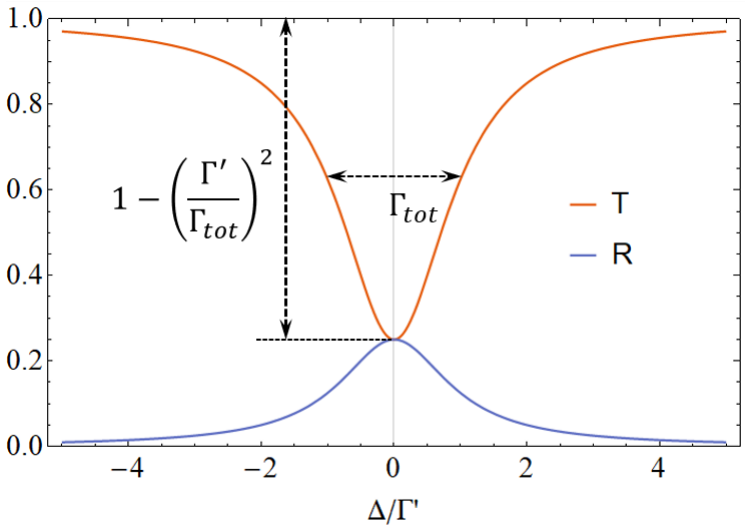

Figure 2.7: Example of power transmission of a single atom inside infinite 1D scatterer array with $\Gamma_{1D} = \Gamma'$.

Single atom inside 1D finite scatterer array

Now, let's consider a single atom inside a unit cell of a finite scatterer array with N_1 cell on the left side and N_2 cell on the right side ($N_1 + N_2 = N$). The atom position

x is defined as in the previous section with $-a/2 \leq x < a/2$. The total matrix can be written as

$$\begin{aligned}\mathcal{M}_{N,\text{atom}} &= \mathcal{M}^{N_2}\mathcal{L}[-x]\mathcal{M}_a[\zeta]\mathcal{L}[x]\mathcal{M}^{N_1} \\ &= \mathcal{O}\Lambda^{N_2}\mathcal{O}^{-1}\mathcal{L}[-x]\mathcal{M}_a[\zeta]\mathcal{L}[x]\mathcal{O}\Lambda^{N_1}\mathcal{O}^{-1} \\ &= \mathcal{O}\Lambda^{N_2}\mathcal{L}[-l_{\text{eff}}(x)]\mathcal{M}_a[\zeta_{\text{eff}}(x)]\mathcal{L}[l_{\text{eff}}(x)]\Lambda^{N_1}\mathcal{O}^{-1}.\end{aligned} \tag{2.51}$$

We can extract the new transmission coefficient with atom from the matrix element M_{22}, and divided by the transmission coefficient without atom, we get the normalized transmission as

$$\frac{t_{N,atom}}{t_N} = \frac{1}{1 - i\zeta_{\text{eff}} I(N_1, x)} \tag{2.52}$$

where

$$I(N_1, x) = \frac{(1 + fe^{2i\phi_1})(1 + fe^{2i\phi_2})}{1 - f^2 e^{2iNqa}}, \tag{2.53}$$

where $\phi_1 = N_1 qa + kl_{\text{eff}}(x)$ and $\phi_2 = Nqa - \phi_1 = N_2 qa - kl_{\text{eff}}(x)$.

To see the physical meaning of $I(N_1, x)$, consider q is on the power transmission resonances as shown in Fig. 2.4 and $q = q_m = (1 - m/N)\pi/a$ (Eq. 2.34) with index m refer to the mth resonance from the band-edge. For simplicity, we also assume that the atom locates in the intensity maximum position ($x = 0$) for the upper band. In this case, $I_+(N_1, x)$ can be simplified as

$$I_{m,+}(N_1, x = 0) = \frac{(1 + f)^2 - 4f\cos^2(m\frac{N_1}{N}\pi)}{1 - f^2}, \tag{2.54}$$

where the '+' sign represents the upper band. The maximum of $I_{m,+}(N_1, x = 0)$ can be calculated as

$$I_{m,+,\max}(x = 0) = \frac{1 + f}{1 - f}. \tag{2.55}$$

This agrees with the expression for cavity intensity maximum expression with $R = f^2$ and suggests that $I(N_1, x = 0)$ is the intensity profile of the cavity mode. It is worth noting that the maximum value $I_{m,+,\max}(x = 0)$ is different for different resonances as f is also a function of q_m from Eq. 2.22 and Eq. 2.36. For the case $n_g \gg 1$, we can simplify Eq. 2.55 as

$$I_{m,+,\max}(x = 0) \simeq 2|n_{g,m}| \simeq \frac{2\zeta N}{m\pi}. \tag{2.56}$$

Fig. 2.8 shows the plot of $I_{m,+}(N_1, x = 0)$ vs. N_1 for first three resonances with $\zeta = 0.2$ and $N = 150$ with the gray dashed indicating the approximated maximum $2|n_{g,m}|$. The parameters are chosen so that the group velocity at first resonance $|n_{g,1}| = \zeta N/\pi \sim 10$ which is close to the setting of the APCW [68, 86].

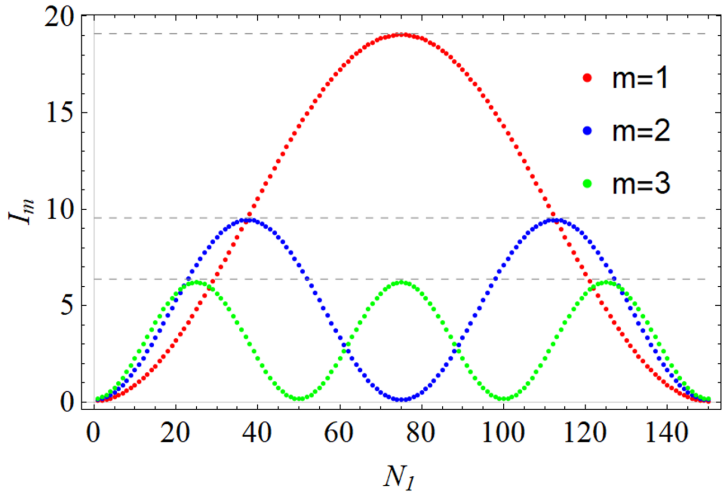

Figure 2.8: A plot of $I_{m,+}(N_1, x = 0)$ vs. N_1 for first three resonances with $\zeta = 0.2$ and $N = 150$. The gray dashed lines are calculated with the approximated maximum $2|n_{g,m}|$ for $m = 1, 2, 3$.

Similar to the definition of Γ_{1D} in Eq. 2.49, the term $I(N_1, x)$ in Eq. 2.52 can also be absorbed into the definition of Γ_{1D} and we define

$$\boxed{\Gamma_{1D,N}(N_1, x) = \gamma_{1D} \times |n_g| \times |E_q(x)|^2 \times I(N_1, x)}. \tag{2.57}$$

We see from this new definition $\Gamma_{1D,N}$ that the overall coupling rate to the 1D finite PCW is the product of slow-light enhancement, Bloch mode profile and cavity enhancement. For a finite structure with $\zeta = 0.2$, $N = 150$ and assuming the coupling rate to unstructured waveguide is $\gamma_{1D}/\Gamma' \simeq 0.05$, the maximum $\Gamma_{1D,N}$ is achieved at $\Gamma_{1D,N=150}(N_1 = 75, x = 0)/\Gamma' \simeq 18.2$ for the lower band first resonance. This requires the lower band first resonance is aligned to atom transition and the atom is placed at the centered of the cavity profile and the peak intensity of Bloch mode.

Now let's see how the coupling rate $\Gamma_{1D,N}$ scales with the total unit cell number N. Near the band-edge, using the fact that $|n_{g,m}| \simeq N\zeta/m\pi$ (Eq. 2.36), $I_m(N_1, x) \simeq 2|n_{g,m}| \simeq 2N\zeta/m\pi$ and $|E_q(x)|^2 \simeq 2$, Eq. 2.57 can be written as

$$\Gamma_{1D,N,m,\max} \simeq 4\gamma_{1D}\left(\frac{\zeta N}{m\pi}\right)^2. \tag{2.58}$$

And the Purcell factor can be written as

$$P_{1D,N,m,\max} \equiv \frac{\Gamma_{1D,N,m,\max}}{\Gamma_0} = \frac{3\lambda_0^2}{\pi A_{\text{eff}}}\left(\frac{\zeta N}{m\pi}\right)^2. \tag{2.59}$$

Recall that in conventional cavity QED, the Purcell factor in a cavity with quality Q and mode volume V_{m} is defined as

$$P_{\mathrm{cav}} = \frac{3Q}{4\pi^2}\frac{\lambda_0^3}{V_{\mathrm{m}}}. \tag{2.60}$$

Similarly, we can define the quality Q_m for m-th resonance as $Q_m = \omega_m/\kappa_m$ with κ_m defined in Eq. 2.40 and mode volume $V_{\mathrm{m}} = A_{\mathrm{eff}}Na$, we can rewrite Eq. 2.59 as

$$P_{1\mathrm{D},N,m,\max} = \frac{3Q_m}{\pi^2}\frac{\lambda_0^3}{V_{\mathrm{m}}} = 4P_{\mathrm{cav}}. \tag{2.61}$$

Here the factor of 4 difference should be gone if averaging over Bloch mode and averaging over the cavity profile.

Finally, it worth noting that away from resonances, $I(N_1, x)$ is generally a complex function. This will result in asymmetric transmission spectrum with respect to detuning Δ_A (as shown later in Fig. 2.11). The physical meaning of the asymmetry will be addressed later in the sections with Green's function approach.

Summary of transfer matrix model

In this section, we have shown the transfer matrix model to understand the basic properties of photonic crystal and atom-light interactions. We have shown that the photonic band in infinite PCW is equivalent to free-space in Bloch space with a modified group index that diverges at the band-edge. For finite PCW, we have shown that it is equivalent to a Fabry-Perot cavity with two effective mirrors in the Bloch space. As a result, the single atom-light interaction near the band-edge of a infinite PCW is enhanced by the group index (the Bloch mode which contributes at most a factor of 2). For finite structure, the enhancement is broke down into the product of cavity enhancement and the group velocity enhancement.

Despite our analysis is for only a single atom, extensions can be easily made to multiple atoms by inserting more atom transfer matrix into the structure. As the single atom can be viewed as a lossy scatter, the transfer matrix model we presented here can also provide some insights for purely atom arrays, e.g. PCWs formed by atoms [12].

However, there are several limitations in the transfer matrix model. First, it is a 1D model and extensions to 2D or 3D will be challenging. Second, it is typically hard to gain physical insight from the total product of transfer matrices. Another limitation of the transfer matrix model is the assumption of low saturation limit, which does

not incorporate the "quantumness" of an atom. For a more rigorous analysis, we turn to the Green's function approach of atom-light interactions in complex optical structures. We will see that within the Green's function approach, the information of complex optical structures is encoded in the Green's function and the interactions between atom-atom and atom-light are more explicit.

2.4 The Green's function in classical electromagnetic theory

In this section, we will present the Green's function approach to the atom-light interaction in nanophotonics which provides a rigorous and quantitative framework to describe atom-nanophotonic interfaces. This is based on a series of works developed by Welsch and colleagues [30, 31, 74] and extended more explicitly to quasi-1D systems by Ana Asenjo-Garcia and Jonathon Hood in Ref. [11] and Ref. [88]. As Jonathon Hood already gave a very nice description to this topic in his thesis [88], here we follow his thesis and give a relative short introduction for completeness.

The Green's function in electromagnetic wave equation

Before introducing the Green's function approach of the quantum theory, we would like to have a quick review of the Green's function in the classical electromagnetic theory. We start our discussion from the Maxwell's wave equation in the frequency domain [137] (i.e. $\mathbf{E}(\mathbf{r},t) = \mathrm{Re}\left[\mathbf{E}(\mathbf{r},\omega)e^{-i\omega t}\right]$), namely

$$\nabla\times\nabla\times\mathbf{E}(\mathbf{r},\omega) - \frac{\omega^2}{c^2}\epsilon(\mathbf{r},\omega)\mathbf{E}(\mathbf{r},\omega) = i\mu_0\omega\mathbf{J}_f(\mathbf{r},\omega). \tag{2.62}$$

Here $\epsilon(\mathbf{r},\omega)$ is medium relative permittivity, allowed to be position and frequency dependent. For simplicity, we have assumed the material is non-magnetic $\mu(\mathbf{r},\omega) = 1$ and has no free charge $\rho_f(\mathbf{r}) = 0$, which is typically case for dielectric optical structures. Here the right hand side $\mathbf{J}_f(\mathbf{r},\omega)$ is the free current density that excites the electromagnetic wave and is related to the oscillating polarization density by $\mathbf{J}_f(\mathbf{r},t) = \frac{d}{dt}\mathbf{P}(\mathbf{r},t)$, or $\mathbf{J}_f(\mathbf{r},\omega) = -i\omega\mathbf{P}(\mathbf{r},\omega)$ in the frequency domain. The wave equation can then be written in terms of oscillating polarization density as

$$\nabla\times\nabla\times\mathbf{E}(\mathbf{r},\omega) - \frac{\omega^2}{c^2}\epsilon(\mathbf{r},\omega)\mathbf{E}(\mathbf{r},\omega) = \mu_0\omega^2\mathbf{P}(\mathbf{r},\omega). \tag{2.63}$$

In electromagnetic theory, the Green's function is defined by the electric field $\mathbf{E}$ at position $\mathbf{r}$ generated by a radiating electric dipole $\mathbf{p}$ located at position $\mathbf{r}'$ as

$$\mathbf{E}(\mathbf{r}) = \mu_0\omega^2\mathbf{G}(\mathbf{r},\mathbf{r}';\omega)\cdot\mathbf{p}. \tag{2.64}$$

Here $\mathbf{G}(\mathbf{r}, \mathbf{r}')$ is a tensor quantity due to possible polarizations (e.g. x,y,z) of the field at $\mathbf{r}$ and possible source orientations (e.g. x,y,z). Replacing the polarization density $\mathbf{P}(\mathbf{r}, \omega)$ with a point dipole source $\mathbf{p}\delta(\mathbf{r} - \mathbf{r}')$, we get the equation for the Green's function $\mathbf{G}(\mathbf{r}, \mathbf{r}'; \omega)$ (in the frequency domain) as

$$\nabla \times \nabla \times \mathbf{G}(\mathbf{r}, \mathbf{r}'; \omega) - \frac{\omega^2}{c^2}\epsilon(\mathbf{r}, \omega)\mathbf{G}(\mathbf{r}, \mathbf{r}'; \omega) = \overleftrightarrow{\mathbf{I}}\delta(\mathbf{r} - \mathbf{r}'). \tag{2.65}$$

With the Green's function satisfies Eq. 2.65, the electric field for an arbitrary polarization source can then be obtained by integrating the Green's function over the polarization density, in the form of Dyson's equation

$$\mathbf{E}(\mathbf{r}, \omega) = \mathbf{E}_0(\mathbf{r}, \omega) + \mu_0\omega^2 \int d^3\mathbf{r}'\mathbf{G}(\mathbf{r}, \mathbf{r}', \omega)\mathbf{P}(\mathbf{r}'; \omega), \tag{2.66}$$

with $\mathbf{E}_0(\mathbf{r}, \omega)$ being the homogeneous solution without sources.

It is generally hard to find the explicit solution of the Green's function to Eq. 2.65 for complex optical structures. However, analytic solutions do exist for a few simple cases. First, for the scalar Green function in free-space (in this case the Maxwell wave equation becomes Helmholtz equation in wave optics)

$$\left[\nabla^2 + \frac{\omega^2}{c^2}\right] G_0(\mathbf{r}, \mathbf{r}') = -\delta(\mathbf{r} - \mathbf{r}'). \tag{2.67}$$

In this case, the Green's function solution of this scalar wave equation is [98]

$$G_0(\mathbf{r}, \mathbf{r}'; \omega) = \frac{1}{4\pi}\frac{e^{ik|\mathbf{r}-\mathbf{r}'|}}{|\mathbf{r} - \mathbf{r}'|}. \tag{2.68}$$

In physics, this corresponds to a spherical wave propagating out of the source. From the scalar Green's function $G_0(\mathbf{r}, \mathbf{r}'; \omega)$, the 3D tensor Green's function is given as

$$\mathbf{G}_0(\mathbf{r}, \mathbf{r}'; \omega) = \left[\overleftrightarrow{\mathbf{I}} + \frac{c^2}{\omega^2}\nabla\nabla\right] G_0(\mathbf{r}, \mathbf{r}'; \omega). \tag{2.69}$$

For the case when dielectric material is presented, if the structure's electric field eigenmodes are already given, we can then construct the Green's function from its eigenmodes[1] [162]

$$\mathbf{G}(\mathbf{r}, \mathbf{r}', \omega) = \frac{c^2}{\epsilon(\mathbf{r}', \omega)} \sum_n \frac{1}{\omega_n^2 - \omega^2}\mathbf{E}_n(\mathbf{r}) \otimes \mathbf{E}_n^*(\mathbf{r}'), \tag{2.72}$$

[1]This can be very generically proved and here we show a simple proof for 1D scalar Green's function. The Green function for a generic eigenvalue function takes the form

$$[\mathcal{L} - \lambda]G(x, x') = \delta(x, x'). \tag{2.70}$$

Assume we know the orthogonal eigenfunction basis $\phi_n(x)$ with eigenvalues λ_n, that is, $\mathcal{L}\phi_n(x) =$

where $\mathbf{E}_n(\mathbf{r})$ is the eigenmode of the system with index n.

For complex optical dielectric structures, numerical methods such as finite-difference time domain (FDTD) simulations [126, 137] can be used to solve the Green's function. This is performed by simulating the electric field pattern from a point dipole source placed inside the optical structure, as will be discussed in detail in Chapter 3.

Despite the difficulty of solving Eq. 2.65 analytically for complex structures, a few important identities with the Green's function can be made based on arguments from the general physics. First, a system with Lorentz reciprocity requires

$$\mathbf{G}^T(\mathbf{r}, \mathbf{r}'; \omega) = \mathbf{G}(\mathbf{r}', \mathbf{r}; \omega), \tag{2.73}$$

with T stands for transpose. Physically, the Lorentz reciprocity states if one interchanges the points where the current is placed and where the field is measured, the resulting electric field is unchanged. Second, to maintain a real Green's function $\mathbf{G}(\mathbf{r}, \mathbf{r}', \tau)$ in the time domain requires that

$$\mathbf{G}^*(\mathbf{r}, \mathbf{r}'; \omega) = \mathbf{G}(\mathbf{r}, \mathbf{r}'; -\omega). \tag{2.74}$$

These identities will be useful in the derivations associated with the Green's functions.

Finally, it can be shown that the power radiating from the point dipole is related to the imaginary part of the self-Green's function $\mathbf{G}(\mathbf{r}', \mathbf{r}'; \omega)$. Recall that in classical electromagnetic theory, the radiation power can be calculated by performing a surface integral of the normal component of the Poynting vector over a surface surrounding the oscillating dipole [98, 137]

$$P_{\text{rad}} = \int_{\partial V} \langle \mathbf{S} \rangle \cdot \mathbf{n} da = -\frac{1}{2} \int_V \text{Re}[\mathbf{j}^* \cdot \mathbf{E}] dV, \tag{2.75}$$

$\lambda_n \phi_n(x)$. Assuming the Green's function can be expand with the eigenfunction basis as $G(x, x') = \sum_n g_n(x') \phi_n(x)$, with the coefficient $g_n(x')$ to be solved. On the right hand side of Eq. 2.70, the δ-function also be expanded with the eigenfunction basis as $\delta(x, x') = \sum_n d_n(x') \phi_n(x)$ with the coefficient $d_n(x') = \int dx \phi_n^*(x) \delta(x - x') = \phi_n^*(x')$. Plug these eigenvector expansions into Eq. 2.70, we can solve for $g_n(x')$ as $g_n(x') = \frac{1}{\lambda_n - \lambda} \phi_n^*(x')$, and the Green's function as

$$G(x, x') = \sum_n \frac{1}{\lambda_n - \lambda} \phi_n^*(x') \phi_n(x). \tag{2.71}$$

Eq. 2.70 can be mapped to the wave equation by $\mathcal{L} \to \frac{1}{\epsilon(\mathbf{r}, \omega)} \nabla \times \nabla \times$, $\lambda \to \frac{\omega^2}{c^2}$ and $\delta(x - x') \to \frac{1}{\epsilon(\mathbf{r}, \omega)} \overleftrightarrow{\mathbf{I}} \delta(\mathbf{r} - \mathbf{r}')$.

where $\langle \mathbf{S} \rangle = \frac{1}{2}\mathrm{Re}[\mathbf{E} \times \mathbf{H}^*]$ is the time average of the Poynting vector. With $\mathbf{j}(\mathbf{r}, \omega) = -i\omega \mathbf{p} \delta(\mathbf{r} - \mathbf{r}')$ and $\mathbf{E}(\mathbf{r}, \omega) = \mu_0 \omega^2 \mathbf{G}(\mathbf{r}, \mathbf{r}'; \omega) \cdot \mathbf{p}$, we rewrite the radiation power in terms of the Green's function as

$$P_{\mathrm{rad}} = \frac{\omega^3 |\mathbf{p}|^2}{2\epsilon_0 c^2} \hat{\mathbf{n}}_p \cdot \mathrm{Im}[\mathbf{G}(\mathbf{r}', \mathbf{r}'; \omega)] \cdot \hat{\mathbf{n}}_p. \tag{2.76}$$

with $\hat{\mathbf{n}}_p$ being the unit vector of the dipole, $\mathbf{p} = |\mathbf{p}|\hat{\mathbf{n}}_p$ and we assumed $\hat{\mathbf{n}}_p$ is real, e.g. for a linear dipole moment. We will see later in the quantum theory of the Green's functions that the decay rate of an atom is also proportional to the imaginary part of its self-Green's function. This is because the atom, in the classical limit, can be approximated as an oscillating point dipole.

Examples of the Green's function in quasi-1D systems

As mentioned in the previous section, it is generally hard to find analytic solutions of the Green's function in Eq. 2.65 with the presence of complex dielectric structures. However, for simple structures in 1D or quasi-1D system, analytic forms of the Green's function can be derived or approximately evaluated. To simplify our discussion, we assume the polarization and dipole source are in the same transverse direction to replace the tensor Green's function with a scalar Green's function.

From the 1D wave equation, Eq. 2.65 can be simplified as

$$\left[\frac{d^2}{dx^2} + k^2 \epsilon(x) \right] G(x, x'; \omega) = -\delta(x - x'), \tag{2.77}$$

with wavevector $k = \omega/c$. Here we assumed the electric field is linearly polarized in the transverse direction which allows us to reduce the Green's function tensor into a scalar. For free-space with $\epsilon(x) = 1$, the solution of the Green's function of the 1D wave equation is

$$G_{0,1\mathrm{D}}(x, x'; \omega) = \frac{i}{2k} e^{ik|x - x'|}. \tag{2.78}$$

From this 1D free-space Green's function, one can simply find the 1D uniform waveguide Green's function with $\epsilon(x) = n^2$

$$G_{\mathrm{wg},1\mathrm{D}}(x, x'; \omega) = \frac{i}{2k} \frac{c}{v_g} e^{ik|x - x'|}. \tag{2.79}$$

with $v_g = c/n$ being the group velocity.

We can further derive the Green's function for a 1D Fabry-Perot cavity by employing the Wronskian with the 1D free-space Green's function as shown in Jonathon Hood's

thesis [88]

$$G_{\text{cav}}(x,x';\omega) = \frac{i}{2k}\frac{1}{1-r_L r_R e^{2ikL}} \times \left[e^{ik|x-x'|} + r_L e^{ik(L+x+x')} + r_R e^{ik(L-(x+x'))} + r_R r_L e^{ik(2L-|x-x'|)}\right]. \tag{2.80}$$

Here L is the cavity length and r_R (r_L) is reflection coefficient of the right (left) mirror. As a sanity check, we find $G(x,x';\omega) = G(x',x;\omega)$ and the Green's function becomes that of free-space when the reflection coefficients become zero. For a symmetric cavity with $r_L = r_R = r$, Eq. 2.80 can be simplified as

$$\begin{aligned} G_{\text{1D,cav}}(x,x';\omega) &= G_{0,\text{1D}}(x,x';\omega)\frac{(1+re^{ik(L-|x-x'|+x+x')})(1+re^{ik(L-|x-x'|-(x+x'))})}{1-r^2e^{2ikL}} \\ &= G_{0,\text{1D}}(x,x';\omega) + \frac{i}{2k}\frac{2re^{ikL}}{1-re^{ikL}}\cos kx\cos kx' \\ &+ \frac{i}{2k}\frac{2re^{ikL}}{1+re^{ikL}}\sin kx\sin kx'. \end{aligned} \tag{2.81}$$

We can further simplify this expression for high finesse cavity ($|r| \approx 1$) with probe frequency close to resonances. For example, for the odd modes resonance ($k_c L = m\pi$, with $m = 1,3,5...$), we have $(1+r)^{-1} \gg (1-r)^{-1}$ (assuming $r < 0$ which is typically the case for reflective mirrors) and we can further neglect the first and the third terms in Eq. 2.81. This leads to the cavity Green's function near m-th odd resonances[2] as

$$\begin{aligned} G_{\text{1D,cav}}(x,x';\omega) &\approx \frac{i}{2k}\frac{2re^{ikL}}{1-re^{ikL}}\cos kx\cos kx' \\ &\approx \frac{ic}{m\pi}\frac{1}{\kappa/2+i\Delta_c}\cos kx\cos kx', \end{aligned} \tag{2.82}$$

where Δ_c is the detuning to the cavity resonance, $\Delta_c = \omega - \omega_c$ and we have used the relation for the cavity linewidth $\kappa \approx \frac{2c}{L}\frac{1+r}{|r|}$. Note that the peak value of Green's function scales with $1/m$ which is consistent with Eq. 2.56 in the transfer matrix model.

[2]For even modes, we have the $\sin kx \sin kx'$ term dominant. The reason we have two different expressions for odd and even modes is simply due to the choice of origin where we set $x = 0$ corresponds to the cavity center, to be consistent with the choice in the transfer matrix model. In fact, if we choose the left mirror position as $x = 0$, both even and odd resonances are dominant with $\cos kx \cos kx'$ term.

Besides, the self-Green's function at the cavity center can be found with $x = x'$ in Eq. 2.81

$$\begin{aligned} G_{\mathrm{1D,cav}}(x', x'; \omega) &= \frac{i}{2k} \frac{(1 + re^{ik(L+2x')})(1 + re^{ik(L-2x')})}{1 - r^2 e^{2ikL}} \\ &= G_{0,\mathrm{1D}}(x', x'; \omega) F(x'), \end{aligned} \tag{2.83}$$

with

$$F(x) \equiv \frac{(1 + re^{ik(L+2x)})(1 + re^{ik(L-2x)})}{1 - r^2 e^{2ikL}}. \tag{2.84}$$

We can see $F(x)$ is mathematically very similar to the $I(N_1, x)$ defined in Eq. 2.53 in the previous section and it is related to the Finesse of the cavity. To see this, consider a special case with $x = x' = 0$ and $kL = \pi$ (on resonance)

$$F(0) = \frac{1 - r}{1 + r} \approx \frac{2}{1 + r} \approx \frac{4\mathcal{F}}{\pi} \tag{2.85}$$

where $\mathcal{F} = \pi(R_1 R_2)^{1/4}/(1 - \sqrt{R_1 R_2})$ is the finesse of the Fabry-Perot cavity.

Next, for the infinite 1D PCW, since we already know the eigenmode is Bloch mode with Bloch index q, we can write down the Green's function explicitly using Eq. 2.72

$$G_{\mathrm{pcw,1D}}(x, x', \omega) = \int_0^{\pi/a} dq \frac{2c^2}{\omega_q^2 - \omega^2} E_q(x) E_q^*(x'). \tag{2.86}$$

From the transfer matrix model in the previous section, we have derived the Bloch mode electric field $E_q(x)$ (Eq. 2.23). One can in principle insert Eq. 2.23 into Eq. 2.86 and use the dispersion relation (Eq. 2.11) to work out the integral. Since we are interested in the atom-light interaction near the band-edge, the Green's function near the band-edge can be approximately given as

$$G_{\mathrm{pcw,1D,+}}(x, x'; \omega) \approx \frac{i}{k} \frac{c}{v_g} e^{i(k - \frac{\pi}{a})|x - x'|} \cos\left(\frac{\pi}{a} x\right) \cos\left(\frac{\pi}{a} x'\right). \tag{2.87}$$

for the upper band-edge ($\omega \simeq \omega_+$), with $k \approx \pi/a$ with the group velocity $v_g = \frac{d\omega}{dq}$ and

$$G_{\mathrm{pcw,1D,gap}}(x, x'; \omega) \approx \frac{1}{k} \frac{c}{v_g} e^{-q_{\mathrm{im}}|x - x'|} \cos\left(\frac{\pi}{a} x\right) \cos\left(\frac{\pi}{a} x'\right). \tag{2.88}$$

for the bandgap (near upper band-edge) with the imaginary Bloch vector q_{im} defined in Eq. 2.15. The lower band-edge can be similarly given by replace the $\cos(k_+ x)$ term with $\sin(k_- x)$ term as shown in Eq. 2.25.

For finite PCWs, Ana Asenjo-Garcia shows (in an unpublished note) that the self-Green's function close to transmission resonance can be modelled as the cavity

Green's functions in the Bloch-space with linewidth given in Eq. 2.40. This observation is consistent with the result predicted by the transfer matrix model as in Eq. 2.57.

Finally, to connect to 3D Green's function, we would like to point out the 3D Green's function for quasi-1D systems such as nano-fiber or waveguides can be approximated as a product of the 1D Green's function with a geometric area factor. As an example, the 3D Green's function for a uniform waveguide is given as (see Jonathon Hood's thesis [88] for detailed derivations)

$$G_{\mathrm{wg}}(\mathbf{r},\mathbf{r}';\omega) = \frac{i}{2k}\frac{c}{v_g}\frac{1}{A_{\mathrm{k}}}e^{ik|x-x'|}, \tag{2.89}$$

where v_g is the group velocity and A_k is the effective mode area in the transverse direction, defined as

$$A_k = \frac{\int_s d\mathbf{r}^2\epsilon(\mathbf{r})|\mathbf{E}_k(\mathbf{r})|^2}{\max[\epsilon(\mathbf{r})|\mathbf{E}_{\mathbf{k}}(\mathbf{r})|^2]}. \tag{2.90}$$

Similarly, for 3D Fabry-Perot cavity with transverse mode area A, the 3D Green's function near resonance is given as

$$G_{\mathrm{cav,3D}}(\mathbf{r},\mathbf{r}';\omega) \approx \frac{ic}{kL}\frac{1}{A}\frac{1}{\kappa/2+i\Delta_c}\cos kx\cos kx'. \tag{2.91}$$

2.5 The quantum theory of atom-light interaction with Green's functions

In the previous sections, we have introduced the Green's function in the classical electrodynamics. In this section, we will see the Green's function is a suitable tool to describe the quantum atom-light interaction with the presence of complex dielectric materials.

To describe the quantum atom-light interaction, we first write down the system's total Hamiltonian as

$$\hat{H} = \hat{H}_F + \hat{H}_A + \hat{H}_{\mathrm{int}}, \tag{2.92}$$

where $\hat{H}_F$, $\hat{H}_A$ and $\hat{H}_{AF}$ represents the Hamiltonian for the light field, the Hamiltonian for the atom and Hamiltonian of atom-light interaction.

For the field Hamiltonian H_A, recall that in the canonical quantization technique, the field is expressed in terms of a set of eigenmodes of the system, with corresponding creation and annihilation operators $a^\dagger$ and a. However, the quantization of field here is not straightforward as there is no simple eigenmode decomposition for complex dielectric structure. Further, the presence of material dispersion and loss can break the conservation of commutation relations for the field operators. From a series of

work by Welsch and colleagues [30, 31, 74] it turns out the Green's function provides a suitable framework for the quantization of field with the presence of complex structures. The detailed quantization of electric field within the Green's function language is described in Refs. [30, 88] and for simplicity, we only summarize the main results here. Within this Green's function quantization framework, the field Hamiltonian takes the form

$$H_F = \int d^3\mathbf{r} \int_0^\infty d\omega \hat{\mathbf{f}}^\dagger(\mathbf{r},\omega)\hat{\mathbf{f}}(\mathbf{r},\omega). \tag{2.93}$$

Here, the field creation and annihilation operators $\hat{\mathbf{f}}$ is associate with the degrees of freedom of local material polarization noise and is related to the electric field $\hat{\mathbf{E}}(\mathbf{r})$ by

$$\begin{aligned}\hat{\mathbf{E}}(\mathbf{r},\omega) &= i\mu_0\omega^2\sqrt{\frac{\hbar\epsilon_0}{\pi}}\int d\mathbf{r}'\sqrt{\mathrm{Im}[\epsilon(\mathbf{r}',\omega)]}\mathbf{G}(\mathbf{r},\mathbf{r}';\omega)\cdot\hat{\mathbf{f}}(\mathbf{r}',\omega) + \text{h.c.} \\ &= \hat{\mathbf{E}}^+(\mathbf{r},\omega) + \hat{\mathbf{E}}^-(\mathbf{r},\omega).\end{aligned} \tag{2.94}$$

Here $\hat{\mathbf{E}}(\mathbf{r},\omega)$ is the electric field frequency component and is related to the total electric field by $\hat{\mathbf{E}}(\mathbf{r}) = \int d\omega\hat{\mathbf{E}}(\mathbf{r},\omega)$. The presence of $\mathrm{Im}[\epsilon(\mathbf{r},\omega)]$ in the expression indicates the material dissipation which is a result of fluctuation-dissipation theorem [30]. The commutation relations for $\hat{\mathbf{f}}$ are defined as

$$[\hat{f}_k(\mathbf{r},\omega), \hat{f}_k^\dagger(\mathbf{r}',\omega')] = \delta_{kk'}\delta(\omega-\omega')\delta(\mathbf{r}-\mathbf{r}'), \tag{2.95}$$

$$[\hat{f}_k(\mathbf{r},\omega), \hat{f}_{k'}(\mathbf{r}',\omega')] = 0. \tag{2.96}$$

With the definitions of field operators above, the last two Hamiltonians H_A and H_{AF} are straightforward to work out. For atomic part, H_A (assuming single atom) is expressed as

$$H_A = \frac{1}{2}\hbar\omega_A(|e\rangle\langle e| - |g\rangle\langle g|) = \frac{1}{2}\hbar\omega_A\hat{\sigma}^z, \tag{2.97}$$

with $|g\rangle$ and $|e\rangle$ represents the two level atom's ground state and excited state with energy separation $\hbar\omega_A$. And the interaction Hamiltonian H_{AF} is given as

$$H_{AF} = -\hat{\mathbf{E}}(\mathbf{r})\cdot\hat{\mathbf{d}} = -\hat{\mathbf{E}}(\mathbf{r})\cdot(\mathbf{d}\hat{\sigma} + \mathbf{d}^*\hat{\sigma}^\dagger), \tag{2.98}$$

where $\hat{\mathbf{d}}$ is the dipole operator of the atom $\hat{\mathbf{d}} = e\hat{\mathbf{r}}$ and we have projected the dipole operator $\hat{\mathbf{d}}$ onto the atom states with the dipole matrix elements $\mathbf{d} = \langle g|\hat{\mathbf{d}}|e\rangle$, $\mathbf{d}^* = \langle g|\hat{\mathbf{d}}|e\rangle$ and the Pauli spin operators $\hat{\sigma} = |g\rangle\langle e|$ and $\hat{\sigma}^\dagger = |e\rangle\langle g|$.

With the system's Hamiltonian defined, we can now calculate the evolution of the light field and the N identical two-level atoms from the Heisenberg equation

$$\dot{\hat{O}} = \frac{1}{i\hbar}[\hat{O}, H]. \tag{2.99}$$

The equations for the atomic operators are

$$\dot{\hat{\sigma}}_j = -i\omega_A \hat{\sigma}_j - \frac{i}{\hbar}\hat{\sigma}_j^z \hat{\mathbf{E}}(\mathbf{r}_j) \cdot \mathbf{d}, \tag{2.100}$$

$$\dot{\hat{\sigma}}_j^z = \frac{2i}{\hbar}\hat{\sigma}_j^\dagger \hat{\mathbf{E}}(\mathbf{r}_j) \cdot \mathbf{d} + \text{h.c.}, \tag{2.101}$$

for the j-th atom at position $\mathbf{r}_j$. And the equation for the field operator is

$$\dot{\hat{\mathbf{f}}}(\mathbf{r}, \omega) = -i\omega \hat{\mathbf{f}}(\mathbf{r}, \omega) + \frac{\omega^2}{c^2}\sqrt{\frac{\text{Im}[\epsilon(\mathbf{r}, \omega)]}{\pi\epsilon_0\hbar}} \sum_{j=1}^{N} \hat{\mathbf{d}}_j \cdot \mathbf{G}^*(\mathbf{r}, \mathbf{r}_j; \omega). \tag{2.102}$$

We can formally integrate the field operator equation and insert it into Eq. 2.94 to find the electric field. As already shown in Ref. [88], after some algebraic manipulation and performing the Markov's approximation (which assumes the response of the light field is much faster than the atomic evolution), we finally arrive at the expression for the electric field operator

$$\boxed{\hat{\mathbf{E}}^+(\mathbf{r}) = \hat{\mathbf{E}}_0^+(\mathbf{r}) + \mu_0\omega_A^2 \sum_{j=1}^{N} \mathbf{G}(\mathbf{r}, \mathbf{r}_j; \omega_A) \cdot \mathbf{d}\hat{\sigma}_j}. \tag{2.103}$$

Here $\hat{\mathbf{E}}_0^+(\mathbf{r})$ denotes the electric field without atoms, for example, due to the probe light. The physics picture behind this expression is very intuitive: the total field is the sum of the homogeneous field solution of the structure without atom plus the field radiated by the atoms. This suggests the exiting quantum field of the complex optical structure is completely described in terms of the correlations of atoms and input field, while the interactions within the complex optical structure is encoded in the Green's function. It can be viewed as a generalization of the classic input-output equations developed within cavity QED settings [64] to arbitrary dielectric environments.

By inserting the expression of electric field (Eq. 2.103) into the Heisenberg equations for atoms (E) and applying the rotating wave approximation by neglecting counter-rotating terms, we get the equations of the atomic operators with the drive from the

input field $\hat{\mathbf{E}}_0^+(\mathbf{r})$ (in the rotating frame)

$$\dot{\hat{\sigma}}_j = -i\Delta_A\hat{\sigma}_j - \frac{i\mu_0\omega_A^2}{\hbar}\hat{\sigma}_j^z\sum_{i=1}^{N}\hat{\sigma}_i\mathbf{d}^*\cdot\mathbf{G}(\mathbf{r}_j,\mathbf{r}_i;\omega_A)\cdot\mathbf{d} - i\hat{\Omega}_j\hat{\sigma}_j^z, \tag{2.104}$$

$$\dot{\hat{\sigma}}_j^z = \frac{2i\mu_0\omega_A^2}{\hbar}\hat{\sigma}_j^\dagger\sum_{i=1}^{N}\hat{\sigma}_i\mathbf{d}^*\cdot\mathbf{G}(\mathbf{r}_j,\mathbf{r}_i;\omega_A)\cdot\mathbf{d} + 2i\hat{\Omega}_j\hat{\sigma}_j^\dagger + \text{h.c.}, \tag{2.105}$$

with $\Delta_A = \omega - \omega_A$ and the driving term $\hat{\Omega}_j = \mathbf{d}\cdot\hat{\mathbf{E}}_0^+(\mathbf{r}_j)/\hbar$.

The equations above are essentially nonlinear with presence of the product of atomic operators, e.g. $\hat{\sigma}_j^z\hat{\sigma}_i$. To simplify our discussion, we linearize the equations above by considering the case under low saturation limit where atoms mostly stay in the ground state, that is, $\langle\sigma^z\rangle \approx -1$. In this case, the linearized equation of motion is

$$\begin{aligned}\dot{\hat{\sigma}}_j &= -i\Delta_A\hat{\sigma}_j + \frac{i\mu_0\omega_A^2}{\hbar}\sum_{i=1}^{N}\hat{\sigma}_i\mathbf{d}^*\cdot\mathbf{G}(\mathbf{r}_j,\mathbf{r}_i,\omega_A)\cdot\mathbf{d} + i\hat{\Omega}_j \\ &= -i\Delta_A\hat{\sigma}_j + i\sum_{i=1}^{N}g_{ij}\hat{\sigma}_i + i\hat{\Omega}_j,\end{aligned} \tag{2.106}$$

with $g_{ij} = J_{ij} + i\frac{\Gamma_{ij}}{2}$ and the spin-exchange rate J_{ij} and the decay rate defined as

$$J_{ij} = \frac{\mu_0\omega_A^2}{\hbar}\mathbf{d}^*\cdot\text{Re}\mathbf{G}(\mathbf{r}_i,\mathbf{r}_j;\omega_A)\cdot\mathbf{d}, \tag{2.107}$$

$$\Gamma_{ij} = \frac{2\mu_0\omega_A^2}{\hbar}\mathbf{d}^*\cdot\text{Im}\mathbf{G}(\mathbf{r}_i,\mathbf{r}_j;\omega_A)\cdot\mathbf{d}. \tag{2.108}$$

Specifically, for the case $i = j$, we have the decay rate of the j-th atom as

$$\Gamma_{jj} = \frac{2\mu_0\omega_A^2}{\hbar}\mathbf{d}^*\cdot\text{Im}\mathbf{G}(\mathbf{r}_j,\mathbf{r}_j;\omega_A)\cdot\mathbf{d}. \tag{2.109}$$

For free-space, the imaginary part of the Green's function is given as[3]

$$\text{Im}[\mathbf{G}_0(r,r;\omega)] = \frac{\omega}{6\pi c}. \tag{2.110}$$

Insert this result into Eq. 2.109, we recover the free-space decay rate for a two-level atom

$$\Gamma_0 = \frac{\mu_0|\mathbf{d}|^2\omega_A^3}{3\pi\hbar c}. \tag{2.111}$$

[3]This can be derived by calculating the imaginary part of the electric field of a finite size dipole at the limit $kr \to 0$, as shown in Jonathon Hood's thesis [88]. Interestingly, at the limit $kr \to 0$, the real part of electric field diverges but the imaginary part stays finite.

Under the low saturation limit, we can further derive an effective atom-atom Hamiltonian of the system (non-Hermitian character due to the presence of decay rates) [65]

$$H_{\text{eff}}/\hbar = -\sum_j \Delta_A \sigma_j^\dagger \sigma_j - \sum_{i,j} g_{ij}\sigma_j^\dagger \sigma_i - \sum_j \left(\hat{\Omega}_j \sigma_j^\dagger + \text{h.c.}\right). \tag{2.112}$$

It is clear from this effective Hamiltonian that the dynamics of atom-light interactions within nanophotonic structures is described by the atomic state and the input driving field, while the information of the complex optical structure is encoded inside spin-exchange and decay rates through the Green's functions. As the form of Eq. 2.112 is very similar to the Hamiltonian of quantum spin-1/2 system, the effective Hamiltonian is also called spin model of atom-light interactions. The effective Hamiltonian (Eq. 2.112), together with the linearized equations of motion for σ_j (Eq. 2.106) will be the starting point of our discussion in following sections. It should be pointed out that these results are valid under low saturation limit, and we will always assume this limit in our following discussion unless otherwise stated.

Steady state response and diagonalization of the effective Hamiltonian

From the linearized equation of motion under low saturation limit, we can calculate the steady state response by setting $\langle \dot{\hat{\sigma}}_j \rangle = 0$. This leads to

$$0 = i\Delta_A \sigma_j + i\sum_{i=1}^{N} g_{ij}\sigma_i + i\Omega_j, \tag{2.113}$$

where we defined $\sigma = \langle \hat{\sigma} \rangle$, $\Omega = \langle \hat{\Omega} \rangle$. The can be written in a compact form as

$$\mathcal{M}\boldsymbol{\sigma} = -\boldsymbol{\Omega}, \tag{2.114}$$

where $\boldsymbol{\sigma} = (\sigma_1, ..., \sigma_N)$, $\boldsymbol{\Omega} = (\Omega_1, ..., \Omega_N)$, $\mathcal{M} = \Delta_A \mathcal{I} + \mathcal{G}$ and $\mathcal{G}$ is the matrix with element g_{ij}. The solution can be easily constructed from the eigenvector and eigenvalues of the matrix $\mathcal{M}$ as

$$\boldsymbol{\sigma} = -\sum_i \frac{\mathbf{v}_i^* \cdot \boldsymbol{\Omega}}{\lambda_i}\mathbf{v}_i, \tag{2.115}$$

with λ_i and $\mathbf{v}_i$ being the i-th eigenvalue and eigenvector of matrix $\mathcal{M}$. It is worth noting that $\mathcal{M}$ and $\mathcal{G}$ have same eigenvectors and related eigenvalues (shift by constant Δ_A). Thus analyzing the eigenvector and eigenvalue provides direct information of the system's steady state response.

In steady state, the electric field ($\mathbf{E}^+(\mathbf{r}) = \langle\hat{\mathbf{E}}^+(\mathbf{r})\rangle$) at the observation position $\mathbf{r}_{out}$ is given as

$$\mathbf{E}^+(\mathbf{r}_{\text{out}}) = \mathbf{E}_0^+(\mathbf{r}_{\text{out}}) + \mu_0\omega_A^2 \sum_{j=1}^{N} \mathbf{G}(\mathbf{r}_{\text{out}}, \mathbf{r}_j; \omega_A) \cdot \mathbf{d}\sigma_j. \tag{2.116}$$

Assume the input field is excited by a classical dipole source $\mathbf{p}_{\text{in}}$ at position $\mathbf{r}_{\text{in}}$, we can express $\mathbf{E}_0^+(\mathbf{r}_{\text{out}})$ as

$$\mathbf{E}_0^+(\mathbf{r}_{\text{out}}) = \mu_0\omega^2\mathbf{G}(\mathbf{r}_{\text{out}}, \mathbf{r}_{\text{in}}; \omega) \cdot \mathbf{p}_{\text{in}}. \tag{2.117}$$

Similarly, Ω_j can be written as

$$\Omega_j = \frac{1}{\hbar}\mathbf{d} \cdot \mathbf{E}_0^+(\mathbf{r_j}) = \frac{\mu_0\omega^2}{\hbar}\mathbf{d} \cdot \mathbf{G}(\mathbf{r}_j, \mathbf{r}_{\text{in}}; \omega) \cdot \mathbf{p}_{\text{in}}. \tag{2.118}$$

Plug this into σ_j, we get

$$\begin{aligned} \sigma_j &= -\sum_i \sum_k \frac{v_{ik}^* \Omega_k}{\lambda_i} v_{ij} \\ &= -\frac{\mu_0\omega^2}{\hbar}\frac{v_{ik}^* v_{ij}}{\lambda_i}\mathbf{d} \cdot \mathbf{G}(\mathbf{r}_k, \mathbf{r}_{\text{in}}; \omega) \cdot \mathbf{p}_{\text{in}}, \end{aligned} \tag{2.119}$$

where in the last step we used Einstein summation rule to sum over repeated indices. Plug Eq. 2.117 and Eq. 2.119 into Eq. 2.116, we get

$$\begin{aligned} \mathbf{E}^+(\mathbf{r}_{\text{out}}) = &\mu_0\omega^2\mathbf{G}(\mathbf{r}_{\text{out}}, \mathbf{r}_{\text{in}}; \omega) \cdot \mathbf{p}_{\text{in}} \\ &- \frac{\mu_0^2\omega^2\omega_A^2|\mathbf{d}|^2}{\hbar}\frac{v_{ik}^* v_{ij}}{\lambda_i}\mathbf{G}(\mathbf{r}_{\text{out}}, \mathbf{r}_j; \omega_A)\mathbf{G}(\mathbf{r}_k, \mathbf{r}_{\text{in}}; \omega) \cdot \mathbf{p}_{\text{in}}. \end{aligned} \tag{2.120}$$

We can define an effective Green's function of the system that relates the input dipole source to the observed field, that is

$$\mathbf{E}^+(\mathbf{r}_{\text{out}}) = \mu_0\omega^2\mathbf{G}_{\text{eff}}(\mathbf{r}_{\text{out}}, \mathbf{r}_{\text{in}}; \omega) \cdot \mathbf{p}_{\text{in}}, \tag{2.121}$$

and the effective Green's function is

$$\begin{aligned} \mathbf{G}_{\text{eff}}(\mathbf{r}_{\text{out}}, \mathbf{r}_{\text{in}}; \omega) = &\mathbf{G}(\mathbf{r}_{\text{out}}, \mathbf{r}_{\text{in}}; \omega) \\ &- \frac{\mu_0\omega_A^2|\mathbf{d}|^2}{\hbar}\frac{v_{ik}^* v_{ij}}{\lambda_i}\mathbf{G}(\mathbf{r}_{\text{out}}, \mathbf{r}_j; \omega_A)\mathbf{G}(\mathbf{r}_k, \mathbf{r}_{\text{in}}; \omega), \end{aligned} \tag{2.122}$$

where we used Einstein summation rule to sum over repeated index. This effective Green's function can be used to calculate light scattering of atoms within an optical structure, given the structure's original Green's function without the atom is known. For example in the 1D or quasi-1D, this expression can be used to calculate the transmission and reflection, as shown in next section.

2.6 Atom-light interaction in quasi-1D systems with Green's functions

In the previous section, we presented the Green's function approach of atom-light interaction with the presence of complex optical structures. In this section, we apply this approach to specific 1D or quasi-1D systems. The material here is largely based on Ref. [11].

Unstructured waveguides

First, let's consider the simplest case, the unstructured waveguide. We have already shown the 3D Green's function for a quasi-1D waveguide in Eq. 2.89. Thus, the spin-exchange and decay rate for the unstructured waveguide[4] is written as

$$J_{\mathrm{wg},ij} = -\frac{\Gamma_{\mathrm{1D,wg}}}{2}\sin k\left|x_i - x_j\right|, \tag{2.123}$$

$$\Gamma_{\mathrm{wg},ij} = \Gamma_{\mathrm{1D,wg}}\cos k\left|x_i - x_j\right|, \tag{2.124}$$

where $\Gamma_{\mathrm{1D,wg}} = \frac{1}{2}\Gamma_0\frac{c}{v_g}\frac{\sigma_0}{A_k}$ equals to $\Gamma_{\mathrm{wg},jj}$ with $x_i = x_j$. The definition of $\Gamma_{\mathrm{1D,wg}}$ here is consistent with previous definition of Γ_{1D} in the transfer matrix model (Eq. 2.49) with the Bloch mode profile $|E(x)|^2 = 1$ for the unstructured waveguide case.

Remarkably, the spin-exchange and decay rate is oscillatory when varying two atoms' relative distance $d = \left|x_i - x_j\right|$. Specifically, for two atoms with distance $d = n\lambda/2$, where n is an integer number, the atom-atom interaction is purely dissipative while when $d = n\lambda/2 + \lambda/4$, the atom-atom interaction is purely coherent, corresponding to the purely spin-exchange interactions (together with free-space decay). This unique feature allows engineering the dissipative interactions by carefully tuning the distance between the emitters. For the case when $d = n\lambda/2$, we have $g_{ij} = i\Gamma_{\mathrm{1D,wg}}/2$. As $\mathcal{G}$ is of rank one, it only has one nonzero eigenvalue $\lambda_B = iN\Gamma_{\mathrm{1D,wg}}/2$. The special collective mode is called "bright mode", as compared to other $N-1$ "dark modes" which do not couple into the probe light.

Now let's consider the transmission and reflection coefficient for the unstructured waveguide. The transmission and reflection coefficient can be derived from the generalized input-output equation (Eq. 2.103). For general quasi-1D structures (e.g. waveguides and Fabry-Perot cavities), it was shown in Ref. [11] and [88] that the

[4]Here we separate the Green's function as a sum of the free-space Green's function and the waveguide Green's function, that is, $\mathbf{G}_{\mathrm{tot}}(\mathbf{r},\mathbf{r}';\omega) = \mathbf{G}_0(\mathbf{r},\mathbf{r}';\omega) + \mathbf{G}_{\mathrm{wg}}(\mathbf{r},\mathbf{r}';\omega)$. As a result, we need to add the free-space spin-exchange rate and decay rate to get the total rates, e.g. $\Gamma_{\mathrm{tot}} = \Gamma_{\mathrm{1D}} + \Gamma_0$. This approximation is valid for quasi-1D systems when the dielectric material does not significantly change the free-space property of the atom. To further consider the impact of free-space decay rate, one can replace Γ_0 with Γ' which represents decay rates into all other channels except the 1D structure.

normalized transmission (which is defined as the ratio of transmission with atoms over the transmission without atoms) is directly related to the eigenvalues of the Green's-function matrix g_{ij} as

$$\frac{t(\Delta_A)}{t_0(\Delta_A)} = \prod_{k=1}^{N} \frac{\Delta_A + i\Gamma'/2}{\Delta_A + J_{k,1D} + i(\Gamma' + \Gamma_{k,1D})/2}, \tag{2.125}$$

where $J_{k,1D}$ and $\Gamma_{k,1D}/2$ are the real and imaginary part of the k-th eigenvalue $\lambda_k = J_{k,1D} + i\Gamma_{k,1D}/2$.

For N atoms with spacing $d = n\lambda/2$, the transmission can be written as (assuming $t_0 = 1$ for unstructured waveguide)

$$t(\Delta_A) = \frac{\Delta_A + i\Gamma'/2}{\Delta_A + i(\Gamma' + N\Gamma_{1D})/2}. \tag{2.126}$$

Compared to the single atom transmission (Eq. 2.50), the N atoms in this "bright mode" behave like a "superatom" with total decay rate $\Gamma_{tot} = \Gamma' + N\Gamma_{1D,wg}$. A classical analog of this "bright mode" corresponds to the case where the radiation fields into the guided mode from each dipole source are constructively enhanced due to the dipole array spacing $d = \lambda/2$.

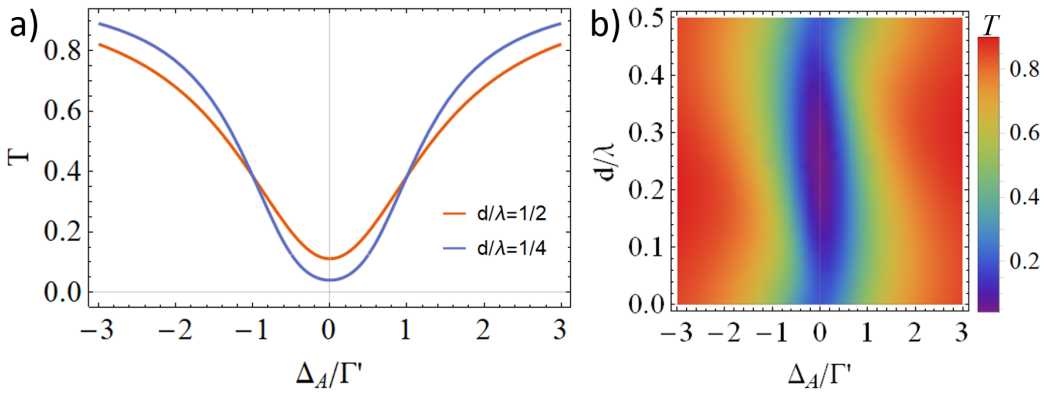

Figure 2.9: (a) Transmission spectra for two atoms with spacing $d = \lambda/2$ (orange) and $d = \lambda/4$ (blue). (b) 2D map of the transmission spectra as a function of atom spacing d and detuning Δ_A. For both figures, we have chosen $\Gamma_{1D,\,wg} = \Gamma'$.

For other atom spatial configurations, the transmission expression can be complicated. As an example we show the case for two atoms with spacing d. The eigenvalues and eigenvectors of $\mathcal{G}$ are $\lambda_\pm = i\frac{\Gamma_{1D,\,wg}}{2}(1 \pm e^{ikd})$ and $\mathbf{v}_\pm = \frac{1}{\sqrt{2}}(1, \pm 1)$. The transmission takes the form

$$t(\Delta_A) = \frac{(\Delta_A + i\Gamma'/2)^2}{[\Delta_A + i\frac{\Gamma'}{2} + i\frac{\Gamma_{1D}}{2}(1 + e^{ikd})][\Delta_A + i\frac{\Gamma'}{2} + i\frac{\Gamma_{1D}}{2}(1 - e^{ikd})]}. \tag{2.127}$$

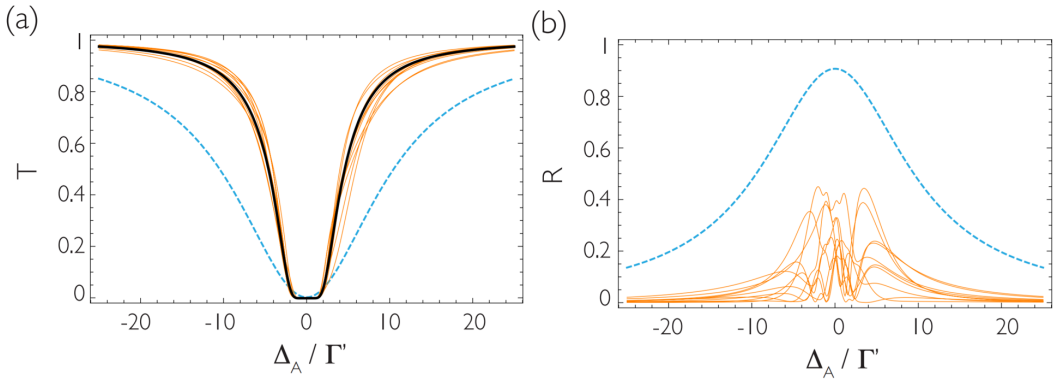

Figure 2.10: (a) Transmission spectra for $N = 20$ atoms along an unstructured waveguide. The blue dashed curve represents an ordered array with atom spacing $d = \lambda/2$. The orange curves show 10 different spectra with 20 atoms randomly placed along the unstructured waveguide. The black curve represents the non-interacting limit for $N = 20$ atoms. (b) The reflection spectra for the same settings as in (a). In both plots, we have chosen $\Gamma_{1D,\,wg} = \Gamma'$. Figures adapted from Ref. [11] with permission.

For large N randomly placed on the waveguide, it was shown in Ref. [11] that the transmission can be approximated as the transmission of N "noninteracting" atoms ($\Gamma_{ij} = 0, J_{ij} = 0$ for $i \neq j$)

$$t(\Delta_A) \approx \left(\frac{\Delta_A + i\Gamma'/2}{\Delta_A + i(\Gamma' + \Gamma_{1D,wg})/2} \right)^N . \tag{2.128}$$

Fig. 2.10 (a) shows 10 examples of the transmission (orange curves) for $N = 20$ atoms randomly placed along an unstructured waveguide, as compared to the order array with spacing $d = \lambda/2$ (blue dashed curve) and the "non-interacting" limit (black curve). Interestingly, unlike the transmission, the reflection for N randomly placed atoms on unstructured waveguide carries more information about the system, as shown in the 10 examples (orange curves) in Fig. 2.10 (b). However, the mapping of reflection spectra to atom positions is not quite clear due to the lack of simple explicit expression for reflection.

One can further calculate the transmittance and recover the Beer-Lambert law for light attenuation

$$\begin{aligned} T(\Delta_A) &\approx \exp\left[-N \ln \frac{\Delta_A^2 + (\Gamma' + \Gamma_{1D,wg})^2/4}{\Delta_A^2 + \Gamma'^2/4} \right] \\ &\approx \exp\left[-\frac{\mathrm{OD}}{1 + (2\Delta_A/\Gamma')^2} \right], \end{aligned} \tag{2.129}$$

where $\mathrm{OD} = 2N\Gamma_{1D,wg}/\Gamma'$ is the optical depth and we have assumed $\Gamma_{1D,wg} \ll \Gamma'$.

Fabry-Perot cavities

Let's examine atom-light interactions inside a Fabry-Perot cavity. In the good cavity limit ($|r| \approx 1$) and probe close to resonance ($\Delta_c/\Delta_{\mathrm{FSR}} \ll 1$), the cavity spin-exchange and decay rates can be evaluated from the cavity Green's function given in Eq. 2.91, namely

$$J_{\mathrm{cav},ij} \approx -2g^2 \frac{\Delta_c}{\Delta_c^2 + \kappa^2/4} \cos kx_i \cos kx_j \equiv J_{\mathrm{1D,cav}} \cos kx_i \cos kx_j, \tag{2.130}$$

$$\Gamma_{\mathrm{cav},ij} \approx 2g^2 \frac{\kappa}{\Delta_c^2 + \kappa^2/4} \cos kx_i \cos kx_j \equiv \Gamma_{\mathrm{1D,cav}} \cos kx_i \cos kx_j, \tag{2.131}$$

where $g = \sqrt{|\mathbf{d}|^2 \omega / 2\epsilon_0 \hbar A L}$ is the atom-cavity coupling rate defined in conventional cavity QED [154]. Note that the maximum $\Gamma_{\mathrm{1D,cav,max}} = 2g^2/\kappa = P_{\mathrm{cav}}\Gamma'$ where P_{cav} is the Purcell factor for cavity. It is also easy to show the atom-cavity coupling rate g is related to the $\Gamma_{\mathrm{1D,wg}}$ in waveguide by $\Gamma_{\mathrm{1D,wg}} = 2Lg^2/v_g$.

From the cavity spin-exchange and decay rate (Eq. 2.130), we can see here when the probe light is on resonance ($\Delta_c = 0$), $J_{\mathrm{cav},ij} = 0$ and there is only the dissipative interaction $\Gamma_{\mathrm{cav},ij}(\Delta_c = 0) = 8g^2\kappa^{-1} \cos kx_i \cos kx_j$. For detuning away from the cavity resonance ($\Delta_c > \kappa$), the spin-exchange rate $J_{\mathrm{cav},ij}$ dominates as it scales with $1/\Delta_c$ while the decay rate $\Gamma_{\mathrm{cav},ij}$ scales with $1/\Delta_c^2$. Interestingly, the ratio of the coherent spin-exchange rate to the dissipative rate equals to the ratio of the detuning Δ_c to linewidth κ, that is $J_{\mathrm{cav},ij}/\Gamma_{\mathrm{cav},ij} = \Delta_c/\kappa$.

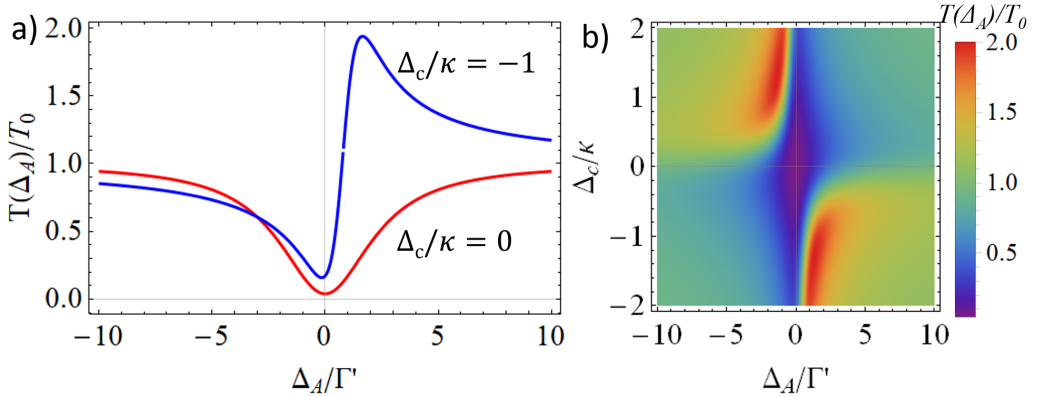

Figure 2.11: Normalized transmission spectra for single atom at cavity antinode. (a) For cavity detuning $\Delta_c/\kappa = -1$ (blue curve) and $\Delta_c = 0$ (red curve) with respect to atomic detuning Δ_A. (b) Full 2D map of normalized transmission for different cavity detuning Δ_c and atomic detuning Δ_A. In both plots, we have chosen $\Gamma_{\mathrm{1D,\,cav,\,max}} = \Gamma'$.

Remarkably, regardless of detuning Δ_c, the cavity matrix $\mathcal{G}$ is a separable matrix as $g_{ij} \propto \cos kx_i \cos kx_j$ (mathematically a matrix is separable if it can be written as a tensor product of two vectors). As a result, the matrix $\mathcal{G}$ is of rank 1 and it has only one nonzero eigenvalue $\lambda_B = \sum g_{ii} = (J_{1\text{D,cav}} + i\Gamma_{1\text{D,cav}}/2) \sum_i \cos^2 kx_i$. The normalized transmission thus takes the form

$$\frac{t(\Delta_A)}{t_0} = \frac{\Delta_A + i\Gamma'/2}{\Delta_A + J_{1\text{D,cav}} \sum_j \cos^2 kx_j + i(\Gamma' + \Gamma_{1\text{D,cav}} \sum_j \cos^2 kx_j)/2}. \tag{2.132}$$

Fig. 2.11 shows the normalized transmission spectra under different cavity detuning Δ_c and atomic detuning Δ_A for a single atom at cavity antinode. Note that the normalized transmission spectra becomes asymmetric with non-zero spin-exchange rate.

The "bright mode" here may appear to be very similar to the "bright mode" in unstructured waveguides when the atom are placed by $d = n\lambda/2$. However, the difference is there is always one "bright mode" in the cavity, no matter the separation between the atoms or whether they form an ordered or disordered chain. The fundamental difference arises from the standing wave nature of the cavity when close to resonance which eliminate the propagation phase. This physics here is essentially the same as Dicke's superradiance which in its original form, requires atom spacing smaller than the wavelength so that the light propagation phase can be neglected.

Photonic crystal waveguides

Finally, let's consider the an infinite PCW. For atomic resonance far away from the band-edge and bandgap, the photonic crystal is close to a waveguide which we already investigated in the previous sections. For close to the band-edge (for simplicity, we consider close to the upper band-edge), the spin-exchange and decay rates is given as

$$J_{\text{pcw},ij} \approx -\frac{\Gamma_{1\text{D, pcw}}}{2} \sin\Big((k - \frac{\pi}{a})|x_i - x_j|\Big) \cos\Big(\frac{\pi}{a}x_i\Big) \cos\Big(\frac{\pi}{a}x_j\Big), \tag{2.133}$$

$$\Gamma_{\text{pcw},ij} \approx \Gamma_{1\text{D, pcw}} \cos\Big((k - \frac{\pi}{a})|x_i - x_j|\Big) \cos\Big(\frac{\pi}{a}x_i\Big) \cos\Big(\frac{\pi}{a}x_j\Big). \tag{2.134}$$

Here the photonic crystal $\Gamma_{1\text{D, pcw}}$ is defined as $\Gamma_{1\text{D, pcw}} = \Gamma_0 \frac{c}{v_g} \frac{\sigma_0}{A_k} = 2\Gamma_{1\text{D, wg}}$, where the factor of 2 comes from Bloch mode standing wave. As we can see from Eq. 2.133, the spin-exchange and decay rates are oscillatory with two spacing frequencies $2\pi/(k - \pi/a)$ and $a/2$. For near the upper band-edge, $2\pi/(k - \pi/a)$ can be much larger than the physical separation of atoms. With atom maximum

separation $d_{\max} \ll 2\pi/(k - \pi/a)$, the spin-exchange rate can be approximate as

$$J_{\text{pcw},ij} \approx 0 \tag{2.135}$$

$$\Gamma_{\text{pcw},ij} \approx \Gamma_{\text{1D, pcw}} \cos\Big(\frac{\pi}{a}x\Big) \cos\Big(\frac{\pi}{a}x'\Big). \tag{2.136}$$

This suggests atom-atom interaction near the band-edge of a 1D infinite photonic crystal is dominant by collective dissipative interaction. As the matrix $\mathcal{G}$ is separable as in cavity case, the eigenmodes consist of only one "bright mode" and $N - 1$ "dark mode" with the "bright mode" eigenvalue $\lambda_B = \Gamma_{\text{1D, pcw}} \sum_j \cos^2(\frac{\pi}{a}x_j)$ and the normalized transmission as

$$\frac{t(\Delta_A)}{t_0} = \frac{\Delta_A + i\Gamma'/2}{\Delta_A + i(\Gamma' + \Gamma_{\text{1D,pcw}} \sum_j \cos^2(\frac{\pi}{a}x_j))/2}. \tag{2.137}$$

This superradiance behavior in PCW is similar to the one in standing wave cavity. The formation of Bloch mode standing wave near band-edge suppresses the propagation phase term and atoms at different positions are coupled to the light field with same phase, leading to constructive superposition of decay field. However, it is worth noting that the physics origins of the enhancement of atom-light interactions are different in cavity and PCW. Recall that in the cavity case, the $\Gamma_{\text{1D, cav}} \propto g^2/\kappa \propto 1/V\kappa$. In order to increase the atom-light coupling rate, one has to reduce the mode volume V and cavity linewidth simultaneously. This poses a significant challenge to scale up to multiple cavities and to multiple atoms inside one cavity. As a contrast, the enhancement of atom-light interaction comes from the slow light and $\Gamma_{\text{1D, pcw}} \propto v_g^-1$ and is independent of device size[5]. This slow light enhancement allows one to scale up to multiple devices and to multiple atoms along PCW.

So far, it seems the physics of atom-light interaction inside the PCW can be either approximated by a waveguide (when far from band-edge) or a cavity (when close to the band-edge). This is not true. As we show below, the physics of atom-light coupling inside a photonic crystal bandgap is completely different from the cavity or the waveguide. From the Green's function for the bandgap (Eq. 2.86)

$$J_{\text{pcw,gap},ij} \approx \frac{\Gamma_{\text{1D, pcw}}}{2} e^{-q_{\text{im}}|x_i - x_j|} \cos\Big(\frac{\pi}{a}x_i\Big) \cos\Big(\frac{\pi}{a}x_j\Big) \tag{2.138}$$

$$\Gamma_{\text{pcw,gap},ij} = 0, \tag{2.139}$$

[5]In fact, for finite device, the first resonance v_g scales with $1/N$ as shown in Eq. 2.36. In principle, one can simply increase the length of device to increase the coupling strength. In practice, this is typically limited by the material loss which we didn't consider here.

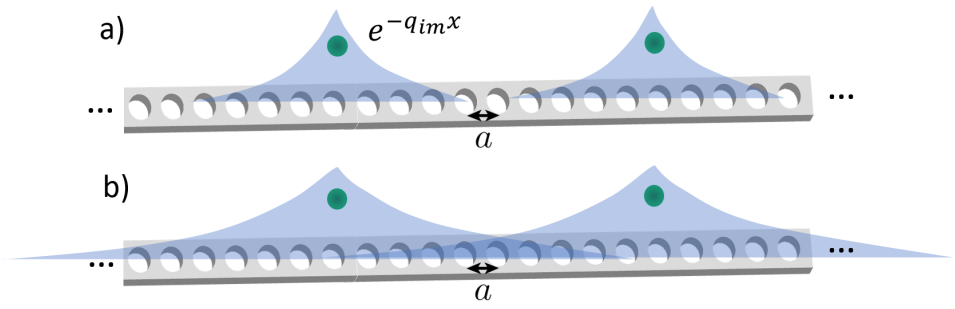

Figure 2.12: Illustration of tuning the interaction length by changing the relative position of the band-edge frequency with respect to atomic transition frequency. (a) Deep inside the bandgap with short interaction range. (b) Close to the band-edge with long interaction range.

we can see the atom-atom interactions inside photonic crystal bandgap is purely coherent with the spatial field decay constant q_{im}. As already shown in the transfer matrix model (Eq. 2.15), q_{im} is a function of the detuning to band-edge. By changing the detuning to the band-edge, one can tune the interaction range between two atoms from tightly bonding model to infinite long range interactions [52] as illustrated in Fig. 2.12. Finally, we notice the matrix $\mathcal{G}$ is not a separable matrix. As a result, there is no single "bright mode". However, for the case the atomic frequency is close to the band-edge (but still within the bandgap), $q_{\text{im}} \simeq 0$ and we can neglect the exponential term $e^{-q_{\text{im}}|x_i - x_j|}$ term if the maximum separation $q_{\text{im}} d_{\text{max}} \simeq 0$. Given this approximation, the matrix $\mathcal{G}$ is again separable and we recover the single "bright mode" as in the cavity case.

2.7 Summary

In this chapter, we have discussed two different methods to understand the atom-light interaction in nanostructures, namely the transfer matrix method and the Green's function approach. Each method provides valuable information of about physics of atom-light interaction in nanostructures, from different perspectives. In the transfer matrix model, we have presented a series of scaling analysis of atom-light interaction in the 1D infinite and finite PCW with respect to a variety of device parameters. More importantly, we broke down the enhancement of atom-light coupling into a few separate physical origins, namely cavity enhancement and the group velocity enhancement for the finite PCW. The Green's function approach provides a very rigorous framework for describing atom-light interactions and can be used to study atom-light interactions in 3D complex optical structures. It was shown

that by tracing out the field operators, the information of complex optical structures is encoded into dissipative and dispersive interactions between atoms. We also applied the Green's function approach explicitly to quasi-1D structures, namely the waveguide, cavity and PCW and characterized their transmission/reflection spectra. Importantly, we show the bandgap in PCWs provides a unique frontier to study atom-atom interactions with tunable interaction range.

We emphasize that the methods we have described here not only apply to atom-light interactions but can also be applied to other emitters such as quantum dots, NV centers, rare earth ions and superconducting qubits [123, 124, 134, 206].

While we focus on understanding the basic physics of atom-light interactions in nanostructures in this chapter, connections to the real world experiment will be presented in the next chapter.

Chapter 3

ATOM-LIGHT INTERACTIONS IN NANOSTRUCTURES: A REAL-LIFE STORY

3.1 Introduction

In the previous chapter, we presented the basic theory of atom-light interaction in nanophotonic structures. There, for simplicity, we restricted the discussion within two-level atoms on quasi-1D structures. In real world, the structures are complex 3D structures and the atoms have multiple electronic levels. It is of interest to see how the simple story can be extended to apply to the real world nanophotonic structures and atoms. Furthermore, the extra degrees of freedom from both the nanostructures and atoms may allow us to observe new phenomena not presented in the 1D two-level atoms scenario. In this chapter, we will show how the simple theory in the previous chapter connects to the real world experiment. Most importantly, we show examples of new exciting opportunities for atom-light interactions on specially engineered nanophotonic structures that are reachable in experiment in the near future.

The topics in this chapter are arranged as follows: We will first start with an overview of the general theory photonic crystals and the photonic crystal waveguides (PCWs) designed and tested within the Caltech Quantum Optics Group (QOG) for atom-light interaction applications. After that we will give an introduction of electronic levels in the cesium atom used in our experiment and understand the associated transition strengths of different transitions. With the understanding of both the photonic world and the atomic world, we then present the general theory of atom-light interaction with multi-level atoms on complex nanophotonic structures and the FDTD numerical simulations of the interaction rates on different photonic crystals. In the end, we will show the general design principles for guided-mode traps and review some other potential extensions to the physics described in this chapter.

The materials in this chapter will also serve as an overview of previous experimental achievements made by generations of the QOG members, for example, Chen-Lung Hung, Akihisa Goban, Jonathon Hood, Mike Martin, Juan Muniz, Su-Peng Yu, Andrew McClung, Alex Burgers, Lucas Peng, Jae Lee and many others. Main references in this chapter are Refs. [33, 40, 66–68, 86, 92, 200, 204] and PhD thesis

from previous graduated students [69, 88, 130, 146, 171, 202].

3.2 Photonic crystal devices in the real world

In the previous chapter, we introduced some basic concepts of the PCW with 1D periodic scatter array model. In this section, I will introduce more formally about the theory of photonic crystals. Specifically, I will go through 1D PCWs and 2D photonic slabs.

General theory of photonic crystals

The concept of photonic crystals originates from early works by Eli Yablonovitch [197] and Sajeev John [100] in 1987. In their seminal papers, they suggested that the materials where the dielectric constant is modulated in a periodic way will affect the structure and dispersion of their photonic modes. This idea is in analog to the electron band structure in crystals. In the case of photons, the spatial periodicity of the dielectric function constitutes a periodic potential, enabling the emergence of photonic bands and band gaps. To introduce the theory behind photonic crystal, let's start our discussion from the Maxwell's wave equation (Eq. 2.62) in the frequency domain [137] with $\mathbf{E}(\mathbf{r}, t) = \mathrm{Re}\left[\mathbf{E}(\mathbf{r})e^{-i\omega t}\right]$

$$\mathcal{L}\mathbf{E} = \frac{1}{\epsilon(\mathbf{r})}\nabla \times \nabla \times \mathbf{E}(\mathbf{r}) = \frac{\omega^2}{c^2}\mathbf{E}(\mathbf{r}). \tag{3.1}$$

Note that different from Eq. 2.62, we further assumed there is no free current density, e.g. $\mathbf{J}_f(\mathbf{r}) = 0$. We also explicitly write the wave equation as a form of an eigenvalue equation for the operator $\mathcal{L} = \frac{1}{\epsilon(\mathbf{r})}\nabla \times \nabla \times$ with ω^2/c^2 as the eigenvalue and $\mathbf{E}(\mathbf{r})$ as the eigenfunction[1]. When $\epsilon(\mathbf{r})$ is a periodic function of the spatial coordinate $\mathbf{r}$, we can apply Bloch's theorem

$$\mathbf{E}_{n,\mathbf{k}}(\mathbf{r}) = \mathbf{u}_{n,\mathbf{k}}(\mathbf{r})e^{i\mathbf{k}\cdot\mathbf{r}}, \tag{3.2}$$

where $\mathbf{k}$ is wavevector and n is the band index. $\mathbf{u}_{\mathbf{k}}(\mathbf{r})$ are periodic vectorial functions that satisfy

$$\mathbf{u}_{\mathbf{k}}(\mathbf{r} + \mathbf{a}_i) = \mathbf{u}_{\mathbf{k}}(\mathbf{r}), \tag{3.3}$$

and $\mathbf{a}_i$ are the elementary lattice vectors with $i = 1, 2, 3$. Plug the Bloch mode solution $\mathbf{E}_{n,\mathbf{k}}(\mathbf{r})$ into Eq. 3.1, one can obtain the dispersion relations $\omega_n(\mathbf{k})$. The plot of the dispersion relations for all n band within the Brillouin zone is called

[1] Strictly speaking, the magnetic field $\mathbf{H}$ is a better choice as an eigenvalue equation as the $\mathcal{L}$ for electric field can be non-Hermitian, as pointed out in Ref. [99].

band diagram. Band diagrams are typically projected to a finite range of k vectors within the Brillouin zone (for example, in 1D $-\pi/a < k < \pi/a$). Because the function $\omega_n(\mathbf{k})$ possess the full symmetry of the photonic crystals [99], we only need to consider the smallest region within the Brillouin zone called the irreducible Brillouin zones. Further, it can be shown that the band frequencies typically take extreme values at the edge of the irreducible Brillouin zones (for example $k = \pi/a$ in 1D) [111]. As a result, 2D or 3D band diagram are typically plotted along the path through these high symmetry k points labelled as 'Γ', 'X', 'M', etc., following the solid state convention. An example of the band diagram for 2D square array with infinite long dielectric rods is shown in Fig. 3.1. The left panel in Fig. 3.1 shows the contour plots of $\omega(k_x, k_y)$ for the lowest band, with the first Brillouin zone shown as a black square and the irreducible zone shown as a red triangle. The right panel in Fig. 3.1 shows two different bands that are labelled based on their mode polarizations along the path $\Gamma - X - M - \Gamma$, as will be explained in detail in next sections. Band diagrams for more realistic photonic structures for atom-light interaction applications will be shown in Fig. 3.2, Fig. 3.5 and Fig. 3.4.

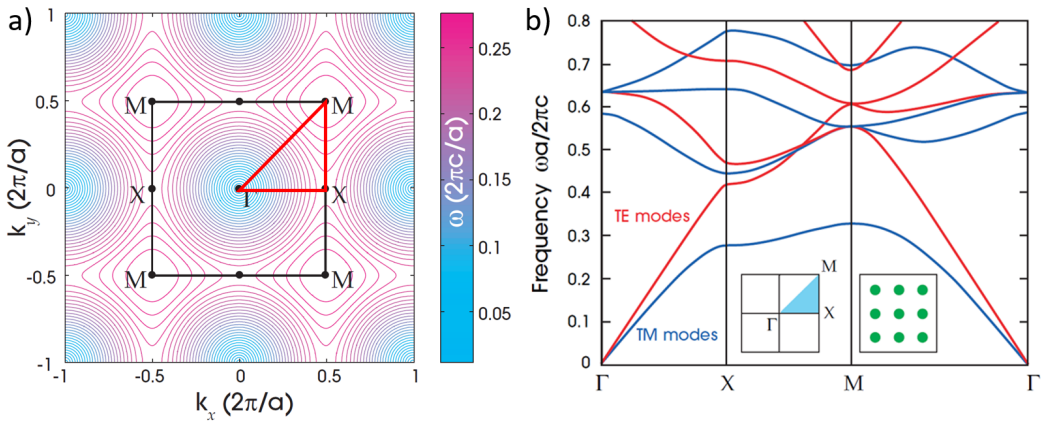

Figure 3.1: Examples of band diagrams for photonic crystals. Here the band diagrams are calculated for a square array of dielectric columns with $r = 0.2a$ and $\epsilon = 8.9$. (a) Contour plots of $\omega(k_x, k_y)$ for the lowest band. The first Brillouin zone is shown as a black square, and the irreducible zone is shown as a red triangle. (b) The blue bands represent TM modes and the red bands represent TE modes. *Left inset*: The Brillouin zone, with the irreducible zone shaded light blue. *Right inset*: The cross-sectional view of the dielectric structure under study. Figures adapted from Ref. [99] for illustration purpose.

Numerical methods for modelling photonic crystals

For complex nanophotonic structures, it is typically hard to solve for the Bloch modes analytically. While analytic models such as the 1D transfer matrix model described in the previous chapter can be used to qualitatively analyze the performance, rigorous numerical methods are typically required for a precise modelling. In the past, several numerical methods have been employed inside the QOG to design and model the real photonic devices for atom-photonic purpose. Typically for time domain simulation or Green's function calculation, we use finite-difference time-domain method (FDTD) with the open software Meep [140] developed by the MIT group and the commercial software Lumerical [126]. For solving photonic crystal band diagram, we use the eigenmode expansion methods based open software MPB [103] (also developed by MIT group) and the finite element method based commercial software COMSOL®[45] .

Generally speaking, a good design of nanophotonic structures for the purpose of atom-light interactions should fulfill a few main criteria. First, it should be able to support strong atom-light interactions. For the PCW case, this directly corresponds to the small effective mode volume and the small group velocity. The small group velocity is achieved by aligning the Cs transitions to the band-edge. Second, it should be able to support stable optical traps for atoms. A stable trap site for atoms ensures long interaction time between atom and light which is the basis of many quantum applications, such as quantum memory. Third, it should be able be fabricated with sufficient precision to match atomic transitions and the material should be compatible with atomic operations. Lastly, it should be mechanically stable and rigid. In the following sections, we will show the design principles behind a variety of structures developed in the QOG and basic techniques to quantify a good design vs. a bad design.

Three types of photonic crystal waveguides

As our focus here is atom-light interaction in do nots, there are three different kind of do nots we have designed for trapping and strong atom-light interactions, namely the APCW, the SPCW and the 2D photonic crystal slabs.

Fig. 3.2 shows an example of the band diagram for the APCW. This double nanobeam structure is designed with corrugated modulations on the outer side of the double nanobeams and a flat air gap in the center. At first glance, this design is different from conventional 1D nanobeam do nots with periodic air holes [56]. This is due

the "small" wavelength difference of the cesium atom's two main transitions, D_1 and D_2 lines. To align the bandgap (red area in Fig. 3.2) to the D_1 and D_2 frequency difference, will require the size of the air holes in 1D down to < 100 nm, which is challenging for nano-fabrication [92, 200]. Further the flat air gap in the center of APCW also helps making a stable guided-mode trap, which will be explained in detail in Section 3.5.

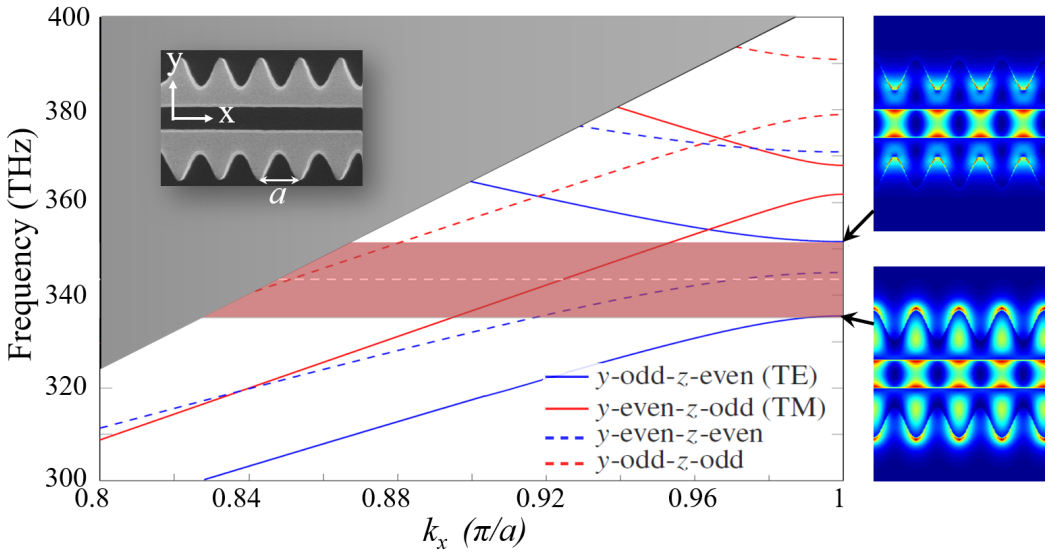

Figure 3.2: (a) The band diagram for the APCW. Blue curves are bands with even z symmetry and red curves are bands with odd z symmetry. Solid lines represent the modes which can be directly excited in the experiment. On the right side are simulated field profiles for the two TE bands. Figures adapted from Andrew McClung's thesis [130] with modifications.

The band diagram in Fig. 3.2 for the APCW has clearly more bands than the one presented (Fig. 2.2) in the 1D transfer matrix model. As claimed in the previous section, the number of modes is related to the symmetries of the structure under study. In this case of the APCW, this double-nanobeam structure has two mirror-symmetry planes ($y = 0$ and $z = 0$ for propagating along x axis). These symmetries allow classify the modes as either even or odd with respect to both types of reflections, z and y. For example, for a mode with electric field that satisfies $\mathbf{E}(x, y, z) = -\mathbf{E}(x, -y, z)$, this mode is said to have even y symmetry (similarly, odd y symmetry if $\mathbf{E}(x, y, z) = \mathbf{E}(x, -y, z)$). Under this definition, there are four different modes for the APCW structure, namely y-odd-z-odd, y-odd-z-even, y-even-z-odd and y-even-z-even as shown in Fig. 3.3. Specifically, the y-even-z-odd mode and y-odd-z-even mode are also called 'TM-like' and 'TE-like', respectively. They are analog to

the TE and TM polarization light in free-space, as their polarization are polarized mostly along z axis (TM) and y axis (TE). This similarity also leads to the fact that the TE-like and TM-like are easier to be excited by a free-space linear polarized light input from the end of the do not. For this reason, we will focus the TE-like and TM-like modes in the rest of our discussion.

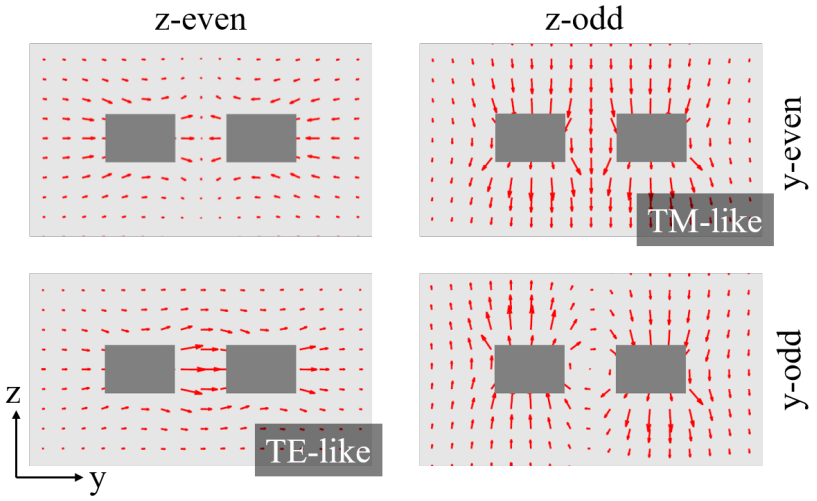

Figure 3.3: Example of the mode symmetry of the APCW. Arrows indicate the direction and magnitude of the electric field vector. The top (bottom) row has even (odd) y symmetry and the left (right) column has even (odd) z symmetry. TE-like and TM-like modes are indicated. Figures adapted from Andrew McClung's thesis [130].

The band diagram in Fig. 3.2 is also different from the 'true' photonic crystal band diagram as shown in Fig. 3.1 with the presence of the gray shaded area. This is an effect of index guiding, a phenomenon similar to the total reflection when light entering from an optically denser material to an optically rarer material. For several practical reasons (e.g. device fabrication), the physical devices we worked on in our experiments are either 1D do nots or 2D photonic crystal slabs. In these devices, confinement of light in the transverse direction is achieved by index guiding, In these cases, the wavevector projected into propagation direction and perpendicular to propagation direction $\omega = c|\mathbf{k}| = c\sqrt{k_\perp^2 + k_\parallel^2}$. For a given value $k_\parallel$, there will be modes with every possible frequency greater than $ck_\parallel$. Thus, $\omega = ck_\parallel$ defines separation which the spectrum of states above is continuous, as marked gray area in Fig. 3.2. By convention, the region of band structure with $\omega > ck_\parallel$ is called the light cone. Further, as light does not propagate along transverse direction, $k_\perp$ has to be imaginary for modes below the light line with $k_\perp = i\kappa_\parallel = i\sqrt{k_\parallel^2 - \omega^2/c^2}$. The fields

for these index-guided modes decay exponentially decay in the transverse direction with e^{-1} decay length $\kappa_{\|}^{-1}$. As a simple example, for the band-edge of the APCW with $a = 370$ nm, $\omega_{\mathrm{BE}} = \omega_{\mathrm{D1}} \approx 2\pi\times335$ THz, we have the decay length $\kappa_{\|}^{-1} \approx 209.4$ nm. Similarly, for D_2 transitions at the band-edge, we get $\kappa_{\|}^{-1} \approx 235.9$ nm. These evanescent fields, together with their different decay lengths, are important for the guided-mode trap design, as shown later in Section 3.5.

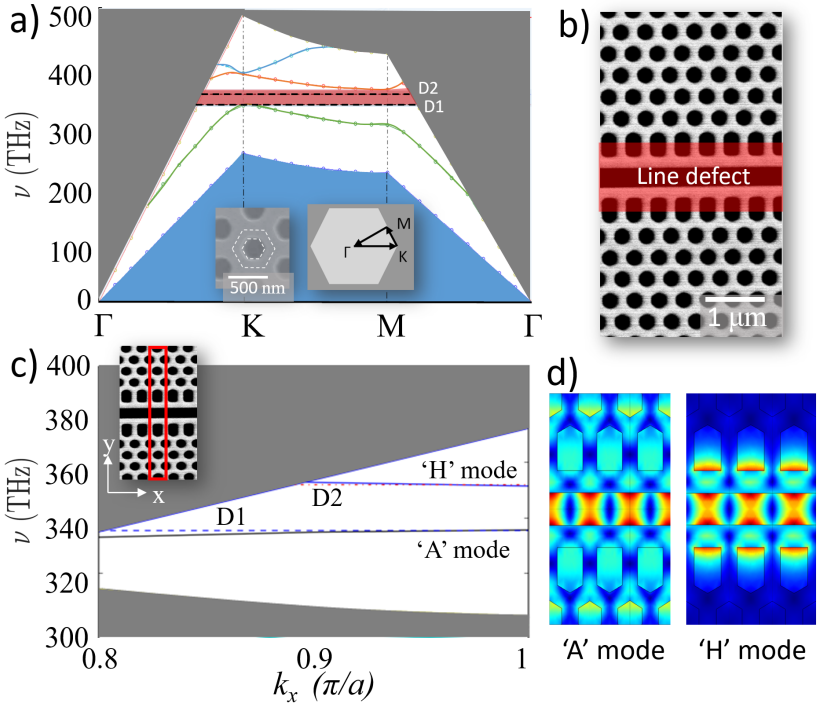

Figure 3.4: (a) An example of the reduced band diagram for TE modes of the hexagonal lattice with hexagonal hole. The red shaded region represents the bandgap and the D_1 and D_2 lines are indicated with black dashed lines. *Insets*: *left* the hexagonal lattice in real space with the unit cell marked with white dashed hexagons; *right* the Brillouin zone in the momentum space, with the high symmetry points labelled 'Γ', 'K' and 'M'. (b) The SEM image of the slot photonic crystal waveguide (SPCW). Red shaded regions indicating the line defect inside the 2D hexagonal lattice. (c) Band diagram of the SPCW with the unit cell aligned to Cs D_1 and D_2 transitions. *Inset* SEM image of the SPCW with the unit cell indicated with red rectangle. Detailed design parameters can be found in Su-Peng Yu's thesis [202]. (d) Simulated field profiles for the upper ('A' mode) and lower band ('H' mode). Fig. (a) is adapted from Su-Peng Yu's thesis [202] with modifications.

For 2D slabs, one can replace the index guiding in one transverse direction (y direction) by embedding the 1D waveguide into a 2D photonic crystal with a band gap. Technically, this is done by generating a line defect (e.g. removing a row of

holes) in 2D photonic crystals, as shown in Fig. 3.4 (b). In the y direction, the mode for the line defect has been localized to the line defect in the bandgap of the 2D photonic crystal. Meanwhile, the new system still has translational symmetry along x direction so the localized line defect mode can freely propagate along the line defect. A specific example within our group is the design of the slot photonic crystal waveguide (SPCW) as shown in Fig. 3.4 (b). Here the perfect 2D photonic is a hexagonal lattice with hexagonal holes and it has a bandgap larger than the cesium D_1 and D_2 lines. The line defect is generated by adding an air gap and increasing the air hole size of the first row. This design appear to be different from the conventional 'W1' defect slot-waveguides [198] as the 2D crystal has been pulled further apart. This is again a consequence of aligning the two line defect modes to the cesium D_1 and D_2 lines, as shown in the band diagram in Fig. 3.4 (c) with the unit-cell of the SPCW indicated in red rectangle. The intensity profiles of the two aligned modes are shown in Fig. 3.4 (d), with the 'A' mode aligned to D_1 and 'H' mode aligned to D2. Inside the air gap, the mode profile looks very similar to the mode intensity profile of the APCW in Fig. 3.2. The advantages of the SPCW over the APCW is the stronger group velocity enhancement in atom-light interactions. This difference is visible from the flatness of the band (as $v_g = d\omega/dk$).

Finally, it is worth noting that 2D photonic crystal slabs itself (without the line defect) can also guide the light by aligning the propagation k vector to the flat isofrequency contours in the band diagram in Fig. 3.1 (a) and more explicitly in Fig. 3.5 (b). As an example, we show the reduced band diagram and the isofrequency contour plot of the lower band for square lattice with circle holes in Fig. 3.5 (a) and (b). For a beam with wavevector lying along the $\vec{k}_{\Gamma M}$ direction and frequency within the black rectangular region in Fig. 3.5 (b), the beam will spread out very slowly as the group velocities for different k-component are parallel to each other in the flat contour region. As a result, the beam is self-collimated inside the 2D photonic crystal slab and can freely propagate for a long distance. This effect is called supercollimation and was first proposed by Kosaka et al. [113] in 1999. Follow this idea, a design for the application of atom-light interactions is shown in Fig. 3.5 (e) and (f) [171]. Despite having a relatively larger mode area compared to APCW and SPCW, this supercollimation effect may allow one to design chips to address atoms from different input ports as shown in Fig. 3.5 (f). This might be useful in building a 2D atomic network with directional emissions, as will be discussed in Section 3.4.

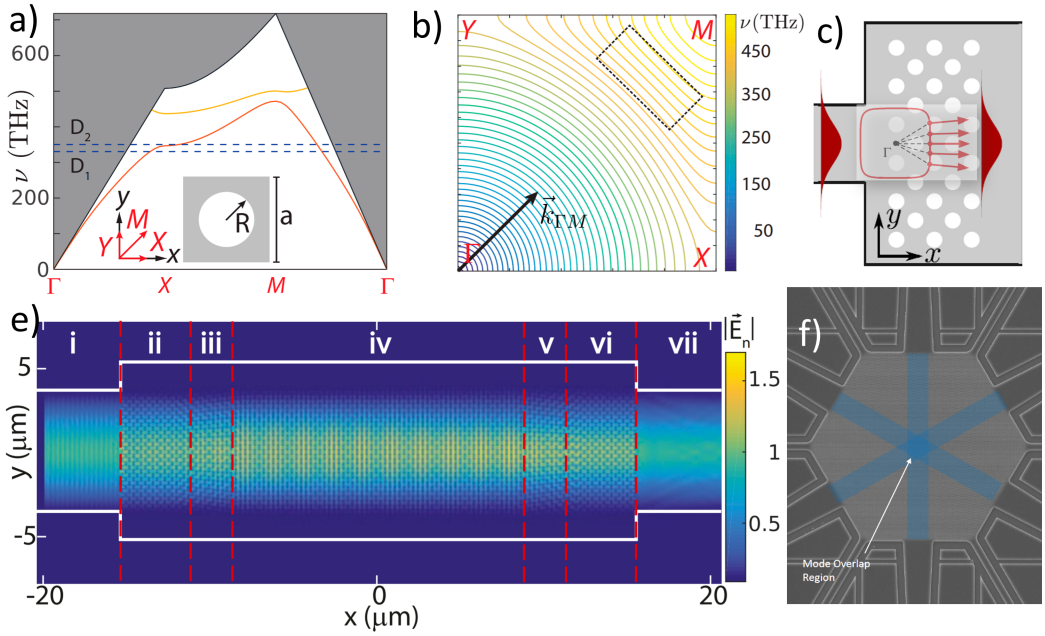

Figure 3.5: (a) The reduced band structure for a unit cell with lattice constant $a = 290$ nm, hole radius $R = 103$ nm, thickness $t = 200$ nm and reflective index $n = 2$ (i.e. SiN). Dashed lines mark Cs D_1 and D_2 transition frequencies. *Inset* shows the real space (black arrows) and momentum space (red arrows) basis vectors. (b) Isofrequency contours in momentum space for the lowest band shown in (a). The dashed black rectangle shows the region where the group velocity has uniform direction along $\vec{k}_{\Gamma M}$. (c) Illustration of waveform stays the same shape when propagating on a 2D photonic crystal with flat isofrequency contours (transparent inset). (e) Simulated field profile for an incident guided mode with frequency near Cs D_2 line propagating along x axis. Region (i,vii) are the input/output rectangular waveguide. Region (ii,vi) provide supercollimation with the $\Gamma - M$ direction aligned along x axis. Region (iv) is aligned to Cs D_2 line at M point for slow light enhancement and region (iii, v) are transition regions connecting (iv) to (ii,vi). (f) Example of devices of a hexagonal slab with 2D photonic crystals designed to have supercollimation effect at working wavelength. The connected six ports allow addressing atoms in the overlapped region in the center from six different directions independently. The Figs. (a-e) are adapted from Juan Muniz's thesis [171] and Fig. (f) is adapted from Su-Peng Yu's thesis [202].

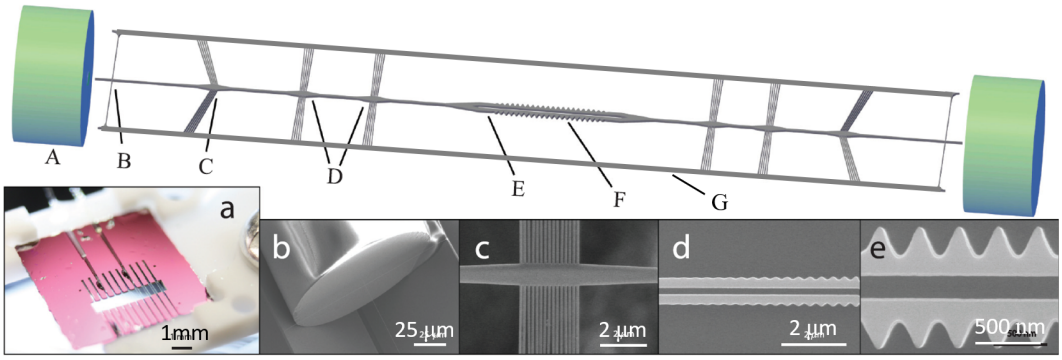

Figure 3.6: The APCW chip and support components. Center: Schematic of the waveguide chip, illustrating the various regions of the waveguide. Bottom: (a) Optical image of the fiber-coupled waveguide chip showing the through-hole for optical access. Zoom-in SEM image of (b) the adiabatic fiber-coupling region (A), (c) the alignment, mechanical support, and thermal heat-sink tethers (B, C, D), (d) the tapered region of the APCW (E), and (e) the central APCW region (F). The sinusoidal modulation facilitates high-precision fabrication. (G) the side thermal/mechanical contracts which consist of a pair of 7.5 μm wide SiN rails extending across the entire length ($\simeq$ 2 mm) of the waveguide and connecting to the SiN, Si substrate. Figure adapted from Ref. [200].

Full chip-scale design

A good design of the do not is not the full story for the applications to atom-light interactions. In order to be compatible with atomic setup and allow light coupled in and out from the device, more chip level engineering is required. As an example, Fig. 3.6 shows an illustration of the full chip design for the APCW device together with zoomed images of other essential components on the chip. This device is fabricated on a 200 μm thick Silicon chip coated with a high-stress 200 nm thick silicon nitride (SiN) film. As shown in Fig. 3.6 (a), the SiN device is suspended across a 2-mm-wide window after the silicon substrate beneath it is removed. This window allows optical access for the trapping and cooling of atoms around the device. The full device is $\simeq$ 3 mm long with $\simeq$ 300 nm beam width in the center and tapered down to $\simeq$ 130 nm at the end facet. The etched V-grooves on each end provide optimized coupling positions for fiber-butt coupling [43]. The thin nanowire structure design suppresses the scattering of atomic beams (e.g. the cooling beam) but is not mechanical stable with itself. Supporting tethers on the side (labelled as 'B', 'C', 'D' in Fig. 3.6) together with two side rails (7.5 μm each) provide a rigid frame for both mechanical support and thermal dissipation to the center nanowire device. Finally, in order to match the mode profile from single nanobeam

to double nanobeam and suppress the group index mismatching at boundary of the do not, a tapered region (region 'E' in Fig. 3.6) is introduced by linearly ramping the amplitude of modulation from zero to the value in the APCW.

It is worth mentioning new generation of chips for SPCW and free-space couplers has been also designed and tested. These new type of couplers provides better mechanical stability and much higher damaging threshold than the structure described here and will be described in detail in Chapter 5.

Device characterization

Finally, after a device is designed and fabricated, it is important to characterize the device performance before further integration with the cold atom setup. Typically the device characterization is done by transmission/reflection measurements [68, 200] and the scattering light measurements [86] as explained below.

Fig. 3.7 shows the measured transmission/reflection spectra of the APCW for TE and TM polarizations. Here the spectra are measured by coupling the light source from a broadband superluminescent diode into the device and detecting the transmitted/reflected signal using an optical spectrum analyzer. From the measured spectra, one can extract substantial information about the optical properties of the whole device. First, one can directly read out the position of the bandgap from the reflection spectra and mark the relative position to cesium D_1 and D_2 lines (indicated with red dashed lines in Fig. 3.7). More quantitatively, the transmission and reflection spectra are fitted by transfer matrix models or FDTD simulations to find the correct group index n_g and the reflectivity R_t at the boundary due to group index mismatch. An example of the fitted transmission spectra is shown in Fig. 3.7 (b) with the black solid line representing the measured transmission and red solid line representing the fitted from 1D transfer matrix model. The estimated group index n_g and boundary reflectivity R_t is plotted in Fig. 3.7 (c) and at the first resonance position (indicated by black vertical dashed line), the group index is $\simeq 11$ and $R_t \simeq 0.48$. This can be used to estimate the total enhancement of atom-light interaction as already shown in Chapter 2

$$\frac{\Gamma_{1D}}{\Gamma'} = \frac{\gamma_{1\mathrm{D}}}{\Gamma'} n_g \frac{1+R_t}{1-R_t} \simeq 1.56, \tag{3.4}$$

where we have assumed the unstructured decay rate $\gamma_{1D}/\Gamma' \simeq 0.05$. This simple estimation agrees qualitatively with the FDTD simulation with Green's function calculation in Ref. [68, 86]. Slight difference comes from the assumed unstructured decay rate γ_{1D} which is the value measured in the nanofiber experiment [66].

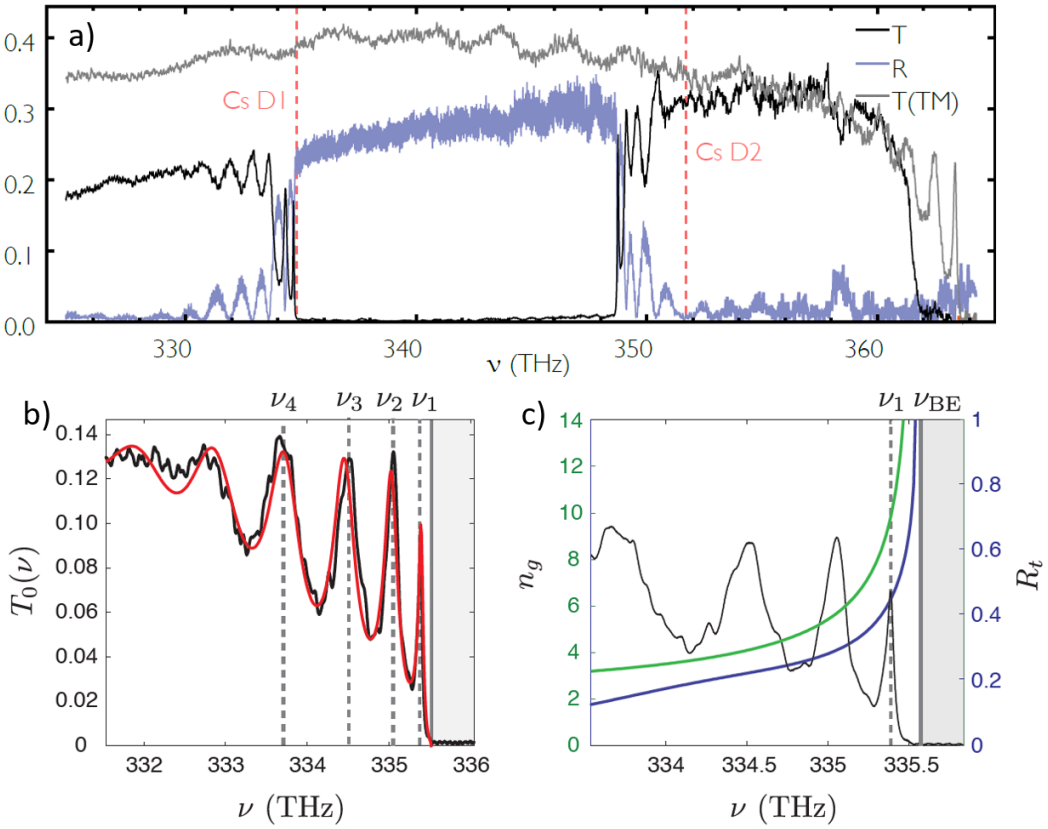

Figure 3.7: (a) Measured transmission (black curve) and reflection (blue curve) spectra for the TE mode. The red dashed lines are the Cs D_1 and D_2 lines. The band edges of the TE mode are at positions $\simeq$ 335 THz and $\simeq$ 348 THz. The TM transmission (gray curve) is plotted as a comparison with the band-edge at $\simeq$ 365 THz. (b) The model fit (red) of a measured TE transmission spectra around the edge of the dielectric band. The dashed lines mark the resonant frequencies ν_i and the solid line marks the inferred band-edge frequency ν_{BE}. (c) Estimated group index n_g (green) and taper reflection R_t (blue) from the fitted model, with the transmission spectra overlaid for reference. The dashed line indicates the position of the first resonance ν_1 with the fitted group velocity $n_g \simeq 11$ and the taper reflection $R_t \simeq 0.48$. Figure (a) is adapted from Ref. [86] and Figure (b,c) is adapted from Ref. [68].

It is worth mentioning that in real experiment, this process is iterated with the measurement result fed into the fabrication process to find the optimal 'magic factors' for fabricating the desired device [130, 202].

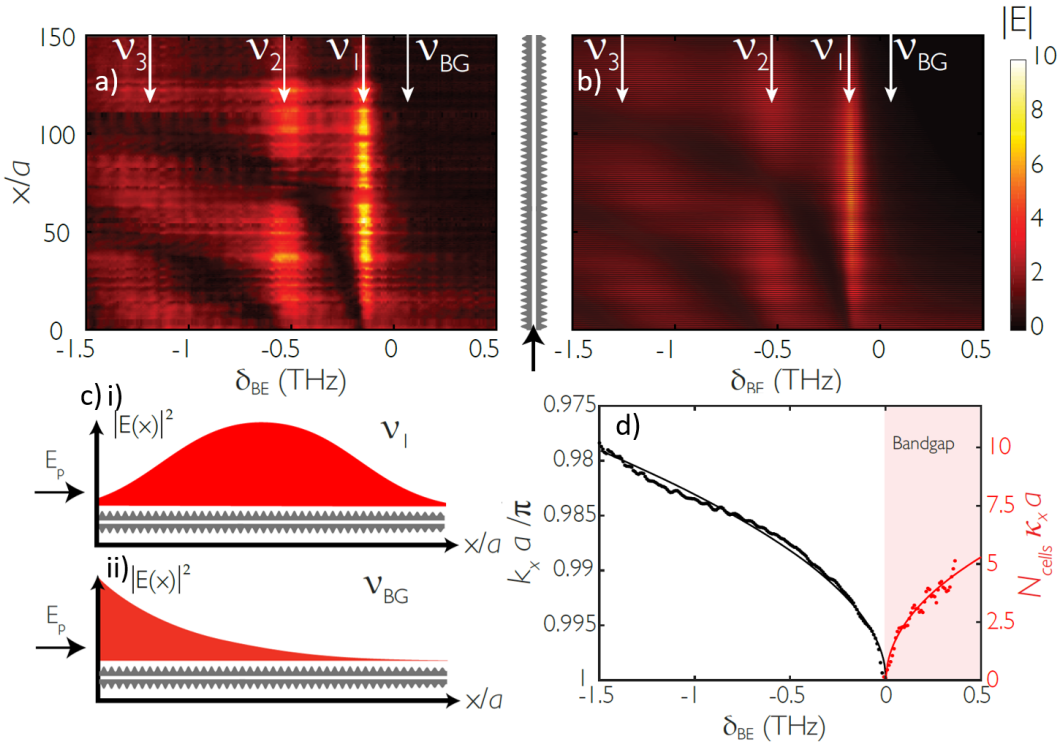

Figure 3.8: (a) The measured scattering light from the APCW. The 2D map is generated by scanning the frequency and integrating the scattering light in each image. The resonances' positions and the band-edge position is also marked with arrows. (b) A FDTD simulation of the field profile near the band-edge shows good agreement with the scattering light measurement in (a). (c) An illustration of the intensity profile at first resonance and at the bandgap. (d) The fitted k_x (dots) from the scattering light measurement matches very well with the simulated dispersion relation (solid lines) in both the propagating band (black) and the band gap (red). Figures adapted from Ref. [86].

The dispersion relation can also be directly measured by imaging the scattering light along the device with a microscope. Scanning the probe frequency, the distribution of the scattering light can provide the information about field distribution within the device. Fig. 3.8 shows an example of such measurement. Here the data under each frequency is integrated from a single scattering image and the line data under different frequencies are taken to produce this 2D map. From the scattering light stacked images (a), one can identify the position of the first few resonances near the band-edge together with its field distribution. One can further extract the spatial

k_x from this scattering light plot. Recall that in the 1D transfer matrix model (Chapter 2), the finite photonic crystal is equivalent to a Fabry-Perot cavity in the Bloch space. Thus, the electric field within a finite photonic crystal can be written as

$$|E(x)|^2 = I_1 \left| e^{i(\delta k_x)x} - R_t e^{2i\delta k_x L} e^{-i\delta k_x x} \right|^2, \tag{3.5}$$

where $\delta k_x = \pi/a - k_x$ and R_t is the reflectivity of the boundary due to index mismatch. By fitting the measured scattering light data, one can extract the information about the k_x under different frequency ω and thus infer the dispersion relation. Similarly, for the light field in the band gap, by replacing the δk_x with $i\kappa_x$, we can also extract the decay constant as an function of detuning to the band-edge δ_{BE}. An example of the fitted δk_x is shown in Fig. 3.8 (d) and the measured result (dots) matches very well with the simulated dispersion relation (solid lines) in both the band (black) and the band gap (red).

In the previous discussions, we have skipped the nano-fabrication process for simplicity. However, it is worth pointing out it is non-trivial to achieve high yield rates and precise alignment of the spectra to Cs D_1 and D_2 lines, given the extraordinary aspect ratio of the device (L_x/L_y =2 mm/ 500 nm= 4000). Readers who interested in this fabrication process can refer to the theses from Su-Peng Yu [202] and Andrew McClung [130] for details.

3.3 The multilevel nature of atoms in the real world

The electronic structure of the cesium atom

We have introduced the complex optical structures in the real world. Now, let's recognize the real atom we work with in our experiment. In the previous chapter, we model atom as a two-level system. This is apparently oversimplified from the real cesium atoms we are working on. The reason we choose cesium atoms (^{133}Cs) is for their relatively simple electronic configuration ([Xe]6s^1) and relatively heavy mass which is suitable for laser cooling and trap. Despite the single valence electron, the cesium atom exhibits multiple levels due to the coupling of spin-orbit momentum. First, the fine structure is a result of the coupling between the orbital angular momentum $\mathbf{L}$ of the outer electron and its spin angular momentum $\mathbf{S}$. The total angular momentum quantum number of the atom $\mathbf{J} = \mathbf{L} + \mathbf{S}$ can takes the values in the range $|L - S| \leq J \leq L + S$. For Cs ground state, we have $L = 0$ and $S = 1/2$ so $J = 1/2$ and for the excited state, we have $L = 1$ and $J = 1/2$ or $J = 3/2$. These two excited states corresponds to state $6P_{1/2}$ and state $6P_{3/2}$ and the two transitions from ground state are called D_1 ($6S_{1/2} \rightarrow 6P_{3/2}$) and D_2

($6S_{1/2} \rightarrow 6P_{3/2}$) lines. The corresponding transition wavelengths for these two D lines are at $\simeq$ 852.347 nm (corresponding frequency at $\simeq$ 351.726 THz) for D_2 line and 894.593 nm (corresponding frequency at $\simeq$ 335.116 THz) for D_1 line.

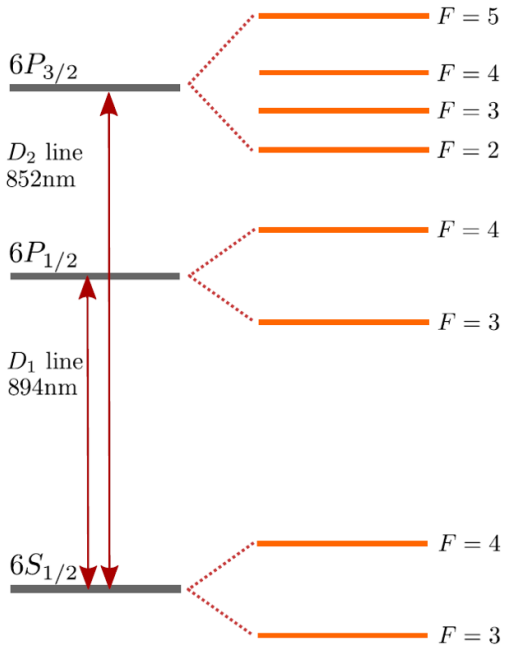

Figure 3.9: (a) The fine and hyperfine structure for cesium 133. The two main transitions D_1 and D_2 correspond to $6S_{1/2} \rightarrow 6P_{1/2}$ and $6S_{1/2} \rightarrow 6P_{3/2}$, respectively.

The hyperfine structure is a result the coupling of $\mathbf{J}$ with the total nuclear angular momentum $\mathbf{I}$. The total atomic angular momentum $\mathbf{F}$ is $\mathbf{F} = \mathbf{J} + \mathbf{I}$ with value range $|J - I| \leq F \leq J + I$. For the cesium ground state, $J = 1/2$ and $I = 7/2$, so $F = 3$ or $F = 4$. Similarly for the D_1 excited state $F = 3$ or $F = 4$ and for the D_2 excited state F takes 2,3,4,5. A full level diagram of the fine and hyperfine splittings is shown in Fig. 3.9.

In the presence of external field, the hyperfine structure can be further split into different sublevels. For example, under DC magnetic fields, each of the hyperfine levels can split into $2F + 1$ magnetic sublevels labelled as $|F, m_F\rangle$ with Zeeman splitting approximately given as

$$\Delta E_{|F,m_F\rangle} = \mu_B g_F m_F B_z, \tag{3.6}$$

where μ_B is the Bohr magneton, g_F is the hyperfine Landé g-factor (with expression given in Ref. [173]) and we have explicitly assumed the magnetic field is along z axis. Lastly, it is worth mentioning these magnetic sublevel degeneracies can break

without the presence of magnetic field, for example, due to vector light shifts of an optical field. We will discuss the AC stark of atomic levels in detail in Section 3.5.

Reduction of the dipole operator

With the complexity of fine and hyperfine levels, it is important to determine the transition strength of a specific atom transition when the laser linewidth is narrow enough to address each hyperfine levels (which is the case in our experiment). Recall that in the previous Chapter, the interaction between atom and light is characterized by the dipole moment elements. Thus for different hyperfine levels $|Fm_F\rangle$ (as the ground states) and $\left|F'm'_F\right\rangle$ (as the excited states), the transition strength can be determined by evaluating the dipole moment elements $\langle Fm_F|\,\hat{\mathbf{d}}\,\left|F'm'_F\right\rangle$. In the following derivations, we follow Ref. [173] closely for the definitions[2]. To calculate the matrix element, we can further factor out the angular dependence by expressing the matrix element as a product of Clebsch-Gordan coefficient and a reduced matrix element, using the Wigner-Eckart theorem

$$\begin{aligned}\langle Fm_F|\,\hat{d}_q\,\left|F'm'_F\right\rangle &= \langle F\left\|\hat{\mathbf{d}}\right\|F'\rangle C_{m_F,q} \\ &= \langle F\left\|\hat{\mathbf{d}}\right\|F'\rangle(-1)^{F'-1+m_F}\sqrt{2F+1}\begin{pmatrix} F' & 1 & F \\ m'_F & q & -m_F\end{pmatrix}.\end{aligned} \tag{3.7}$$

Here, q is an index labelling the component of $\mathbf{r}$ in the spherical basis, that is

$$\hat{\mathbf{e}}_{\pm1} = \mp\frac{1}{\sqrt{2}}(\hat{x} \pm i\hat{y}),\ \hat{\mathbf{e}}_0 = \hat{z}. \tag{3.8}$$

$\hat{d}_q$ is the projected dipole moment operator in spherical basis $\hat{\mathbf{e}}_q$, that $\hat{\mathbf{d}} = \sum_q \hat{d}_q\hat{\mathbf{e}}_q^*$. The double bars in the notation $\langle F\left\|\hat{\mathbf{d}}\right\|F'\rangle$ indicate that matrix is reduced (see, for example, Ref.[173] for details). In the last step, we have written the expression in terms of a Wigner 3-j symbol. Note that the 3-j symbol vanishes unless $m_F = m'_F + q$. The reduced matrix element $\langle F\|e\mathbf{r}\|F'\rangle$ can be further simplified by factoring out the F and F' dependence into a Wigner 6-j symbol as

$$\langle F\left\|\hat{\mathbf{d}}\right\|F'\rangle = \langle J\left\|\hat{\mathbf{d}}\right\|J'\rangle(-1)^{F'+J+1+I}\sqrt{(2F'+1)(2J+1)}\begin{Bmatrix} J & J' & 1 \\ F' & F & 1\end{Bmatrix}. \tag{3.9}$$

Finally, the reduced matrix element $\langle J\left\|\hat{\mathbf{d}}\right\|J'\rangle$ is related to the decay rate of $J' \to J$ transition as [173]

$$\Gamma_{JJ'} = \frac{\mu_0\omega_A^3}{3\pi\hbar c}\frac{2J+1}{2J'+1}|\langle J\left\|\hat{\mathbf{d}}\right\|J'\rangle|^2. \tag{3.10}$$

[2]Note that in Ref. [118], a different definition is used. The final expression for reduced dipole matrix element is also different. See Ref. [66] for more discussions.

In experiment, the decay rate in free-space can be measured precisely from the lifetime of the excited J' state. Based on the information about lifetime, we can calculate the transition dipole moment for any hyperfine transition following the relations defined in Eq. 3.7 and Eq. 3.9. For Cs D_1 and D_2 lines, the reduced dipole matrix elements $|\langle J\|\hat{\mathbf{d}}\|J'\rangle|$ are given as [173]

$$\langle J = 1/2\|\hat{\mathbf{d}}\|J' = 1/2\rangle = 3.1822ea_0, \tag{3.11}$$

$$\langle J = 1/2\|\hat{\mathbf{d}}\|J' = 3/2\rangle = 4.4786ea_0, \tag{3.12}$$

where a_0 is the Bohr radius and e is the electron charge.

Finally, it is worth mentioning that despite the considerable complexity of real atomic electronic structure, the two-level atom model can still be a useful in some important situations. One of the examples is the stretched states under optical pumping [81] where a σ^+ polarized light is driving $J = 1/2 \rightarrow J' = 3/2$ transition. In this transition, $J = 1/2, m_J = 1/2 \rightarrow J' = 3/2, m'_J = 3/2$ is a closed transition and atoms starting in any other state will eventually become pumped into the this cycling transition. As a result, in the steady state limit, we effectively have a two-level atom.

3.4 Atom-light coupling in nanophotonic structures

Green's function approach with multilevel atoms

In the previous section, we have shown that the atomic level structure is complex compared with a simple two-level atom due to fine and hyperfine splittings. We also showed that the transition strength of a particular hyperfine transition can be associated with a reduced dipole operator and an appropriate Clebsch-Gordan coefficient (Eq. 3.7). With this information, we can rewrite the effective Hamiltonian (Eq. 2.112) for two-level atoms in the previous chapter to include the hyperfine levels for a real atom as (without derivation) [11]

$$\begin{aligned} H_{\text{eff}}/\hbar = &- \sum_{j=1}^{N}\sum_{q=-1}^{1} \Delta_q \Sigma_{jq}^{\dagger}\Sigma_{jq} - \sum_{i,j=1}^{N}\sum_{q,q'=-1}^{1} g_{ijqq'}\Sigma_{iq}^{\dagger}\Sigma_{jq'} \\ &- \sum_{j=1}^{N}\sum_{q=-1}^{1}\left(\Omega_{jq}\Sigma_{jq}^{\dagger} + \text{h.c.}\right). \end{aligned} \tag{3.13}$$

Here we have defined a new spin operator $\Sigma_q^{\dagger}$ as

$$\hat{\Sigma}_{jq} = \sum_{\substack{m_F=-F,\\ m'_F=m_F-q}}^{F} C_{m_F,q}\hat{\sigma}_{jF'm'_FFm_F} \equiv \sum_{\substack{m_F=-F,\\ m'_F=m_F-q}}^{F} C_{m_F,q}\left|jFm_F\right\rangle\left\langle jFm'_F\right|. \tag{3.14}$$

The Green function matrix element $g_{ijqq'} = J_{ijqq'} + i\Gamma_{ijqq'}/2$ is

$$J_{ijqq'} = \frac{\mu_0\omega_{qq'}^2}{\hbar}\left|\langle F\left\|\hat{\mathbf{d}}\right\|F'\rangle\right|^2\hat{\mathbf{e}}_q\cdot\mathrm{Re}\mathbf{G}(\mathbf{r}_i,\mathbf{r}_j;\omega_{qq'})\cdot\hat{\mathbf{e}}_{q'}^*, \tag{3.15}$$

$$\Gamma_{ijqq'} = \frac{2\mu_0\omega_{qq'}^2}{\hbar}\left|\langle F\left\|\hat{\mathbf{d}}\right\|F'\rangle\right|^2\hat{\mathbf{e}}_q\cdot\mathrm{Im}\mathbf{G}(\mathbf{r}_i,\mathbf{r}_j;\omega_{qq'})\cdot\hat{\mathbf{e}}_{q'}^*. \tag{3.16}$$

The driving term is $\hat{\Omega}_{jq} = \hat{\mathbf{e}}_q^*\cdot\hat{\mathbf{E}}_0^+(\mathbf{r}_j)\langle F\left\|\hat{\mathbf{d}}\right\|F'\rangle/\hbar$

Similarly, the generalized input-output equation (Eq. 2.103) can be modified as

$$\hat{\mathbf{E}}^+(\mathbf{r}) = \hat{\mathbf{E}}_0^+(\mathbf{r}) + \mu_0\omega^2\sum_{j=1}^{N}\sum_{q=-1}^{1}\mathbf{G}(\mathbf{r},\mathbf{r}_j;\omega)\cdot\hat{\mathbf{e}}_q^*\langle F\left\|\hat{\mathbf{d}}\right\|F'\rangle\hat{\Sigma}_{jq}. \tag{3.17}$$

Finally, the total decay rate for a multilevel atom near the photonic crystal can also be explicitly given. Recall that in Chapter 2, for N two-level atoms near a nanophotonic structure, the collective decay rate is obtained from the imaginary part of the eigenvalues of the Green function matrix $\mathcal{G}$ with element $g_{ij} = J_{ij} + i\Gamma_{ij}/2$. In the case when single atom is presented ($N = 1$), we have $\Gamma = \Gamma_{ii}$. For the case of multiple atoms with multiple levels, the decay rate can be obtained from a similar process, except the matrix element is $g_{ijqq'}$ and an additional step to sum over all ground states and average over all single excitation excited states, if the different m_F levels are not distinguished. For a single atom case ($N = 1$), the total decay rate from excited state F' level to ground state F level can be written as

$$\begin{aligned}\Gamma_{\mathrm{ii,FF'}} &= \frac{2}{2F'+1}\sum_{m_F'}\sum_{m_F}\mathrm{Im}\left\langle iFm_FF'm_F'\right|\sum_{q=-1}^{1}g_{iiqq}\Sigma_{iq}^\dagger\Sigma_{iq}\left|iFm_FF'm_F'\right\rangle \\ &= \frac{2\mu_0\left|\langle F\left\|\hat{\mathbf{d}}\right\|F'\rangle\right|^2}{(2F'+1)\hbar}\sum_{q=-1}^{1}\sum_{m_F}\omega_{qq}^2\left|C_{m_F,q}\right|^2\hat{\mathbf{e}}_q\cdot\mathrm{Im}\mathbf{G}(\mathbf{r}_i,\mathbf{r}_j;\omega_{qq})\cdot\hat{\mathbf{e}}_q^*\end{aligned} \tag{3.18}$$

where we have used the fact that only $m_F = m_F' + q$ term is non-vanishing to remove summation over m_F'.

For the case where the eigenmodes of the photonic crystal are TE-like or TM-like, the polarization is mostly linear near the atomic position. In experiment, when the Cs transition is aligned to the band-edge of one specific guided mode (TE-like or TM-like), the atom is coupled dominantly to this specific guided mode due to slow-light enhancement near the band-edge. In this case, we can choose the spherical basis to be aligned with the polarization axis and the summation can be carried out

approximately with $q = 0$ subspace.[3] Using the identity $\sum_{m_F} \left|C_{m_F,0}\right|^2 = 2F + 1$, the decay rate in Eq. 3.18 can be further simplify as

$$\Gamma_{\text{ii,FF'}} \approx \Gamma_{\text{ii,FF',00}} = \frac{2\mu_0\omega_{00}^2}{\hbar}\frac{2F+1}{2F'+1}\left|\langle F\|\hat{\mathbf{d}}\|F'\rangle\right|^2 \hat{\mathbf{e}}_0 \cdot \text{Im}\mathbf{G}(\mathbf{r}_i, \mathbf{r}_i; \omega_{00}) \cdot \hat{\mathbf{e}}_0^* \quad (3.19)$$

Here ω_{00} refer to the transition frequency from F to F' with $q = q' = 0$. As a sanity check, for free-space two-level atoms, $(2F+1)/(2F'+1) \to 1$, $\left|\langle F\|\hat{\mathbf{d}}\|F'\rangle\right|^2 \to |\mathbf{d}|^2$ $\text{Im}G_{zz}(\mathbf{r}_i, \mathbf{r}_i; \omega_{00}) = k_0/6\pi$, we then get $\Gamma_{ii00} = \Gamma_0/3$. Here the factor of 3 shows up as we only consider the decay into one polarization in the spherical basis.

So far, we have explicitly derived the total decay rate for the hyperfine transitions. This expression is particular useful since we always probe transmission with a specific hyperfine transition in experiment. For general applications without hyperfine structures, it was shown in Ref. [92] that the decay rate can be expressed in terms of the ground state $|g_i\rangle$ and excited state $\left|e_j\right\rangle$ (with index i and j label the number of states) as

$$\Gamma_{\text{tot}} = \frac{2\mu_0}{\hbar}\sum_i \omega_{ij}^2 \text{Tr}[D_{ij} \cdot \text{Im}]\mathbf{G}(\mathbf{r}_0, \mathbf{r}_0; \omega_{ij})] \quad (3.20)$$

for atom at position $\mathbf{r}_0$, with D_{ij} defined as $D_{ij} = \langle g_i| \hat{\mathbf{d}}^\dagger \left|e_j\right\rangle \left\langle e_j\right| \hat{\mathbf{d}} |g_i\rangle$.

Atom-light interactions in real 1D and 2D nanophotonic structures

In the previous section, we have derived the expression for multi-level atom decay rate near a nanophotonic structure with the Green's function lies at the core of the calculation. To calculate the Green's function for complex optical dielectric structures, FDTD simulation is used to simulate the Green's function of a given structure. This is performed by simulating the electric field pattern from a point dipole source placed inside the optical structure under different dipole orientations. In Lumercial [126], the built-in 'dipolepower()' function computes the output power at each Fourier frequency component which is proportional to the imaginary part of the self-Green's function (Eq. 2.76). The output is normalized to the imaginary part of the free-space self-Green's function. Finally, to convert to atomic decay rate for specific transitions, Eq. 3.18 or more general Eq. 3.20 are used to account for the correct transition strength. It is worth noting that since the Green's function physically represents the electric field radiated from a dipole source inside the

[3] Here we also assumed that there is no cross-talk between TE-like and TM-like mode. This is not precisely true. For example, if the atom excited by $q = 0$ polarization can decay into superposition of $q = -1$ and $q = 1$ polarization. The superposition of $q = -1$ and $q = 1$ can be projected in another TM-like mode, introducing cross-talk between TM-like mode and TE-like mode. We have measured this TE-TM cross-talk in experiment (unpublished results).

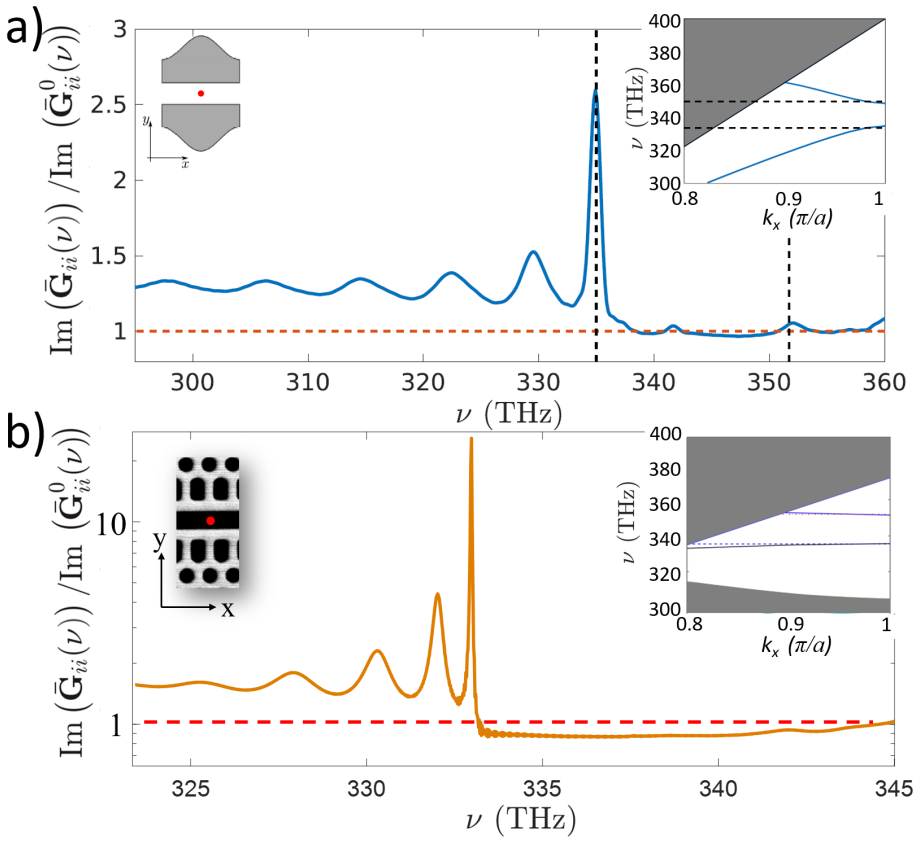

Figure 3.10: The normalized imaginary part of simulated Green's function (a) for the APCW structure and (b) for the SPCW structure. In both plots, the dipole positions are indicated by the red circle in the left inset and the band structures for a unit cell are indicated in the right insets. The vertical black lines indicate the Cs D_1 and D_2 transitions and the horizontal red dashed lines indicate the ratio 1, corresponding to the situation where the total decay rate equals to the free-space decay rate. Note that in (b), the normalized ratio is below 1 in the bandgap, suggesting that the presence of the SPCW structure suppress the total decay rate. Detailed parameters of the structures under simulation can be found in Juan Muniz's thesis [171] for (a) and Su-Peng Yu's thesis for (b).

nanostructure, it respects the symmetry of the structure under simulation. As a result, the Green's tensor is diagonalized at the structure's high-symmetry points.

Fig. 3.10 (a, b) show two examples of the simulated imaginary part of the Green's function tensor for the APCW and SPCW structures with similar dimensions ($N_{\text{cell}} = 60$), both normalized to the free-space Green's function. Here, the dipole positions are placed at the center of the gap to the dielectric mode, as indicated in the inset on the left. From Fig. 3.10, it is clear to see the total decay rate is enhanced due to the slow-light enhancement near the band-edge, with the peak position corresponding to the resonance position of transmission near the band-edge. Follow a more quantitative comparison, we find that the SPCW structures exhibits a stronger enhancement near the band-edge, given the similar structure dimensions. This difference is due the different dispersion relations in the APCW and SPCW. As shown in the right insets in Fig. 3.10 (a, b), the SPCW has a much 'flatter' dispersion curve compared with the one in APCW. This is a result of anti-crossing between the index-guided band and the gap guided band, where two bands that are expected to 'intersect' will instead couple to one another and the bands repel. This anti-crossing effect in the 'W1' do not was first noticed by Notomi et al. [136] in 2001 but the general physics is actually very common in many different physics settings [99].

From Fig. 3.10 (a, b), we notice that the normalized ratio of the imaginary Green's function can be below 1 in the bandgap (where the ratio 1 is indicated with horizontal red dashed lines). This suggests that the presence of the photonic structure can suppress the total decay rate in the bandgap. Intuitively, this can be understood as the presence of the bandgap eliminates the decay of the atom into the structure. The finite solid angle of the structure effectively reduces the number of spatial modes the atom can decay to, leading to an reduction in the total decay rate. This also explains why the SPCW has more significant effect than the APCW due to the 2D photonic bandgap of surrounding photonic crystal (vs. 1D photonic bandgap in the APCW).[4]

In experiment, the dissipative rate Γ_{1D} and J_{1D} in quasi-1D systems can be determined from the normalized transmission and reflection spectra with atoms, as already shown in Chapter 2. In Fig. 3.11, we show an example of such measurement for the APCW. Fig. 3.11 (b-c) shows the measured normalized transmission (T/T_0) versus probe detuning Δ_A at the peak of the first resonance (ν_1) and the two sides of the first resonance ν_+ and ν_-, with positions indicated in the device

[4]Following this argument, one can imagine that if the atom is within a true 3D photonic crystal bandgap, the total decay rate can be suppressed to zero, as suggested in original papers by John [100] and Yablonovitch [197].

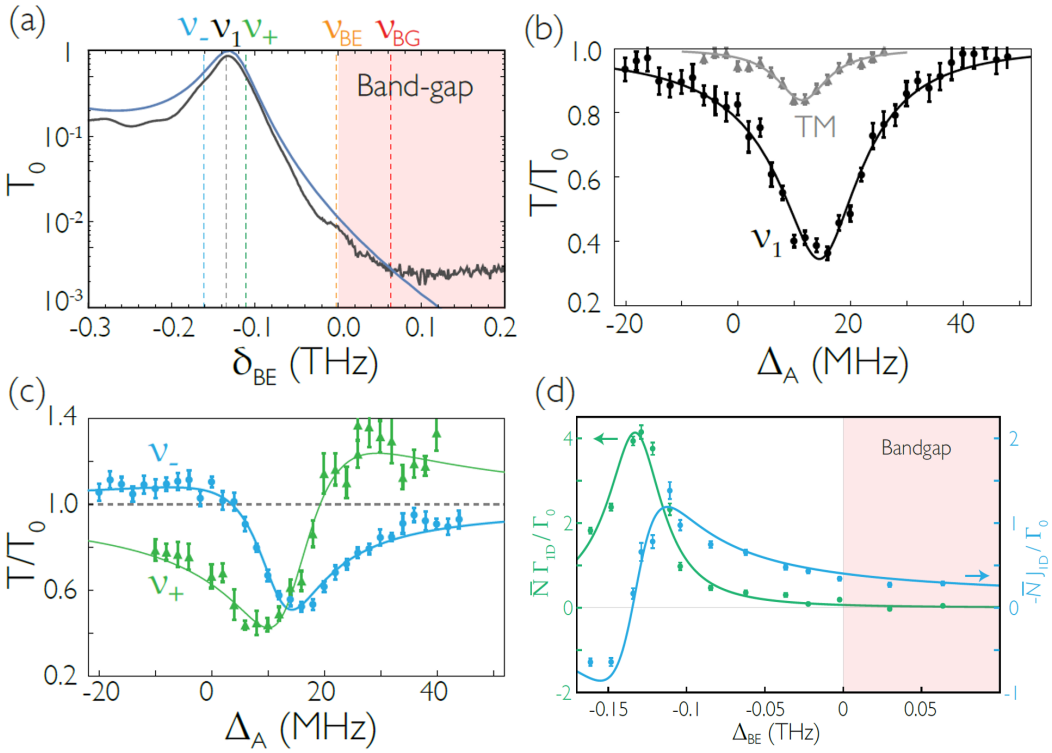

Figure 3.11: (a) Measured (black) and FDTD simulated (blue) transmission spectra of the APCW without atom as a function of the probe detuning from the band-edge, $\delta_{\mathrm{BE}} = \nu_p - \nu_{\mathrm{BE}}$. (b, c) Measured normalized transmission with atoms as a function of probe detuning $\Delta_A = \nu_p - \nu_{\mathrm{D1}}$ for TE (black dots) and TM (gray dots) polarization (b) at first resonance ν_1 and (c) at the two sides of the first resonance $\nu_\pm$ for the APCW. The corresponding positions of ν_1, ν_+ and ν_- are indicated in the transmission spectra in (a) with same color vertical dashed lines. Solid lines are from fitting model as shown in Eq. 2.132. (d) The fitted dissipative rate $\bar{N}\Gamma_{1\mathrm{D}}$ (green) and coherent spin-exchange rate $\bar{N}J_{1\mathrm{D}}$ around the band-edge. The solid lines are the predictions from the 1D transfer matrix model. Figure adapted from Ref. [86].

transmission spectra in Fig. 3.11 (a). By fitting the normalized transmission with Eq. 2.132, we can extract the position averaged $\bar{N}\Gamma_{1D}$ and $\bar{N}J_{1D}$. Fig. 3.11 (d) shows the fitted $\bar{N}\Gamma_{1D}$ and $\bar{N}J_{1D}$ measured at different position with respect to the band-edge. Interestingly, it is found in Ref. [86] that $J_{1D}/\Gamma_{1D} \propto e^{\kappa_x L}$ with $\kappa_x \propto \sqrt{\Delta_{BE}}$ which deviates from the conventional cavity QED $J_c/\Gamma_c = \kappa_c/\Delta_c$ law derived in Chapter 2. This deviation will be helpful for the observation of spin-spin exchange in the bandgap as will be shown shortly. It is worth noting that dissipative rate $\bar{N}\Gamma_{1D}$ and spin-exchange rate $\bar{N}J_{1D}$ fitted here are atom position averaged and atom number averaged from experimental cycle to cycle. To get the value of single atom Γ_{1D} and J_{1D} with respect to the Bloch mode intensity peak, one needs to determine the average atom number $\bar{N}$ and perform a position average over the Bloch mode. The average atom number can be determined from the pulse decay measurement, as demonstrated in Ref. [68]. Beyond this atom number average and atom position average, we will show in Chapter 4 and Chapter 5 that the integration with optical tweezers allows deterministic atom number and atom positioning near the nanophotonic structure in both 1D and 2D.

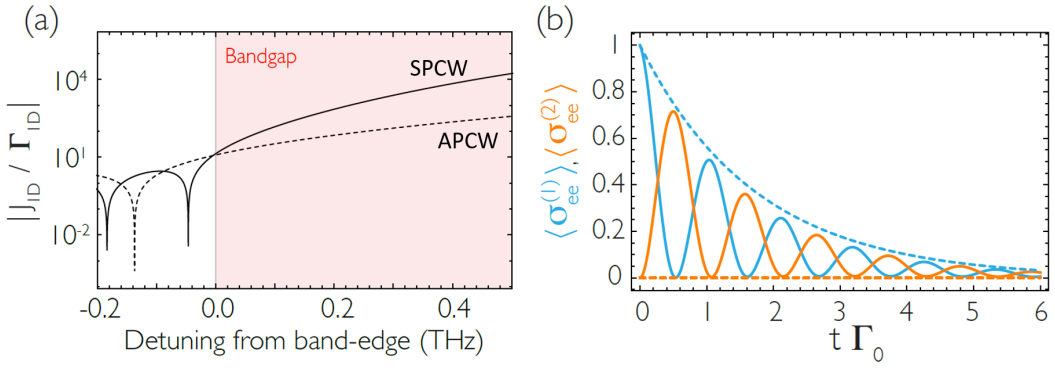

Figure 3.12: (a) The ratio of the coherent rate and the dissipative coupling rate as a function of detuning to the band-edge, for the APCW (dashed line) and the SPCW (solid line). (b) Evolution of the excited states population (solid lines) for two atoms placed at successive even antinodes on the SPCW, with atomic transition frequency inside the bandgap of the SPCW. Dashed lines represent the non-interacting scenario as defined in Chapter 2. The spin exchange and decay rates are chose to be $J_{1D} = -3\Gamma_0$, $\Gamma_{1D} = 0.15\Gamma_0$, and $\Gamma' = 0.5\Gamma_0$. Figure adapted from Ref. [11].

The strong atom-light interaction and the suppression of free-space decay rate in the SPCW can allow us to observe interesting physics that are difficult to observe in the APCW. For example, in Fig. 3.12 (a), we plot the ratio of the coherent spin-exchange rate and the dissipative rate, $|J_{1D}/\Gamma_{1D}|$ from the FDTD simulation. At a

detuning $\simeq 0.5$ THz from the band-edge, we have $|J_{1D}/\Gamma_{1D}| \simeq 10^4$ for the SPCW, two order of magnitude higher than the ratio in the APCW at similar detunings. Under this large spin-exchange rate J_{1D}, it should be possible to observe coherent spin-spin exchange between two neighbor atoms, as shown in the solid curves in Fig. 3.12 (b). Here the two atoms are placed at successive even antinodes with their transition frequencies in the bandgap of the SPCW. The time evolution of the excited-state populations are solved by Eq. 2.106 with the spin exchange and decay rates chosen to be $J_{1D} = -3\Gamma_0$, $\Gamma_{1D} = 0.15\Gamma_0$, and $\Gamma' = 0.5\Gamma_0$. The excited state population evolution for the non-interacting scenario is also plotted (dashed lines) as a comparison.

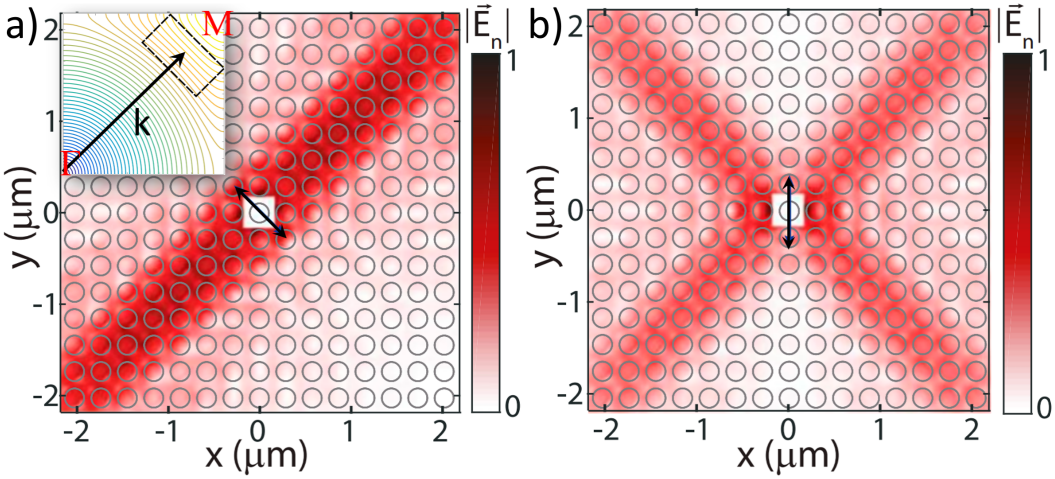

Figure 3.13: (a, b) Field profile from a dipole at the center of the center hole, normalized after removing the field in the immediate vicinity of the dipole. When the emission wavevector lies in the flat isofrequency contour region (as indicated with black rectangle in the inset in (a)), the emission field pattern is directional. Depending on the dipole orientations (indicated with black arrows), the emission field can propagate along selective $\vec{k}_{\Gamma M}$ directions as indicated in (a) for polarized along diagonal direction and (b) for polarized along y direction. Figure adapted from Ref. [204].

So far, we have focused our discussion of atom-light interactions on quasi-1D do nots. Recall that in Section 3.2, we showed that a 2D square lattice exhibits an anisotropic dispersion relation (Fig. 3.5 (a, b)) and allows supercollimation effect when the wavevector is aligned to the flat isofrequency contours (black rectangle in Fig. 3.5 (b) and Fig. 3.13 (a) inset). Thus, it is expected that atoms near 2D photonic crystal slabs should exhibit rich spatial profiles of the emitted electric fields, and one may be able to observe anisotropic dissipative and spin-spin interactions. For the square lattice with parameters the same as in Fig. 3.5 (a, b), we numerically

simulated the emission field pattern by placing a dipole source in the center of the center holes, as shown in Fig. 3.13. Here the emission field is normalized after removing the field in the immediate vicinity of the dipole. As we can see in Fig. 3.13, when the emission wavevector lies in the flat isofrequency contours (black rectangle in Fig. 3.13 (a) inset), the emission field pattern is directional in space. Depending on the dipole orientation (indicated with black arrows), the emission field can propagate along selective $\vec{k}_{\Gamma M}$ directions. For example, in Fig. 3.13 (a), the dipole is polarized along the diagonal direction, only the orthogonal direction is excited. When the dipole is polarized along y axis, as shown Fig. 3.13 (b), emission along all $\vec{k}_{\Gamma M}$ directions is excited. Intuitively polarized along y direction can be decomposed as a superposition of two orthogonal diagonal directions. As the atom-atom interactions on photonic crystal are fully characterized by the Green's function, this field pattern will represent the directionality of atom-atom interaction. For example, if a 'test' atom is placed one of the corner in Fig. 3.13 structure, one can control the two atom interactions by change of their dipole orientations. In experiment, this can be achieved by applying a magnetic bias field or by the local vector shifts with side-illumination tweezer beams, as will be shown in Chapter 4. Further, by placing atoms periodically along all $\vec{k}_{\Gamma M}$ directions, one can build a 2D atomic network with switchable interactions. For example, by rotating the atom dipole moment orientation, one can choose to have interactions between atoms along $(1, 1)$ direction or along $(-1, 1)$ direction, or any superposition of these two directions (full 2D interactions).

In experiment, the anisotropic emission and spin-spin exchange interaction can be measured by involving two atoms, that is, one as the 'emitter' atom and one as the 'probe' atom. By varying their relative angle and distance, we can measure the anisotropic emission of 'emitter' atom and from that infer the spatial information of the 2D Green's function. The detailed experiment protocol is presented in Chapter 4 with the integration of optical tweezer traps.

Beyond the anisotropic emission discussed here, the atom-light interaction on 2D photonic crystal also opens the possibility to observe topological protected states and explore exotic quantum many-body phases as proposed in Refs. [93, 204].

3.5 Atom trapping in guided-mode traps

In previous chapters, the trapping of atoms inside nanophotonic structures is taken for granted. In this section, we will show that designing and implementing the

guided-mode traps is actually non-trivial. Before considering the design of traps for atoms on nanostructures, we would like to review the basics forces on nanophotonic structures. In our scenario, main forces on atoms near a dielectric surfaces are the dipole forces from guided-mode traps, external illumination traps (as will be shown in Chapter 4), surface forces such as the Casimir-Polder potential, and scattering and push effect from near resonant probe light. For guided-mode trap design, we mainly consider the first three forces. Other forces can be electric field formed by surface defects/adsorbed atoms that remain to be investigated in quantitative measurements.

Scalar, vector and tensor light shifts

In the presence of an electric field $\hat{\mathbf{E}}(\mathbf{r})$, the atom will be polarized by the electric field corresponding to an induced dipole moment

$$\hat{\mathbf{d}}_{\text{ind}} = \boldsymbol{\alpha}(\omega) \cdot \hat{\mathbf{E}}(\mathbf{r}). \tag{3.21}$$

Here the term $\boldsymbol{\alpha}(\omega)$ is called the polarizability of the atom and in its most general form, is a tensor. The coupling of the induced dipole moment to the light field $\hat{\mathbf{E}}(\mathbf{r})$ introduces an effective interaction Hamiltonian [118]

$$\hat{H}_{\text{ls}} = -\hat{\mathbf{E}}(\mathbf{r}) \cdot \hat{\mathbf{d}}_{\text{ind}} = -\hat{\mathbf{E}}(\mathbf{r}) \cdot \boldsymbol{\alpha}(\omega) \cdot \hat{\mathbf{E}}(\mathbf{r}). \tag{3.22}$$

One can explicitly write the polarizability tensor in terms of scalar, vector and tensor components as

$$\boldsymbol{\alpha}(\omega) = \alpha_s(\omega)\mathcal{I} + \alpha_v(\omega)\,(i\boldsymbol{\epsilon} \times \boldsymbol{\epsilon}^*) \cdot \frac{\mathbf{F}_z}{F} + \alpha_t(\omega)\,(3|\boldsymbol{\epsilon} \cdot \mathbf{e}_z| - 1)\,\frac{3\mathbf{F}_z^2 - \mathbf{F}^2}{2F(2F-1)}, \tag{3.23}$$

where $\alpha_s(\omega)$, $\alpha_v(\omega)$, $\alpha_t(\omega)$ are called scalar, vector and tensor polarizabilities, respectively. The exact expression for $\alpha_s(\omega)$, $\alpha_v(\omega)$, $\alpha_t(\omega)$ is given in Ref. [118]. $\boldsymbol{\epsilon}$ represents the unit vector of the field polarization in the spherical basis.

As a special case, the scalar optical Stark shifts of the ground and excited states in the two-level atom model are

$$\Delta E_g = -\Delta E_e = \frac{\hbar|\Omega(\mathbf{r})|^2}{4\Delta_A} = \frac{|\langle g|\,\boldsymbol{\epsilon} \cdot \mathbf{d}\,|e\rangle|^2 \left|E_0^+(\mathbf{r})\right|^2}{\hbar(\omega - \omega_A)}. \tag{3.24}$$

This expression suggests the scalar light shift is proportional to the intensity profile of the light field. The spatially dependent energy shift leads to a spatially dependent potential. For red-detuned light ($\Delta_A < 0$), this potential is attractive for ground state atoms and can be used to trap atoms when atom temperature is lower than this

energy shift. Similarly, for blue-detuned light ($\Delta_A > 0$), this potential is repulsive as an anti-trap. Also note that the ground state and excited state have the opposite sign of light shift. This suggests that the trap for the ground state can be an anti-trap for the excited state, causing potential heating when atoms are excited.

For real atoms with multiple transitions, this simple estimation above is only valid for linear polarized light at detuning close to the transition frequency ω_A so that the scalar shifts from other transitions are negligible. However, the fact that the energy shift $U(\mathbf{r})$ is spatially dependent and atomic electronic state dependent can introduce inhomogeneous broadening and limit long-lived trap and coherent times necessary for repeated coherent operations [199]. Very interestingly, the presence of multiple atomic levels adds more degree of freedom in the polarizability, allows one to engineer the scalar polarizability. A state-insensitive optical trap can be designed at the "magic" wavelength where the scalar polarizabilities $\alpha_s(\omega)$ for the ground and excited state are equal [199]. For Cs D_2 transition $6S_{1/2}, F = 4 \rightarrow 6P_{3/2}$, two magic wavelengths are at $\lambda_{\text{red}} \simeq 935.7$ nm for a red-detuned trap and $\lambda_{\text{blue}} \simeq 684.8$ nm for a blue-detuned anti-trap.

For the vector light shift, we notice it is proportional to $i\boldsymbol{\epsilon} \times \boldsymbol{\epsilon}^*$. For linear polarized light field, we have $\boldsymbol{\epsilon} \times \boldsymbol{\epsilon}^* = 0$ and this vector shift term vanishes. This suggests that the vector shift only presents when the light field has elliptical components. In fact, $\text{Im}(\boldsymbol{\epsilon} \times \boldsymbol{\epsilon}^*)$ is a direct measure of ellipticity of light in classical optics [174]. Interestingly, the vector shift also explicitly dependents on $\mathbf{F}_z$ (or m_F if projected on $|Fm_F\rangle$ basis). This is very similar to the Zeeman shift under magnetic field (Eq. 3.6). For this reason, the vector shift is often referred to as a "fictitious magnetic field" and can typically be cancelled or suppressed by adding a magnetic bias field[181].

For guided-mode traps, the strong guiding nature of the structure inevitably leads to non-negligible longitudinal (along propagation direction) electric fields in the evanescent region, which are $\pi/2$ out of phase with the transverse electric field. Furthermore, the spatially varying elliptical polarization of the evanescent field is typically on a scale less than λ. This makes it difficult to cancel it from an external magnetic bias field. In this case, the vector shift can be cancelled by adding a counter-propagating field with same amplitude, as demonstrated in Ref. [66] for the nano-fiber traps.

Casimir-Polder potential

For trapping atoms at submicron distances away from dielectric surfaces, it is important to include the effect of Casimir-Polder interactions[34] for the trap design. Unlike the optical dipole forces introduced in the previous section, the Casimir-Polder interaction is essentially a fluctuation-induced force. It arises from an atomic dipole interacting with electromagnetic vacuum fluctuations near a dielectric surface. For atomic ground states, the Casimir-Polder interaction can be understood as an energy shift resulting from counter-rotating terms in the full atom-light interaction Hamiltonian (Eq. 2.98) [30]. During this counter-rotating process, fluctuations introduce the simultaneous creation of a photon and transition to the excited state. Similar to the light shifts from a dipole trap, this energy shift of the ground state is also position dependent. As a result, it can also be interpreted as an attractive motional potential. For scales under 100 nm, this force can be so strong that it can weaken or completely open a guided-mode trap and crash the trapped atom into the dielectric surface.

For simple dielectric structures, analytic forms for the Casimir-Polder potential can be obtained from full QED calculations [122]. For example, the approximate potential for an atom near a planar dielectric surface takes the form [61, 169]

$$U_{\mathrm{CP}}(d) = -\frac{C_4}{d^3(d+\lambda)}. \tag{3.25}$$

Here d is the distance between an atom and the proximal dielectric surface, C_4 is the coefficient for the retarded $1/d^4$ long-range potential that depends on the atomic polarizability and dielectric permittivity of the surface. The characteristic length scale is $\lambda = \lambda/2\pi$ with λ being the effective atomic transition wavelength that contributes most to the polarizability of the atom. For $d \ll \lambda$, U_{CP} recovers the classic van der Waals potential d^{-3} scaling while for $d \gg \lambda$, the relativistic retardation leads to a d^{-4} dependence [34]. For Cs atoms near a SiN surface, $C_4/k_B \sim 5$ nKμm^4 and $\lambda \sim 100$ nm [175], resulting in a substantial potential energy variation $\Delta U_{\mathrm{CP}} \sim -k_B \times 250\ \mu$K as d changes from 100 to 50 nm.

Generally, the Casimir-Polder potential for complex nanostructures can be calculated within the Green's function approach introduced in Chapter 2 [32]. Following Ref. [30], we write the ground-state Casimir-Polder potential as an integral over a continuous frequency spectrum with range $(0, \infty)$

$$U_{\mathrm{CP}}(\mathbf{r}) = -\frac{\mu_0\hbar}{2\pi}\mathrm{Im}\int_0^\infty d\omega\omega^2\mathrm{Tr}[\boldsymbol{\alpha}(\omega)\cdot\mathbf{G}_{\mathrm{sc}}(\omega)], \tag{3.26}$$

where we have utilized the fluctuation-dissipation theorem and assumed that the temperature of the nanostructure is much smaller than the atomic transition energies $k_B T \ll \hbar\omega_j$ [30, 92]. The $\mathbf{G}_{\text{sc}}$ in the integral is defined as the scattering Green's function without the free-space component $\mathbf{G}_0$, that is $\mathbf{G}_{\text{sc}}(\omega) \equiv \mathbf{G}(\mathbf{r}, \mathbf{r}, \omega) - \mathbf{G}_0(\mathbf{r}, \mathbf{r}, \omega)$. The dynamic polarizability tensor $\boldsymbol{\alpha}(\omega)$ is defined in Eq. 3.23, and we rewrite it more explicitly in terms of atomic transitions as

$$\boldsymbol{\alpha}(\omega) \equiv \lim_{\epsilon \to 0} \frac{1}{\hbar} \sum_j \frac{2\omega_j D_{0j}}{\omega_j^2 - \omega^2 - i\omega\epsilon}, \tag{3.27}$$

where ω_j is the transition frequency from ground state j, and the tensor $D_{0j} = \langle 0 | \hat{\mathbf{d}}^\dagger | e_j \rangle \langle e_j | \hat{\mathbf{d}} | 0 \rangle$ is defined in Eq. 3.20.

As Eq. 3.26 also involves the evaluation of the Green's function tensor, numerical methods such as FDTD are typically required for solving complex optical structures. Furthermore, note that different from the expression for the spontaneous emission rate (Eq. 3.20) where the Green's function is evaluated only at the atomic frequencies, the expression for the Casimir-Polder potential (Eq. 3.26) is integrating over all positive frequencies. As a result, this makes the integral difficult to converge and special numerical techniques have been developed to ensure accurate and fast converging results as shown in Refs. [129, 158]. However, the analytical models can provide useful sanity checks for the results obtained from numerical simulations.

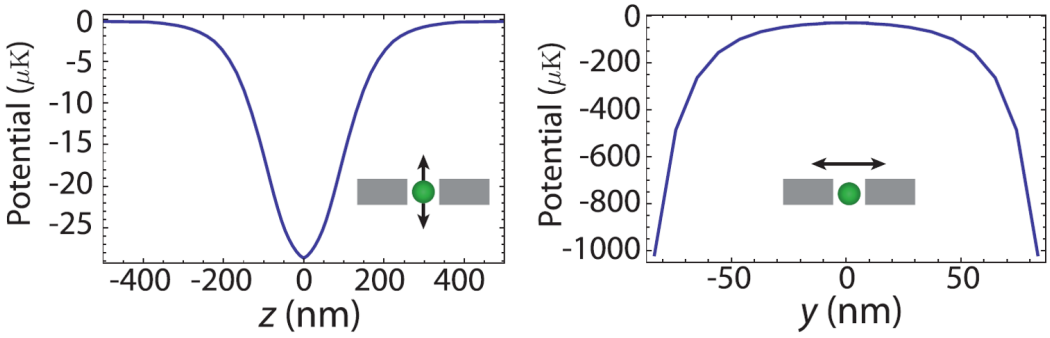

Figure 3.14: Numerically computed Casimir-Polder potential for Cs $6S_{1/2}, F = 4$ ground state in the gap of the APCW. *left* along z direction. *right* along y direction. The position and directions are also indicated with the green dots and black arrows in two plot. Figure adapted from Ref [200].

As an example, Fig. 3.14 shows the numerically computed Casimir-Polder potential for Cs $6S_{1/2}, F = 4$ ground state in the gap of the APCW. As shown in Fig. 3.14 (a), the Casimir-Polder potential creates a weak 30 μK trap along along z direction.

However, for along y direction, the Casimir-Polder potential is so strong that atom deviates from the trap center by 50 nm can experience a 100 μK attractive potential. As a result, a strong repulsive potential is required to prevent an atom from crashing into the surfaces, as will be discussed in the next section.

Design of a stable guided-mode trap

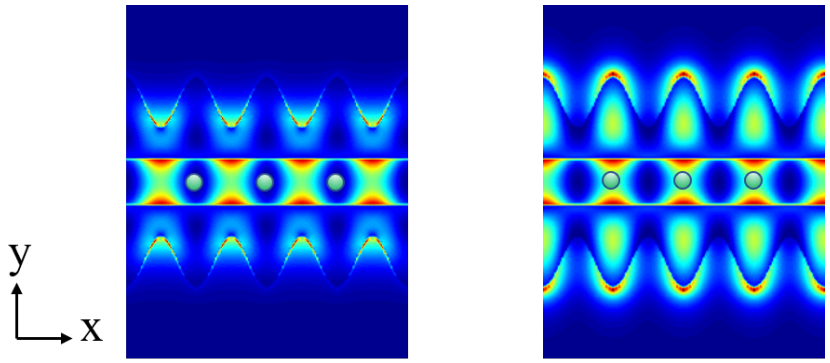

Figure 3.15: The field profile near the band-edge of the APCW *left* for the air and *right* for the dielectric band. Green dots indicate atom trap positions with blue-detuned air mode trap and red-detuned dielectric mode trap as in Ref. [67].

As we find from the previous section, the presence of the strong attractive Casimir-Polder potential requires a repulsive potential to prevent atom from being lost to the surface. This can be accomplished by introducing a blue-detuned guided mode as the field is more concentrated near the dielectric surfaces. However, the combination of the blue-detuned guided mode with the Casimir-Polder potential will only lead to a trap depth on the order of $\simeq$ 30 μK along z direction, as already shown in Fig. 3.14 (a) and in Ref. [92]. It is challenging to trap an atom in such a shallow trap, given the atom temperature after the sub-Doppler cooling near a dielectric surface is on the order of 10 μK [67]. For this reason, it generally requires additional red detuned guided-mode trap to make a stable trap with reasonable trap depth. This can be fulfilled by having one trap light at the lower dielectric band as a red-detuned trap and the another trap light at the higher air band as a blue-detuned trap. As the field maximum positions for air band and dielectric band are concentrated at different position, atom will localized in the red trap position along the x direction, as indicated with green dots in Fig. 3.15 for the APCW. However, the trap center of the red-detuned dielectric mode trap is a saddle point with the intensity concentrated more on the dielectric surfaces. To make a closed trap along y direction, the blue-detuned air mode trap has to compensate both the Casimir-Polder potential and

the red-detuned dielectric mode trap. The blue-detuned air mode trap cannot be arbitrarily large, since we still require the trap center position to be a trap with $U_{\text{tot}} < 0$. Mathematically, these two arguments give two constraints that define a closed guided-mode trap.

$$\left.\frac{\partial^2 U_{\text{tot}}}{\partial y^2}\right|_{x=0} = \left.\frac{\partial^2 U_b}{\partial y^2}\right|_{x=0} + \left.\frac{\partial^2 U_r}{\partial y^2}\right|_{x=0} + \left.\frac{\partial^2 U_{\text{CP}}}{\partial y^2}\right|_{x=0} < 0, \tag{3.28}$$

$$U_{\text{tot}}(x=0) = U_b(x=0) + U_r(x=0) + U_{\text{CP}}(x=0) < 0. \tag{3.29}$$

Here we have assumed the trap center is at $x = 0$ along x axis within a unit cell. The first inequality ensures the trap has the correct curvature while the second inequality ensures the trap minimum is lower than free-space zero point.

Subject to these two constraints, we calculated different combinations of blue and guided-mode traps and the result is shown in Fig. 3.16 (a) where x axis corresponds to the blue trap maximum ($|U_{\text{b,max}}|$, at $x = a/2$) and y axis corresponds to the red trap minimum ($|U_{\text{r,min}}|$, at $x = 0$). Here, four different regions are identified: the 'anti-trap' region (purple shaded) corresponds to when the trap minimum is larger than zero; the 'open trap' (red shaded) corresponds to when the blue trap is not strong enough to compensate the Casimir-Polder and red-detuned trap curvature; 'closed trap' (white triangle region) corresponds to when a close trap is formed and the color indicates the effective trap depth measured from trap minimum to the turning point (as indicated in Fig. 3.16 (c) with black point), and finally the 'forbidden zone' which corresponds other physical constraints such as the limitation of total guided-mode power from thermal damage (which is actually a main limitation in the APCW as shown in Ref. [125]). Generally, a large trap potential is not preferred as this will increase the heating rate due to any residual vector shift or anti-trap heating for the excited state atoms when the trap frequency is close to the atomic decay rate. Thus, the 'safe delta' in Fig. 3.16 (a) provides the guidance for making a stable guided-mode trap and the optimal ratio is given with the black dashed line in Fig. 3.16. As an example, we calculate the trap profile for one optimal combination at $|U_{\text{r,min}}| = 4.3$ mK and $|U_{\text{b,max}}|/k_B = 40$ mK (indicated with red dots in Fig. 3.16 (a)) on the optimal ratio line. Fig. 3.16 (b) shows the calculated trap potential in the y-z plane at $x = 0$. Fig. 3.16 (b, c) show the calculated trap potential along y direction and along x direction, with each trap potential contribution plotted separately for comparison.[5] From the total trap (solid blue curves) along x and $y$directions, we

[5]Here we have assumed that the dipole potential and the Casimir-Polder potential can be simply

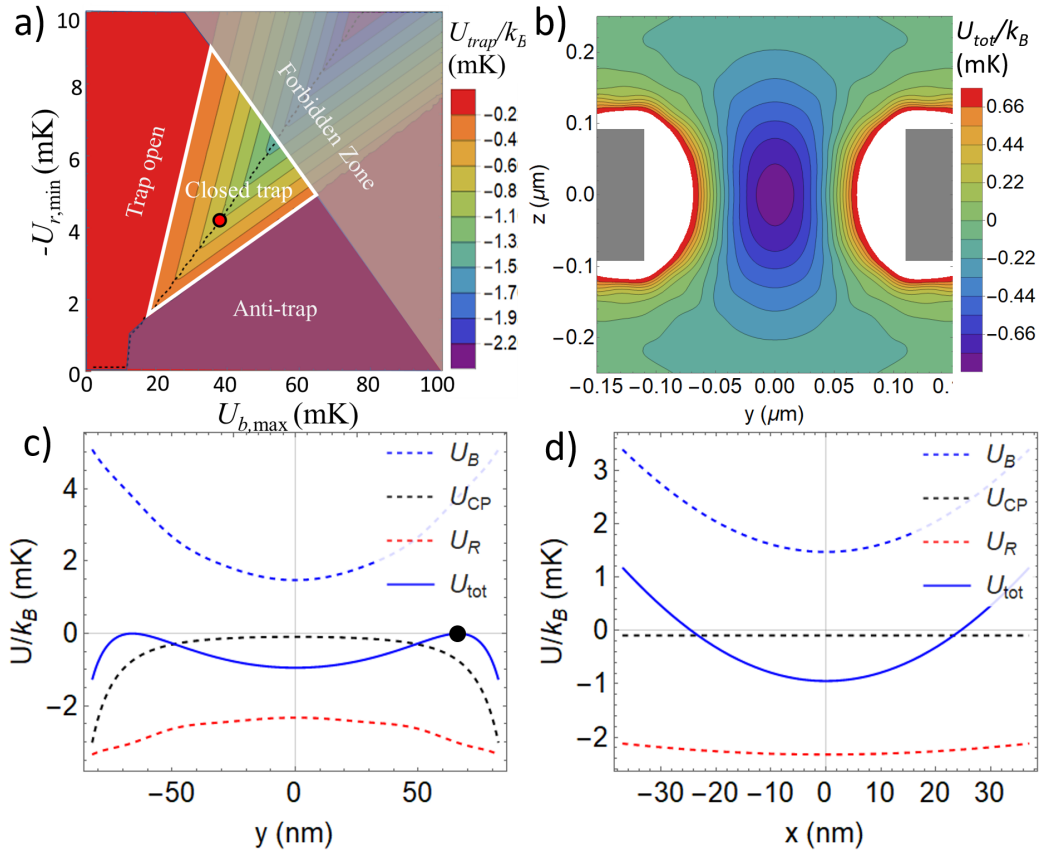

Figure 3.16: (a) Combined guided-mode traps as a function of the blue detuned trap maximum ($|U_{\mathrm{b,max}}|$ at $x = a/2$) (x axis) and the red detuned trap minimum ($|U_{\mathrm{r,min}}|$, at $x = 0$) (y axis). Four different regions are identified: the 'anti-trap' region (purple shaded), 'open trap' (red shaded), 'closed trap' (white triangle region) and the 'forbidden zone' (gray shaded). The physical meaning of each region is explained in text. (b) The calculated trap potential in the y-z plane at $x = 0$ for $|U_{\mathrm{r,min}}| = 4.3$ mK and $|U_{\mathrm{b,max}}|/k_B = 40$ mK as indicated with red dots in (a). (c, d) show the calculated trap potential along y direction and along x direction, with each trap potential contributions plotted separately for comparison. Here the total potential, blue-detuned guided mode potential, red-detuned guide mode potential and the Casimir-Polder potential are indicated with blue solid curve, blue dashed curve, red dashed curve and black dashed curve, respectively. All potentials are calculated for Cs $6S_{1/2}$, $F = 4$ ground state and we have chosen $k_x = 0.98\pi/a$ for the TE air mode Bloch wavevector and $k_x = 0.99\pi/a$ TE dielectric mode. The black dot in (c) refers to the turning point of the trap along y direction.

can estimate the span of the trapped is on the order of $\sim$ 20 nm, this will create a tightly confined atom with trap frequencies $\sim$ 1 MHz.

For the optimal trap ratio, one may notice that in Fig. 3.16 that the blue trap maximum ($U_{\mathrm{b,max}}$) is typically 10X larger than the red detuned trap minimum ($|U_{\mathrm{r,min}}|$). This is because along the x direction, the blue detuned air mode typically has an intensity minimum at the trap position $x = 0$. As a result, the air band blue-detuned trap potential has to be much stronger than the red-detuned dielectric trap in order to make a closed trap. However, recall that at the band-edge, the Bloch mode has a visibility of 1, while away from the band-edge, the Bloch mode visibility decreases. Thus, this ratio of $U_{\mathrm{b,max}}/|U_{\mathrm{r,min}}|$ for optimal can be sensitive to the exact position in frequency of air and dielectric modes with respect to the band-edge and a precise design of the relative guided-mode power ratio is critical [67, 92]. Finally, It is worth noting that this 'safe delta' generally applies to any photonic crystal structure where the blue detuned trap and red detuned trap are peaked at different positions. However, it does not apply to the unstructured waveguide such as the nanofiber where the blue and red trap peak positions are located at the same position along the fiber. In that case, a stable trap can be made by similar trap depths for blue and red trap but with different evanescent decay length due to the wavelength difference, as demonstrated in Ref. [66].

In the previous analysis, we focused on the trap potentials within one unit cell and assumed the trap potential is the same for all unit cells through the whole device. This is however, not true for finite devices. Recall that in Fig. 3.8, we showed that the field near the band-edge will have cavity 'supermode' profiles along the device due to reflection on the boundaries, with 'supermode' profiles replicated for the air band in Fig. 3.17 (a). As our previous discussion relies on the optimal trap ratio of blue and red guided-mode traps, the presence of this 'supermode' profile will break the optimal ratio and make it spatially dependent along the whole device. Furthermore, the presence of 'supermodes' will lead to 'phase slips' where the intensity maximum position of the air mode is deviated from its normal position (e.g. $x = a/2$ inside a unit cell) as shown in Fig. 3.17 (d) (i). Here the 'phase slip' for air mode is defined as $\Delta x/a = (x_{\mathrm{peak}} - a/2)/a$, i.e. the offset of the Bloch mode from the unit cell center along x. One may achieve more uniform field distributions by avoiding the 'supermodes' and aligning the trap frequency far away from the

added together to get the total potential. Strictly speaking, this is not true as both the Casimir-Polder potential and the dipole potential depends on the atomic state and an exact diagonalization of the full Hamiltonian may lead to crossed terms as shown in Refs. [62, 63].

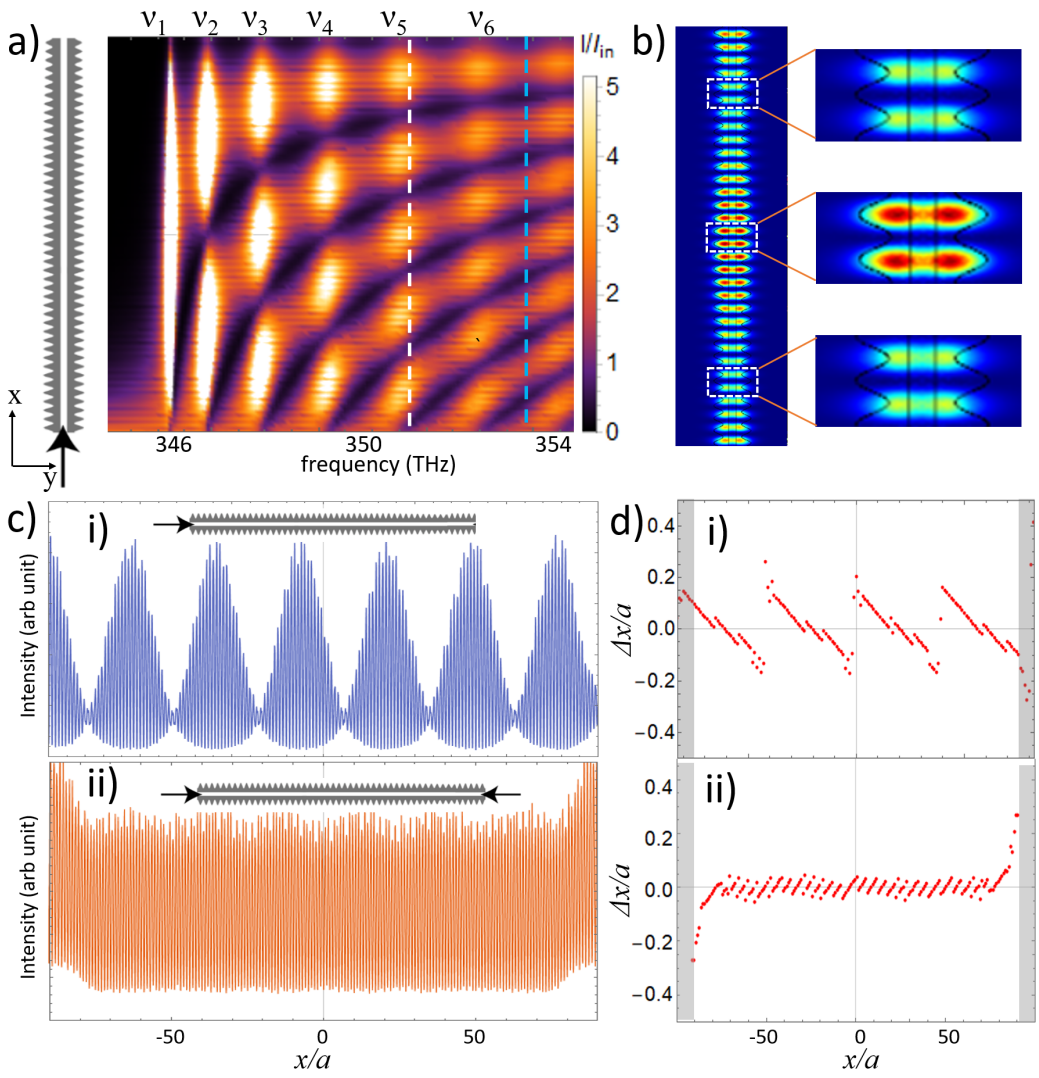

Figure 3.17: (a) The intensity profiles along the full APCW as a function of frequency with first six resonances' frequencies indicated with ν_i, $i = 1, 2, 3..., 6$. Cs D_2 frequency is indicated with white dashed line. *Left* illustration indicates the port the input light is excited for the APCW. (b) An example of intensity distribution from COMSOL®[45] simulation for frequencies far from band-edge with two-ports excitation. The standing-wave envelop is not uniform as indicated by the color. More importantly, significant 'phase slip' deviation to the Bloch mode is observed as shown in the insets. *Top* and *Bottom*: fields concentrate on the air mode intensity maximum position. *Center*: field concentrates on the dielectric mode intensity maximum position. (c) The intensity distribution for (i) single-port excitation (ii) double-port excitation at the anti-resonance between sixth (ν_6) and seventh (ν_7) resonances (not labelled), as indicated blue dashed line in (a). (d) the 'phase slip' measured by the offset of intensity maximum position to the nearest unit cell center $x = a/2$, (i) for single port excitation and (ii) double port excitation.

band-edge (i.e. the 'waveguide region'). However, as shown in Fig. 3.17 (b), away from the band-edge will actually lead to more significant 'phase slip' due to the mismatch of the wavevector k_x to the lattice reciprocal vector π/a. To overcome this nonuniform field intensity problem and the phase-slip problem, a few methods have been proposed and here we present a method with double-port excitation at anti-resonance frequencies.

The working principle of this method is illustrated in Fig. 3.17 (c). As shown in Fig. 3.17 (c) (i), when the guided-mode light is excited from one port at the anti-resonance frequency, the 'supermode' envelope is asymmetric with the device center. Thus, if one excites the guided-mode light from both ports at the same anti-resonance, adding two asymmetric profiles coherently will finally lead to one symmetric and uniform profile along the whole device, as shown in Fig. 3.17 (c) (ii). We further calculated the phase slip for this double-port excitation at anti-resonance method and the result in Fig. 3.17 (d) (ii) suggests that we can also suppress the 'phase slip' for more than 100 unit cells near the center of the device. Here, the residual fluctuations of 'phase slip' are due to mesh resolution in the simulation. Finally, it is worth mentioning that such double-port excitation is also necessary for the cancellation of vector shifts from the guided mode, as demonstrated in Ref. [66].

As a summary, we have shown the general principle of designing a stable guided-mode trap by combining both red-detuned and blue-detuned guided modes. When combining the guided-mode traps with field maxima locate at different position, the constraints for making a stable trap are explicitly given. Numerically, it was shown that these constraints lead to 'safe delta' in the parameter space. Further, beyond the unit cell analysis, we showed how the 'supermode' profile and 'phase slip' problem can be solved by employing the double-port excitation at anti-resonance method. Combining all these techniques presented here, we can design a stable guided-mode trap along the finite devices [146]. It is worth mentioning that stable surface traps above the nanostructure can also been generated from external illuminations, as suggested in Refs. [68, 171, 182]. We will discuss the surface traps formed by external illuminations in detail in Chapter 4.

3.6 Other considerations

Finally, it is worth mentioning that there are a few other topics we did not discuss in detail but might still be relevant. Here we provide an incomplete list

Atomic motion and tunneling effect

In our previous Green's function approach, the atomic motion is treated as an classical variable and the atom state evolution is solved quasi-statically at every fixed atom position (or equivalently averaging over all atomic positions). However, this quasi-static approximation may fail when atom trapped inside the guided-mode trap as the atom oscillation frequency is comparable to the atom decay rate, leading to coupling between atomic internal state and motional state. Furthermore, when atom are cooled to the trap's ground state, the coupling of photon and phonon at these discrete motional levels can lead to entanglement between the photonic state and the motional state [106]. In both cases, a rigorous quantum treatment of atom motion is required with the atom position as quantum variable. Example of such treatment can be found in Ref. [178].

Imperfections and material loss

In reality, the photonic crystal structure can be full of local defects and imperfections due to imperfect fabrication process. The imperfections and local defects might change the local density of states and change the Green's function locally [40].

Mechanical mode of the nanophotonic structure

When the atom trap frequency is close to one the mechanical modes of the nanostructure, the thermal motion of the nanostructure may introduce heating effect on atoms, as found in Ref. [90]. We will study the optomechanical properties of the APCW in Chapter 7 and evaluate the heating effect on trapped atoms.

Chapter 4

THE PROPOSAL FOR ATOM ASSEMBLY ON NANOPHOTONIC STRUCTURES

In previous chapters, we have introduced the basic theory (Chapter 2) and the real world practices (Chapter 3) for understanding atom-light interactions in nanophotonic structures. Since the starting of this project, a few important experimental milestones in this subject have been achieved within the QOG [33, 66–68, 86]. However, one of the major experimental challenges for studying atom-light interaction in nanophotonic systems is to achieve efficient and controllable atom delivery to positions near and within the photonic crystal structures. In this chapter, we will present an approach for achieving deterministic atom delivery and assembly on nanophotonic structures by the integration with optical tweezer arrays. From our initial analysis, this method is promising to extend our ability to control and manipulate each individual atom near dielectric materials. This proposal is inspired by recent exciting achievements in free-space atom assembly [16, 17, 57] and also early success for delivering single atoms to nanophotonic crystal cavities [182]. Part of the materials presented in this chapter are adapted from Ref. [125].

4.1 Introduction

The research described in this chapter attempts to create novel paradigms for strong quantum interactions of light and matter by way of single atoms and photons in nanoscopic dielectric lattices. Nanophotonic structures offer the intriguing possibility to control interactions between atoms and photons by engineering the medium properties through which they interact [40, 42, 124]. Opportunities beyond conventional quantum optics thereby emerge for unconventional quantum phases and phenomena for atoms and photons in one and two-dimensional nanophotonic lattices [52, 71, 204]. The research is inherently multidisciplinary, spanning across nanophotonics, atomic physics, quantum optics, and condensed matter physics.

Beyond the advances reported here, this general area has diverse implementations for quantum information science, including the realization of complex quantum networks [110] and the exploration of quantum many-body physics with atoms and photons [93]. Further avenues of interest are the investigation of quantum metrology and long-distance quantum communication [47] combined with the integrated

functionality of nanophotonics and atoms. As a comparison, solid-state emitters coupled to nanophotonic structures [49, 172, 207] provide a complementary route to some of the physics described here. However, these systems exhibit inhomogeneous broadening which can make the coupling of even two such emitters in a single nanophotonic structure a challenging experimental task [58] and they are not, in their current form, designed to generate controllable interactions across a large system of emitters as has been demonstrated with numerous atomic physics platforms.

While exciting theoretical opportunities of atoms coupled to nanophotonics have emerged, this research only moves forward in the laboratory by advancing nanophotonic device fabrication and by integrating these novel devices into the realm of ultracold atoms. Important experimental milestones have been reached [67, 68, 86, 164, 182, 184], but generally laboratory progress has lagged theory in combining ultracold atoms and novel nanophotonic devices. A grand challenge for experiments in this new field is the realization of atomic arrays with high fractional filling of single atoms into unit cells of 1D and 2D lattices [40, 124].

Previously in the QOG at Caltech, two major atom-delivery schemes were demonstrated in experiments for delivering atoms to the positions near the APCW as summarized in Fig. 4.1. For example, in Lab 11, the side-illumination (SI) trap was used for loading and trapping atoms above the APCW [68, 86]. As illustrated in Fig. 4.1 (a), the SI beam with a beam waist $w_0 \simeq 50\ \mu$m is perpendicularly aligned to the APCW. Due to the interference of incident light and reflection light from the APCW, reflective traps are formed near the APCW, labelled as 'z_1', 'z_2' etc., as indicated in Fig. 4.1 (b) on the simulated intensity profile. As demonstrated in Ref. [68], the averaged trapped atom number is ~ 3 with atoms spanning $\sim 20\ \mu$m along the x axis of the device. Despite recent progress in increasing the trapped atom number by engineering the collision blockade physics during the loading process, one of the major limitations in this side-illumination approach is the fluctuating atom numbers from experimental cycle to cycle and the large and uncontrollable atom spacing along x axis as compared to the APCW lattice constant $a = 370$ nm.

In Lab 2, a conveyor belt approach was implemented for delivering atoms near the APCW [33]. In this approach, atoms are first loaded in the lattice (called 'pancakes') formed by a pair of counter-propagating beams with waist $w_0 \simeq 60\ \mu$m [33]. The atoms inside the 'pancakes' are then transferred to the APCW by chirping the frequency of one beam with respect to another. Fig. 4.1 (d) (i-iv) shows the

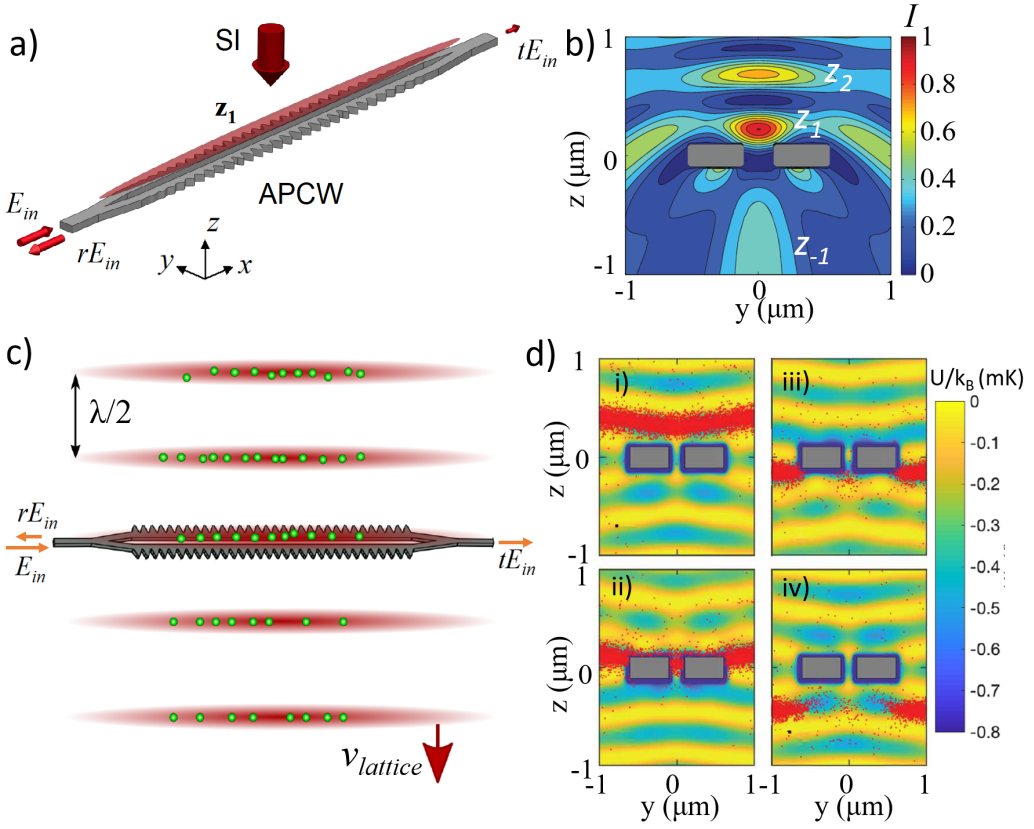

Figure 4.1: Two different atom-delivery schemes developed in the QOG. (a) Illustration of the side-illumination (SI) trap where a focused beam with beam waist $w_0 \simeq 50\ \mu$m is perpendicularly aligned to the APCW. Atoms are loaded and trapped in the first reflective trap called the 'z_1' trap. (b) The simulated intensity profile of the SI beam near the device in the $y-z$ plane. Trapping positions of 'z_1', 'z_2' and 'z_{-1}' are indicated with text. (c) Illustration of the conveyor-belt atom delivery scheme. Atoms are transferred by the 'pancake' lattice with spacing $\lambda/2$, as explained in the text. (d) The simulated atom positions (red dots) as a 'pancake' moves across the APCW at four different times: (i) before reaching the APCW (ii) 'pancake' aligned to the top surface of the APCW (iii) 'pancake' aligned to the bottom surface (iv) 'pancake' exits from the APCW. Exact timing of each plot can be found in Ref. [33]. Figs. (a, b) are adapted from Ref. [68] and Figs. (c, d) are adapted from Ref. [33].

simulated atom positions of the pancakes moving across the APCW. We can see that a small portion of the delivered atoms can pass through the gap of the APCW [146], but with a significant portion of atoms crashing to the top surface of the APCW. This inefficiency of atom delivery and trapping leads to rapid Cs coating on the APCW and degrades the device's performance and lifetime as documented in details in Ref. [130]. Despite guided-mode heating method are developed to reverse the adsorption process [146], it is still challenging to achieve deterministic atom delivery with known atom number and position with this approach.

Given the constraints of previous atom delivery schemes described above, it is desired to develop a new atom delivery scheme where atom number and positions can be controlled precisely above the nanostructure. Inspired by recent breakthroughs of free-space atom assembly with optical tweezer arrays [16, 17, 57], we believe the integration of nanophotonics with optical tweezer arrays could be one promising path that provides feasible manipulation of atoms on nanostructures down to single atom level and would ultimately allow us to build the nanoscopic atomic arrays with one atom per photonic crystal unit cell, as illustrated in Fig. 1.4. In the rest of this chapter, we will discuss in detail how to apply the current state-of-art free-space atom assembly techniques into our nanophotonic system and evaluate the potential requirements and challenges for achieving the cartoon illustration in Fig. 1.4.

4.2 Atom assembly: from free-space to near nanostructures

Optical tweezers and atom assembly in free-space

Before introducing the proposal of atom assembly on nanostructures, here we first give a short review on the optical tweezers and atom sorting techniques in free-space, following Ref. [28].

The trapping of single atom in a tightly focused dipole trap, or an optical tweezer trap was demonstrated by Schlosser et al. in 2001 [167]. There, an optical dipole trap with a waist ($1/e^2$ intensity radius) ~ 1 μm is immersed in a magneto-optical trap (MOT). When an atom is cooled from the MOT into the optical tweezers and gets trapped inside, the continuously emitted fluorescence light under near-resonant illumination will signal the presence of this single atom in the optical tweezer. Now if a second atom enters the trap, the fast light-assisted collisions between the two atoms will lead to the immediate loss of both atoms [168], limiting the number of atoms in this optical tweezer trap to be either zero or one with probability $p \sim 1/2$ for each. This effect is called 'collision blockade' in the optical tweezer trap [167, 168]. One

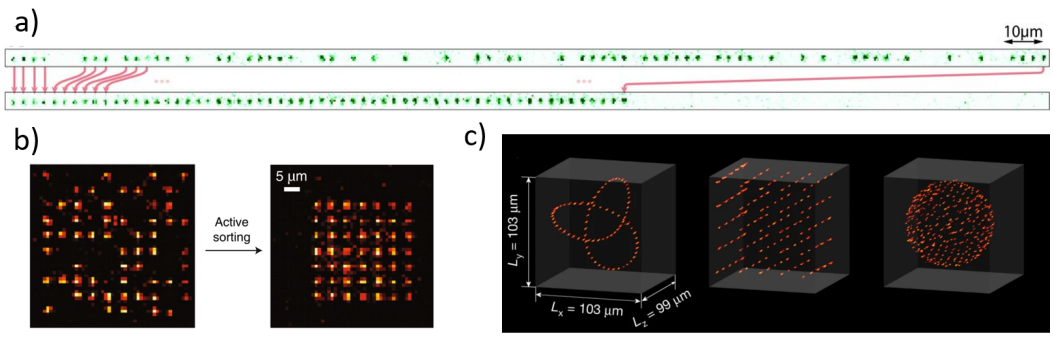

Figure 4.2: Atom assembly in (a) one dimensional chain, (b) two dimensional array and (c) three dimensional lattices with arbitrary structures. Details of the methods are explained in the text. Figure (a) adapted from Ref. [57], Fig. (b) adapted from Ref. [16] and Fig. (c) adapted from Ref. [17], with permission.

can scale up the optical tweezer traps with an array of optical tweezers. However, due to the stochastic loading of optical tweezers, the probability p_N of having all N traps simultaneously filled decreases as $1/2^N$. Careful engineering of the light-assisted collisions to lose just one atom of the pair [29, 75, 120] was shown to enhance the probability of one atom up to $p \sim 0.9$. Still, the probability of creating a N-trap defect-free array decreases very quickly with N ($p_N = p^N$). As a result, the size of optical tweezer arrays was limited to just a few atoms for a long time [28].

In 2016, this limitation was circumvented with the demonstration of atom sorting techniques [16, 57, 107], which making it possible to achieve fast atom assembly of defect-free arrays with atom number $N \sim 100$. The basic idea of atom sorting is to start from a large array with $2N$ traps with randomly loaded $\sim N$ atoms (each with zero or one atom). By measuring the random configuration in each experiment cycle and matching it to the pre-calculated sorting algorithm, one can actively sort the atoms into the target configuration (e.g., an ordered array) in real time. In experiment, this sorting technique can be achieved with two methods, depending on whether the optical tweezer array is moving or not. In the first method, the optical tweezer array is generated by acousto-optical deflectors (AODs) where multiple radio-frequency (RF) tones are fed into the AOD, creating multiple first order beams before focusing [166]. The trap depth and the spacing of optical tweezers are controlled by the RF power and frequency separation, respectively. For the atom sorting in experiment, a fluorescence image of the tweezer array is taken to distinguish the loaded tweezers from the empty ones and then the the empty tweezers are removed and the loaded optical tweezers are dynamically moved using the AODs

to create a fully loaded array, as shown in Fig. 4.2 (a) in the case of 1D (Figure adapted from Ref. [57]). Extensions to 2D and 3D were also demonstrated in Ref. [107] and Ref. [119] in the same year. In the second method, the optical tweezer arrays are generated by a spatial light modulator (SLM) which imprints an appropriate phase pattern on the trapping beam before focusing. After the fluorescence imaging of the loading configuration, a moving optical tweezer generated and controlled by the AOD captures an atom from a filled site, then moves and releases it to the target site one at a time [16], as shown in Fig. 4.2 (b). Sorting in 2D optical tweezer arrays forming by microlenses arrays was also demonstrated in Ref. [139]. Recently, this method has been extended to the assembly of 3D arrays with arbitrary designed structures [17], as shown in Fig. 4.2 (c). This sorting of atoms has also been applied in two and three dimensions in optical lattices with large spacing between sites [116] and arrays of optical tweezer trapped molecules [4].

Protocol for atom assembly on nanostructures

Inspired by the success of free-space atom assembly, it is natural to wonder if this method can be applied to atom assembly on nanostructures. However, it is soon realized that it is challenging to directly apply the atom assembly techniques in free-space to the arrays on nanophotonic structures. Recall that in free-space, the success of atom assembly relies on three basic requirements: 1) The initial optical tweezer array should fill with zero or one atom in each trap; 2) the two configurations (zero or one atom) can be determined quickly from non-destructive methods (fluorescence imaging); 3) the lifetime of trapped atoms is relatively long with respect to the sorting time in order to achieve high fidelity.

The presence of a dielectric structure destroys all the three bases. For the first basis, the presence of the dielectric material will diminish the density of atoms in the MOT near the material, leading to inefficient loading of the optical tweezer array ($p < 1/2$). Despite the success of direct loading in reflective dipole traps on quasi-1D structures such as nanofibers [135] and the APCW waveguide [68] where the impact to the MOT is minimal, this method does not apply to general structures such as the 2D photonic crystal slabs [204] presented in the previous chapter or structures with supporting substrate [108]. Furthermore, immersing the nanophotonic structure in the MOT will cause rapid Cs adsorption on the nanophotonic structure, shift the spectrum of the device and degrade its performances. For the second basis, when aligning the optical tweezer arrays with the nanophotonic structures, the reflection/scattering light from the structure interferes with the incident tweezer

beam, forming reflective fringes (or 'pancakes') similar to a 1D optical lattices. As a result, the optical tweezers are no longer a single trap and each of the pancakes can trap zero or one atom. This makes it challenging to determine the initial configuration for the trap closest to the structure (the 'z_1' trap, as shown in Fig. 4.1 (b)). Finally, the lifetime of the trapped atom next to the dielectric material is typically limited to $\sim$ 10 ms under probe light and $\sim$ 100 ms without probe light [68, 182]. This is in contrast to the typical lifetime of $\sim$ 1 s under illumination and $\sim$ 10 s lifetime of atoms without illumination in free-space [16, 57]. Furthermore, the presence of the dielectric material makes the conventional cooling schemes such as PGCsnot efficient near the dielectric surfaces [68]. Without long lifetime and efficient cooling methods, it is hard to determine the loading configuration accurately (as atom will be lost) and to achieve high fidelity sorting. Since the presence of the dielectric material breaks all the three basis of atom assembly in free-space, this makes the direct atom assembly on nanostructures very challenging in the near future.

Instead of direct atom assembly on nanostructures, here we circumvent the difficulties above by first assembling the atom array in free-space and then transfer to the target positions on device. Typical experimental steps for achieving N_s atom array on device can be as follows

Step 1: Loading an array of N_0 ($N_0 \gg N_s$) optical tweezers at distance far away from the device (for example, distance >50 μm).

Step 2: Determine the configurations of the N_0 array by fluorescence imaging.

Step 3: Free-space atom sorting and creating a defect-free array of N_1 atoms (with $N_0 > 2N_1$).

Step 4: Transfer array of N_2 ($N_s < N_2 < N_1$) atoms from free-space to the device. Depending on the transfer probability and lifetime of the trapped atoms on device, one can decide whether it is necessary to perform atom sorting on device.

Step 5: Perform science experiment with the array of N_s ($N_s < N_2$) atoms on the nanostructures.

Step 6: Transfer back to free-space and determine the atom configurations for further rearrangement.

Step 7: Repeat steps 4-6, until the total atom number N_{tot} is not enough for the intended science experiment ($N_{\text{tot}} < N_s$), repeat 1-6.

In the proposed protocol above, the first three steps are relatively straightforward. When the distance of the loading position is sufficiently far away from the nanostructure, it can be safely assumed that the free-space atom assembly techniques can be well applied. Step 5-7 is also self-explanatory. Due to the fact that the lifetime of free-space trapped atoms are much longer than the lifetime on the device (e.g., 10 s vs. 100 ms), we have purposely used the free-space atom array as atom reservoir for continuous single atom supply, to increase the repetition rate of the experiment. Thus, in our following discussions, we will mainly focus on addressing step 4.

Specifically, there are two important parameters in step 4: the free-space to target device trap transfer probability and the lifetime of trapped atoms on the devices. These two parameters determine whether it is necessary or possible to perform an additional atom sorting on the device. On the one hand, high transfer probability to the target trap can ensure that the transferred atom array on the device is still defect-free and thus circumvent atom resorting above the device. For example, given the free-space assembled 10 atom array and the single atom transfer probability $p_t \simeq 0.94$ (which is demonstrated in Ref. [182]), the probability of having a 10 atom array to be defect-free on device is $p_t^{10} \simeq 0.54$ while a lower transfer probability, for example, $p_t = 0.8$, the probability of having a 10 defect-free atom array is $p_t^{10} \simeq 0.11$. On the other hand, the lifetime on the device is also critical. For any operations on the device (e.g., sorting or science measurement) that take time Δt and the corresponding lifetime τ, the probability of having a full array without atom loss is $p_o = \exp(-N_s \Delta t/\tau)$. For $N_s = 10$, $\Delta t = 5$ ms and $\tau = 100$ ms, we have $p_o = 0.6$, while if the trapped lifetime is extended to 1 s, the probability of no atom loss after the operation is $p_o = 0.95$. Thus, it is important to find the ideal method for free-space to device transfer and to push the lifetime of trapped atoms on nanostructures or equivalently, to reduce the time needed for a specific operation.

First, for transferring from a free-space array to target positions on the device, a few methods have been proposed and demonstrated, namely, the conveyor belt method [33, 108], the side-transfer method [164, 182] and the transfer using superposed Laguerre-Gaussian modes[20]. The conveyor belt method has already been discussed in detail in Lucas Peng's thesis [146] and in Ref. [108] for optical tweezers. For the transfer method using superposed Laguerre-Gaussian modes, we will discuss in detail in Chapter 6. In this chapter, we will mainly focus on the side-transfer

method [164, 182] in our discussion. As this subject of transferring from free-space to device is strongly depends on the device design parameters, we will offer detailed discussions in following sections.

Second, the trapping lifetime can be extended by suppressing the potential heating sources for trapped atoms near dielectric structures. This can include state-dependent trap potential [199], vector shifts due to elliptical polarization near dielectric surfaces [46], and mechanical motion of the device [90]. For the first two heating sources, heating can be suppressed by employing the 'magic' wavelength for the trap design and having counter-propagating guided modes for cancelling the vector shifts [66, 199]. The impact of light shifts can also be fully eliminated for atoms without 'magic' wavelengths by temporally alternating the trapping beam with cooling and imaging beams as reported in Ref. [94]. For the heating from the device's mechanical vibrations, this can be suppressed by a better design of the mechanical properties of the device, for example, switching from the APCW to SPCW. Furthermore, efficient cooling is critical to suppress the potential atom loss due to heating. This can be achieved by conventional Doppler or sub-Doppler cooling near the dielectric surfaces. For example, lower temperatures can be achieved by using Doppler cooling with narrow linewidth transitions, for example, $6S_{1/2} \rightarrow 5D_{5/2}$ in Cs atoms [36]. Recently, nearly ground state cooling for atoms trapped 300 nm near the nanofiber is demonstrated in Ref. [132] with guided-mode polarization gradient cooling (PGC) and degenerate Raman cooling (DRC). The observed lifetimes for surface trapped atoms are extended to 1.5 s for PGC and 1.7 s for DRC, compared to the 75 ms lifetime in the absence of cooling, as reported in Ref. [132].

Reducing the sorting time near the device is also critical for atom assembly on the nanostructures. This can be achieved by making use of the strong atom-light coupling within the nanostructure and improving the signal-to-noise ratio in atom detection. For example, for PCWs such as the APCW with $\Gamma_{1D} > \Gamma'$, the atom can be excited illuminated from beams collinear with the optical tweezers (to minimize the direct scattering into device), as shown in Fig. 4.3 (b). The fluorescence counts will be efficiently collected from the guided mode due to large Γ_{1D} and used to determine the atom number versus defect number. Alternatively, the transmission and reflection spectra can also be used to determine the atom number, as shown in Fig. 4.3 (c-d). By probing on the red detuned side $\Delta_A/\Gamma' \sim 1$ (as indicated with red dashed line) and measuring the phase shift due to the presence of atoms, one can resolve the atom number and also reduce heating from the probe light [18].

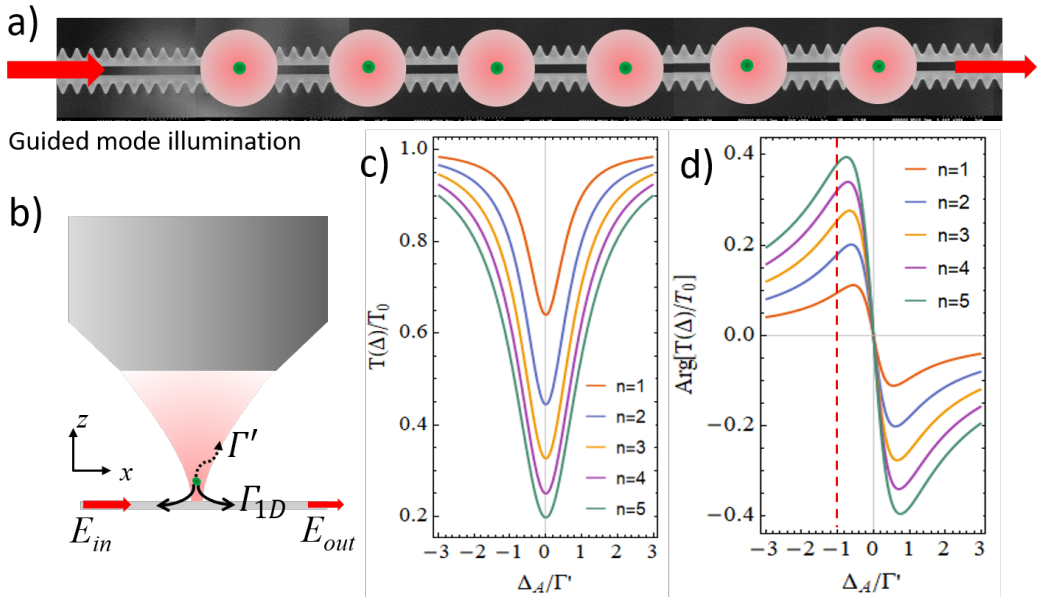

Figure 4.3: (a) Illustration of guided mode illumination. (b) The basic rates of atom trapped in an optical tweezer trap aligned to the PCW (c) The typical transmission spectrum for the APCW at first resonance for 1-5 atoms (d) The phase shift due to the presence of atoms on the APCW. By probing on the red detuned side $\Delta_A/\Gamma' \sim 1$ (as indicated with red dashed line), one can resolve the atom number and also reduce heating from probe light.

4.3 Atom assembly on quasi-1D nanostructures

Transfer free-space atom array to the z_1 traps above the APCW

As mentioned in the previous section, the transferring of free-space atom arrays to nanostructures is particularly important as a high success rate transfer can circumvent the step of atom sorting on nanostructures. In this section, we investigate the side-transfer scheme where the tweezer is initial on the side of the device and transfer to the device by simply moving the tweezer to align on it. The side-transfer technique was originally demonstrated by Thompson et al. [182] for transferring an atom from a single optical tweezer to a one-dimensional nano-beam photonic crystal cavity. In Ref. [182], the transfer success rate was measured to be 94 ± 6%. Given the structural similarity between the 1D nanobeam cavity and the APCW, it is expected that the side-transfer technique should also lead to high delivery efficiencies for transferring free-space trapped atoms to reflective traps above the APCW.

Fig. 4.4 (a, b) illustrates the side-transfer scheme where the tweezer array is on the side of the APCW and moving towards the APCW. Here, the tweezer array is generated by an AOD with axis along x and moving the entire tweezer array

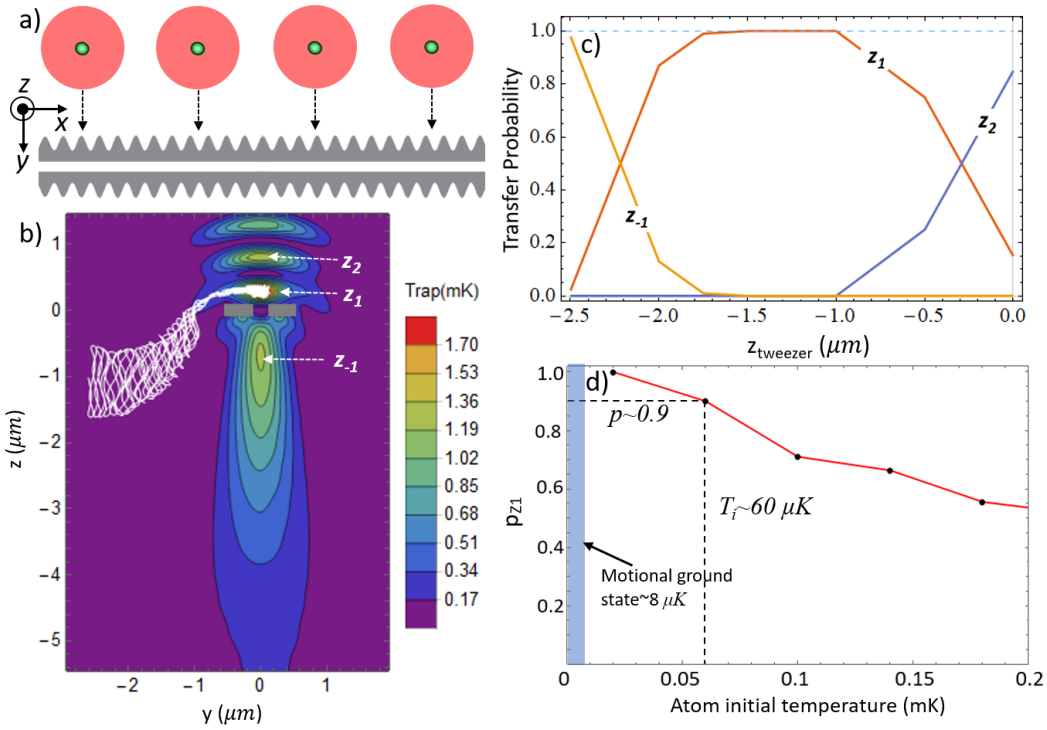

Figure 4.4: (a) An illustration of the scheme for transferring a free-space array of single atoms to reflective traps above the APCW. The red circles indicate the size of a tweezer with radius equal to the waist $w_0 = 850$ nm and green dots indicate the rms span sizes of ~ 100 μK trapped atoms in a 1 mK tweezer trap. (b) A COMSOL® [45] simulation of the tweezer trap when aligned on PCWs with tweezer focus position at $z = -1$ μm and polarization along x direction (out of page), with the closest three reflective traps labelled as 'z_1', 'z_{-1}' and 'z_2'. The white curve shows a typical atom trajectory starting at initial tweezer trap minimum $(x, y, z) = (0, -2.5, -1)$ μm with initial temperature ~ 50 μK. (c) Probability of transferring into different reflective traps at different tweezer focus positions along z direction, with atom initial temperature $T_i = 20$ μK. (d) Probability of transferring into z_1 trap at different atom initial temperatures at 1 mK tweezer trap.

vertically along the y direction is achieved by sweeping the RF drive frequency of a second AOD with axis along y. Due to π-phase shift of the reflection light from dielectric surface, the interference between the reflection light and the tweezer light leads to an intensity minimum at the surface of the dielectric material. As a result, for the red-detuned tweezer trap, the atom will stay in the intensity maximum region and avoid from colliding to the dielectric surface. Fig. 4.4 (b) shows a typical atom trajectory (white curve) from numerical simulation being successfully transferred into the so-called z_1 trap close to the upper surface of the APCW trap with the largest coupling rate to TE mode of the APCW [68, 86]. Here, the free-space initial position of the tweezer waist is located at $(x, y, z) = (0, -2.5, -1)$ μm with the atom initial temperature ~ 50 μK in a free-space tweezer trap depth $U_0/k_B = 1$ mK.

Generally, the probabilities of transferring into different reflective trap sites $\{z_i\}$ can be tuned by changing the initial tweezer focus along the z direction. This is further quantified by a Monte-Carlo simulation of atom trajectories as shown in Fig. 4.4 (c) for tweezer waist $w_0 = 850$ nm and atom initial temperature 20 μK. The simulated probability of transferring into the z_1 trap is peaked at $\sim 100\%$ between $z = -1$ μm and $z = -1.7$ μm which indicates a relatively large tolerance of tweezer focus positions along z. Our investigations of atom trajectories via Monte-Carlo simulation show that achieving high probability transfer with ($p > 0.9$) into the z_1 trap also requires that the atom starts initially with a temperature less than 60 μK, as shown in Fig. 4.4 (c) for tweezer waist $w_0 = 850$ nm, trap depth $U/k_B = 1$ mK and focus position $z = -1.5$ μm. Absent the difficulties brought by the dielectric boundary, this can be achieved with PGC in the tweezer or Raman sideband cooling as shown in Refs. [105, 181].

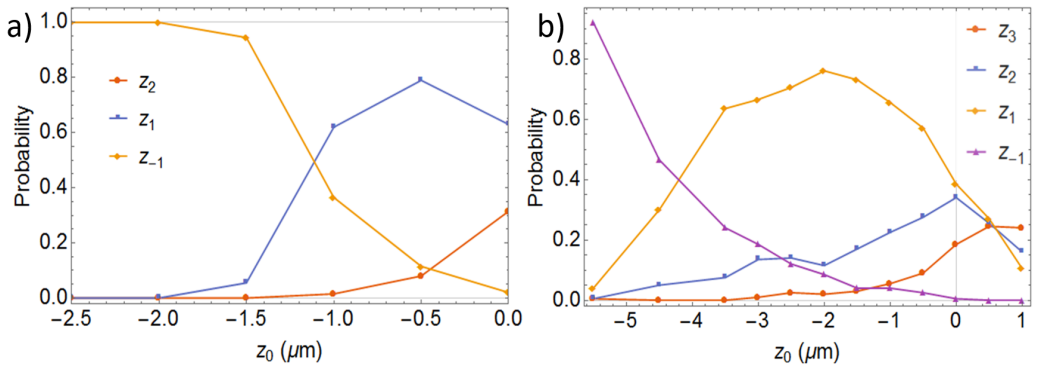

Figure 4.5: Transfer probability for atoms trapped in an optical tweezer (a) with polarization along y axis and waist $w_0 = 850$ nm (b) polarization along x axis but with waist $w_0 = 1.26$ μm. All other parameters are the same as in Fig. 4.4

Further, we numerically investigated the transfer probability dependence on the tweezer polarization and waist. Fig. 4.5 (a) shows an example of the calculated transfer probability for the tweezer with polarization along y axis (perpendicular to the APCW), with all other parameters the same as in Fig. 4.4, we observe significant probability of transferring into 'z_{-1}' and 'z_2' traps which limit the peak probability into the 'z_1' trap under 80%. The simple explanation of this difference can be made from the weaker reflection from the APCW for light polarized along y direction, which leads to weaker pancakes as the tweezer moves towards the device. Another variable to consider relative to Fig. 4.4 is the tweezer waist with Fig. 4.5 showing an example of the calculated transfer probability for $w_0 = 1.26$ μm. Here this specific choice corresponds to the setting for a NA= 0.4 objective in our current setup, as discussed in Chapter 5. As we can see from Fig. 4.5, transfer into other traps such as z_2 and z_{-1} is not negligible due to the relative larger span of atoms along z direction. As a result, the highest transfer probability into z_1 trap is $p \sim 0.75$ at an optimal position of $z_0 = -2$ μm, where z_0 refers to the tweezer focus position along z axis. Compared to Fig. 4.4 (c), the range for transfer probability $p = 0.9p_{\max} \simeq 0.65$ along z axis is $\Delta z \simeq 2.5$ μm. Next, we investigated the dependence of transfer probability on the device parameters. The dependence of z_1 trap position and trap depth with respect to the device thickness t was already investigated Juan Muniz's thesis [171]. Here we focus on trap deformation under different transverse dimensions for a double-nanobeam waveguides, as an analog to the APCW. Fig. 4.6 shows the simulated tweezer intensity profile in $y - z$ plane when aligned to a double-nanobeam waveguide for a set of nanobeam widths w (the gap size and the thickness is the same as the APCW). For $w \leq 500$ nm, the z_1 trap is well-defined above the double nanobeams and the trap size along y direction is defined by the gap of the double nanobeam. However, for $w \sim 600$ nm, the z_1 trap is connected to the upper corners of the two nanobeams, suggesting being not suitable for trapping atoms. For larger nanobeam widths ($w > 700$ nm), the z_1 trap recovers as a well defined trap for trapping atoms above the device. The deformation of the z_1 trap at different nanobeam widths w is related to the interference of the scattered light from the nanobeam. Specifically, at $w \simeq 600$ nm, the light scattered from the nanobeam forms a destructive interference at the conventional z_1 trap center.

It turns out that the transverse dimension of the double nanobeams will have a significant impact on the transfer efficiency in the side-transfer method. Fig. 4.7 (b) shows an example for side-transfer to a double-nanobeam waveguide with nanobeam width $w = 450$ nm. As we can see, for tweezer focus position between $z_0 = -1$ μm

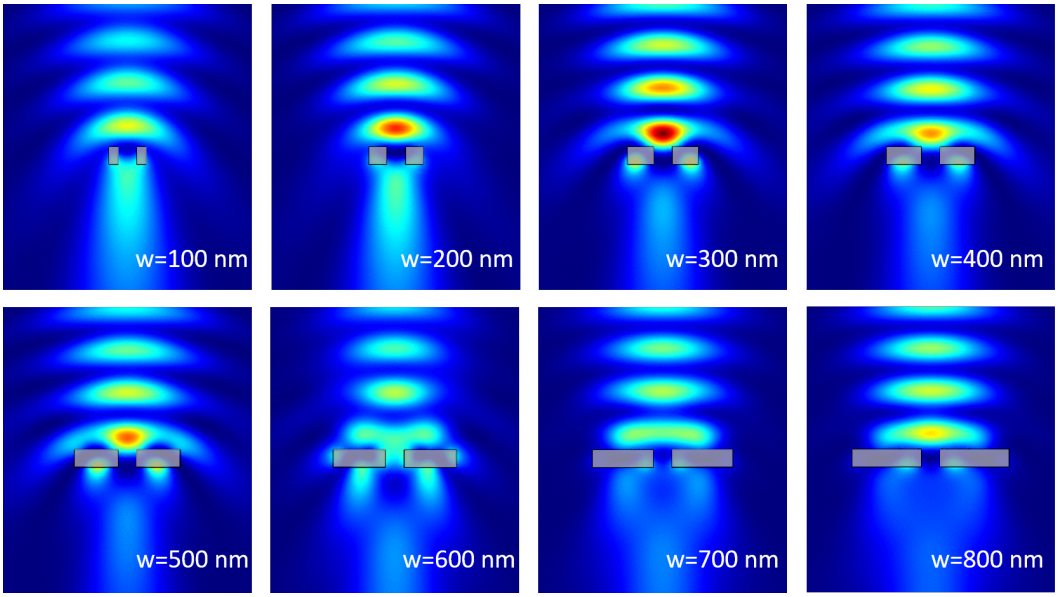

Figure 4.6: COMSOL®[45] simulated tweezer intensity profile in $y-z$ plane when aligned to a double nano-beam structure for different widths w of the nanobeam. Here the double-nanobeam gap is fixed at $g = 220$ nm (as in the APCW) and the tweezer focus is at the top surfaces of the double-nanobeams and aligned to the center of the gap. The gray shaded region indicates the cross-section of the double-nanobeam waveguide.

and -3 μm, there is a significant probability of atom trapped on the side of the z_1 trap, called $z_{1,1}$ trap, as indicated in Fig. 4.7 (a). Recall that the polarization in our previous simulations are all along the waveguide by default (as indicated in the inset in Fig. 4.7 (a)), one can adjust the input tweezer polarization to suppress the two side traps $z_{1,1}$ and $z_{1,-1}$. For example, Fig. 4.7 (c) shows the simulated intensity profile for tweezer polarization orthogonal to the nanobeam (or y-polarized as indicated in the inset in Fig. 4.7 (c)). Clearly, the two side traps $z_{1,1}$ and $z_{1,-1}$ are gone, despite the z_1 trap itself having two intensity maximums above each nanobeam.[1] One can utilize this difference of z_1 trap between x-polarized tweezer and y-polarized tweezer to further transfer the $z_{1,1}$ trapped atoms into the z_1 trap. This is achieved by adding an additional step to rotate the polarization of the tweezer from x-polarized to y-polarized. The trajectory simulation suggests that almost all atoms originally trapped in $z_{1,1}$ trap can then be transferred into the z_1 trap, as shown in Fig. 4.7 (d). With these two steps, one can achieve a high transfer probability as for the case of

[1]The trajectory simulation for transferring atom with the y-polarized tweezer (not shown) suggests that there is significant probability of transferring into z_2 or z_{-1} traps due to the lower reflectivity from the nanobeam during the transport.

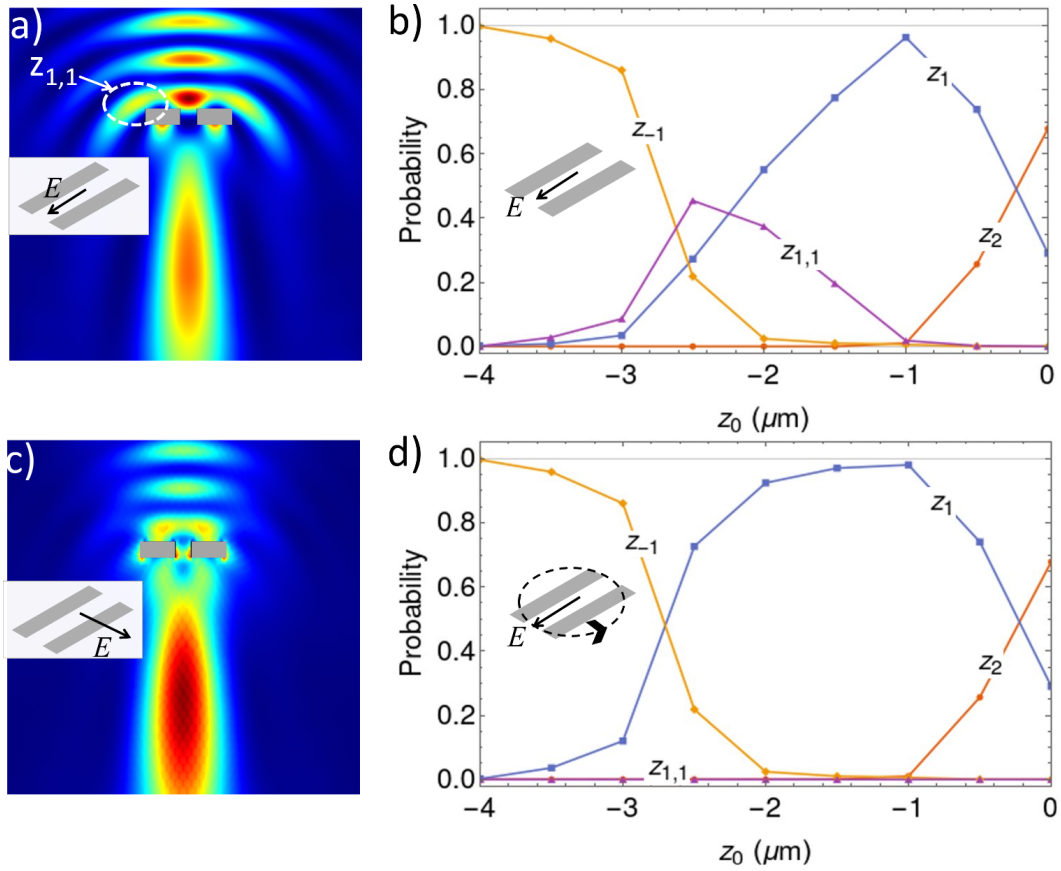

Figure 4.7: (a) COMSOL®[45] simulated intensity profile for an optical tweezer aligned with the double-nanobeam waveguide (gray rectangles) with waist $w_0 = 850$ nm and focus position at $z_0 = -2.5$ μm (2.5 μm lower than the nanobeam top surface). A new trap $z_{1,1}$ on the side of z_1 trap is indicated with white dashed circle. Here the nanobeam width is $w = 450$ nm. The inset indicates the polarization of the optical tweezer along the double-nanobeam waveguide. (b) The numerically calculated transfer probability from trajectory simulation at different focal positions. Inset indicates the polarization of the optical tweezer. The probability of transfer into z_1 (blue curve) peaks at $z_0 = -1$ μm but with significant probability of ending into the new trap site $z_{1,1}$ (purple curve) at other tweezer focal positions (z_0). (c) COMSOL®[45] simulated intensity profile for polarization perpendicular to the double nanobeams, as indicated in the inset. Other parameters are the same as in (a). Note that the trap sites $z_{1,1}$ and $z_{1,-1}$ are now not relevant. (d) The numerically calculated transfer probability with additional step of rotating the polarization from along waveguide to perpendicular to the waveguide when the tweezer is aligned to the waveguide, as indicated in the inset.

transferring to smaller nanobeam width waveguides.

Loading into a subwavelength array on the APCW

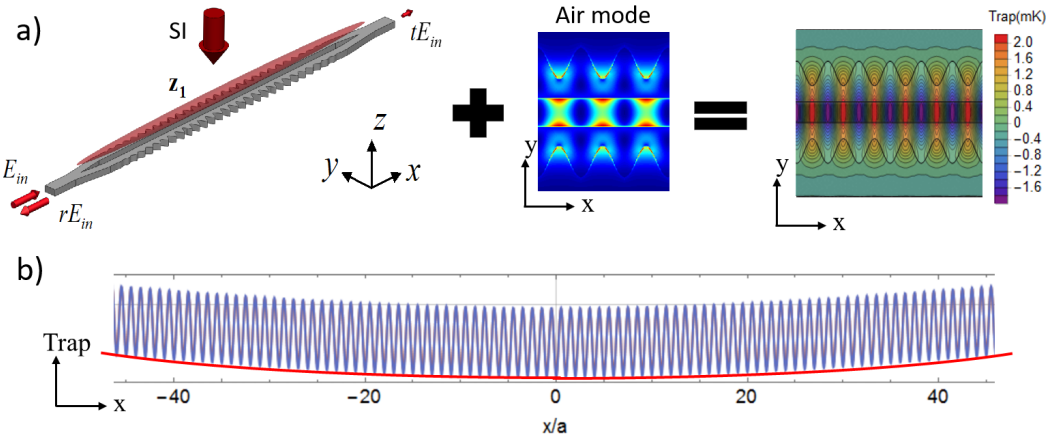

Figure 4.8: (a) The subwavelength z_1 lattice (*right*) formed by adding the long cigarette-shaped z_1 trap from conventional side-illumination beam (*left*) with the blue-detuned air mode (*middle*). The evanescent field of the air mode will divide the long z_1 trap into different sites with period the same as the APCW structure. The *right* plot is a COMSOL®[45] simulation of the total combined trap at the plane $z = z_1$. (b) The z_1 trap along device at position $y = 0$ and $z = 130$ nm (with the surface at $z = 0$). The red curve indicates the conventional z_1 trap from the side-illumination beam with waist $w_0 = 55$ μm. The blue curve represents the total trap formed by adding blue-detuned air mode and the z_1 trap.

In the previous section, we have shown the side-transfer method can be applied to quasi-1D system to achieve high transfer efficiency. There the tweezer itself forms the z_1 trap when aligned to the APCW. However, such z_1 trap arrays formed by optical tweezers cannot be subwavelength. In fact, in order to have well separated traps and avoid frequency beating, the distance between neighbor tweezers are typically kept larger than $2w_0$, with w_0 being the tweezer waist. However, a subwavelength lattice can be formed above the nanostructure by combining the guided-mode traps with the reflective traps (z_1 trap) from the conventional side-illumination beam, as already suggested in Ref. [71]. In this section, we will show how to apply the side-transfer method to transfer free-space atom array into a subwavelength lattice on the APCW.

Fig. 4.8 shows the basic idea for the case of the APCW. Here the trap lattice above the APCW is a combination of the conventional side-illumination beam (with waist w_{0x} along the device $\simeq 55$ μm formed by a cylindrical lens) and the blue-detuned air mode. Due to the Bloch mode periodicity and the finite decay length of the

evanescent field, the blue-detuned air mode will extend to the z_1 trap region and separate the long cigarette-shaped z_1 trap into many isolated trap sites, as shown in Fig. 4.8 (b) for the total trap along the line $z = z_1$ and $y = 0$. As the combined trap is formed with the blued-detuned guided mode, it naturally inherits the lattice constant from the APCW and form a 1D lattice at the original z_1 trap position. For brevity, we refer this combined trap lattice as 'z_1 lattice'.

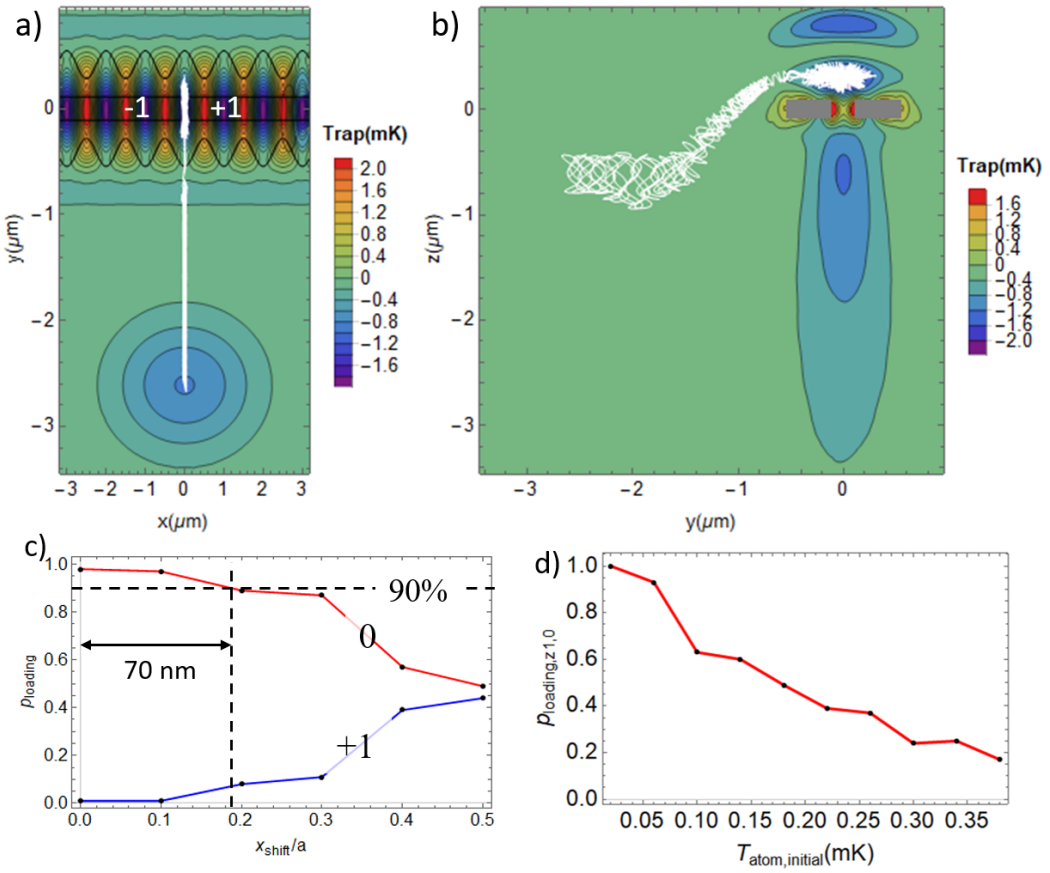

Figure 4.9: (a, b) Example of simulated trajectory (white curves) for transferring into the z_1 trap lattice above the APCW in (a) $x - y$ plane and (b) $y - z$ plane. The free-space tweezer has a trap depth $U_0/k_B = 1$ mK, the side-illumination beam has a trap depth $U_{SI}/k_B \simeq 2$ mK at z_1 trap position and the blue-detuned air mode has a peak trap depth (anti-trap) $U_{air} \simeq 2$ mK at z_1 trap position. (c) The numerically calculated transfer probability into the target site at $x = 0$ (label as '0' site) and neighbor sites at $x = a$ and $x = -a$ (labelled as '+1' and '-1' in (a)) as a function of the tweezer initial position x, for atom initial temperature $T_a = 25$ μK. The dashed lines indicate the range to maintain 90% efficiency into the target '0' trap site at $x = 0$ ($z = z_1$). (d) The probability of transferring into the '0' trap site as a function of atom initial temperature.

With the fixed z_1 lattice above the APCW, we now investigate how the side-transfer

technique can be applied to transferring into the z_1 lattice site. Fig. 4.9 (a, b) shows one example of the simulated trajectory for transferring into the target trap site at $x = 0$ for an atom with an initial temperature $T_a \simeq 25$ μK in an optical tweezer with trap depth $\simeq 1$ mK and waist $w_0 = 850$ nm. As indicated in Fig. 4.9 (a), the precise alignment of free-space tweezer to the desire trap site is critical for achieving high transfer probability. This is further quantified in Fig. 4.9 (c) where we calculated the probability of transferring into target trap site at $x = 0$ with the initial tweezer position misaligned by x_{shift}, with condition same as in Fig. 4.9 (a, b). From this numerical result, it shows that for an misalignment within $\Delta x = \pm 70$ nm, the transfer probability can still maintain at $p > 0.9$. Of course, this tolerance in the x direction dependents on the atom's initial temperature. For example, for the setting in Fig. 4.9 (a-c), the estimated rms. size along x direction is $\langle x^2 \rangle^{1/2} \simeq 60$ nm. We further calculate the transfer probability under different atom initial temperature with $x_{\text{shift}} = 0$ and the result is summarized in Fig. 4.9 (d). It suggests that for high transfer probability, the initial atom temperature should be lower than 50 μK. This temperature limit should be accessible with conventional polarization gradient cooling.

With the demonstration of transferring into a single site in the z_1 lattice, it might seem to be straightforward to transfer the free-space trapped atoms array to each site of the z_1 lattice and creating a fully loaded subwavelength array. However, this is not true given the mismatch of the free-space lattice constant d (e.g., $d \leq 2w_0$) and the APCW lattice constant a.[2] Here we propose a simple geometric trick for loading into the subwavelength z_1 lattice with one step side-transfer as shown in Fig. 4.10. This trick is based on the fact the projected spacing can be much smaller than original spacing of the tweezer array. For the case of the APCW with $a = 370$ nm and free-space tweezer array with spacing $d = 2w_0$, the correct angle θ for projecting each optical tweezer to each z_1 lattice site is $\theta = \arccos(a/d) \simeq 76°$. To load the free-space tweezer into each z_1 lattice site, the RF frequency tones applied to each AOD are illustrated in Fig. 4.10 (b), with the AOD axis f_1 and f_2 indicated in Fig. 4.10 (a). Here the slopes of the frequency ramping in f_1 and f_2 are chosen

[2] One may wish to transfer the free-space atom one by one into the subwavelength lattice to avoid overlapping between tweezers. However, to achieve this, the system's degree of freedom needs to be $DOF \sim 2N$ which is much larger than the two AOD system with $DOF \sim N_1 + N_2$. Here N refers to the atom number and N_1 and N_2 refer to the number of frequency tones applied to each AOD. For fully loaded 2D array, $N = N_1 \times N_2$. Here, we assumed the tweezer array is generated by the AODs. If the tweezer array is generated from spatial light modulator with one moving tweezer, as in Ref. [16], each atom can be individually moved to the z_1 lattice but it requires N steps for fully loading N sites.

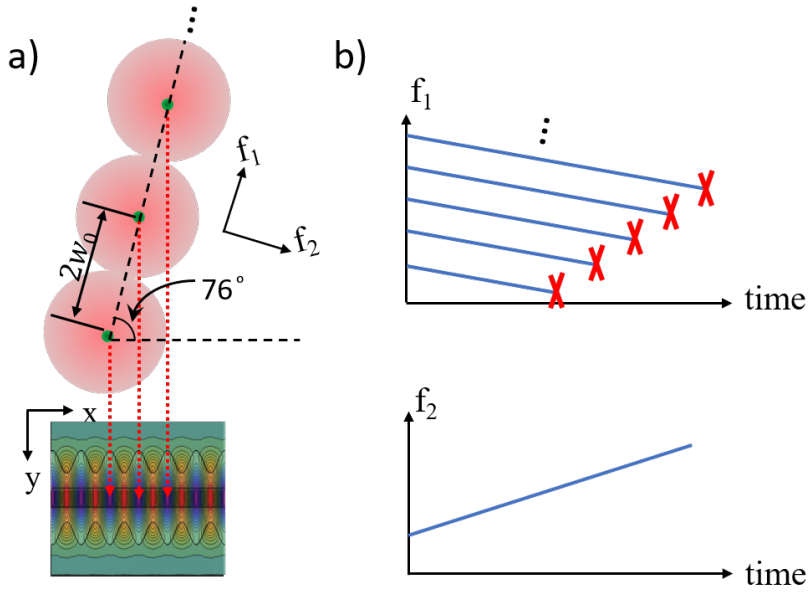

Figure 4.10: The proposal for loading the subwavelength z_1 lattice from 1D atom array. (a) The tweezer array is at an angle to the APCW so that the projection of tweezer focus positions are aligned to each trap site of the z_1 lattice. Here the axes of the two AODs are indicated by f_1 and f_2 and the red arrows indicate the moving path of the tweezer. For tweezer distance $d = 2w_0$, the angle is calculated to be $\simeq 76°$. (b) Illustration of RF-driving frequencies for AOD_1 (f_1) and AOD_2 (f_2) as functions of time during the transfer. The slopes of the frequency ramping in f_1 and f_2 are chosen to keep tweezer moving along the red dashed lines in (a). The red 'X' indicates the marked frequency tone is turned off at the time when the corresponding tweezer has reached the center of the APCW.

to keep tweezer moving straight towards the trap site (as indicated with red dashed lines in Fig. 4.10 (a)). The red 'X' markers in the AOD_1 frequency tones indicate the time when the corresponding tweezer has reached the center of the APCW and the corresponding RF power should be adiabatically tuned off. It is worth mentioning that for minimizing the impact to neighbor site atoms, it requires the free-space tweezer trap depth to be smaller than the blue air mode trap barrier to ensure the neighbor atom not be pushed into the $x = 0$ trap. Mathematically, this corresponds to $|U_{\text{tw}}(x = a/2, y = 0, z = z_1)| < U_{\text{blue}}(x = a/2, y = 0, z = z_1)$.

One can further reduce the footprint of the titled 1D tweezer array by creating a compact 2D tweezer array with the two AOD axes take an angle at $\theta = \arccos(a/d)$. For example, a 4 by $N/4$ free-space atom array can be used to load total N sites in the z_1 lattice, as shown in Fig. 4.11 (a). The corresponding frequency tones in time

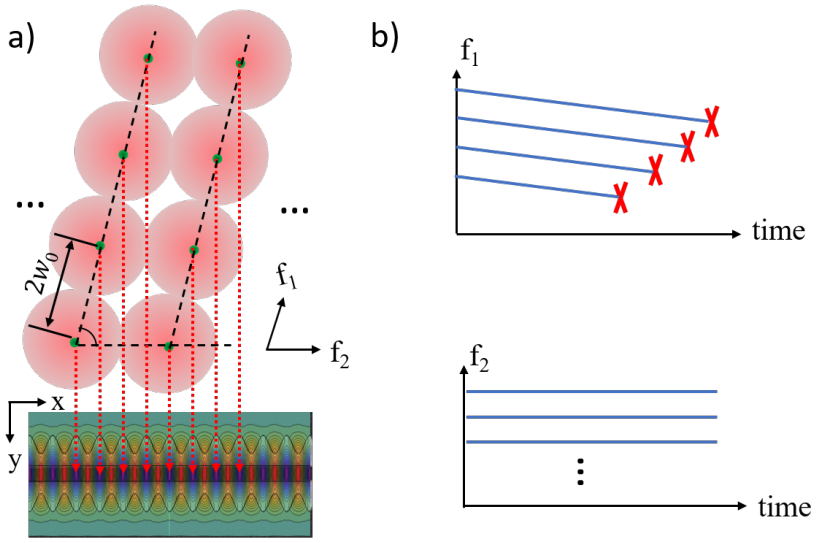

Figure 4.11: The proposal for loading the subwavelength z_1 lattice from 2D tweezer array. (a) Here the 2D tweezer array is generated by a pair of AODs with non-orthogonal axis as indicated by f_1 and f_2. (b) Illustration of RF-driving frequencies for AOD_1 (f_1) and AOD_2 (f_2) as a function of time during the transfer. Compared with Fig. 4.10 (b), the RF driving frequency for AOD_1 and AOD_2 are decoupled.

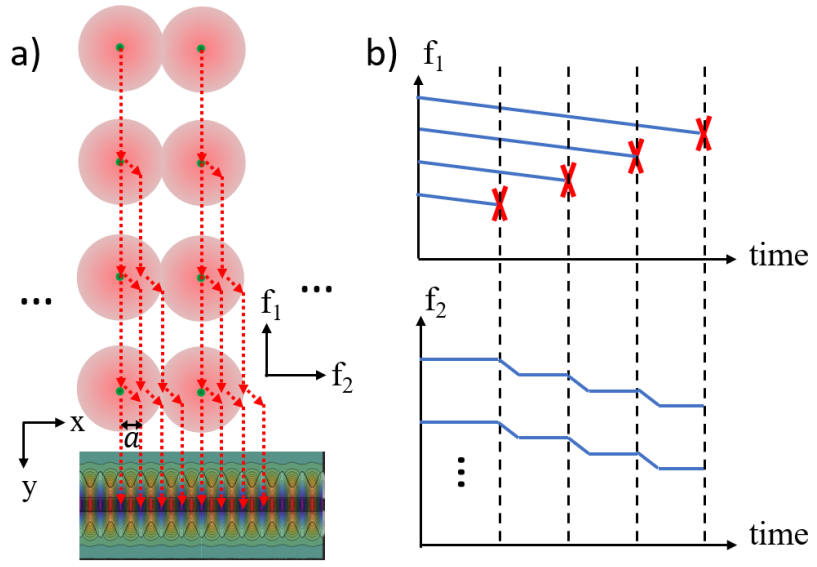

Figure 4.12: The proposal for loading the subwavelength z_1 lattice from 2D tweezer array by using time domain frequency programming. (a) Here the 2D tweezer array is generated by a pair of AODs with orthogonal axes as indicated by f_1 and f_2. The moving trajectory of tweezers are indicated with red dashed arrows. Note that transverse shift along x direction which are different from previous proposals. (b) Illustration of RF-driving frequencies for AOD_1 (f_1) and AOD_2 (f_2) as a function of time during the transfer.

are illustrated in Fig. 4.11 (b).

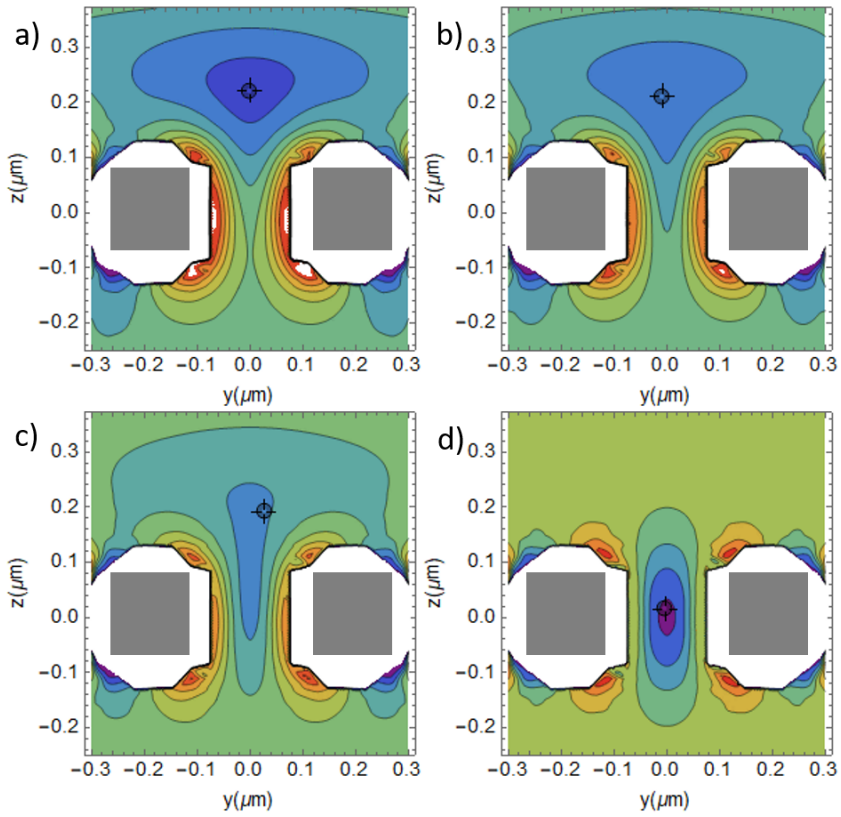

Figure 4.13: Transfer into the guided-mode trap by linearly ramping down the side-illumination power and linear ramping up the red-detuned dielectric guided mode power. (a-d) shows the combined trap profile in $y-z$ plane at (a) $t = 0$, (b) $t = 0.3t_f$, (c) $t = 0.6t_f$ and (d) $t = t_f$, where $t_f = 5$ ms is the total ramping time. The pointer indicates an example of the atom position in one snapshot.

Finally, a third method for loading a subwavelength z_1 lattice without rotating the free-space atom array is also proposed as shown in Fig. 4.12. Here the 2D lattice are generated by a pair of AODs with orthogonal axes and the loading into subwavelength arrays are achieved by shifting the frequency along x direction as the tweezer array moving towards the device, as shown in Fig. 4.12 (b). The advantage of this method is it does not require the 2D atom arrays to take a specific angle with respect to the PCWs and can be then generally apply to more complicated structures such as 2D photonic crystals.

Once atoms are transferred into z_1 lattice, one can further transfer them into the guided-mode trap described in Chapter 3. This is achieved by adiabatically turning off side-illumination traps and turning on suitable guided-mode traps as shown in

Fig. 4.13 for example [86]. It is worth mentioning that such transfer from z_1 trap to guided-mode trap can also apply to the case without the z_1 lattice, for example, a tweezer array with position aligned to the red-detuned dielectric mode positions.

Thus, till now, we have shown the basic steps from free-space atom array to fully loaded guided-mode traps.

4.4 Atom assembly on 2D nanostructures

In the previous section, we have shown the steps to transfer from free-space atom arrays to fully loaded subwavelength array in guided-mode traps for the APCW. In this section, we will show how the side-transfer technique can be applied to transfer to 2D photonic crystal devices as shown in Ref. [204] and also Chapter 2. Unlike the quasi-1D structures where atoms can be directly transfer to the target positions with one step side-transfer, the target position in 2D devices are typically far from the edge of the 2D slab. For this reason, transport for 2D devices requires the free-space assembled atoms first transfer to the edge of the 2D slab and then move to the target position inside the 2D photonic crystal. Following this logic, we split the transport of atoms in 2D devices into two separate problems, as shown below.

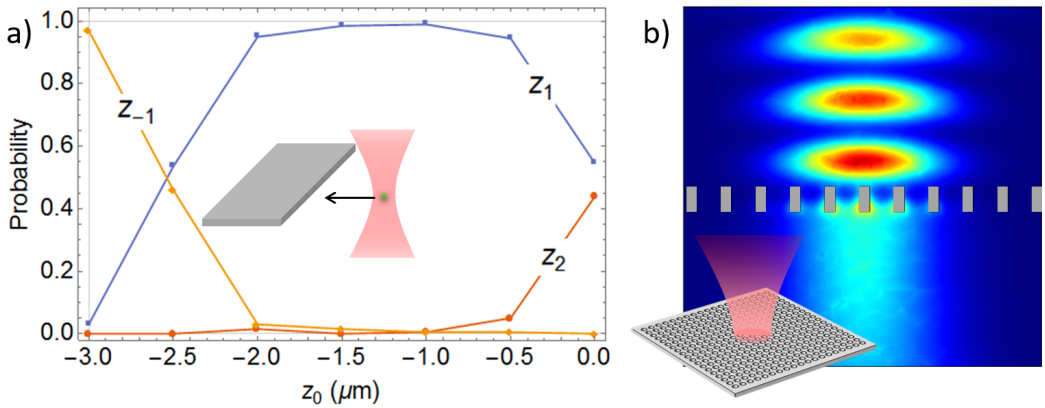

Figure 4.14: (a) Calculated transfer probability for transferring to an unstructured 2D slab with thickness $t = 200$ nm, based on Monte-Carlo trajectory simulation with atom initial temperature $T_a = 50$ μK in a 1 mK trap depth tweezer trap with waist $w_0 = 850$ nm. The tweezer polarization is parallel to the edge of the 2D slab. *Inset*: Illustration of the optical tweezer trap moving towards the 2D unstructured slab. (b) COMSOL®[45] simulated intensity profile in the $y - z$ plane for an optical tweezer with $w_0 = 850$ nm aligned to the 2D square photonic crystal slab with parameters defined in Ref. [204]. *Inset* shows the illustration of an optical tweezer aligned to the 2D square photonic crystal slab.

First, we investigate the transfer of atoms from free-space to the edge of an un-

structured 2D slab, as indicated in the inset in Fig. 4.14 (a). From the Monte-Carlo simulation of atom trajectories, we calculated the transfer probability into the reflective traps on an unstructured slab under different tweezer focus z positions, as shown in Fig. 4.14 (a). This produces similar results as in the case for transferring to the APCW (Fig. 4.4 (c)) under the same initial parameters, with the simulated transfer probability into z_1 trap $p > 95\%$ under a wide range $|\Delta z| \sim 2\ \mu$m.

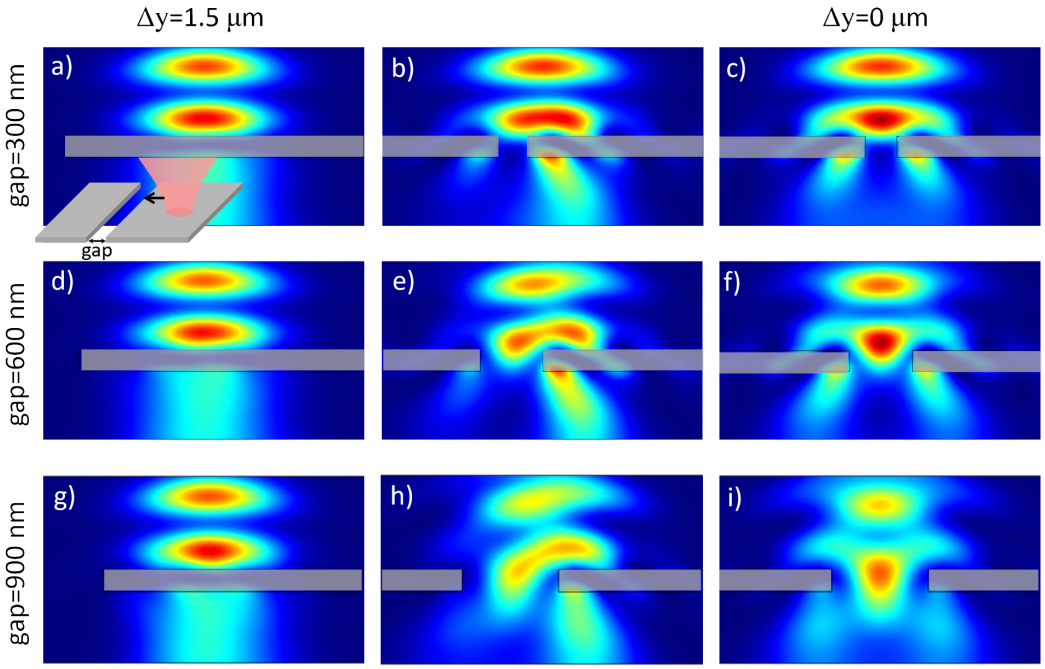

Figure 4.15: The simulated intensity profile for an optical tweezer with waist w = 850 nm and focus on the surface of a 2D SiN slab (200 nm thick) with different gap size. The optical tweezer is moving across the gap as illustrated in the inset in (a). Here (a-c) are for gap size 300 nm, (d-h) are for gap size 600 nm and (g-i) are for gap size 900 nm. The first column (a, d, g) corresponds to tweezer focus position 1.5 μm away from the gap center and the last column (c, f, i) corresponds to tweezer position aligned to the center of the gap. Center column corresponds to the position where the z_1 trap splits with two intensity maxima.

After the atom is transferred to the z_1 trap above the unstructured slab, it needs to be further transfer to the target position on the photonic crystal slab. Before investigating the transport on 2D slabs, we first make sure that when the tweezer is aligned to the 2D photonic crystal slab, a stable z_1 trap can be formed without unwanted deformations as shown previously for double-nanobeam waveguides (Fig. 4.6). Fig. 4.14 (b) shows an example of the simulated intensity profile for an optical tweezer with waist w_0 = 850 nm, aligned to the 2D square lattice with holes of radius r = 103

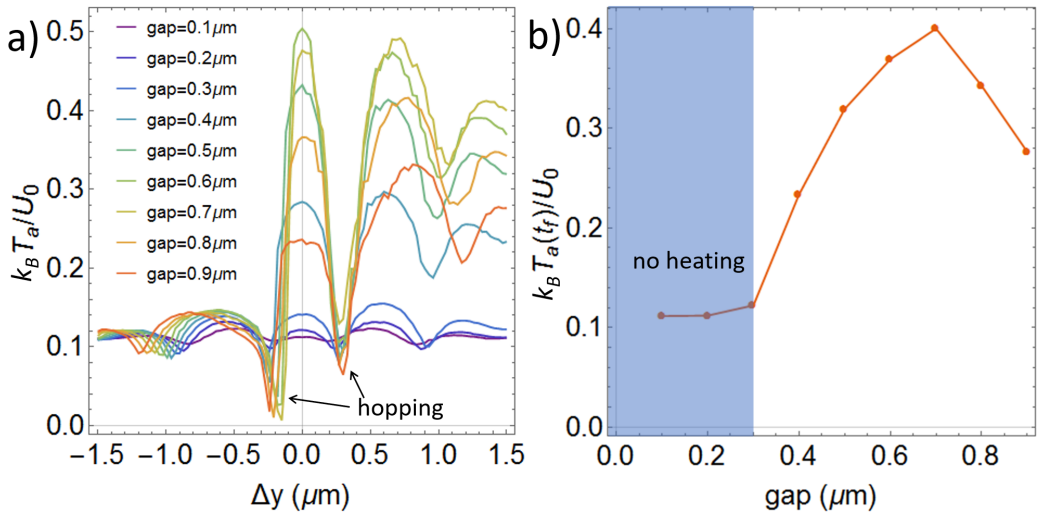

Figure 4.16: (a) The calculated trapped atom temperature (normalized by free-space tweezer trap depth $U_0 = 1$ mK) as the tweezer moves from $y = -1.5$ μm to $y = 1.5$ μm with the gap center at $y = 0$. Here the trapped atom temperature is inferred from Monte-Carlo trajectory simulations. For large gap size (gap> 300 nm), the positions of atom hopping from one local trap minimum to another minimum is indicated with arrows. (b) The trapped atom final temperature at position $y = 1.5$ μm as a function of gap size. The blue shaded area represents the region where there is no significant heating after crossing the gap.

nm and lattice constant $a = 290$ nm. The reflective trap has very similar shape to the one on a unstructured slab (shown in Fig. 4.15 (a)). This similarity is due to the hole size on the 2D slabs are smaller than the half wavelength $\lambda/2$. Intuitively, the tweezer samples effectively an unstructured dielectric material with an effective reflective index (lower than the real unstructured material). To further understand the z_1 trap deformation during the transport on the 2D slabs, we simulated the process of an optical tweezer moving across an air gap on the 2D slab with different gap size (as indicated in the inset in Fig. 4.15 (a)). The simulated intensity profiles for different gap size and at different positions are summarized in Fig. 4.15 with three rows here correspond to different gap size (gap=300, 600 and 900 nm) and columns correspond to the tweezer at different positions with respect to the gap. First, when the tweezer is aligned to the center of the gap (Fig. 4.15 (c, f, i)), the z_1 trap has one single intensity maximum but with an additional shift in z position as the gap size become wider. Further, by comparing the plots in the middle columns (Fig. 4.15 (b, e, h)), we find that for gap=600 nm and 900 nm, the z_1 trap splits into two local intensity maxima. This splitting can be a problem for atom transport and will lead to heating to the trapped atoms or even atom loss.

To evaluate the impact of the z_1 trap deformation to atom transport, we performed a Monte-Carlo atom trajectory simulation as the optical tweezer moved across the gap, for atom initial temperature of 100 μK. The extracted atom temperature as an function of tweezer position for different gap sizes is summarized in Fig. 4.16 (a). Here the gap center position is at $y = 0$ and around the gap center position, we observed two hopping positions (indicated two arrows) as the trapped atom hopping from the surface z_1 trap to the gap z_1 trap and then hopping back again to surface z_1 trap. After the first hopping (from surface z_1 trap to gap z_1 trap), the atom temperatures increase. To visualize the overall heating effect during the transport, the final temperature at position $y = 1.5$ μm is plotted in Fig. 4.16 (b) under different gap size. Here, we can identify that for gap size smaller than 300 nm, there is no significant heating as the optical tweezer moving across the gap. However, for gap size larger than 300 nm, we observed a significant heating effect as the gap getting larger with the heating effect peaks at gap=700 nm.

This heating effect can be understood from the simple hopping model illustrated in Fig. 4.17. The splitting of trap centers creates a trap barrier U_0 between two local trap minimum. Initially, for an atom with kinetic energy E smaller than the barrier U_0, the atom is localized in one trap minimum as illustrated in Fig. 4.17 (a). However, as the tweezer moves more towards the gap center (here corresponds to the left trap minimum), the right trap become shallower and at an critical position $U_0 - E = |U_L - U_R| = \Delta U$, the atom will hop into the left trap and gain kinetic energy ΔU, as illustrated in Fig. 4.17 (b). The total kinetic energy for atom in the left trap is $E' = E + \Delta U = U_0$, which is exactly the trap barrier (independent of atom initial energy E, if $E < U_0$). This model is consistent with the intensity profile simulation in Fig. 4.15 (b). For gap=300 nm, there is no apparent heating as the trap is not split. However, for gap=700 nm, the trap splitting has the largest barrier and thus leads to largest heating in atom temperature. The heating analysis from the z_1 trap deformation perspective suggests for dimension smaller than 300 nm, the heating impact should be negligible. This is typically the case for 2D square lattices where the air hole diameter is close to 200 nm, when aligned to Cs transitions. We would like to emphasize that in the model described in Fig. 4.17, the hopping heating is a 'one-time' heating, that is, if one further reduce the trap depth of the left trap while lower the trap depth of the right trap, the kinetic energy of the atom is still E' as long as the barrier is the same. This corresponds to the second hopping as indicated in Fig. 4.16 (a) when atoms 'hop' out from gap z_1 trap into surface z_1 trap when the tweezer moves away from the gap. Thus, we expect the heating effect

described here will not accumulate when tweezer moves over multiple gaps (when they are separated far enough without additional interferences).

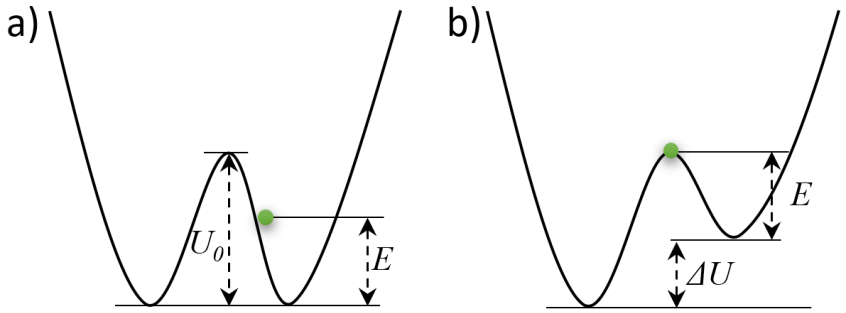

Figure 4.17: The basic heating process for hoping between trap local minimums. (a) For an atom with kinetic energy E smaller than the barrier U_0, the atom is localized in one trap minimum. (b) When the right trap is continuously lifted up, at an critical position $U_0 - E = |U_L - U_R| = \Delta U$, the atom will hop into the right trap and gain kinetic energy ΔU and the total kinetic energy is $E' = E + \Delta U = U_0$.

Finally, it is worth mentioning that additional oscillations in atom temperature in Fig. 4.15 are due to the change of trap depth which is a result of interference with scattering light near the gap. In the actual 2D photonic crystal slabs, this trap oscillation may generate additional parametric heating when the time crossing one unit cell is close to the period of atom oscillation in the z_1 trap.

After transport to the target position in 2D photonic slab, one can further transfer to the guided-mode trap generated from 2D photonic crystal guided modes. The process should be very similar to the case in the APCW. For simplicity, we skip this discussion here.

4.5 Summary and outlook

As a summary, in this chapter, we have presented a general analysis of atom assembly on nanophotonic structures. Attaining deterministic atom arrays, in the spirit of recent worldwide advances with free-space tweezer arrays [16, 57, 105, 181], will allow us to probe the physics of strong, photon-mediated interactions between many atoms, as well as atom-mediated interactions between photons.

With the full control of the atom number and position with optical tweezers, we expect to have the ability to observe many new experiments. For example, for operating with the Cs frequency within the bandgap, the authors of Ref. [11] project the ratio R of coherent 'spin' exchange J_{1D} to incoherent guided-mode loss Γ_{1D}

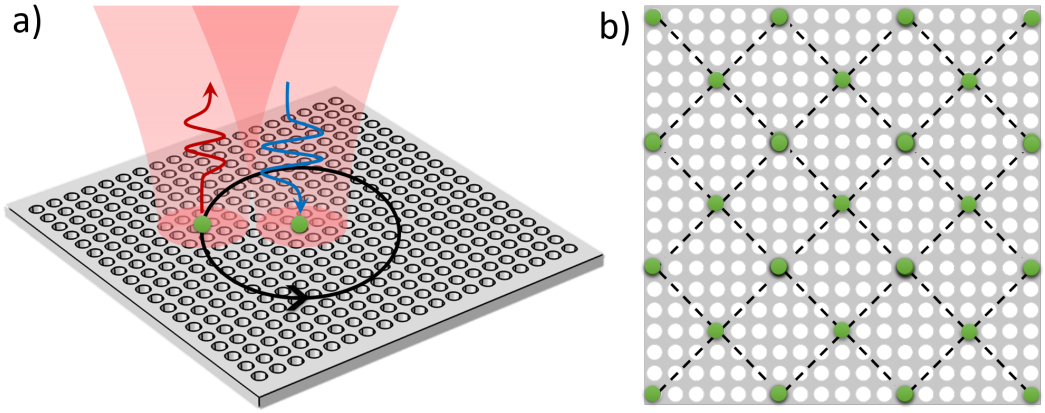

Figure 4.18: Possible investigations with optical tweezer arrays on a 2D square photonic crystal slab. (a) An example of experiments involves two atoms, the 'emitter' and the 'probe' atoms. The 'emitter' atom is excited through by a π-pulse (indicated with blue curves) the optical tweezer and the fluorescence (red curves) is collected for the 'probe' atom due to atom-atom interactions. By moving the probe atom around the 'emitter' atom from trial to trial (as indicated by black circle) and recording the fluorescence counts, one could map the anisotropy of the 2D Green's function for atom-atom interaction on the 2D slab. (b) By transferring a 2D square lattice tweezer array to the 2D square photonic crystal slab, one could observe the evolution of the 2D atomic network with programmable atom-atom interactions.

to be $R = J_{1D}/\Gamma_{1D} \simeq 20$ at a detuning of 20 GHz from the band edge, with the possibility to observe coherent spin-exchange oscillations between two proximal atoms trapped within the SPCW shown in previous chapter [11]. To achieve such an advance would require a) the capabilities described in this chapter for placing two tweezer-trapped atoms precisely along the SPCW, transfer from the tweezer traps to guided mode traps within the vacuum gap for 5× increased coupling rate, and c) a next generation PCW such as the SPCW.

Furthermore, switching to 2D nanophotonic structures offers many new opportunities such as anisotropic emissions [72, 204], Markovian and non-Markovian dynamics [70] and topological quantum optics [147]. An example of a basic experiment can involve only a pair of atoms in two tweezer traps near the surface of the 2D photonic crystals, as shown in Fig. 4.18 (a). The anisotropic character of 2D photonic bands for photonic crystal structures described in Ref. [204] could be mapped by exciting one 'emitter' atom and monitoring the fluorescence counts from another neighbor 'probe' atom. By varying the relative angle and distance between the 'emitter' and 'probe' atoms, we could measure the anisotropic emission of 'emitter' atom and from that infer the spatial information of the 2D Green's function as

described in Ref. [11]. With the formation of 2D atom arrays on the square lattice described in Ref. [204], one can observe the evolution of the 2D atomic network with programmable atom-atom interactions.

Chapter 5

THE NEW APPARATUS FOR INTEGRATION OF OPTICAL TWEEZERS AND NANOPHOTONICS

Nanophotonic structures offer the intriguing possibility to control interactions between atoms and photons by engineering the medium properties through which they interact [40, 124]. Opportunities beyond conventional quantum optics thereby emerge for unconventional quantum phases and phenomena for atoms and photons in one and two-dimensional nanophotonic lattices [52, 71, 204]. While several important experimental milestones [33, 67, 68, 86, 164, 182, 184] have been reached, the experimental progress has generally lagged theory in combining ultracold atoms and novel nanophotonic devices. The simple reason behind experimental difficulty is that cold atoms naturally prefer free-space and vacuum. The presence of dielectric materials and the supporting structures typically deteriorate the vacuum system, deflects and scatters the cooling light beams and adsorb cold atoms with their strong surface forces. All these result in the difficulty of loading and trapping of cold atoms near the nanophotonic structures. In this chapter, we present our design and experimental progress on the integration of optical tweezers and nanophotonics. Through a series of technical innovations, namely 1) a vacuum-compatible silicate-bonding technique, 2) a free-space coupling with 'Y-couplers' and 3) efficient loading and transport of tweezer array with single atoms, we developed a new apparatus that overcame several important experimental limitations and challenges, making a significant step towards atom assembly near nanophotonic structures.

The work described in this chapter is largely based on Refs. [19, 125]. It represents a group effort where each individual inside QOG has made critical contributions to this work. Starting from June 2018, Zhongzhong Qin, Jean-Baptiste Béguin and I set up the laser systems and built the vacuum systems where we achieved efficient atom delivery to the science cell. Later, with the joining of Alex Burgers from Lab 2 in November 2018, Alex and I worked together on the single atom loading into tweezer arrays and atom transfer to the APCW device. Independently, Jean-Baptiste Béguin adapted the silicate-bonding technique used in LIGO into our system with glass cells. Jean-Baptiste and Zhongzhong also contributed to improve the free space coupling efficiency into the chip with the new 'Y-coupler', designed and fabricated by Su-Peng Yu. My advisor Prof. Jeff Kimble supervised

all these activities and contributed his rich experimental expertise and innovative ideas throughout the whole research project.

5.1 Introduction

With the challenges from previous generation of setup in mind, in this chapter, we describe an new generation of apparatus that provides several significant advances relative to prior technical capabilities, which are summarized as follows:

1. Silicate bonding – We have previously used large manipulators inside conventional stainless steel chambers for mounting our silicon chips illustrated in Fig. 5.1 (a). This method posed several limitations in our previous experiments [33, 67, 68], including mechanical and thermal instability, complexity in fiber alignment and assembly, and limitations on baking temperature and out-gassing due to various epoxy resins and bonding agents used for "gluing" optical fibers to silicon chips and chips to vacuum mounting hardware. Following discussions with Jun Ye and John Hall at JILA, we have developed a new platform to mount our chips in vacuum. As shown in Fig. 5.1 (b) and also described in detail in Section 5.2, we now bond a Si chip to an SiO_2 substrate by way of silicate bonding that we have developed in our group (with significant input from a LIGO research team at Caltech). This bonding technique has extremely low out-gassing properties compared to our previous chip mounting configurations and enables high temperature baking of our vacuum cell for ultra-high vacuum (UHV) operation.

2. A new generation of PCWs – We have developed optical chips that eliminate fiber optics within the vacuum chamber, achieve more efficient coupling of light into and out of our PCWs, increase power handling capabilities by twenty fold to facilitate long-lived guided-mode optical traps [92], and enable high-temperature baking for improved atom trapping times [202]. All of these goals have been met by way of the design and fabrication of devices that utilize free-space optical coupling whereby input laser light is coupled from outside the vacuum chamber directly into individual PCWs. As described in Section 5.3, we have removed the need for in-vacuum fibers by designing and fabricating a new Y-coupler at the terminating ends. The silicon chip also has a significantly reduced footprint necessitated by having the terminating Y-couplers much closer to the edges of the silicon chip to allow free-space coupling for NA $\sim 0.1 - 0.2$ of the new Y-couplers [202].

3. A new laboratory – Free-space coupling and silicate bonding have enabled the construction of a new laboratory in the QOG at Caltech, which is built around

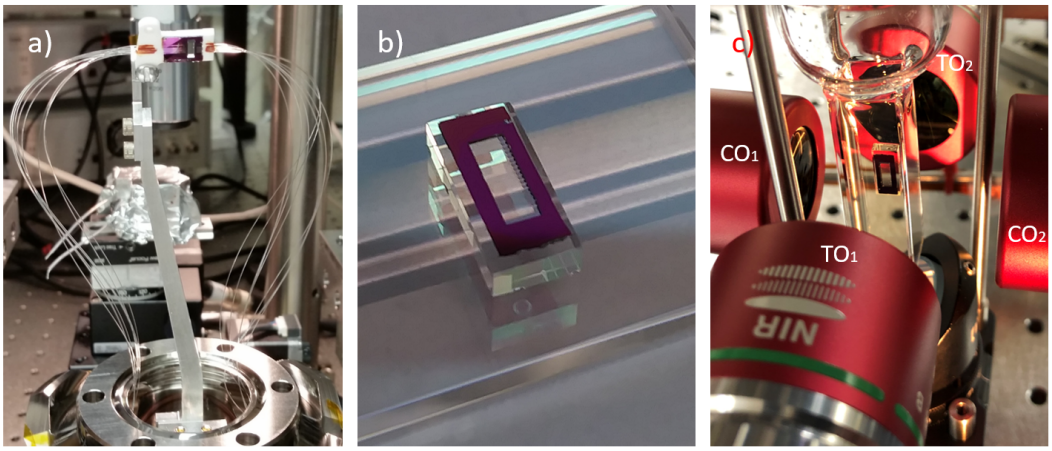

Figure 5.1: The old (a) and new (b,c) ways of integrating nanophotonic chips with cold-atom vacuum systems; (a) scale for old system is set by 2.75" flange to connect to conventional 6" diameter vacuum chamber with chip (top of figure) then centered in chamber. For more details, see Chapter 6 and Fig. 6.4 in Ref. [171]. (b) New system with silicon chip of 4 mm width mounted on a SiO_2 'optical table' of dimensions 5×11×2 mm. For more details, refer to Section 5.2. (c) The assembled system in a SiO_2 glass cell of internal dimension 1×1×4.5 cm (rectangular part), surrounded by two coupling objectives (CO_1 and CO_2 with $NA = 0.4$) for free-space optical coupling to PCWs and two tweezer objectives (TO_1 and TO_2 with $NA = 0.4$) for generating optical tweezer traps and imaging [19].

a vacuum envelope reduced in size by approximately a factor of 10^2 to reach a volume ~ 10 cm^3 with unprecedented optical access relative to our prior chambers, as shown in Fig. 5.1 (c). We aim to achieve nanoscopic lattices of atoms that are assembled deterministically with arrays of single-atom tweezers and that are coupled to guided modes (GMs) of PCWs for efficient atom-photon coupling along the PCW and of GM photons to and from free-space. As described in Section 5.4, our experiment is in the spirit of recent worldwide advances with free-space tweezer arrays [16, 57, 105, 181] but adds the significant complexity of assembling such atomic arrays near the surfaces of 1D and 2D PCWs.

A general summary of our advances is provided by Fig. 5.1, which shows our 'old' [130, 171, 202] and 'new' [19] systems side by side. Of course, small glass cells with volume ~ 1 cm^3 for various optical trapping schemes have been employed by various groups for many years [5]. But to our knowledge, no group has succeeded to implement a compact setup as in Fig. 5.1(b, c) when the difficult constraints of localization of atoms near PCWs have been part of the setup [19].

5.2 Silicate bonding

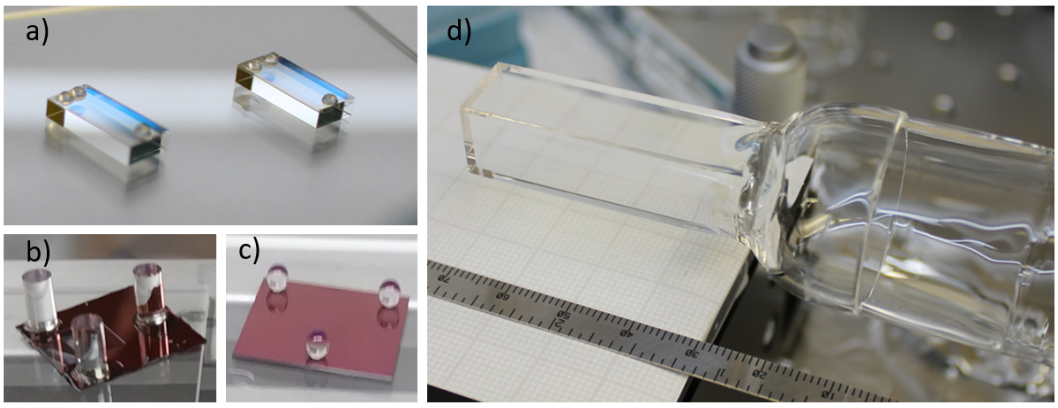

Figure 5.2: Photographs of (a) SiO_2 polished rectangular tables (5×11×2 mm) with three SiO_2 hemispheres silicate-bonded onto the AR-coated table surface, (b) Three parallel SiO_2 cylindrical rods with diameter 1 mm and length 2 mm individually bonded on flat cross-section to an APCW Si chip, (c) Three SiO_2 spheres (diameter 1.5 mm) bonded to a blank 1×1 cm square silicon chip, (d) SiO_2 glass chamber with external AR-coating on all 5 surfaces of the rectangular glass cell with 1.25 mm wall thickness, internal square cross-section 1×1 cm and length 4.5 cm. A Quartz to Pyrex graded seal (internal diameter 2.54 cm) is fused via a cup (for coating protection) to the rectangular cell, for chamber bake-out temperatures up to 400 K.

In previous atom-nanophotonic experiments [33, 67, 68, 86] in the QOG at Caltech, the nanophotonic chips were held inside a stainless vacuum chamber by a long mechanic manipulator (∼ 10 cm) with input-output fibers pre-aligned and glued in the V-groove on chip [200], as shown in Fig. 5.1 (a). This posed three major limitations in our previous experiments: 1) The long mechanical arm did not have sufficient mechanical stability, thereby limiting the ability for precise positioning of atoms on nanophotonic structures and dissipation of guided mode heating power. 2) Fiber coupling of light into and out of the chip involved cumbersome fiber pre-alignment and gluing outside the vacuum chamber, and the number of devices (8 APCWs) that could be coupled was limited by failure probability and the number of vacuum feedthroughs available (8 input plus 8 output fibers). Furthermore, once the chip was inside the vacuum chamber, the coupling efficiency could not be further adjusted or optimized. 3) The usage of UHV compatible epoxy for gluing fibers and the chip prohibited the possibility of significantly baking the entire vacuum chamber. As a result, the typical lifetime for atoms trapped near (∼ 300 μm) the chip was limited to be $\lesssim$ 100 ms [68].

Here, by adapting the silicate bonding method [189] whose reliability was demon-

strated in NASA and ESA astronomical satellite missions (e.g. Gravity Probe B and The LISA Pathfinder) and current LIGO instruments, we are now able to overcome these limitations by mounting the nanophotonic chip inside a glass cell with small footprint that is compatible with free-space coupling from microscope objectives outside the vacuum cell. This largely eliminates the relative motion between chip and vacuum chamber, and also the need of all optical fibers within the vacuum envelope.

The hydroxide catalysis bonding method of Ref. [77] involves strong chemical bonds between oxidizable materials such as SiO_2 and Silicon. Such chemical bonds can be formed at room-temperature. Optically, silicate bonding provides a transparent bond, the refractive index of which between two SiO_2 surfaces, converges to the index of SiO_2 [128] thereby minimizing Fresnel reflections from the bonded surfaces and allowing low-loss optical transmission through the bond. AR-coated glass surfaces can also be silicate bonded if terminal layers of SiO_2 are deposited on the surfaces to be bonded. Silicate bonding allows UHV operation, which is an important requirement for research involving trapped cold atoms near surfaces inside a vacuum chamber. The operating temperature for components secured by silicate bonding ranges from cryogenic to beyond typical bake-out temperatures for UHV chambers (i.e., 300 – 400 K). Because of the UHV compatibility of silicate bonding and the small footprint of the glass cell, a vacuum pressure of $\sim 10^{-11}$ Torr is achieved after the first baking of the entire vacuum setup, as compared to $\sim 10^{-9}$ Torr in previous work.

Turning then to the steps for achieving a mounted silicon chip by way of Silicate bonding, we show in Fig.s 5.2 and 5.3 photographs of various stages of the sequence. Fig. 5.2 (a) shows the glass tables upon which 200 μm thick (4×9 mm) silicon chips will be bonded via three effective contact surfaces as in (b-c) using rods and spheres as well as hemispheres in (a). Here we consider the case of hemispheres for which three SiO_2 hemispheres are first bonded onto a SiO_2 rectangular optical table. The curved caps of the hemispheres are then flat polished to better than $\lambda/10$ over a circular area of diameter $\sim$ 0.8 mm, defining a precision plane (to within 100 nm) for next bonding the silicon chip to the flat tops of the polished hemispheres and hence to the optical table. The table-chip assembly is then itself bonded to the inner wall of a precision Fused Quartz glass cell fabricated by Starna [96] shown in Fig. 5.3(e). It should be noted that the rectangular optical table is AR-coated on its outer side (i.e., facing into the glass cell), while the glass cell is AR-coated on its

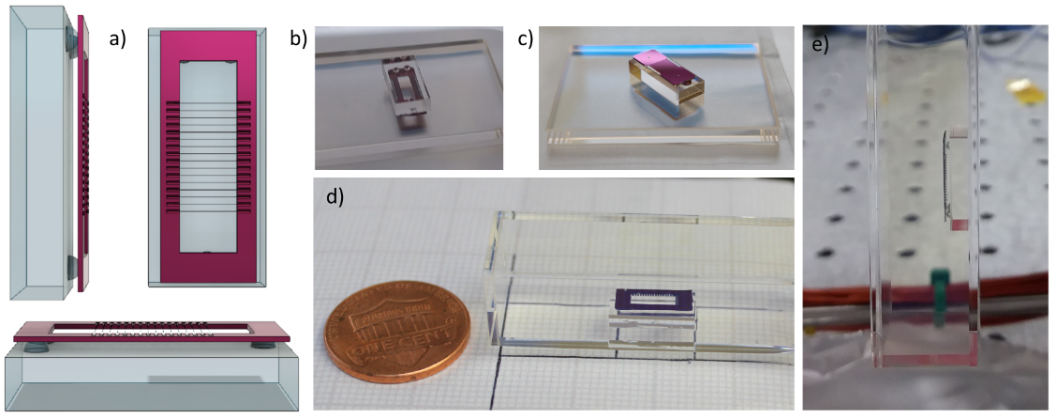

Figure 5.3: (a) 3D model drawings of Fused Silica glass table assembly with silicon chip with three different perspective views. (b,c,d,e) Photographs of table assembly during construction and inside coated vacuum glass cell. (b) The weight of the glass table with hemispheres is used during bonding to the Si-chip frame. (c) Example photograph of a window-less Si-chip bonded to the glass table. (d,e) The small chip-table assembly is finally bonded onto one inner wall of the rectangular glass cell.

outer surface but not inner.

We recall that the nanophotonic structures are e-beam written into a 200 nm sacrificial layer of silicon nitride deposited on the 200 μm thin Silicon substrate [200], so that considerable care is required to avoid damage to the surface containing the devices. Without the use of additional optical elements, the bare divergence angle of the light emerging from the nano-waveguides ($NA \sim 0.15$, as in Ref. [202]) requires elevating the chip base from any surface and to position it in relation to the glass cell geometry to avoid clipping loss.

5.3 The Y-coupler technology

In this section, we present a description of the new "Y-coupler" design which provides efficient free-space coupling, minimal light scattering and better mechanical stability. This design extends the maximum power by roughly 20x beyond the failure power for our previous fiber butt-coupled devices [200] which was a major limitation in our previous atom-nanophotonic experiments [33, 67, 68] for achieving long-lived guided-mode atom trapping at magic wavelengths [92, 199] as previously demonstrated in the optical nanofiber system [66, 191].

The chip design in this work is an adaptation of the system presented in Ref. [200] to enable direct free-space coupling from an objective into the waveguides. The

devices are fabricated from a 200 nm silicon nitride device layer, suspended from a 200 μm Silicon substrate. Precision grooves aligned to the waveguide device layer are etched into the substrate, to enable cleaving of the chip for clearance for free-space beam inputs and outputs. The absence of terminated optical fibers in the vicinity of the waveguide input coupler widens the design space available for coupler designs. Here, we present a Y-coupler design that simultaneously optimizes transmission, suppresses residual reflection, and provides mechanical stability [202]. In order to mode-match the guided mode of a photonic waveguide to a Gaussian beam, we taper the waveguide width to $\simeq$ 130 nm, before terminating the waveguide and launching the mode. The terminated end of the suspended waveguide is affixed to the substrate through two $\leq$ 100 nm wide tethers. Conventionally, the tethers are simply arranged perpendicular to the waveguide [200], as shown in the SEM image in Fig. 5.4 (a) (i). Two issues arise from such tethering design. First, the tether pair is polarized by the guided mode light, creating scattering and back-reflection that are undesirable. Second, the tethers are perpendicular to the waveguide, therefore releasing the tensile stress on the waveguide, potentially making the tapered section of the waveguide mechanically pliable. At high optical power, the waveguide-tether junction is observed to produce fluctuating scattering intensity prior to mechanical failure, which we attribute to thermally-induced stress distributions causing physical movements of the junction. These pose a significant constraint for achieving guided-mode traps at magic wavelengths for Cs with a typical power handling $\sim$ 10 mW, well beyond the $\sim$ 0.5 mW limit found for conventional couplers in Refs. [43, 200].

To overcome this limitation, an unconventional Y-shaped termination of the free-standing end of the waveguide was designed in joint consideration of mechanical and optical properties, as shown in Fig. 5.4 (a) (ii). The termination ends of the suspended waveguide need to be mechanically affixed to the substrate with tethers. By tilting the tethers away from the tapered waveguide, a controllable weak tensile stress can be maintained on the waveguide and tethers to make them mechanically robust. Optically, the tethers are tilted away from the electric field vector of the incoming mode, reducing the polarizability of each tether. This effect, in addition to the partial cancellation of the polarization vectors of the two tethers, reduce the total polarizability of the junction, therefore reducing the scattering loss due to the tethers, as shown in Fig. 5.4 (b) (i) and (ii) with vectorial illustrations for conventional coupler with 90° tethers and the Y-coupler, respectively. In practice, a tilt angle of 60° from perpendicular was chosen from FDTD optimization [126]. The simulated field pattern of a Gaussian beam incident on the junction from below is shown in

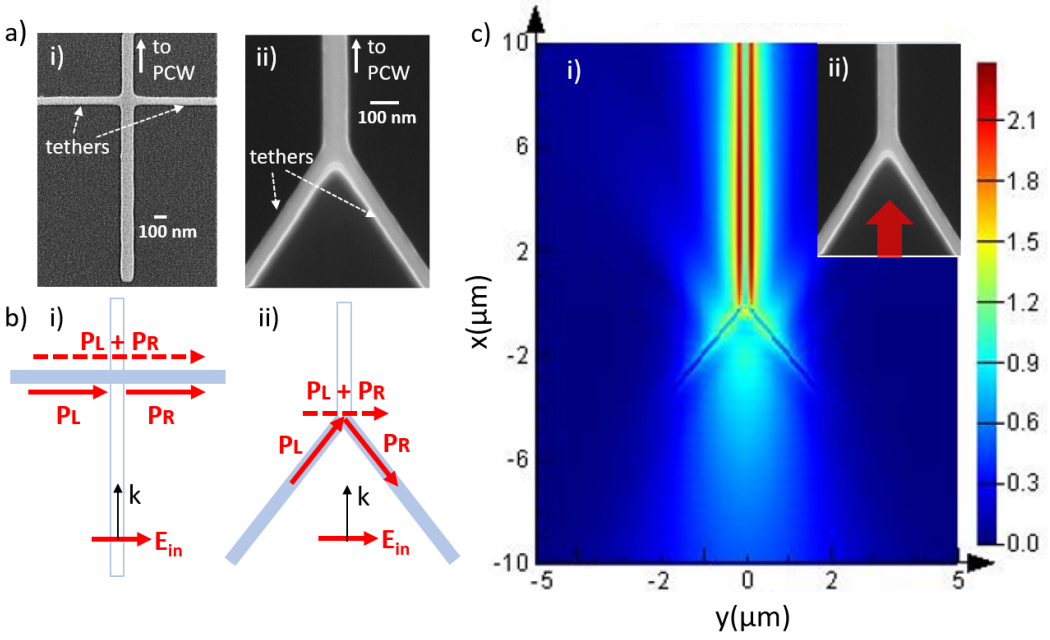

Figure 5.4: (a) SEM images of the coupler with conventional 90°tether termination (i) and the Y-coupler (ii) (b) Vectorial illustration of the polarizabilities on tethers shows the working principle for the coupler with conventional tether termination (i) and the Y-coupler (ii). (c) FDTD simulation of wave propagation in Y coupler for an incident Gaussian beam propagating from the bottom to the top of the figure. Insert is a SEM image of device under simulation with the Gaussian mode input indicated as a red arrow.

Fig. 5.4 (c). Coupling efficiencies of a $1/e^2$ waist $w_0 \sim 2.5$ μm beam with different input polarizations to different couplers are calculated from FDTD simulations and are summarized in Table 5.1. It suggests that, the Y-coupler has a better performance than conventional couplers in terms of Gaussian-beam-to-waveguide transmission (87% vs. conventional 79%) and reflection (< 0.1% vs. conventional 2.7%) for input polarization along y direction (TE), which is critical for quantum correlation measurements in nanophotonics [67]. In experiment, we have measured a coupling efficiency up to 80% for TE input using the Y-coupler design [19].

Table 5.1: **FDTD simulated transmission and reflection efficiencies for different couplers**

Type	TE Transmission	TM Transmission	TE Reflection	TM Reflection
with 90° tethers	79%	65%	2.7%	0.6%
with Y-shape tethers	87%	56%	< 0.1%	< 0.1%

In Fig. 5.5, we show measurement data asserting the power handling capability of the devices with the free-space coupling and Y-coupler design strategy. Fig. 5.5 (a)

shows the optical power transmitted by the device as a function of the input power for light propagating in the TE mode with a magic wavelength for Cs atoms at 935.7 nm. The new design allows a measured 20-fold increase (from ~ 0.5 mW to ~ 10 mW) in the maximum optical light power before breaking or irreversible damages as compared to our previous devices with the butt-coupler design [200]. This should enable long-lived guided-mode atom traps by way of higher intensities required for larger atomic detunings, including for magic-wavelength traps [92, 199].

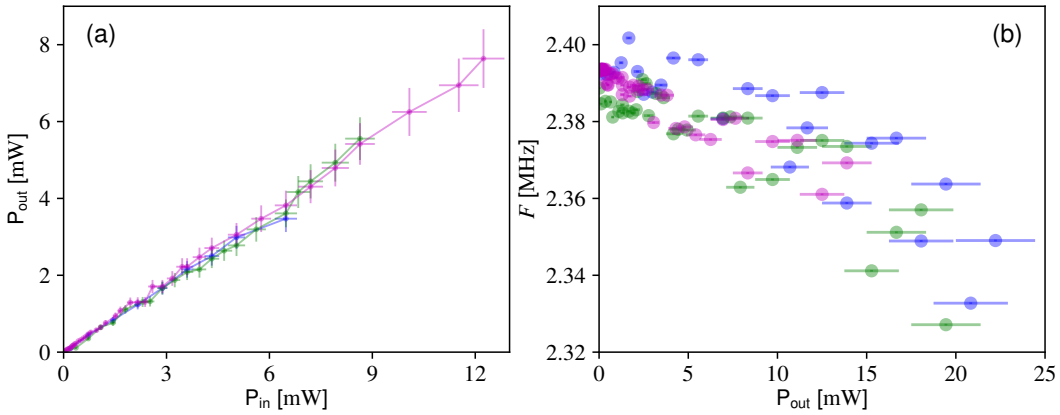

Figure 5.5: (a) Measured output light power P_{out} versus input light power P_{in} for optical light field propagating in the TE mode with vacuum wavelength 935.7 nm and chamber pressure of $\sim 3 \times 10^{-10}$ Torr. (b) Fundamental mechanical frequency of the differential in-plane mechanical mode of APCW as a function of output light power. Different colors correspond to different nanophotonic devices on the same chip.

While the detailed physics of device failure and plastic deformation is beyond the scope of this article, we show in Fig. 5.5 (b) a measurement of the dependence of the mechanical frequency of the fundamental differential in-plane mode of motion of the APCW as a function of the output light power. Devices physically break at $P_{\text{out}} \sim 20$ mW. At the very low powers, the quasi-linear decrease in frequency is compatible with a simple model of reversible thermal elongation of a highly stressed string. At the highest powers before failure, the frequency shift would amount to a relative physical elongation and equivalent strain of ~ 0.04, compatible with typical ratios of the yield strength of silicon nitride to its Young's modulus. More detailed discussion on mechanical vibrations of the APCW will be presented in Chapter 7.

5.4 Single atom trapping in a tweezer array near PCWs

One of the key challenges in atom-nanophotonic experiments is to achieve efficient loading of atoms into guided-mode traps formed on the nanophotonic structures. Given the small guided-mode trap volume and strong Casimir-Polder potential near the dielectric surfaces, it was shown in Ref. [33, 67] that direct loading of background Cs atoms into the APCW guided-mode traps is very difficult. Trapping few atoms *in a single trap* $\sim$ 130 nm above the APCW surface is demonstrated in Refs. [68, 86] by reflecting a waist $1/e^2$ $w_0 \sim 60$ μm dipole trap beam (the so-called side-illumination beam). However, the average trapped atom numbers $\bar{N}$ is restricted to $\sim$ 3 atoms and the trap size along the APCW is $\sim$ 10 μm (along the x direction as in Fig. 1.4 (a)), corresponding to $\sim$ 27 unit cells [68]. Therefore, it was not possible to have precise positioning of individually trapped atoms and full control of their photon-mediated interactions. By adapting techniques developed in free-space 1D, 2D and 3D atom assemblies in optical tweezer arrays [16, 17, 57], our goal here is to achieve efficient atom assembly on the PCWs with each single atom precisely positioned with respect to the nanophotonic structures as in Fig. 1.4. In this section, we present a description of the experimental protocol for trapping single atoms in a 1D tweezer array near PCWs with our advanced apparatus.

Loading single atoms into an optical tweezer array

As shown in Fig. 5.6 (a), our apparatus consists of two vacuum glass cells named source cell (top) and science cell (down) in a top-down configuration which is parallel to the gravity direction. The experiment cycle starts with the loading of a MOT from background, room temperature Cs vapor in the source cell for a duration $\sim$ 1 s. With $\sim 10^7$ atoms loaded into the $\sim$ 2 mm effective diameter MOT, we then perform a 10 ms PGC [133] to cool the dense atom cloud to $\sim$ 10 μK before transferring into a blue-detuned donut-shaped dipole trap beam which guides falling cold atoms down into the science cell. Due to the $\sim$ 0.5 m separation between source cell and science cell, it takes $\sim$ 300 ms for cold atom freely falling from the source cell, with total delivery efficiency $\sim$ 20% which is limited by the lifetime of atoms in the blue dipole trap. The difference of the measured optical density (OD) inside the science cell with donut-shape guiding beam (orange curve) and without guiding beam (blue curve) is shown in Fig. 5.6 (b). Here the OD is measured with a horizontal $\simeq$ 1 mm diameter probe beam on resonance with $6S_{1/2}, F = 4 \rightarrow 6P_{3/2}, F' = 5$. The time span of the measured OD can be used to infer the vertical span size of falling atom cloud which is estimated to be $\simeq$ 8 cm for the free falling atoms and $\simeq$ 20 cm for the

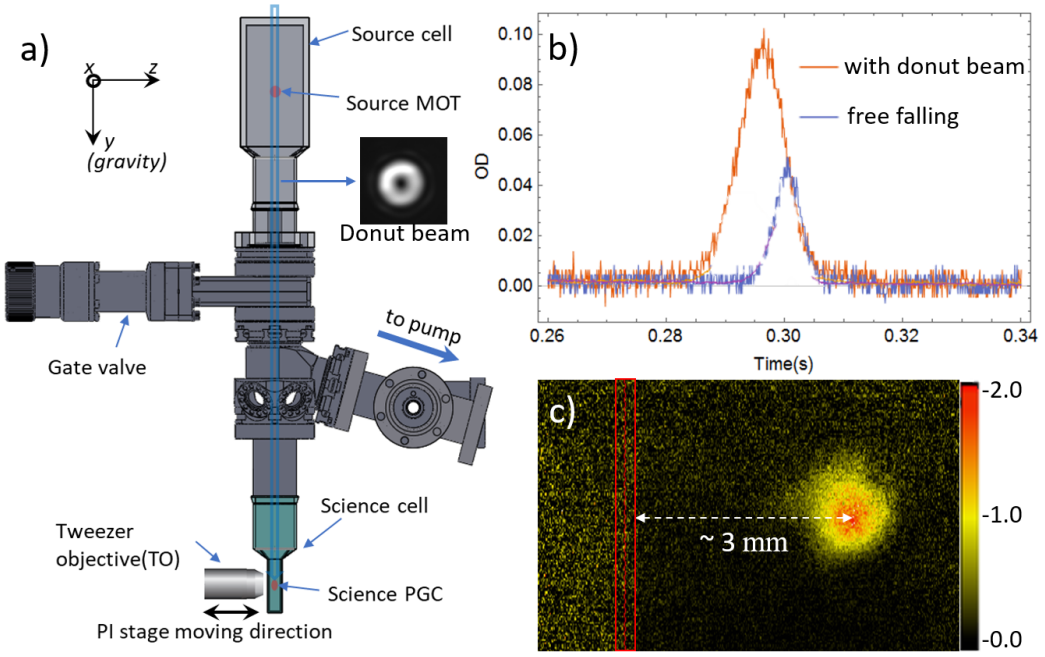

Figure 5.6: (a) A simplified AutoCAD® drawing of the experimental setup. The source MOT and science PGC cloud positions are also indicated with red circles. Falling atoms are delivered from source cell to science cell by the guiding of a blue-detuned donut-shaped beam, indicated with blue double lines with the measured beam profile inserted on the side. (b) The measured optical density (OD) inside science cell with donut-shape guiding beam (orange curve) and without guiding beam (blue curve). The time span of falling cloud can be used to estimate the size of the falling atom cloud in the direction along gravity. (c) An absorption imaging of the PGC atom cloud in the science with peak OD $\sim$ 1.5 and $\sim$ 3 mm away from the chip (indicated with the red rectangle).

blue guided donut beam. In the science cell, atoms are stopped and then cooled by three retro-reflected PGC beams (with diameters $\simeq$ 5 mm) to a volume of $\sim$ (500 μm)^3 with temperature $\simeq$ 20 μK and $\simeq$ 3 mm away from the chip surface, as shown in Fig. 5.6 (c). The three retro-reflected PGC beams are arranged with the 'x', 'y' beams lie in the $x-y$ plane each with $\sim$ 30° to the y axis and 'z' beam lies in the $y-z$ plane with $\sim$ 20° to the y axis), to avoid clipping on the objectives. The science cell PGC beam detunings are tuned continuously with optimized timings from on resonance to -150 MHz red detuned to the $6S_{1/2}, F = 4 \rightarrow 6P_{3/2}, F' = 5$ transition within a time window $\simeq$ 10 ms. Compression of atom density in the science cell is achieved as only the lower part of the elongated falling atom cloud that is overlapped with the cooling beam are cooled and stopped. This design allows us to remove large MOT coils near science cells which was a limitation of optical access in previous

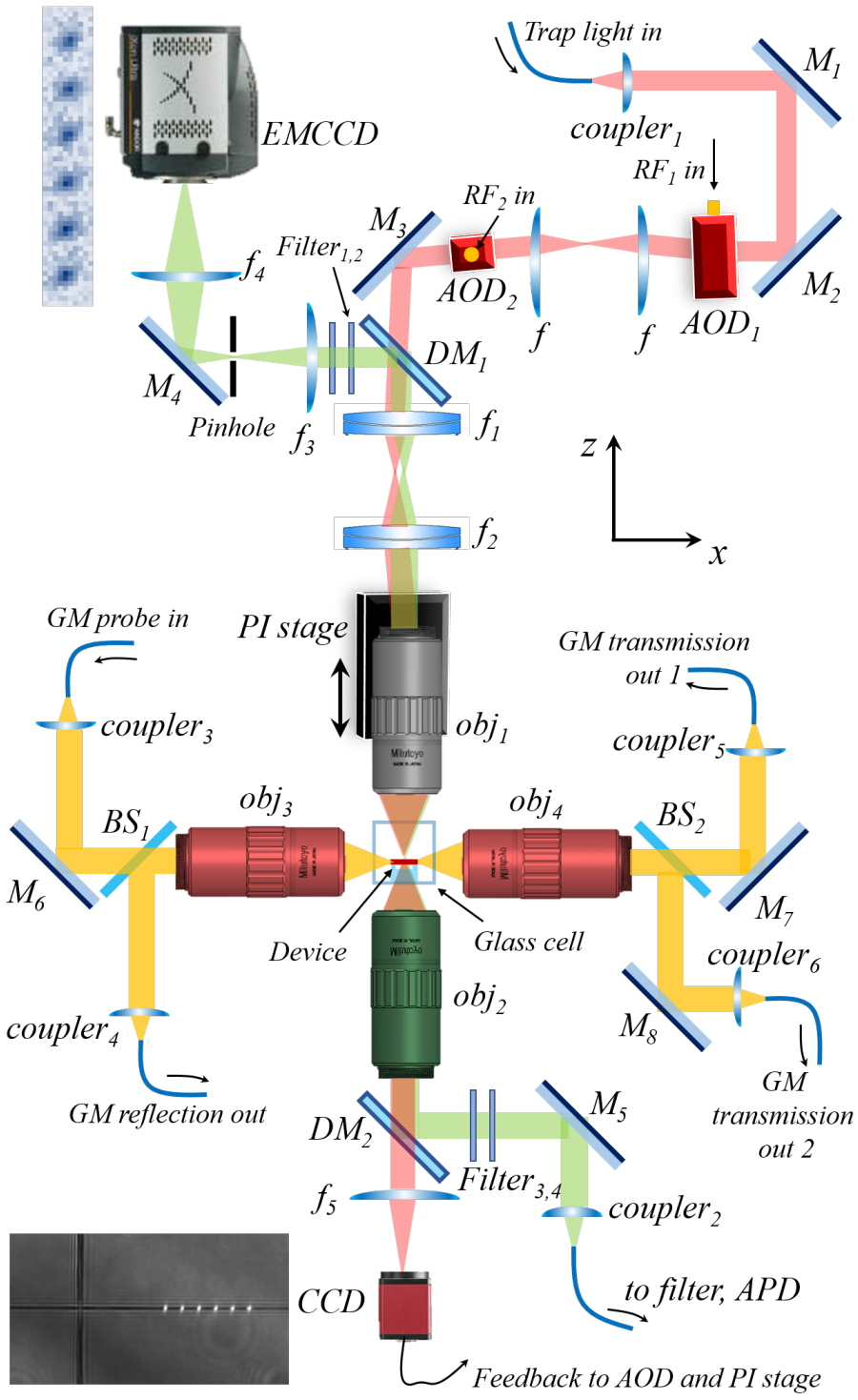

Figure 5.7: A simplified illustration of optics for tweezer array, imaging and guided mode probe. Red beams represent the tweezer trap light at Cs magic wavelength 935.7 nm. Green beams represent the fluorescence from the Cs atom. Yellow beams represent the guided mode probing beams coupled into/from the chip. PGC optics, polarization control components (polarizers/waveplates) and Newport five-axis stages are neglected in this figure for simplicity.

generation setup [67]. It is worth noting that efficient atom delivery with the blue-detuned donut beam is critical to our experiment as this allows to further lowering of the background Cs pressure to improve the lifetime of the trapped atom inside the tweezer and suppress the adsorption rate of background Cs to the device and the degradation of the spectrum quality of the APCW [130].

Next, individual Cs atoms from the PGC cloud are loaded into a linear array of optical tweezers with each trap depth $U_{\text{trap}}/k_B \sim 1$ mK at a Cs magic wavelength (935.7 nm). A simplified illustration of the full setup for the science cell is shown in Fig. 5.7 where we have neglected PGC optics, polarization control components and five-axis mount for objectives (Newport motorized XYZ$\theta_x\theta_y$ tilt aligner, model 8081). Here the red beams represent the tweezer trap light at Cs magic wavelength 935.7 nm. Green beams represent the fluorescence from the trapped Cs atom. Yellow beams represent the guided mode probing beams coupled into/from the chip. In the full setup, four objectives surround the square shape science cell with each objective's function explains as below: obj_1 (gray color) represents the tweezer objective for generating tweezer arrays and also collecting fluorescence counts from trapped atoms; obj_2 (green color) is used to monitor the power of each tweezer site and the relative positions of the tweezer array to the device for stability feedback. obj_3 and obj_4 (red color) are used for free-space coupling light into/from the APCW device inside the science cell.

To minimize the impact of light scattering from the chip during trap loading and also the Cs atoms deposition on PCWs from high Cs densities [130], the tweezer array is loaded approximately 3 mm away from the surface of the silicon chip. As illustrated in Fig. 5.7, the tweezer array is generated by sending the output of the first acoustic-optical deflector (AOD) (AA Opto-Electronic model DTSX-400-900.940) with RF-controlled spacing into a tweezer objective ($NA = 0.4$), forming focal spots with $1/e^2$ waist $w_0 \simeq 1.26 \pm 0.15$ μm. The phase and power of each RF tone are tuned to ensure each trap sites with equal power and avoid interferometric beating and frequency mixing. After 30 ms of PGC and loading into the tweezer array, we turn off the PGC beams for 50ms to let background atoms drop away and then turn on the same PGC beams (15 MHz red detuned from D2, $F = 4 - 5'$ transition) to illuminate the trapped atoms for 50 ms. As shown in Fig. 5.8 (a) (i), (ii) and (iii), by binning fluorescence counts recorded on the EMCCD (Andor Camera iXon 3) around each tweezer location, we demonstrate that the distributions of fluorescence counts are well separated due to discrete loading of either 0 or 1

atom into each tweezer spot with approximately equal probability. This corresponds to the 'collisional blockade' for loading atoms into tightly focused dipole traps [167, 168]. Examples of atom loading into 6 and 17 tweezer sites 3 mm away from the APCW are shown in Fig. 5.8 (b) (iii) and (iv) with 150 experimental shots accumulated fluorescence counts. Generating more tweezer sites is also possible and based on the AOD bandwidth and trap power estimations, our system can be used to generate > 100 tweezer sites [57] with $w_0 = 1.2$ μm and $U_{\text{trap}}/k_B \sim 1$ mK at magic wavelength 935.7 nm.

To determine the lifetime of a trapped atom in the optical tweezer, we measured the occurrence of '1 atom' events after different holding times, with cooling light shut off by an optical shutter. As shown in Fig. 5.8 (a) (iv), we measured $\simeq 25$ s for the first baked vacuum cell and 14 s for the unbaked vacuum cell (not shown). It is worth noting that the final optimal loading condition and long trap lifetime is achieved with the Cs dispenser's current (four dispensers in the source cell) turned down from 3.8 A to 3.2 A and the source MOT loading time reduced from 1 s to $\simeq 100$ ms, corresponding to ~ 2 order of magnitude reduction in the science PGC's atom density.

Due to the relatively long trap lifetime and flexibility afforded by external objective lenses, transport of atoms trapped in the tweezer array to ~ 10 μm from the surface of the silicon chip along the PCW is accomplished over a programmable interval $0.02 < \Delta t < 0.1$ s by mounting the tweezer objective on a precision linear translation stage ("PI stage", model Physik Instrumente V-522, 20 nm unidirectional repeatability) with motion along the z direction defined in Fig. 5.6. A more detailed characterization of PI stage and its heating effect during transport will be presented in the next sub-section.

After transport of atoms to the position on the surface of the silicon chip and ~ 10 μm from the APCW, the 1D atom array can be further transferred into reflective traps near the dielectric surface of the PCW for strong atom-light interactions [33, 108, 182]. This is can be achieved by sweeping the RF input frequency of the second AOD (AOD_2) in Fig. 5.7, a protocol inspired by Ref. [182] and has been discussed in details in Chapter 4. Finally, the pair of AODs in our setup (as illustrated in Fig. 5.7) can also be used to generate 2D tweezer arrays with the axis of AODs and frequency spacing defining primitive vectors of the 2D lattice [16]. Further, we can change the relative angle of the AODs with respect to the APCW to generate a tilted 1D tweezer array. This can be used to transfer 1D free-space tweezer

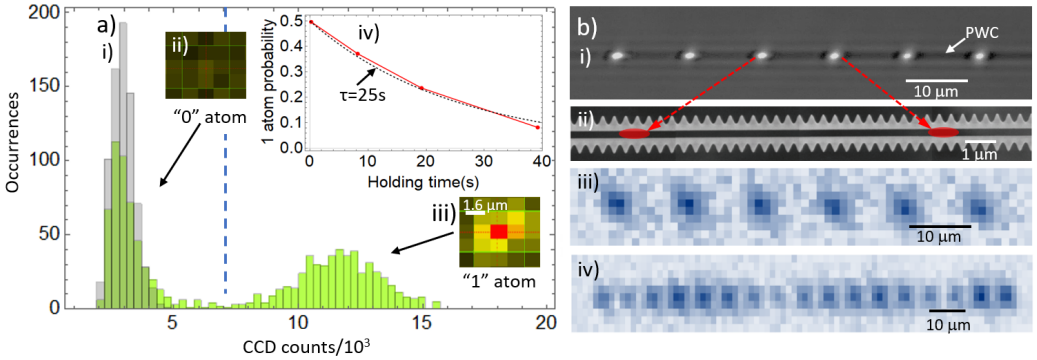

Figure 5.8: (a) (i) A typical histogram of fluorescence counts(green color) measured from a single site of the tweezer traps shows a discrete distribution of 0 and 1 atom loaded each time, as compared to the background(gray) with no loading. The vertical blue dashed line sets the threshold of detecting 1 atom. Inserts (ii) and (iii) indicate the typical image on EMCCD for '0' atom and '1' atom, respectively. Insert (iv) shows the extracted probability of detecting 1 atom after different holding time of the tweezer without cooling. An exponential fit shows the average $1/e$ lifetime of an atom inside the tweezer is 25 s for vacuum cell after baking. (b) (i) Image of scattered light from tweezer spots when aligned with the APCW, collected through the same tweezer objective. (ii) An SEM image of the APCW with red ellipses indicating the separation of two neighbour tweezer spots. The size of red ellipses indicate the estimated confinement of an atom trapped with energy half the trap depth. (iii) Free-space atomic fluorescence from loading of the six tweezer sites with a 1.26 μm beam waist for 150 experimental shots 3 mm away from the chip structure. (iv) Free-space atomic fluorescence from loading of the 17 tweezer sites under same conditions as in (iii).

atom array into each lattice site on the APCW, as proposed in Chapter 4. Thus, the system we described here has fulfilled all requirements to realize the proposals in Chapter 4, from deterministic atom assembly in free-space to the deterministic atom assembly on the APCW and finally loading a full sub-wavelength atom array on each site of the APCW. Fig. 5.8 (b) (i) displays the reflection of multiple tweezer spots when aligned to the APCW. Fig. 5.8 (b) (ii) indicates their separation on the APCW, albeit with no atom imaging, with the size of the red ellipses indicating the estimated confinement of an atom trapped with energy half the trap depth. Beyond these initial measurements, sub-micron waists are achievable with a higher numerical aperture objective (NA $\sim$ 0.7) and will be discussed in Section 5.5.

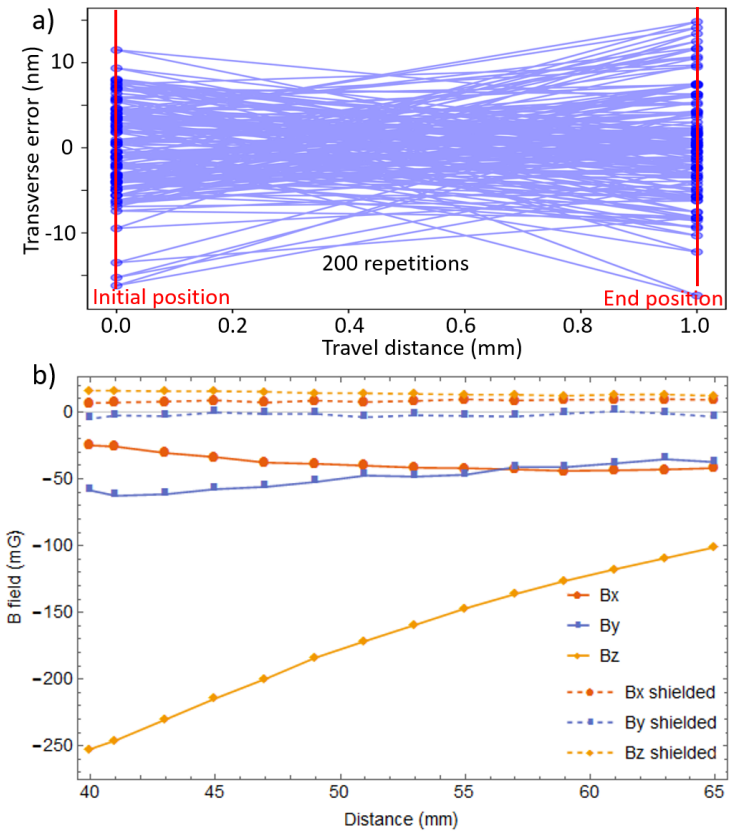

Figure 5.9: (a) Measured repeatability of the PI stage by travelling 1 mm distance with 200 repetitions. (b) Measured DC magnetic field produced by PI stage. Z is along the stage translation direction.

Atom transport to device

In the design of our apparatus, we purposely make the loading position of tweezers 3 mm away from the APCW, to minimize the impact of light scattering from the chip during trap loading and Cs atom deposition on PCWs from high Cs densities [130]. However, the impact of atom transport with PI stage is not elaborated in previous section. In this section, we provide more measurements on the position repeatability, the DC/AC magnetic field and heating on trapped atoms of the PI stage.

First, to quantify the repeatability, we record the "real" position measured by the internal position sensor with respect to the target set position. As shown in Fig. 5.9 (a), the PI stage is moved back-and-forth between the two set values at 0 and 1 mm with 200 repetitions. The observed deviations are in agreement with product specifications ($<$ 20 nm). Other measurements without the use of the internal position sensor have also been implemented to study the position repeatability and

we consistently observed negligible deviation from the target position (< 20 nm).

Second, the motor technology for the PI stage (voice coil) produces both DC and AC magnetic fields. The DC magnetic field in three directions is measured by a high precision magnetometer as shown in Fig. 5.9. The measured total magnetic field produced by the PI stage is around 250 mG at a distance of 6 cm from atoms in the science cell. The magnetic field is zeroed near the PGC cloud position by three pairs of Helmholtz coils and further suppression of magnetic field by a factor of ~ 10 is also achieved by shielding the PI stage with a mu-metal box, as shown in dashed lines in Fig. 5.9.

To investigate the efficiency for transport of single atoms in a linear array of tweezer traps, we measured the conditional survival probability P_s by transporting single atoms from the loading zone to a target position near the PCW ($\Delta t \simeq 0.1$ s), holding still at target position for $\simeq 0.1$ s, and then moving back ($\Delta t \simeq 0.1$ s) to the loading zone for a second fluorescence imaging. In this measurement, a specific target position is chosen to be ~ 10 μm away from the APCW (along y axis) and in the APCW's x-y plane, as indicated by the green dots in Fig. 4.4 (a). After transport from the loading zone to a target position and back to the loading zone again for fluorescence imaging, we find that the survival probability $P_s \simeq 0.90$ for finding an atom in the second fluorescence measurement, given an initial measurement that verifies that a particular tweezer trap is loaded. This observation suggests that the one-way success probability for transport from loading zone to target position is $\simeq 0.95$ and the lifetime of trapped atoms at 10 μm near the PCW is ≥ 2 s.

We further quantify the heating effect of the linear translation stage during atom transport by determining the initial and final atom temperature in the tweezer. This method involves adiabatically lowering of the trap depth and measuring the escape probability of a single atom, which is originally demonstrated in Ref. [2] for an optical dipole trap and Ref. [186] for single-atom tweezers. When lowering the trap adiabatically from U_0 to U_1 as illustrated in Fig. 5.10 (a)(i) and (ii), the atom with initial energy E_0 inside the tweezer trap will also be cooled to energy E_1. The relation between E_0 and E_1 is through the conservative actions during the adiabatic process, namely

$$S(E, U) = \int_0^{x_{\max}} \sqrt{2m(E - U(x))}dx \tag{5.1}$$

$$S(E_0, U_0) = S(E_1, U_1) \tag{5.2}$$

where $x_{\max}$ is the position where the atom has zero kinetic energy. As shown in the gray shaded area in Fig. 5.10 (a) (ii), an atom with energy $E \geq U_1$ in a trap of depth U_1 will eventually escape the trap, as shown in Fig. 5.10 (a) (ii) with the critical escape energy $E_e = U_1$. When adiabatically deepening to the trap depth U_0, the new energy distribution is a truncated energy distribution as shown in Fig. 5.10 (a) (iii) with the cut-off energy E_c depends on from Eq. 5.1 by setting $S(E_c, U_0) = S(U_1, U_1)$. Thus measuring the atom survival probability in the second fluorescence imaging at different trap depth U_1 yields the information about the initial energy distribution.

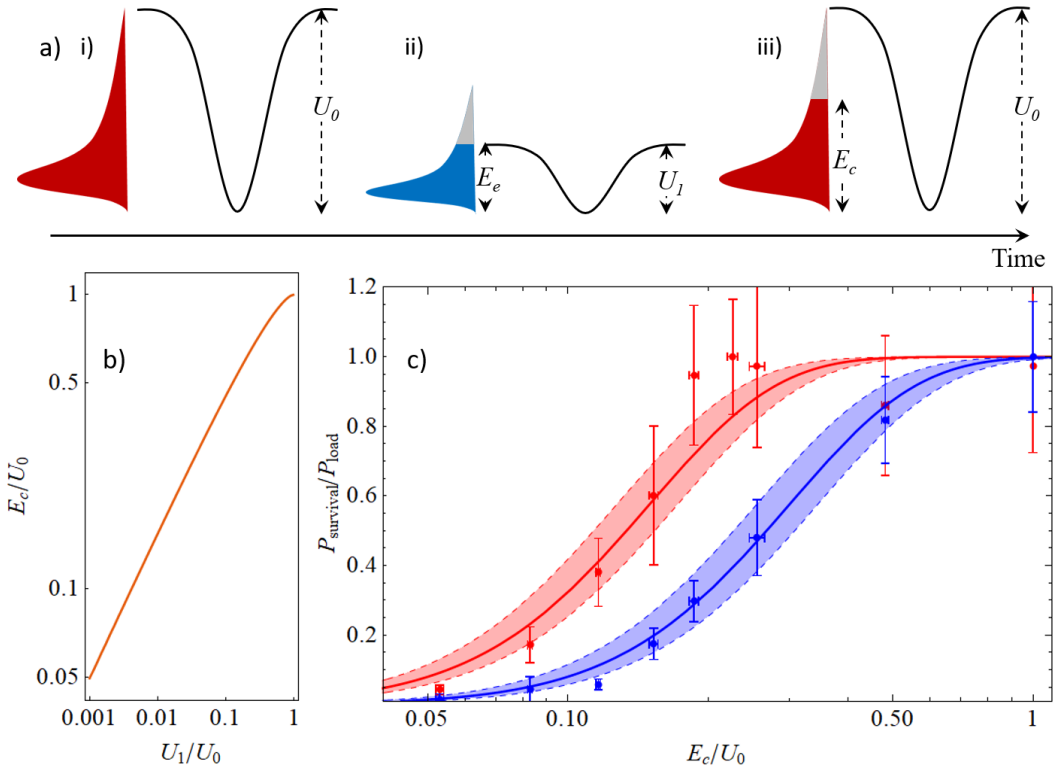

Figure 5.10: (a) Illustration of the measurement scheme for determining atom temperature. (b) Numerical mapping between E_c and U_1, both normalized to U_0. (c) Experiment results of survival probability under transport (blue curve) and no transport (red curve). Initial atom temperature without transport is fitted to be 45 ± 3 μK and the one after moving 2 mm and back is 105 ± 3 μK.

The experiment process is illustrated in Fig. 5.10. After loading a single atom into the optical tweezer trap with trap depth $U_0/k_B \sim 1$ mK, we adiabatically lower the trap depth to U_1 within 10 ms, hold at trap depth U_1 for 10 ms to allow atom escape and then adiabatically deepen the trap depth back to U_0 for a second fluorescence imaging. The measured survival probability (normalized to loading probability) is shown in Fig. 5.10 (c). To fit the atom temperature, a fitting model is developed

based on two main assumptions: 1) the trap potential U is separable so that the action $S(E, U)$ can be evaluated from a 1D potential $U(x) = U_0(1 - \exp\{(-2x^2/w_0^2)\})$. 2) the initial atom energy distribution in the optical tweezer obeys a 3D thermal Boltzmann distribution:

$$f_{\text{th}} = \frac{1}{2(k_B T)^3} E^2 e^{-\frac{E}{k_B T}} \tag{5.3}$$

Both assumptions are proved to be a good approximation under the harmonic trap limit ($k_B T \ll U_0$) as discussed in details in Ref. [2, 186]. The survival probability of the atom remaining in the optical tweezer after lowering the trap is equal to the probability that an atom has an energy less than E_c in the initial distribution $f_{\text{th}}(E)$

$$P_{\text{survival}} = P(E < E_c) = \int_0^{E_c} f_{\text{th}}(E) dE = 1 - (1 + \eta + \frac{1}{2}\eta^2) e^{-\eta} \tag{5.4}$$

where $\eta = E/k_B T$. To relate E_c to the experimentally measured trap depth U_1, we use Eq. 5.1 and for this 1D special case, Eq. 5.1 can be derived in an explicit form

$$u_1 = \frac{2}{\pi} \left(\int_0^{\tilde{x}_{\max}} \sqrt{e_c - 1 + \exp\{(-\tilde{x}^2)\}} d\tilde{x} \right)^2 \tag{5.5}$$

where $e_c \equiv E_c/U_0$, $u_1 \equiv U_1/U_0$, $\tilde{x} \equiv \sqrt{2}x/w_0$ and $\tilde{x}_{\max} = \sqrt{-\ln(1 - e_c)}$. A numerical evaluation of this mapping is plotted in Fig. 5.10 (b). With Eq. 5.4 and Eq. 5.5 , we can then fit the experimental result to extract the atom temperature T. As shown in Fig. 5.10 (c), the initial atom temperature without moving stage is fitted to be $\simeq 45.4 \pm 3$ μK and the atom temperature after a round-trip 2 mm range transport is fitted to $\simeq 103 \pm 3$ μK. The shaded area corresponds to varying the fitting temperature by 15%. Thus, we conclude that the atom transport from the PI stage contributes a small heating ($\Delta T \sim 50$ μK) to the trapped atom temperature but this heating effect is not an important source leading atom loss from the trap.

Finally, it is worth noting that the method we described here for measuring trapped atom temperature can also be used to further cool the trapped atom near the device without introducing additional cooling beams, as already demonstrated in Ref. [186]. In experiment, the initial tweezer loading in the loading zone can start with a relative deeper trap depth (e.g. $U_{\text{trap}} k_B > 3$ mK) and more trap sites. After aligning the tweezer array to the device, we can adiabatically lower the trap depth and truncate the atom distribution in the tweezer trap introducing an evaporative cooling which was used for achieving Bose-Einstein condensates (BECs) [5]. This is particularly useful in the case when PGC fails due to complicated polarization distributions near the dielectric surfaces. Furthermore, vacant tweezer sites generated during the

evaporative cooling process can be removed and rearranged by controlling the RF tones sending into the AOD [57], ending with a fully loaded array of cold atoms on the PCWs. Further transferring atoms from the 'z_1' trap (the first trap above the APCW) into the gap of APCW can be achieved by adiabatically increasing the power of guided-mode trap powers, as already discussed in Chapter 4.

5.5 Towards higher optical resolution

Table 5.2: **Waist benchmark of higher NA objectives.** f and W.D. mean focal length and working distance, respectively.

NA	f (mm)	W.D. (mm)	Input waist (mm)	Waist in air (μm)	Waist in vacuum (μm)
0.4	10	25	2.5	1.22	1.23
0.67	4	10.5	1.8	1.02	1.02
0.7	2	6	1.1	0.91	0.87

Our current apparatus can be improved in terms of optical resolution for both imaging and smaller trap volume. It can accommodate state-of-the-art long-working distance objective lenses with $NA \sim 0.7$. To characterize the tweezer waist under different NA objectives and filling ratio, we employed three different methods for a cross-check: (i) Imaging by a CCD camera and a telescope system which consists of a $NA = 0.8$ objective and 125 mm focal length lens. (ii) A knife-edge experiment [177] with a scalpel blade glued inside a fused silica cell with inner dimensions of 2 cm by 1 cm. The objective is moved on a two-dimensional motorized stage to scan along and perpendicular to the light propagation direction. The Rayleigh range and tweezer waist can be fitted from the transmitted light after the glass cell. To investigate the effect of glass cell bowing on tweezer waist, the measurement is performed when the glass cell is either at atmospheric pressure or under vacuum (below 10^{-4} Torr). (iii) For tweezers inside the science glass cell, the tweezer beam is scanned across a 500 nm wide and 200 nm thick uniform waveguide region inside the glass cell, and the reflection and scattering are imaged by an EMCCD. The Rayleigh range and tweezer waist can be obtained by fitting the images. The tweezer waist measured from these three different methods for the $NA = 0.4$ objective are all around 1.25 μm and consistent within 10%.

Table 5.2 shows the measured beam waist w_0 ($1/e^2$ radius for intensity) with the scalpel blade method for three different NA objectives ($NA = 0.4$ Mitutoyo M Plan Apo NIR B 20X, $NA = 0.67$ OptoSigma PAL-50-NIR-HR, compensated for glass thickness 1.25 mm and Mitutoyo G Plan Apo 100X, compensated for glass thickness

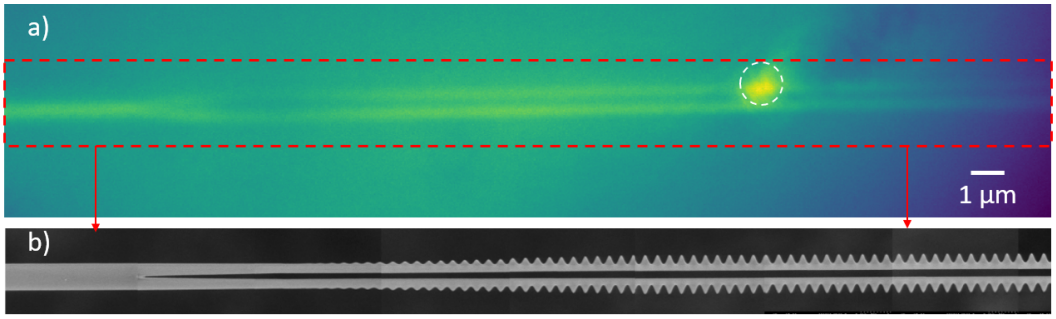

Figure 5.11: (a) A CCD image of APCW inside a glass cell with $NA = 0.7$ objective under broadband illumination at 532 nm. The focused tweezer is at 852 nm with $1/e^2$ waist $w_0 \simeq 0.7$ μm, indicated as white dashed circle with radius = 0.7 μm. The junction between the nanobeam waveguide and the APCW region is resolved on the left end. (b) A SEM image of the part of APCW under image, corresponding to the red dashed box in (a).

1 mm). The tweezer waists can reach 1.02 μm for $NA = 0.67$ objective and sub-μm for $NA = 0.7$ objective. These measurements show that the differences for tweezer waists in air and under vacuum are negligible for all three different NA objectives and thus the bowing effect of the glass cell does not significantly contribute to the tweezer aberration.

In Fig. 5.11 (a), we show an image of the APCW inside a glass cell imaged with $NA = 0.7$ objective under broadband illumination at 532 nm. The high resolution of the $NA = 0.7$ objective allows us to resolve the gap of APCW and precise location of tweezer spot, as shown in Fig. 5.11 (a) with the tweezer aligned on one nanobeam of the APCW (white dashed circle). Further atom trapping near PCWs in tweezer arrays focused by high resolution objectives is a work under progress.

5.6 limitations and future improvements

For an optical tweezer array aligned to APCW, the stability of the whole setup is an important concern for the design of the new apparatus. Instabilities arise from three different time scales: 1) the fastest time scale ($\tau \sim 1$ μs) corresponds to the mechanical oscillation of the nanostructure; 2) the intermediate time scale ($\tau \sim 0.1$ s) corresponds to the vibration of the whole apparatus; 3) The slow position drift ($\tau \sim 1$ h) due to, e.g., temperature drifts of the lab. The first fastest timescale instability is related to the design of the chip and can be suppressed by better mechanical design such as 2D SPCWs will be discussed in Chapter 7. The second instability can be suppressed largely by adapting silicate-bonding method

as compared to previous long mechanical arm holding design Ref. [171]. The last slowest position drift can be suppressed by better temperature control of the lab and the experiment area. Without re-engineering the lab temperature control system, here we show that we can track this slow drift by imaging the target device inside the vacuum cell.

As shown in Fig. 5.7), we can continuously monitor the device and the power of the tweezer array using an objective (obj_2, Mitutoyo G Plan Apo 50X, $NA = 0.55$ and 3.5 mm glass thickness compensated) and a CCD camera (Guppy Pro F-201B) from the back-side. A sample image of the device with the center APCW and two supporting safety rails is shown in Fig. 5.12 (a). As indicated in Fig. 5.12 (a), two region of interests are selected to trace the drift of device: region A (red dashed rectangle) is a region on the APCW and is sensitive to motion in y direction; region B (white dashed rectangle) is on the supporting tethers and is sensitive to trace the drift in x direction. By taking an image of region A every 2 min in 24 hour (starting from 4:00 pm to next 4:00 pm), we get the stacked image as shown in Fig. 5.12 (b). Clearly, we can see the moving of the center peak position corresponds to the APCW motion in the y direction. Defocusing happens when the APCW moves along z direction. By fitting the position of peak intensity and the width of peak in the image with the objective's point spread function, we can estimation the drift of device in the $y - z$ plane. Fig. 5.12 (d) shows the estimated position of device in the $y - z$ plane as a function of time. As indicated, the start position and the final position are not completely overlapped, corresponding to a non-reversible day-to-day drift. In experiment, this non-reversible day-to-day drift can gradually degrade the optical alignment over a long period. The stacked image of the device (Fig. 5.12 (b)) is also compared with the recorded lab temperature near apparatus. As shown in Fig. 5.12 (c) with same time coordinate, the recorded temperature curve shows a similar pattern (blue curve) as the position drift in Fig. 5.12 (b), suggesting the temperature drift is causing the displacement of the device. Similarly, we also continuously monitor of reflection power from device over 24 hour(red curve) and it is also qualitatively overlapped with the record of lab temperature curve (blue curve). The temperature dependent displacement is likely due to the long post supporting the whole platform and this is confirmed with a COMSOL® [45] simulation of the thermal expansion of the simplified apparatus. As we can see in Fig. 5.12 (d), the thermal expansion coefficient near science glass cell is ~ 5 μm/K which is consistent to the displacement we observed in Fig. 5.12 (b, d).

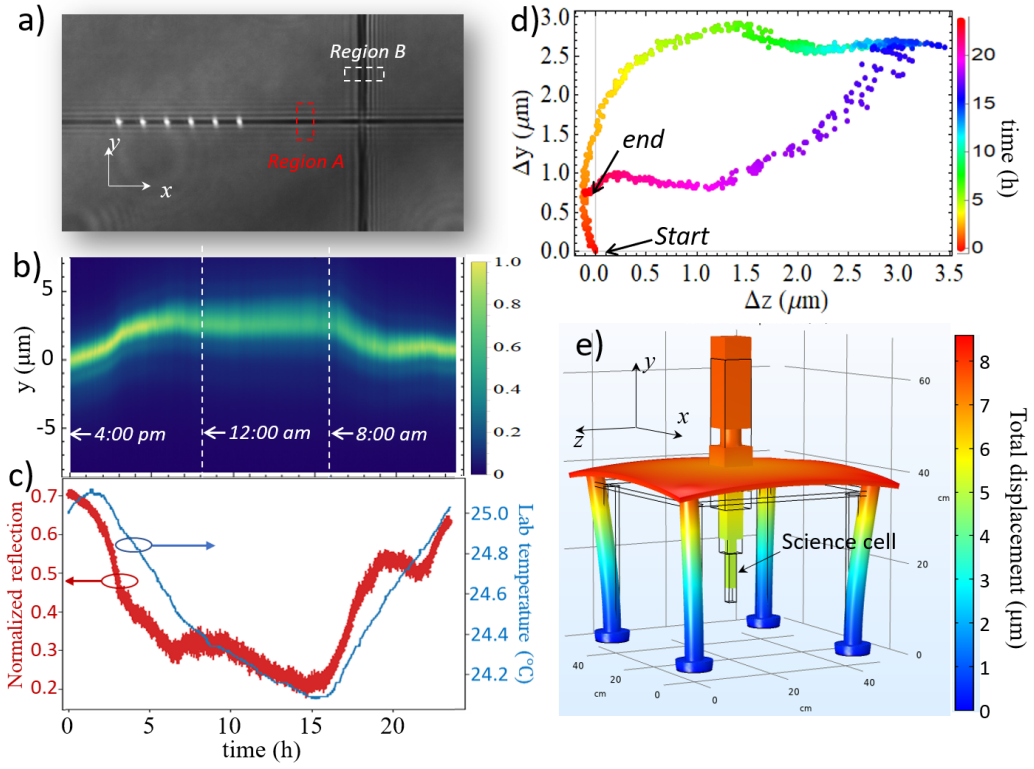

Figure 5.12: (a) A CCD image of the APCW with two side safety rails viewed from the backside objective (obj_2 in Fig. 5.7). Two regions are selected to trace the drift of device: Region A (red dashed rectangle) is sensitive to motion in y direction and region B (white dashed rectangle) is sensitive to trace the drift in x direction. (b) Stacked image from region A taken every 2 min in 24 hour (starting from 4:00 pm to next 4:00 pm). (c) The position drift in y has a very similar shape to the lab temperature change (blue curve). A continuous monitor of reflection power from the device input over 24 hour (red curve) is also overlapped with the record of the lab temperature near apparatus (blue curve), suggesting that temperature drift is the main cause of displacement and reduced coupling efficiency. (d) The extracted position of device from stacked images of region A (b). Here the device y position is from fitting the position of peak intensity and the z position is found by fitting the width of the device's image with the imaging system's point spread function. As we can notice in (d), the final position at the end of 24 hour is not completely overlap with the original position, corresponds to a day-to-day overall drift. (e) A COMSOL® [45] simulation of the thermal expansion of the simplified apparatus. The thermal expansion coefficient near science glass cell is $\sim$ 5 μm/K which is consistent to what we observed in (d).

In the lab, to minimize the impact of thermal drift from day to day, the continuously estimated device position is sent back to the Newport 5-axis stage in which the PI stage and tweezer objective are mounted. However, this solution is not optimal as it did not prevent the day-to-day non-reversible drift as indicated in Fig. 5.12 (d). A better solution is the active temperature control where the whole setup is sealed in an box with the HEPA-filters and sensitive temperature sensors for temperature feedback. A proof of this concept has already been shown in Ref. [25] where mK temperature stability is achieved. With this mK level temperature stability, the overall displacement of the device can be suppressed to 5 nm, which is acceptable for our purpose.

Finally, the differential movement of the tweezer spot and chip can be further suppressed by better design of the mount of the objective. For example, one can bond/glue an aspheric lens on the glass cell with the optical axis aligned to the device. In this case, as along as the input beam angle stays the same, the focus position relative to the device will stay the same and is not sensitive to μm scale thermal drift of glass cell. It should be pointed out the effective focal length of a fixed aspheric lens on the glass cell can still be varied by combining with a tunable lens, as already shown in Ref. [17]. In our group, Jean-Baptiste and Zhongzhong show that a carefully design of the lens system with tunable lens (Optotune, model: EL-10-30) allows $\sim$ 1 mm travel distance along propagation direction (z axis) without significant change in size of focal spot ($\delta w_0/w_{0,\mathrm{min}} < 10\%$). This can be an alternative path to our current "PI stage + objective" setup. However, dispersion problem with single aspheric lens may require additional engineering for fluorescence imaging. Another possible issue with the tunable lens is that they are typically not diffraction limited and the optical liquid inside requires being operated horizontally with respect to the gravity axis to minimize aberrations [95].

5.7 Summary and outlook

We have presented an advanced apparatus for the integration of atoms and nanophotonics with several significant advances, including 1) efficient free-space coupling of light to and from guided modes of PCWs with greatly improved power handling capabilities relative to our previous work [67, 68, 86], 2) silicate bonding of silicon chips within small glass vacuum cells thereby reducing the volume of the (bakeable) vacuum envelope of our systems from $\sim$ 1 liter [171, 200] to $\sim$ 5 cm^3 with an associated drop in pressure $>$ 100x, and 3) deterministic, mechanical delivery of $1D$ single-atom tweezer arrays to near an APCW. Each of these advances elim-

inates significant impediments present in prior experiments in the QOG at Caltech as explained in previous sections.

The advanced atom-nanophotonic platform that we have described can provide a foundation for realizing nanoscopic atomic lattices in $1D$ and $2D$ as envisioned in Fig. 1.4 and thereby for experimental explorations of these systems involving *strong interactions between atoms and photons* in nanophotonic structures as described in Ref. [40, 124]. Attaining deterministic atom arrays, in the spirit of recent worldwide advances with free-space tweezer arrays [16, 17, 57, 105, 181], will allow us to probe the physics of strong, photon-mediated interactions between many atoms, as well as atom-mediated interactions between photons. The versatility of dispersion-engineered nanostructures makes accessing these physical regimes possible in a single cold-atom experiment by changing the nanophotonic structures the atom interacts with.

Moreover, the compact nature of our system also lends itself to more easily deployable quantum technologies that are of growing interest in the community. Possible applications of these nanophotonic systems range from quantum communication using strong atom-photon interactions to probing unconventional quantum phase transitions and investigating quantum metrology applications by combining the functionality of nanophotonics and atoms. One example relates to ongoing investigations of the integration of nanophotonic systems such as described here with on-chip frequency combs for a compact atomic frequency standard [91, 148]. The collective decay of N atoms (known as Dicke superradiance) into PCWs demonstrated in Ref. [68] could provide a simple, deterministic and scalable way to generate Fock states with large and fixed photon numbers, enable quantum-enhanced metrology [145]. Apart from quantum information science, an essential aspect of atom trapping near nanophotonic structures is a quantitative understanding of Casimir-Polder interactions between trapped atoms and the dielectric boundaries [71, 92]. We have taken a modest step toward this end in recent work [33]. With a broad set of such objectives in mind, we have developed the advanced apparatus described in this chapter. Future improvements of our apparatus can be made by 1) adapting to higher NA objectives, 2) better temperature control near the apparatus to minimize the impact of device drifting and 3) better design to minimize the differential drift between tweezer arrays and the device.

Chapter 6

OPTICAL TWEEZERS WITH LAGUERRE-GAUSS BEAMS

Spatially structured light has opened a wide range of opportunities for enhanced imaging as well as optical manipulation and particle confinement. In this chapter, we show that phase-coherent illumination with superpositions of radial Laguerre-Gauss (LG) beams provides improved localization for bright optical tweezer traps, with narrowed radial and axial intensity distributions. Further, the Gouy phase shifts for sums of tightly focused radial LG fields extend the range of imaging methods and permit novel phase-contrast microscopy strategies at the wavelength scale. One application is the suppression of interference fringes from reflection near nano-dielectric surfaces, with the promise of improved cold-atom delivery and manipulation.

The work described in this chapter is partially based on Ref. [20] and is a result of collaboration among individuals inside QOG. My advisor Jeff Kimble first came out this idea about superpositions of radial LG beams in early 2019 and numerically demonstrated the volume reduction under paraxial approximation. Inspired by Jeff's initial success, I carried out the initial COMSOL®[45] simulations and vector field calculation based on Debye-Wolf integral method to verify the volume reduction for tightly focused tweezers (unfortunately, most of files are encrypted after the Ransomware attack in May 2019). Jean-Baptiste Béguin took a lead in the experimental realization with the spatial light modulator (SLMs) and developed scalar/vector diffraction models for designing optimal SLM patterns. Prof. Julien Laurat (who was visiting the QOG on sabbatical) contributed his own vector field calculations with optimized parameters and a large amount of literature research. Alex Burgers and Zhongzhong Qin contributed their valuable suggestions and expertise throughout the research.

6.1 Introduction

Structuring of light has provided advanced capabilities in a variety of research fields and technologies, ranging from microscopy to particle manipulation [1, 13, 73, 205]. Coherent control of the amplitude, phase, and polarization degrees of freedom for light enables the creation of engineered intensity patterns and tailored optical forces. In this context, LG beams have been extensively studied. Among other

realizations, tight focusing with subwavelength features was obtained with radially polarized beams [51, 193], as well as with opposite orbital angular momentum for copropagating fields [195]. LG beams have also attracted interest for designing novel optical tweezers [14, 60, 143]. Following the initial demonstration of a LG-based trap for neutral atoms [114], various configurations have been explored, including 3D geometries with "dark" internal volumes [9, 35, 142] for atom trapping with blue-detuned light [15, 196].

For these and other applications of structured light, high spatial resolution is of paramount importance. However in most schemes, resolution transverse to the optic axis exceeds that along the optic axis. For example, an optical tweezer formed from a Gaussian beam with wavelength $\lambda = 1\,\mu\text{m}$ focused in vacuum to waist $w_0 = 1\,\mu\text{m}$ has transverse confinement w_0 roughly $3\times$ smaller than its longitudinal confinement set by the Rayleigh range $z_R = \pi w_0^2/\lambda$. One way to obtain enhanced axial resolution is known as 4π microscopy [23, 83], for which counterpropagating beams form a standing wave with axial spatial scale of $\lambda/2$ over the range of z_R. However, 4π microscopy requires interferometric stability and delicate mode matching. Another method relies on copropagating beams each with distinct Gouy phases [22, 26, 176], which was proposed and realized mostly in the context of dark optical traps, either with two Gaussian beams of different waists or offset foci [97, 194], or with two LG beams of different orders [9]. However, for bright trap configurations, a comparable strategy has remained elusive.

In this chapter, we show that superpositions of purely radial LG beams can lead to reduced volume for bright optical traps. We also provide a scheme for implementation by way of a SLM for beam shaping extended beyond the paraxial approximation into a regime of wavelength-scale traps. Significantly, apart from reduced trap volume, our study highlights differential Gouy phase shifts at the wavelength scale as a novel tool for imaging. An application is the strong suppression of interference fringes from reflections of optical tweezers near surfaces of nanophotonic structures, thereby providing a tool to integrate cold-atom transport and nanoscale quantum optics.

6.2 Superposition of paraxial radial Laguerre-Gauss beams

In this section, we will discuss the superpositions of LG beams under paraxial approximation. We will find that the paraxial approximation does provide a very clear picture of the essential physics with simple and analytical expressions.

The paraxial LG beams are solutions of paraxial Helmholtz equation under cylindrical coordinates with each transverse mode labelled by the radial index p ($p > 0$) and the azimuthal index l. For a x polarized LG beam propagating along z direction, the electric field take the form $\mathbf{E}_p^l(r, \varphi, z) = u_p^l(r, \varphi, z) \exp(ikz)\hat{x}$ with the LG beam amplitude $u_p^l(r, \varphi, z)$ given by (here we follow the convention in Ref. [137]):

$$\begin{aligned} u_p^l(r, \varphi, z) =& \sqrt{\frac{2p!}{\pi(p + |l|)!}} \frac{w_0}{w(z)} \left(\frac{\sqrt{2}r}{w(z)}\right)^{|l|} \exp\left(-\frac{r^2}{w^2(z)}\right) L_p^{|l|}\left(\frac{2r^2}{w^2(z)}\right) \times \\ & \exp\left(ik\frac{r^2}{2R(z)}\right) \exp(il\varphi) \exp\Big(-i\psi_p^l(z)\Big), \end{aligned} \tag{6.1}$$

where w_0 is Gaussian beam waist ($1/e^2$ intensity radius) defined as in previous chapters, $z_R = \pi w_0^2/\lambda$ is the Rayleigh range, $w(z) = w_0\sqrt{1 + (z/z_R)^2}$ is the beam radius at position z, $R(z) = z\,(1 + (z_R/z))^2$ is the wavefront radius, L_p^l is the generalized Laguerre polynomial and the Gouy phase

$$\psi_p^l(z) = (2p + |l| + 1) \arctan\,(z/z_R)\,. \tag{6.2}$$

The Gouy phase lies in the heart of our discussion in this chapter. Physically, the Gouy phase can be interpreted as a geometric phase shift due to focusing wavefront [170] and it can be measured relative to a plane wave (of same frequency) propagating along z [22, 26, 176]. According to this definition, this is mathematically equivalent to

$$\psi_G \equiv kz - \mathrm{Arg}(\mathbf{E}_p^l(\rho = 0, \varphi = 0, z)) \tag{6.3}$$

It is worth noting that the Gouy phase in Eq. 6.2 is a function of index p and l. Larger p and $|l|$ values leads to a larger phase gradient along propagation direction near the focus as shown in Fig. 6.1(a). As we will show shortly, this unique feature turns out to be the key of reshaping and reducing the focus size along propagation direction.

Throughout our discussion, we mainly focus on radial LG beams with the azimuthal mode number $l = 0$ (i.e., pure radial LG beams with radial number p). With l dropped with $l = 0$, Eq. 6.1 can be simplified as:

$$u_p(r, \varphi, z) = \sqrt{\frac{2}{\pi}} \frac{w_0}{w(z)} \exp\left(-\frac{r^2}{w^2(z)}\right) L_p\left(\frac{2r^2}{w^2(z)}\right) \exp\left(ik\frac{r^2}{2R(z)}\right) \exp\big(-i\psi_p(z)\big). \tag{6.4}$$

It is worth noting that for $l = 0$, each individual p mode has identical spatial profiles $|u_p(0, 0, z)| = \sqrt{2/\pi}w_0/w(z)$ along z. The intensity profile at the focal plane for the

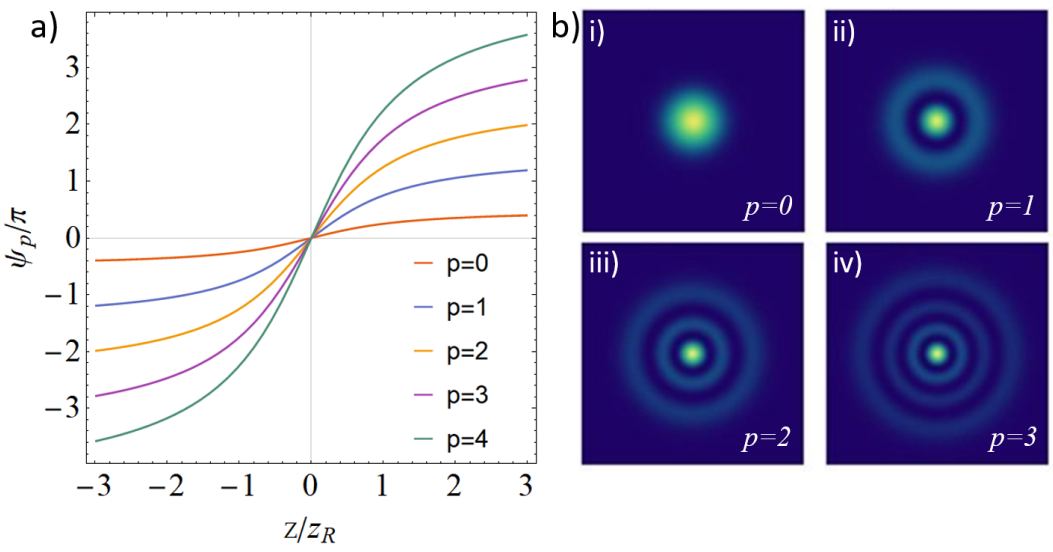

Figure 6.1: (a) Gouy phase for first five radial LG beams ($l = 0$) (b) The intensity profile at the focal plane for the first four radial LG beams ($l = 0$).

first four radial LG beams are shown in Fig. 6.1(b). We can see that as p increases, the size of the intensity center decreases but the overall size of the beam increases.

For the superposition of orthogonal LG beams (that is, of same waist, focus position and propagation direction), the superposed field amplitude u_Σ can be generically written as

$$u_\Sigma(r,\varphi,z) = \sqrt{\frac{2}{\pi}}\frac{w_0}{w(z)}\exp\left(-\frac{r^2}{w^2(z)}\right)\exp\left(ik\frac{r^2}{2R(z)}\right) \times \sum_p a_p L_p\left(\frac{2r^2}{w^2(z)}\right)\times\exp\left(-i\psi_p(z)\right), \tag{6.5}$$

where a_p is the complex amplitude for each p mode in the superposition over a set of mode index p. It can be mathematically proved that in order to keep the intensity of a superposition of modes being symmetric around focus plane at $z = 0$ (that is $I(z) = I(-z)$), a_p should be real numbers (or with a common phase shift). In the following discussion, we will use the notation '$i + j$' to represent the superposition $\mathbf{E}_{p=i} + \mathbf{E}_{p=j}$ while '$i - j$' represents the superposition $\mathbf{E}_{p=i} - \mathbf{E}_{p=j}$, for the sake of brevity.

As an example, we consider a particular superposition '0 + 2 + 4' of the radial LG modes. Fig. 6.2(a, b) provide the calculated intensity distributions for the fundamental Gaussian mode ($p = 0$) (blue) and for the '0 + 2 + 4' superposition (orange) along the radial (x) and axial (z) directions of the focus plane, respectively.

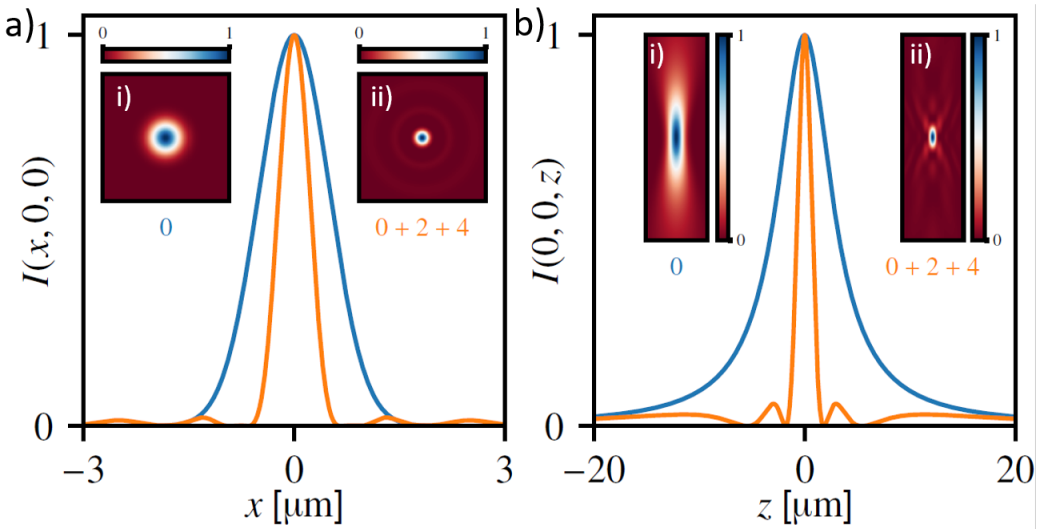

Figure 6.2: Comparison between the fundamental Gaussian mode $\vec{E}_0$ (blue) and the superposition of radial p modes $\vec{E}_\Sigma$ (orange) with $p = 0, 2, 4$. The plots are calculated for the paraxial case, with $w_0 = 1\,\mu\text{m}$ and $\lambda = 1\,\mu\text{m}$. (a) x-line cut transverse intensity profiles. Insets provide the x-y distribution in the focal plane. (b) z-line cut axial intensity profiles. Insets correspond to the x-z distribution in the $y = 0$ plane.

As shown by the line cuts and insets in Fig. 6.2 (a, b), there is a large reduction in focal size in both radial and axial directions for the '$0 + 2 + 4$' superposition relative to the $p = 0$ Gaussian mode. To quantify this reduction in focus spot size in 3D, we define a focal volume $V = \Delta x \Delta y \Delta z$ with $\Delta x, \Delta y, \Delta z$ taken to be the full widths at half maximum (FWHM) for the intensity distributions along x, y, z. Physically, this corresponds to the volume of trapped atom with temperature equals to half the trap depth[1]. Proceeding this focal volume calculation for Fig. 6.2(a, b), we get $V_0 = 8.6\,\mu\text{m}^3$ with $\Delta x_0 = \Delta y_0 = 1.17\,\mu\text{m}$ and $\Delta z_0 = 6.28\,\mu\text{m}$ for the $p = 0$ Gaussian mode and $V_\Sigma = 0.39\,\mu\text{m}^3$ with $\Delta x_\Sigma = \Delta y_\Sigma = 0.51\,\mu\text{m}$ and $\Delta z_\Sigma = 1.5\,\mu\text{m}$ for the '$0 + 2 + 4$' superposition. This leads to a total reduction in volume $V_0/V_\Sigma \simeq 22$. It is worth noting that the envelope of the superposed LG beams will stay the same when focused on a dielectric planar surface. In this case, the focal volume reduction effect will help suppress interference fringes in regions near dielectric boundaries as an example, shown in Fig. 6.3(a) and the z-line cuts (orange curve) in (b) as compared to the $p = 0$ Gaussian mode (blue curve). A more detailed discussion of

[1] It is worth pointing out for the super-resolution community, the first intensity minimum position is frequently quoted to compare spot size. Here, our choice is natural for applications in the trapping of atoms or particles. Generally, there is no direct conversion between these two definitions of spot sizes.

applications in atom transport to nanostructures will be presented in Section 6.7.

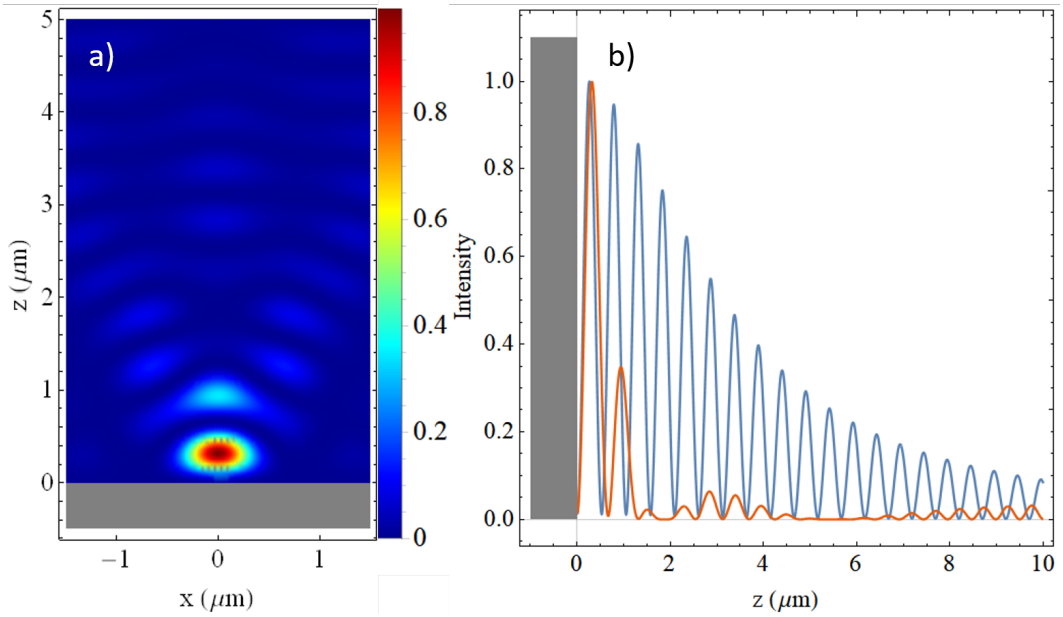

Figure 6.3: (a) Reflection fringes (intensity) of '0+2+4' superposition in the $x-z$ plane due to a semi-infinite planar surface (gray) (b) z-line cuts ($x = y = 0$) of reflection fringes for '0+2+4' superposition (orange curve) as compared the $p = 0$ Gaussian mode (blue curve). Intensity here is calculated with focus at the surface $z = 0$, waist $w_0 = \lambda = 1$ μm, and amplitude reflection coefficient $r = -0.8$. All intensities are normalized to their peak values.

for the reflective fringes, we can show that the reflective fringes take the same envelope as the free-space one.

Another interesting example of LG beam superposition is the destructive '0-1' superposition which is already found to have several promising applications in atomic physics [9, 15]. The '0-1' superposition of LG beams can be used to generate the so-called 'bottle' beam for which the intensity is a minimum at focus center, as shown in Fig. 6.4. This can be used to trap atoms in the minimum position to suppress the trap light scattering and dephasing.

Scaling of the focal volume for superposed Laguerre-Gauss beams

With specific examples of constructive/destructive superpositions in mind, we now turn to a more general analysis of LG beam superposition. To start with, consider the electric field amplitude along the axial direction ($r = \varphi = 0$), Eq. 6.5 can be

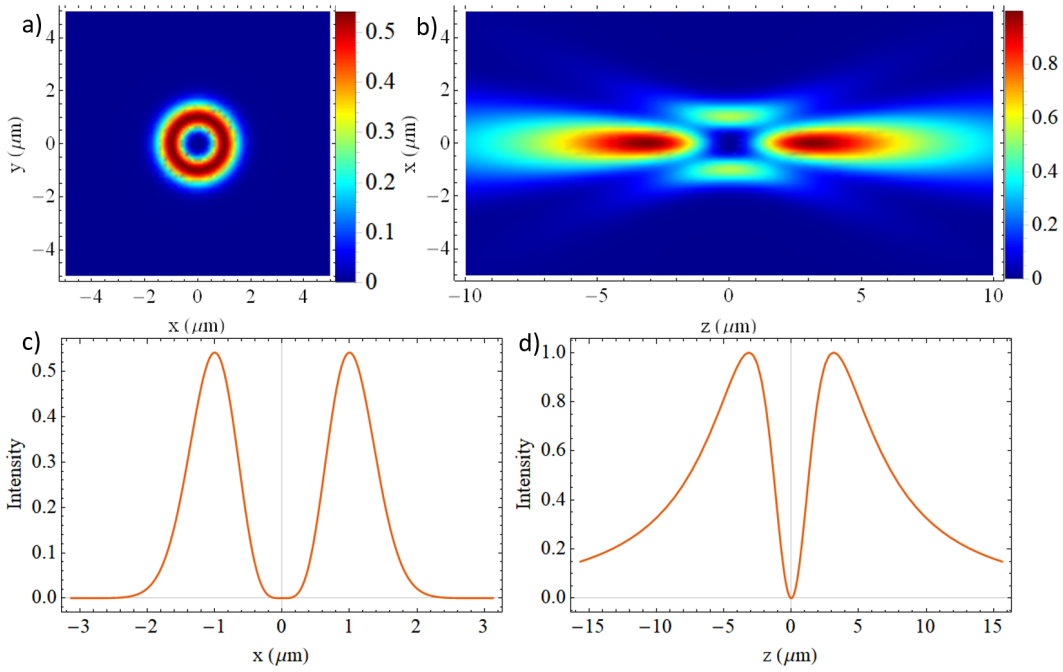

Figure 6.4: (a) Intensity profile for the '0-1' superposition of LG beams in the focal plane ($z = 0$). (b) Intensity profile for the '0-1' superposition of LG beams in the $x - z$ plane ($y = 0$). (c) x-line cut ($y = z = 0$) of radial intensity profiles (d) z-line cut ($x = y = 0$) of axial intensity. All plots are calculated for $w_0 = \lambda = 1$ μm.

further simplified as

$$u_\Sigma(0,0,z) = \sqrt{\frac{2}{\pi}}\frac{w_0}{w(z)}\sum_p a_p \exp\big(-i\psi_p(z)\big) \tag{6.6}$$

This expression suggests that the superposition of radial LG beams axial direction is mathematically equivalent to summing over pure phasors with p-mode Gouy phases.

For the case of strong spatial reduction along z ($\Delta z_\Sigma \ll z_R$, as in the example of '0+2+4'), we have $\psi_p(z) = (2p+1)\arctan(z/z_R) \approx (2p+1)z/z_R$, $w_0/w(z) \approx 1$ and

$$u_\Sigma(0,0,z) \overset{z\ll z_R}{\approx} \sqrt{\frac{2}{\pi}}\sum_p a_p \exp(-i(2p+1)z/z_R) \tag{6.7}$$

We recognize that the RHS of this equation can be viewed as a Fourier transform of $u_\Sigma(0,0,z)$ with spatial frequencies $k_{z,p} = (2p+1)/z_R$. In this picture, the spatial reduction due to LG beams superposition is very similar to the temporal reduction of a pulse with frequency combs. Note that the maximum spatial frequency is given by the maximum p mode ($p_{\max}$) in the summation. With $I_\Sigma(0,0,z) \propto |u_\Sigma(0,0,z)|^2$,

we can claim that the minimum spatial size $\Delta z_{\Sigma,\min}$ scales as

$$\boxed{\Delta z_{\Sigma,\min} \sim \frac{z_R}{2p_{\max}+1}}. \tag{6.8}$$

Note that this minimum can only be achieved in the superposition of a plane wave (spatial "zero" frequency) and $p = p_{\max}$ mode with equal amplitude. However, the intensity of this superposition is oscillatory.

As an example, we consider the case where p summing from $p = 0$ to $p = p_{\max}$ with equal amplitude, the total summing amplitude along z axis can be explicitly written as

$$u_\Sigma(0,0,z) = \sqrt{\frac{2}{\pi}}\frac{w_0}{w(z)}A(z)\exp(-i\Psi(z)), \tag{6.9}$$

with

$$\begin{aligned} A(z) &= \frac{\operatorname{sinc}((p_{\max}+1)\arctan(z/z_R))}{\operatorname{sinc}(\arctan(z/z_R))} \\ \Psi(z) &= (p_{\max}+1)\arctan(z/z_R). \end{aligned} \tag{6.10}$$

In the case when $z \ll z_R$, the total intensity can be approximated as

$$I_\Sigma(0,0,z) \overset{z\ll z_R}{\approx} \operatorname{sinc}^2((p_{\max}+1)\arctan(z/z_R)). \tag{6.11}$$

We can see in this case, the total intensity near the focus is simply a sinc-function. The FWHM Δz is then given as

$$\Delta z_\Sigma \approx 2z_R \tan\left(\frac{\zeta}{p_{\max}+1}\right) \approx \frac{2\zeta}{p_{\max}+1}, \tag{6.12}$$

where $\zeta = 1.39$ is the solution of $\operatorname{sinc}^2\zeta = 1/2$. Fig. 6.5 (a) and its inserted log plot shows the numerical calculated Δz_Σ without $z \ll z_R$ approximation (red dots) with respect to $p_{\max}$, as compared with the $2\zeta/(p_{\max}+1)$ scaling (blue curve). We can see a very good agreement for $p_{\max} \leq 2$. Note that for $p = 0$ Gaussian beam, $\Delta z_\Sigma/z_R = 2$, as the Rayleigh range, by convention, is defined as half maximum at half width (HMHW). Interestingly, Fig. 6.5 (a) suggests that the spatial reduction effect is very significant for the first few p modes ($p_{\max} \leq 4$) and adding larger p modes only contributing marginally. This is important as in practice, larger p modes are typically more challenging to produce experimentally (see Section 6.5 for more details).

Besides the constructive superposition discussed above, the destructive superpositions as '0 − 1' can also be generally analyzed. Consider the 'sign-flipped' superposition

$$u_\Sigma(0,0,z) = \sqrt{\frac{2}{\pi}}\frac{w_0}{w(z)}\sum_{p=0}^{p_{\max}}(-1)^p\exp\big(-i\psi_p(z)\big), \tag{6.13}$$

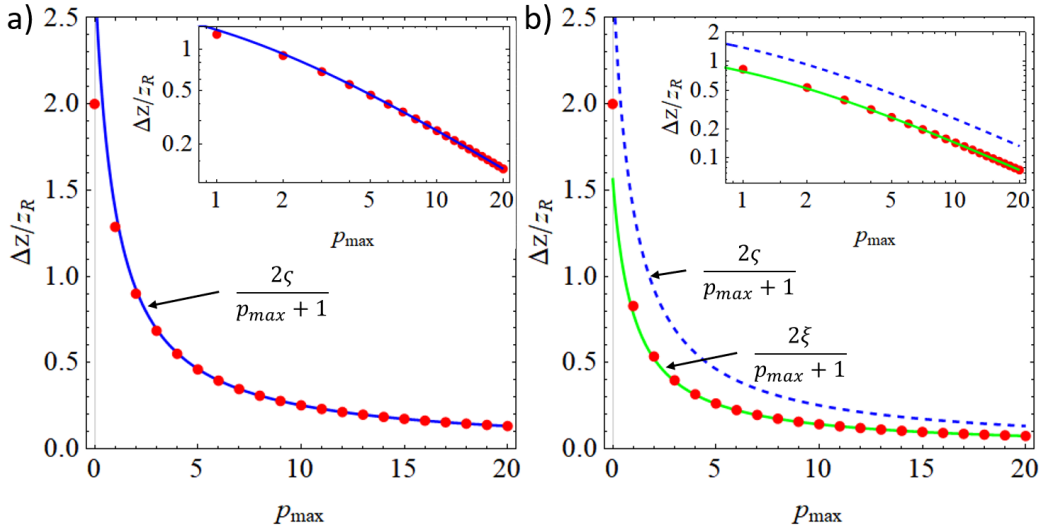

Figure 6.5: The scaling of Δz for superposition of different p modes. (a) the constructive superposition with all p mode amplitude equal. Red dots are numerically calculated Δz without approximation. (b) Sign-flipped superposition, which shows smaller effective Rayleigh range.

with similar derivations as previous case and assuming $z \ll z_R$, the total intensity is given as

$$I_\Sigma(0,0,z) \overset{z\ll z_R}{\approx} \begin{cases} \sin^2((p_{\max}+1)\arctan(z/z_R)), & \text{for odd } p_{\max} \\ \cos^2((p_{\max}+1)\arctan(z/z_R)), & \text{for even } p_{\max}. \end{cases} \tag{6.14}$$

We can see the total intensity near focus is generally oscillatory with the focus intensity takes minimum for odd $p_{\max}$ and maximum for even $p_{\max}$. The FWHM Δz_Σ for this sign-flipped superposition is then given as

$$\Delta z_\Sigma \approx 2z_R \tan\left(\frac{\xi}{p_{\max}+1}\right) \approx \frac{2z_R\xi}{p_{\max}+1}. \tag{6.15}$$

where $\xi = 0.785$ is the solution of $\sin^2\xi = 1/2$. Fig. 6.5 (b) and its inserted log plot shows the numerical calculated Δz_Σ without $z \ll z_R$ approximation (red dots) with respect to $p_{\max}$, as compared with the $2\xi/(p_{\max}+1)$ scaling (green curve) and we can see a very good agreement for $p_{\max} \leq 2$. The scaling for the constructive superposition case is also plotted (blue dashed curve) as a comparison. We can see that for the same $p_{\max}$, the sign-flipped superposition typically has a smaller Δz_Σ.

Now let's look at the spatial reduction in the radial direction. The amplitude of the superposed electric field of radial LG beams (Eq. 6.5) in the radial direction

($z = \varphi = 0$) can be simplified as

$$u_\Sigma(r,0,0) = \sqrt{\frac{2}{\pi}} \exp\left(-\frac{r^2}{w_0^2}\right) \sum_p a_p L_p\left(\frac{2r^2}{w_0^2}\right) \tag{6.16}$$

We see this expression is mathematically equivalent to the summation of Laguerre polynomials for the transverse focus plane. Using the formula

$$L_p^l(x) = \sum_{m=0}^{p} (-1)^m \binom{p+l}{p-m} \frac{x^m}{m!} \tag{6.17}$$

For $x \ll 1$ and $l = 0$, we can approximate this formula with its leading term as $L_p(x) \approx 1 - px$. Using this identity together with $e^{-x} \approx 1 - x$ for $x \ll 1$, we can simplify Eq. 6.16 under $r \ll w_0$ as

$$u_\Sigma(r,0,0) \overset{r \ll w_0}{\approx} \sqrt{\frac{2}{\pi}} \left(1 - \frac{r^2}{w_0^2}\right) \sum_p a_p \left(1 - \frac{2pr^2}{w_0^2}\right) \tag{6.18}$$

From this, we can estimate the FWHM Δx_Σ and Δy_Σ as

$$\boxed{\Delta x_\Sigma = \Delta y_\Sigma \approx \sqrt{2} w_0 \left(\frac{\sum_p a_p}{\sum_p (2p+1) a_p}\right)^{\frac{1}{2}}} \tag{6.19}$$

Note that this expression also valid for single p mode with $p \gg 1$, and by setting one $a_p = 1$ and others zero, we get

$$\boxed{\Delta x_p = \Delta y_p \approx \frac{\sqrt{2} w_0}{\sqrt{2p+1}}} \tag{6.20}$$

for a single p mode without superposition. As a comparison, for the constructive superposition from $p = 0$ to $p = p_{\max}$ with equal amplitude, we get

$$\Delta x_\Sigma = \Delta y_\Sigma \approx \frac{\sqrt{2} w_0}{\sqrt{p_{\max} + 1}} \approx \sqrt{2} \Delta x_{p_{\max}}, \tag{6.21}$$

where $\Delta x_{p_{\max}}$ is the FWHM of $p = p_{\max}$ mode. This suggests the FWHM Δx_Σ,Δy_Σ in the radial direction is not improved compared with a single LG beam with $p = p_{\max}$ (in fact it is getting larger by a factor $\sqrt{2}$ for $p_{\max} \gg 1$). This can also be proved exactly by using the identity[2]

$$\sum_{p=0}^{p_{\max}} L_p^0(x) = L_{p_{\max}}^1(x) \tag{6.22}$$

[2]This identity can be proved by using Eq. 6.17 and the identity $\sum_{p=m}^{p_{\max}} \binom{p}{m} = \binom{p_{\max}+1}{m+1}$

Then, the electric field amplitude for the constructive superposition from $p = 0$ to $p = p_{\max}$ with $a_p = 1$ can be written as

$$\begin{aligned} u_\Sigma(r,0,0) &= \sqrt{\frac{2}{\pi}} \exp\left(-\frac{r^2}{w_0^2}\right) \sum_{p=0}^{p_{\max}} L_p\left(\frac{2r^2}{w_0^2}\right) \\ &= \sqrt{\frac{2}{\pi}} \exp\left(-\frac{r^2}{w_0^2}\right) L^1_{p_{\max}}\left(\frac{2r^2}{w_0^2}\right) \end{aligned} \tag{6.23}$$

Combining the analysis for both axial and radial direction, we reach to the scaling for the focal volume V_Σ as

$$\boxed{V_\Sigma \sim \frac{w_0^2 z_R}{(p_{\max}+1)^2}} \tag{6.24}$$

As a comparison, the focal volume for a single LG beam with index p is

$$\boxed{V_p \sim \frac{w_0^2 z_R}{p_{\max}+1}} \tag{6.25}$$

The main contribution of focal volume reduction is from the interference of Gouy phase along axial direction and this physics can be viewed as an analogy to the pulse width reduction in temporal domain with frequency combs.

6.3 Tightly focused Laguerre-Gauss beams

As shown in previous section, the paraxial approximation provides readily accessible understanding of focused LG beam superpositions and simple analytical forms for analyzing the scaling of volume reduction. However, for tightly focused beams with sub-wavelength waist, the paraxial approximation fails and deviates from the real vectorial solution. In this section, we use the Debye-Wolf integral method [137, 156] to obtain a more accurate description for tightly focused LG beams.

The Debye-Wolf integral

To calculate the vector field of tightly focused LG beams, we turned to the Debye-Wolf integral method which is valid for tight focus and large $F-$number system ($F > 10$)[3]. A detailed derivation and discussion of the Debye-Wolf integral method can be found in Ref. [137]. From Debye-Wolf integral method, the field near focus

[3]The Fresnel F-number is defined as

$$F \equiv \frac{R_p^2}{f\lambda} \tag{6.26}$$

where R_p is the radius of the entrance pupil, f is the focal distance and λ is the wavelength. For our Mitutoyo $NA = 0.7$ objective at $\lambda \sim 1$ μm, we have $F \sim 2000$.

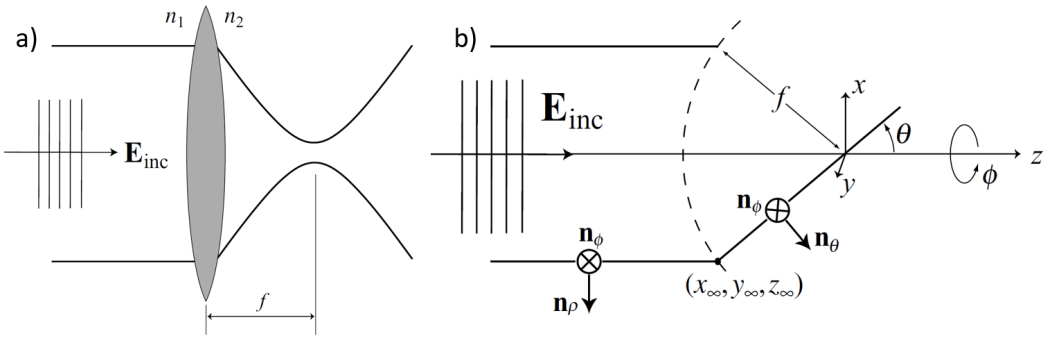

Figure 6.6: (a) Illustration of focusing a beam by an aplanatic lens (b) Illustration of the definition of the symbols in the Debye-Wolf integral. Figs. adapted from Ref. [137].

can be expressed as superposition of spherical waves $\mathbf{E}_\infty$ from the reference plane (indicated as dashed curves in Fig. 6.6) as

$$\begin{aligned}\mathbf{E}(\rho,\varphi,z) = -\frac{ikfe^{-ikf}}{2\pi}\int_0^{\theta_{max}}\int_0^{2\pi}\mathbf{E}_\infty(\theta,\phi) \\ \times e^{ikz\cos\theta}e^{ik\rho\sin\theta\cos(\phi-\varphi)}\sin\theta\,d\phi\,d\theta,\end{aligned} \tag{6.27}$$

where ρ, φ and z are coordinates in the cylinder coordinate with $z = 0$, $\rho = 0$ corresponding to the focus position, θ and ϕ are angles measured from a point on the incident spherical wavefront surface to the focus position with distance f. An illustration of the coordinates is shown in Fig. 6.6. It is easy to see that θ_{max} is related to the NA of an objective by:

$$\text{NA} = n_2\sin\theta_{\text{max}}. \tag{6.28}$$

The far-field $\mathbf{E}_\infty(\theta,\phi)$ in the Debye-Wolf integral (Eq. 6.27) is defined on the reference sphere of the lens (see Ref. [137] Chapter 3 for more details). For input polarization along x axis, the far-field $\mathbf{E}_\infty(\theta,\phi)$ can be expressed as:

$$\begin{aligned}\mathbf{E}_\infty(\theta,\phi) &= E_{\text{inc}}(\theta)[\cos\phi\mathbf{n}_\theta - \sin\phi\mathbf{n}_\phi]\sqrt{\frac{n_1}{n_2}\cos\theta} \\ &= E_{\text{inc}}(\theta)\frac{1}{2}\begin{bmatrix}1+\cos\theta-(1-\cos\theta)\cos2\phi \\ -(1-\cos\theta)\sin2\phi \\ -2\cos\phi\sin\theta\end{bmatrix}\sqrt{\frac{n_1}{n_2}\cos\theta}\end{aligned} \tag{6.29}$$

Insert Eq. 6.29 into Eq. 6.27, and using the mathematical relations for Bessel functions:

$$\int_0^{2\pi} \cos n\phi e^{ix\cos(\phi-\varphi)}\, d\phi = 2\pi(i^n)J_n(x)\cos n\varphi \tag{6.30}$$

$$\int_0^{2\pi} \sin n\phi e^{ix\cos(\phi-\varphi)}\, d\phi = 2\pi(i^n)J_n(x)\sin n\varphi \tag{6.31}$$

where J_n is the nth-order Bessel function results in as an integral form over only variable θ:

$$\begin{aligned}\mathbf{E}(\rho,\varphi,z) =& -\frac{ikfe^{-ikf}}{2}\int_0^{\theta_{max}} E_{\text{inc}}(\theta)e^{ikz\cos\theta}\sqrt{\frac{n_1}{n_2}\cos\theta}\sin\theta \\ &\times\begin{bmatrix}(1+\cos\theta)J_0(k\rho\sin\theta)+(1-\cos\theta)J_2(k\rho\sin\theta)\cos 2\varphi\\ (1-\cos\theta)J_2(k\rho\sin\theta)\sin 2\varphi\\ -2i\sin\theta J_1(k\rho\sin\theta)\cos\varphi\end{bmatrix} d\theta \\ =& -\frac{ikfe^{-ikf}}{2}\sqrt{\frac{n_1}{n_2}}\begin{bmatrix}I_0+I_2\cos 2\varphi\\ I_2\sin 2\varphi\\ -2iI_1\cos\varphi\end{bmatrix}\end{aligned} \tag{6.32}$$

where we have defined $\cos\theta = t$ and the integrals I_0, I_1 and I_2 as:

$$I_0 = \int_{\cos\theta_{max}}^{1} E_{\text{inc}}(t)e^{ikzt}(1+t)J_0(k\rho\sqrt{1-t^2})\sqrt{t}\, dt \tag{6.33}$$

$$I_1 = \int_{\cos\theta_{max}}^{1} E_{\text{inc}}(t)e^{ikzt}\sqrt{1-t^2}J_1(k\rho\sqrt{1-t^2})\sqrt{t}\, dt \tag{6.34}$$

$$I_2 = \int_{\cos\theta_{max}}^{1} E_{\text{inc}}(t)e^{ikzt}(1-t)J_2(k\rho\sqrt{1-t^2})\sqrt{t}\, dt \tag{6.35}$$

We notice that for focusing linear polarization along x, the electric fields near the focus now have non-zero components in y and z direction. Besides, the phase of the electric field in the z component (E_z) is $\pi/2$ out phase of E_x which introduces ellipticity near the focus. As a sanity check, we notice that by neglecting I_1 and I_2, Eq. 6.32 is equivalent to the scalar theory of light propagation.

It is worth noting that there are several symmetries in vector field from Debye-Wolf integral (Eq. 6.32). First, for $x = 0$ ($\varphi = \pi/2$ or $3\pi/2$), we have $\mathbf{E}_y = \mathbf{E}_z = 0$.

This suggests the electric field at $x = 0$ is perpendicular to the $y - z$ plane at $x = 0$ and thus it is Perfect Electric Conductor plane. Next, for $y = 0$ ($\varphi = 0$ or π), we have $\mathbf{H}_x = \mathbf{H}_z = 0$. This suggests the magnetic field at $y = 0$ is perpendicular to the $x - z$ plane and thus it is a Perfect Magnetic Conductor plane. Finally, for the symmetry over $z = 0$ plane ($x - y$ plane). It is easy to show that the real components are symmetric while the imaginary part is anti-symmetric, that is $\mathrm{Re}(I_i(\rho, \varphi, z)) = \mathrm{Re}(I_i(\rho, \varphi, -z))$ and $\mathrm{Im}(I_i(\rho, \varphi, z)) = -\mathrm{Im}(I_i(\rho, \varphi, -z))$ for $i = 0, 1, 2$. These symmetries will be useful in numerical calculations for reducing simulation volume (only need to simulate $1/8$ of the full volume). For the case with a dielectric material present, if the material's polarizability can be approximated as a scalar and the dielectric structure is symmetric with respect to $x - z$ and y_z plane, the scattered field will also respect the same symmetry as the incident field.

Finally, the intensity near the focus is given as

$$I(\rho, \varphi, z) \propto |I_0|^2 + |I_2|^2 + 2\mathrm{Re}(I_0 I_2^*) \cos 2\varphi + 4|I_1|^2 \cos \varphi^2 \tag{6.36}$$

We see that the intensity near focus is not azimuthally symmetric but φ dependent. It can be shown that the waist along main polarization direction (x) is slightly larger than the waist in the direction orthogonal to polarization (y direction).

The Debye-Wolf integral with Laguerre-Gauss beams

For focusing a x-polarized radial LG beam with waist $w_{0,\mathrm{in}}$ ($w_{0,\mathrm{in}} \gg \lambda$) aligned to the lens position, we can express the $E_{\mathrm{inc}}(\theta)$ as

$$\begin{aligned} E_{\mathrm{inc}}(\theta) &= E_0 e^{-(x_\infty^2 + y_\infty^2)/w_{0,\mathrm{in}}^2} L_p(2(x_\infty^2 + y_\infty^2)/w_{0,\mathrm{in}}^2) e^{-i\psi_p(z_\infty)} \\ &= E_0 e^{-f^2 \sin^2\theta / w_{0,\mathrm{in}}^2} L_p(2f^2 \sin^2\theta / w_{0,\mathrm{in}}^2) e^{i(2p+1)\pi/2} \\ &= i(-1)^p E_0 L_p(2s^2(1 - t^2)) e^{-s^2(1-t^2)} \end{aligned} \tag{6.37}$$

Here we defined $s \equiv f/\sin\theta_{\max}$, $t \equiv \cos\theta$. It is worth noting that the infinite plane is defined at the far-field reference sphere and thus the additional phase term $e^{i(2p+1)\pi/2} = i(-1)^p$ will ensure all focused LG modes have zero phase at the focus position $z = 0$.

By convention, the ratio of input waist $w_{0,\mathrm{in}}$ to the pupil radius R_p is called filling factor f_0

$$f_0 \equiv \frac{w_{0,\mathrm{in}}}{R_p} = \frac{w_{0,\mathrm{in}}}{f \sin\theta_{\max}} \tag{6.38}$$

We will see that this filling ratio is an important parameter for focusing a LG beam at finite aperture and different filling ratio may have very different beam shapes.

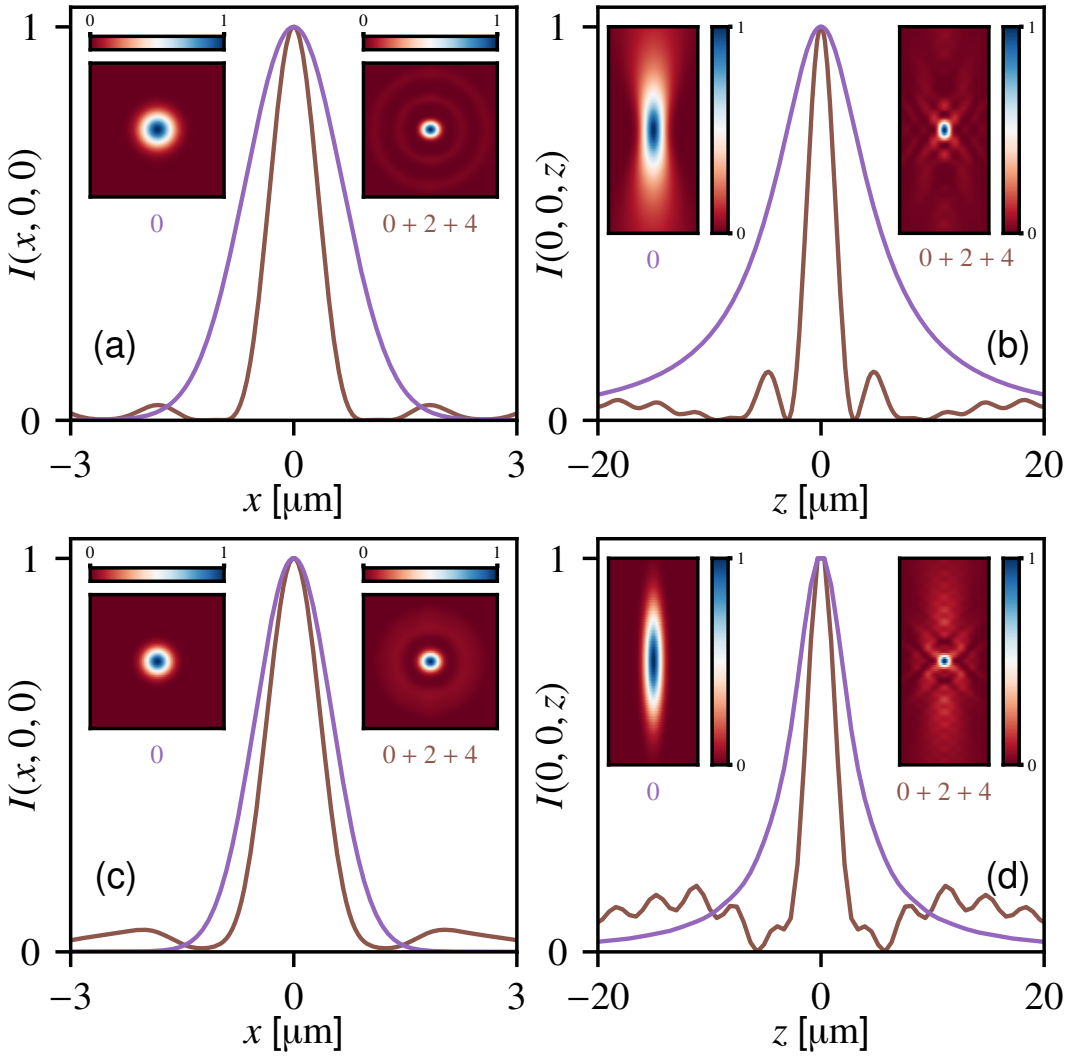

Figure 6.7: Focused intensity distributions calculated within the vectorial Debye approximation for $p = 0$ (violet) and '0+2+4' (brown) inputs for NA = 0.7. Two filling factor values are compared: For $f_0 = 0.35$ (a) x-line cut transverse intensity profiles. The insets provide the x-y intensity distribution in the focal plane $z = 0$. (b) z-line cut axial intensity profiles. The insets correspond to the x-z distribution. For $f_0 = 0.45$ (c,d). Plotted intensities are normalized to their maximum values.

Inserting Eq. 6.37 into Eq. 6.32, we can calculate the field distribution of tightly focused LG beams near the focus of a high NA aplanatic objective. Fig. 6.7(a, b) shows the line-cuts and 2D distribution (inserted) of the intensity profile near focus for focusing $p = 0$ and '0+2+4' superposition beams with NA = 0.7 objective at filling ratio $f_0 = 0.35$ (a, b). For $p = 0$ and $f_0 = 0.35$, the intensity profiles in both radial and axial directions (violet curves in (a, b)) are quite similar to those in Fig. 6.2 with a 1.3 µm waist in the focal plane. The FWHM for each direction are $\Delta x_0 = 1.55\,\mu$m, $\Delta y_0 = 1.51\,\mu$m and $\Delta z_0 = 10.3\,\mu$m, corresponding to a focal volume $V_0 = 24\,\mu\text{m}^3$. As shown in Fig. 6.7(a, b) for input of '0+2+4' superposition at the same filling ratio $f_0 = 0.35$ (brown curves), reductions in both transverse and longitudinal widths relative to $p = 0$ input are evident even in the vector theory with wavelength-scale focusing. The FWHM of focus at each direction for the '0+2+4' superposition input are $\Delta x_\Sigma = 0.84\,\mu$m, $\Delta y_\Sigma = 0.72\,\mu$m and $\Delta z_\Sigma = 2.78\,\mu$m, corresponding to a focal volume $V_\Sigma = 1.7\,\mu\text{m}^3$. The ratio of focal volume for $p = 0$ and '0+2+4' superposition is $V_0/V_\Sigma \simeq 14$.

It is found that further increase the filling ratio f_0 for the '0+2+4' superposition input does not lead to further reduction of the focal volume. As shown with the brown curves in Fig. 6.7 (c, d) for filling ratio $f_0 = 0.45$, the central width of the focus is not reduced but the peak of two side lopes increases. However, this is not the case for $p = 0$ (violet curve in Fig. 6.7 (c, d)) for the same filling ratio $f_0 = 0.45$ where the fitted waist $w_0 \simeq 1\,\mu$m. The existence of the optimal filling ratio is related to the truncation of highest order of LG beam in the superposition which we will discuss in Section 6.4 in detail.

Tight focusing is accompanied by a longitudinal polarization component, which leads to a spatially-dependent elliptical polarization and to dephasing mechanisms for atom trapping [115, 181]. Given the local polarization vector $\hat{\epsilon}$, one can define the vector $\mathbf{C} = \text{Im}(\hat{\epsilon} \times \hat{\epsilon^\star})$, which measures the direction and degree of ellipticity. $|\mathbf{C}| = 0$ corresponds to linear polarization while $|\mathbf{C}| = 1$ for circular polarization. 6.8 (a) provides C_y in the focal plane for the '0+2+4' superposition input. Due to tighter confinement, the polarization gradient reaches $dC_y/dx = 1.6/\mu m$ for '0+2+4' superposition input, to be compared to $0.4/\mu m$ for $p = 0$ input. We can further quantify the impact of this ellipticity for trapping atoms by the light shifts (scalar, vector and tensor shifts) of the '0+2+4' superposition for trapping the Cs atom, as shown in Fig. 6.8 (b, c). Here, we choose the wavelength at a magic wavelength of Cs ($\lambda = 935.7$ nm) with a given trap depth $U/k_B = 1$ mK (for $NA = 0.7$ and

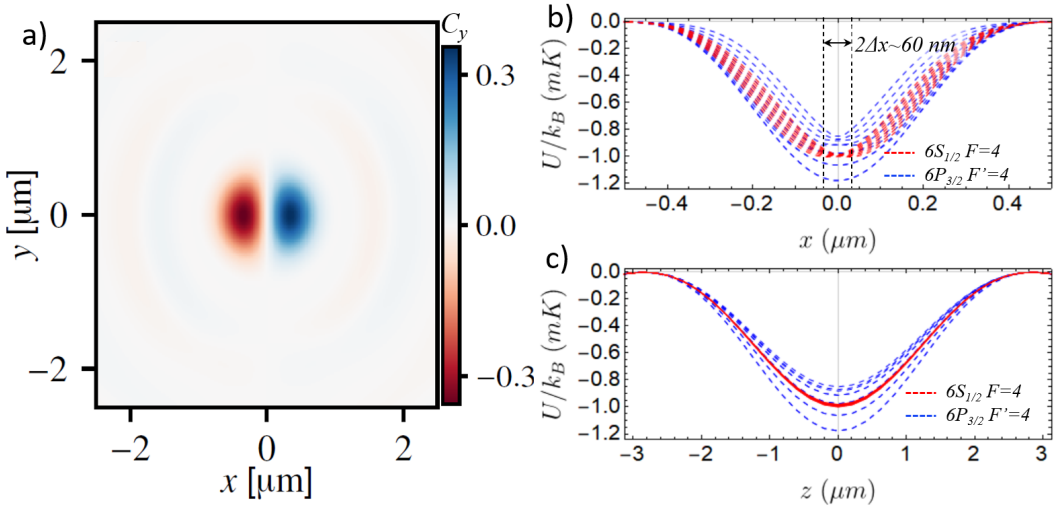

Figure 6.8: (a) Polarization ellipticity C_y in the focal plane for the '0+2+4' input with NA = 0.7 and $f_0 = 0.35$. (b, c) the light shifts for Cs atom at magic wavelength 935.7 nm with trap depth $U/k_B = 1$ mK for transverse (b) and axial direction (c). The dashed lines indicates the m_F levels in $6S_{1/2}$, $F = 4$ ground state (red dashed) and in $6P_{3/2}$, $F' = 4$ excited state (blue dashed). In (b), we can see the ground state trap is shifted away for the center by $\delta x \sim 30$ nm for the $m_F = 4$ sublevel.

$f_0 = 0.35$). Vector light shifts are clearly observed in transverse direction as shown Fig. 6.8 (b). The trap center for different m_F levels in $6S_{1/2}$, $F = 4$ ground state are shifted away from the center by $\delta x \sim 30$ nm. As the vector light shift is equivalent to a magnetic field gradient along x direction, it can be suppressed in experiment by an opposite magnetic gradient as already demonstrated in Ref. [181].

Till now, we have far directed the attention to free-space optical tweezers for atoms and molecules. However, there are important settings for both particle trapping and imaging in which the focal region is not homogeneous but instead contains significant spatial variations of the dielectric constant over a wide range of length scales from nanometers to microns. Important examples in AMO Physics include recent efforts to trap atoms near nano-photonic structures such as dielectric optical cavities and PCWs [19, 33, 40, 86, 108, 181, 184]. These efforts have been hampered by large modification of the trapping potential of an optical tweezer in the vicinity of a nano-photonic structure, principally associated with specular reflection that produces high-contrast interference fringes extending well beyond the volume of the tweezer. With the electric field of the tightly focused LG beams calculated from Debye-Wolf integral, we can further calculate the field distribution with arbitrary dielectric structures. Here the calculation is done by applying the result from

free-space Debye-Wolf as background field without scattering and solve for the scattering field with the presence of a dielectric nano-structure. Results of focused $p = 0$ Gaussian beam input and '0+2+4' superposed LG beams aligning to the APCW are shown in Fig. 6.9 for $NA = 0.7$, $f_0 = 0.35$. This result again confirms the spatial reduction of "fringe" fields from the superposition of LG beams near complex dielectric nanostructures.

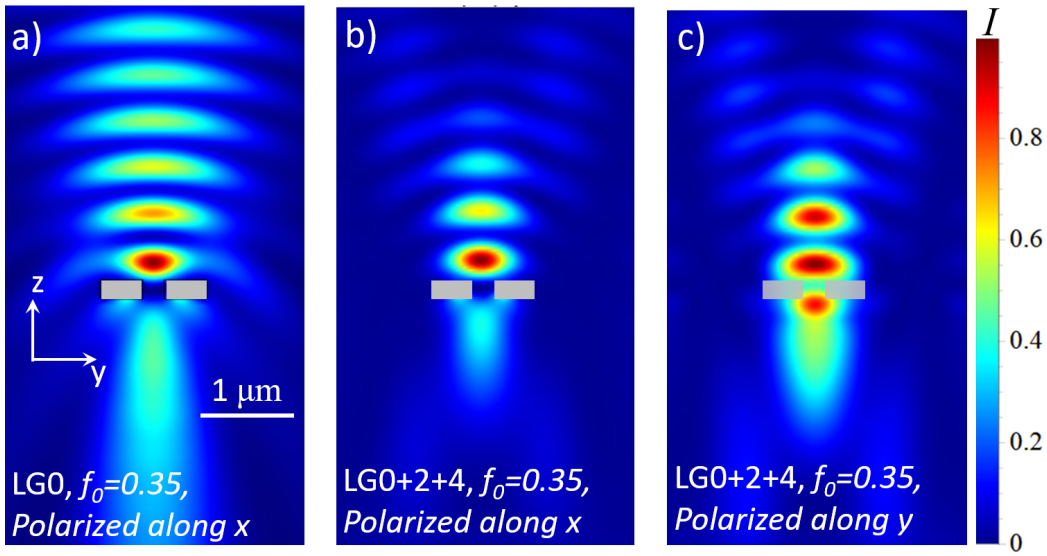

Figure 6.9: COMSOL®[45] simulation of aligning a tightly focused LG beams scatter on the APCW (indicated by gray rectangle). With focus position aligned to the geometric center of the APCW. (a) for the input field distribution is $p = 0$ Gaussian beam, polarization along x; and (b) for the input field distribution is '0+2+4' superposed LG beams and polarization along x. (c) for the input field distribution is '0+2+4' superposed LG beams and polarization along y. All three plots are calculated with the background field calculated from Debye-Wolf integral under NA = 0.7 and $f_0 = 0.35$.

6.4 The optimal filling ratio

As already shown in Fig. 6.7, the truncation of LG beams in finite aperture will lead to an optimal filling ratio for the superposed LG beam input such as the '0+2+4' superposition. To understand this, we plot the electric field amplitude for $p = 0$, $p = 4$ and '0+2+4' superposition at the filling ratio of $f_0 = 0.35$ as in Fig. 6.10 (a). As we can see for $f_0 = 0.35$, the $p = 4$ electric field amplitude (blue curve) has already partially truncated by the aperture (gray area). Further increase the filling ratio will misrepresent the $p = 4$ LG beam on the input pupil and as a result, the

foundation of spatial reduction due to Gouy phase superposition will not be valid any more. The pupil apodization effects will modify the spatial properties of the focused radial LG beams according to their radial mode number p [79]. In fact, larger filling ratio truncates the LG beams and can generate completely different field profile (even bottle beams for a single LG $p = 1$ mode input).

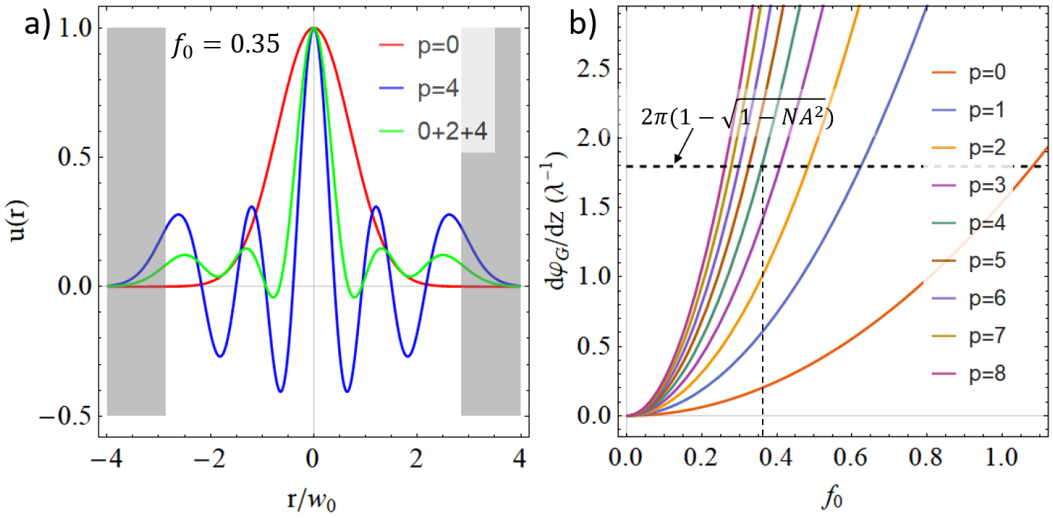

Figure 6.10: (a) Electric field amplitude of $p = 0$ (red curve), $p = 4$ (blue curve) and $0 + 2 + 4$ superposition (green curve) at filling ratio $f_0 = 0.35$. The gray shade region represents the physical cutoff from the entrance pupil of the objective with $NA = 0.7$. (b) Phase gradient of the focused field for different LG beam input assuming $NA = 1$. The horizontal dashed line indicates the maximum available phase gradient from a finite objective with NA = 0.7. The crossing of the horizontal dashed line and phase gradient for $p = 4$ LG beam (green curve) corresponds to a filling ratio $\simeq 0.35$.

Beyond the intuitive picture of truncation of high order LG beams at larger filling ratio, we further developed a simple model based on the analysis of Gouy phase to predict the optimal filling ratio. For focusing a LG beam with waist $w_{0,\text{in}}$ by a lens with focal length f (assuming the input waist is at the lens position), the ABCD matrix from Gaussian optics predicts the input and output waist (w_0) are related by $w_0 = f\lambda/\pi w_{0,\text{in}}$. This leads to a Gouy phase as

$$\begin{aligned} \frac{d\psi_G}{dz} &\approx \frac{2p+1}{z_R} \\ &= \frac{(2p+1)\pi}{\lambda}\frac{w_{0,\text{in}}^2}{f^2} \\ &= \frac{(2p+1)\pi}{\lambda} f_0^2 \text{NA}^2 \end{aligned} \tag{6.39}$$

In the last step, we use the fact that $f_0 = w_{0,\text{in}}/f\text{NA}$. This suggests for NA = 1 system, the phase gradient increases quadratically with f_0 (or input waist $w_{0,\text{in}}$). However, this phase gradient cannot be arbitrary high for a finite aperture objective. As I will prove later in Section 6.6, the maximum phase gradient for an objective with NA is given as

$$\left(\frac{d\psi_G}{dz}\right)_{\max} = k(1 - \sqrt{1 - \text{NA}^2}) \tag{6.40}$$

By equal Eq. 6.39 to this maximum phase gradient, we can solve for the optimal filling ratio as

$$\boxed{f_{0,\text{opt}} = \frac{1}{\text{NA}}\left(\frac{2}{2p+1}\right)^{\frac{1}{2}}\left(1 - \sqrt{1 - \text{NA}^2}\right)^{\frac{1}{2}}} \tag{6.41}$$

For NA = 0.7, $p = 4$, this equation predicts an optimal $f_{0,\text{opt}} \simeq 0.36$. In Fig. 6.10 (b), we show the plot of phase gradient for $p = 0$ to $p = 8$ based on Eq. 6.39. The maximum phase gradient for NA = 0.7 is also indicated with horizontal dashed lines. The crossing of NA = 1 phase gradient (colored curves) with the maximum phase gradient for finite aperture predicts the maximum filling ratio for each p mode to preserve its property.

Finally, for the application of trapping atom, an "optimal" filling ratio might correspond to the highest trap frequency at a given trap depth, as the trap frequency measures how well a particle or atom is confined inside an optical tweezer trap. To find the relation between trap frequency and filling ratio, we further simplify Eq. 6.32 by using the properties of Bessel functions, $J_0(x = 0) = 1$ and $J_n(x = 0) = 0$, for $n \geq 1$ and we find only $\mathbf{E}_x$ component non-vanishing along z axis

$$\mathbf{E}(\rho = 0, \varphi, z) = -\frac{ikfe^{-ikf}}{2}\sqrt{\frac{n_1}{n_2}}\int_{\cos\theta_{max}}^{1} E_{\text{inc}}(t)e^{ikzt}(1+t)\sqrt{t}\,dt \tag{6.42}$$

By taking a norm of the electric field above and extracting the coefficient of z^2 terms, we found the trap frequency is proportional to[4]:

$$\omega_z^2 \propto \left||I_{z1}|^2 - \text{Re}(I_{z0}I_{z2}^*)\right| \tag{6.43}$$

[4]The trap potential is proportional to the intensity in the case where there is no vector shift along z axis.

where the integrals I_{z0}, I_{z1} and I_{z2} are defined as:

$$I_{z0} = \int_{\cos\theta_{max}}^{1} E_{\text{inc}}(t)(1+t)\sqrt{t}\,dt \tag{6.44}$$

$$I_{z1} = \int_{\cos\theta_{max}}^{1} E_{\text{inc}}(t)t(1+t)\sqrt{t}\,dt \tag{6.45}$$

$$I_{z2} = \int_{\cos\theta_{max}}^{1} E_{\text{inc}}(t)t^2(1+t)\sqrt{t}\,dt \tag{6.46}$$

Note that the term $|I_{z1}|^2 - \text{Re}(I_{z0}I_{z2}^*)$ in Eq. 6.43 can be either positive or negative and the equation $|I_{z1}|^2 - \text{Re}(I_{z0}I_{z2}^*) = 0$ defines a critical filling ratio when the potential transforms from a trap (intensity maximum at focus) to a anti-trap (intensity minimum at focus). A plot of Eq. 6.43 is shown in Fig. 6.11 (a). We can see clearly the two local maximum trap frequencies at $f_0 = 0.39$ and $f_0 = 0.74$. Despite the axial trap is higher at $f_0 = 0.74$, the intensity is more oscillatory (with strong side lobes) along axial direction as shown in Fig. 6.11 (b, c). As we will see in Section 6.7, this side lobes can introduce heating and reduce the atom delivery efficiency from free-space to dielectric surface [20]. Two other filling ratio $f_0 = 1$ and $f_0 = 5$ are also presented in Fig. 6.11 (d, e). For $f_0 = 1$, it corresponds to the flatten trap intensity in the axial direction which properties similar to the Bessel beams [55] while the $f_0 = 5$ corresponds to the limit of uniform input with diffraction-limited spot size.

Similarly, we can derive the trap frequency for the transverse direction by expanding to second order of ρ in intensity and we get:

$$\omega_\rho^2 \propto \left|2\text{Re}(I_{z0}I_{\rho 0}^*) - \text{Re}(I_{\rho 1}I_{z0}^*)\cos 2\varphi - 4\left|I_{\rho 2}\right|^2\cos\varphi^2\right| \tag{6.47}$$

with I_{z0} defined as above and $I_{\rho 0}$, $I_{\rho 1}$ and $I_{\rho 2}$ defined as:

$$I_{\rho 0} = \int_{\cos\theta_{max}}^{1} E_{\text{inc}}(t)(1+t)(1-t^2)\sqrt{t}\,dt \tag{6.48}$$

$$I_{\rho 1} = \int_{\cos\theta_{max}}^{1} E_{\text{inc}}(t)(1-t)(1-t^2)\sqrt{t}\,dt \tag{6.49}$$

$$I_{\rho 2} = \int_{\cos\theta_{max}}^{1} E_{\text{inc}}(t)(1-t^2)\sqrt{t}\,dt \tag{6.50}$$

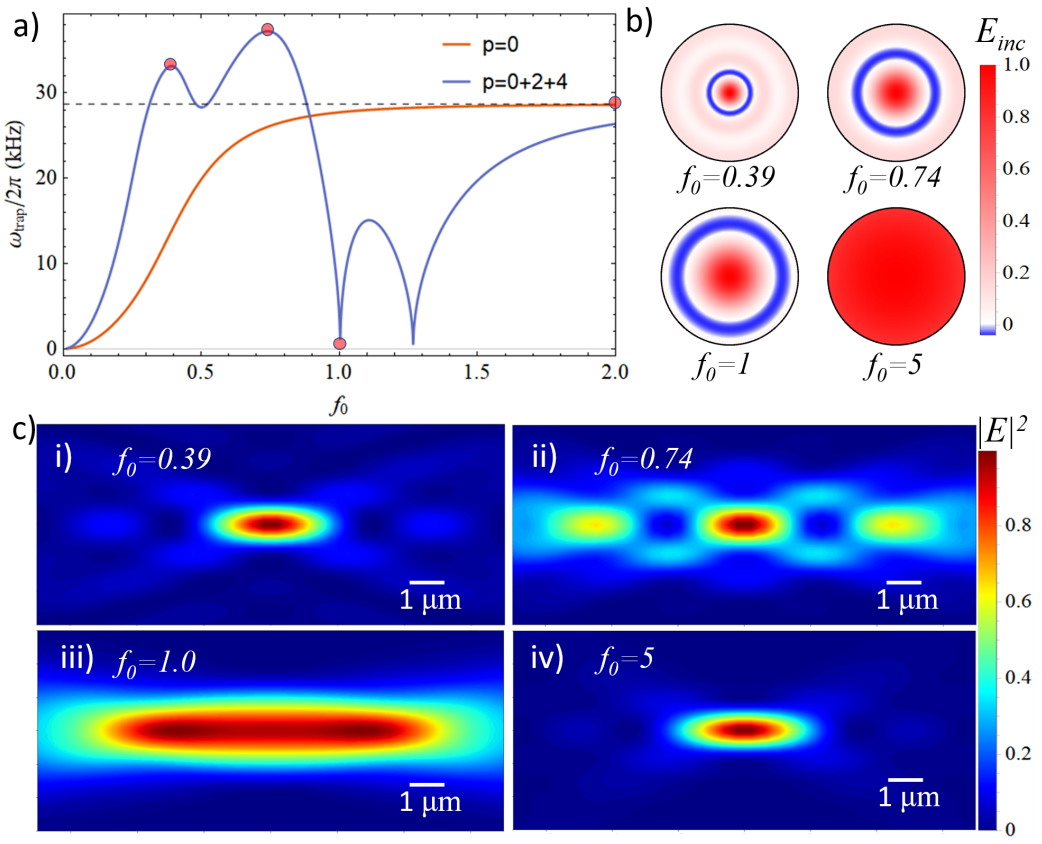

Figure 6.11: (a) Axial trap frequency as a function of filling ratio for the $p = 0$ input (orange) and the '0+2+4' superposition (blue) with $NA = 0.7$ and trap depth (U_{trap}/k_B) in focus position fixed to be 1 mK. (b) The input electric field profile for the '0+2+4' superposition at filling ratios $f_0 = 0.39$, $f_0 = 0.74$, $f_0 = 1$. (c) (i-iv) the intensity profile near focus at filling ratios $f_0 = 0.39$, $f_0 = 0.74$, $f_0 = 1$ and $f_0 = 5$.

To validate the trap frequencies expressions derived above (Eq. 6.43 and Eq. 6.47), we calculated the angular trap frequencies ω_x and ω_z by numerically solving the spatial time-independent Schrödinger's equation for a single Cesium atom and a scalar optical trap potential with depth of 1 mK (for $6S_{1/2}$). The results are presented in Fig. 6.12. As expected, the trap frequencies have significant increases in a wide filling ratio range for the '0+2+4' superposition input (brown) as compared to $p = 0$ Gaussian beam input. Different from monotonic behavior for $p = 0$ Gaussian input, the axial trap frequency for '0+2+4' superposition has a local maximum around $f_0 \simeq 0.39$. This suggest the $f_0 = 0.35$ result we shown in Fig. 6.7 is already close to the optimal value for maximizing trap frequency at a given trap depth. On experimental side, the choice of the local maximum at small value $f_0 \sim 0.35$ not only alleviates practical requirements of the objective lens (e.g., focal length and

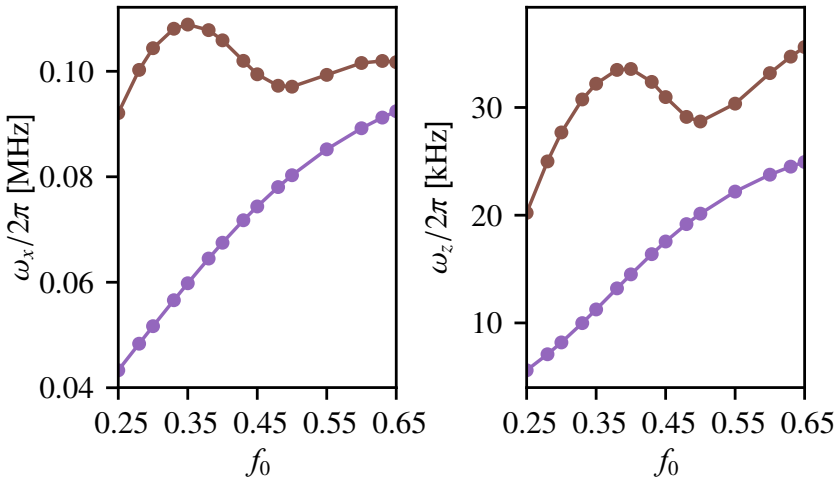

Figure 6.12: Dependence of the angular radial (x-cut) (a) and (b) axial trap frequencies (i.e. ω_x and ω_z at the bottom of the trap) as functions of the objective lens filling factor f_0, with fixed NA = 0.7. (Violet) the input field distribution is $p = 0$ Gaussian beam; (Brown) the input field distribution is '0+2+4' superposed LG beams.

working distance) but also permits a description of the focused fields not dominated by diffraction losses.

Finally, as the trap volume $V_{\text{trap}} \propto (\omega_z \omega_\rho^2)^{-1}$, the expressions for trap frequencies in the axial and transverse directions (Eq. 6.43 and 6.47) can be combined to find the optimal filling ratio for the minimum trap volume, with a given input profile E_{inc}.

6.5 Generate Laguerre-Gauss beams with spatial light modulator

Various methods have been investigated to produce LG beams with high purity [6]. A relatively simple technique consists of spatial phase modulation of a readily available Gaussian source beam with a series of concentric circular binary phase steps to replicate the phase distribution of the targeted field $\vec{E}_{p_{target}}$ with $p_{target} > 0$ [10]. The maximum purity for this technique is ~ 0.8, with the deficit of ~ 0.2 due to the creation of p components other than the single p_{target}. Moreover, it is desirable to generate not only high purity LG beams for a single p_{target} but also arbitrary coherent sums of such modes, as for $0 + 2 + 4$. Rather than generate separately each component from the set of required radial modes $\{p\}_{target}$, here we propose a technique with a single SLM that eliminates the need to coherently combine multiple beams for the set $\{p\}_{target}$. Our strategy reproduces simultaneously both the phase and the amplitude spatial distributions of the desired complex electric field (and in

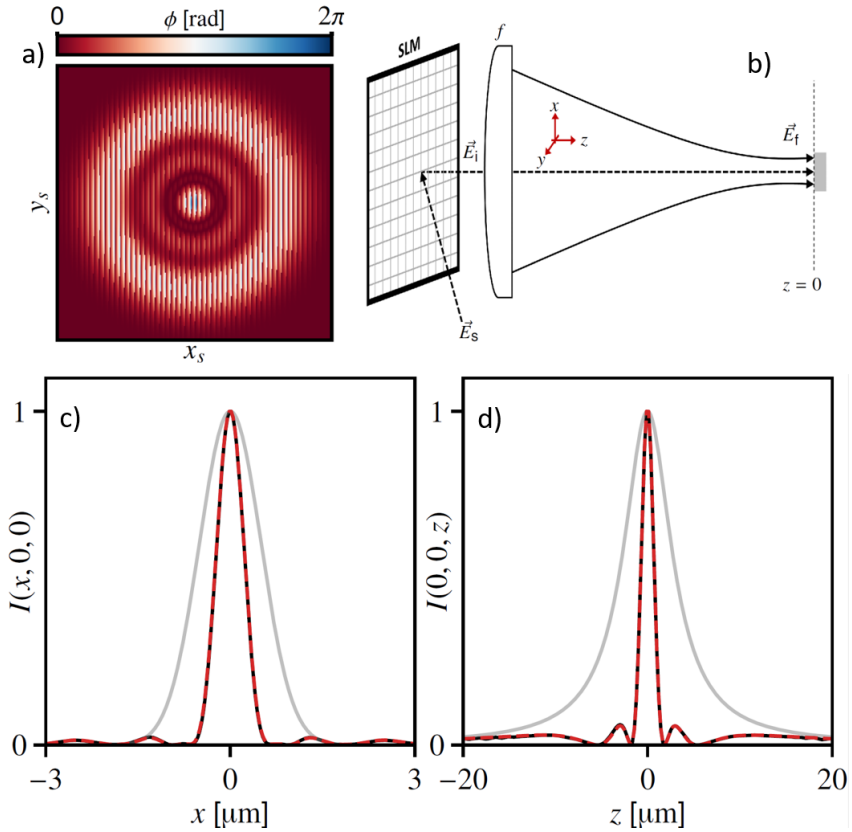

Figure 6.13: (a) Calculated transverse phase profile ϕ applied to the spatial phase modulator (SLM) to generate the field $\vec{E}_\Sigma$. (b) An incident Gaussian source field $\vec{E}_s$ is incident on the SLM. The first order diffracted field $\vec{E}_i$ on the exit plane of the SLM is then focused by an objective lens with effective focal length f to form the field $\vec{E}_f$ in the focal plane at $z = 0$. (c) Line cuts along x of $|\vec{E}_f|^2$ in the focal plane for modulation of the SLM with $\phi(x_s, y_s)$ calculated to generate $0 + 2 + 4$ (red solid line), ideal target intensity $|\vec{E}_\Sigma|^2$ (black dashed line), and Gaussian intensity $|\vec{E}_0|^2$ (gray line). (d) As in (c), but for line cuts along z with $x = y = 0$.

principle, the polarization distribution for propagation phenomena beyond the scalar field approximation).

Figs. 6.13(a, b) illustrate our technique for the case of the target field $\vec{E}_\Sigma$, with Σ represents '$0 + 2 + 4$' superposition. Amplitude information for the sum of complex fields comprising $\vec{E}_\Sigma$ is encoded in a phase mask by contouring the phase-modulation depth of a superimposed blazed grating as developed in [24, 48]. For atom trapping applications with scalar polarizability, the tweezer trap depth is proportional to the peak optical intensity in the focal plan, where for the coherent field superposition $\vec{E}_\Sigma$, the peak intensity reaches a value identical to that for $\vec{E}_0$ at only $1/9$ of the invested trap light power, which helps to mitigate losses associated with the blazed

grating.

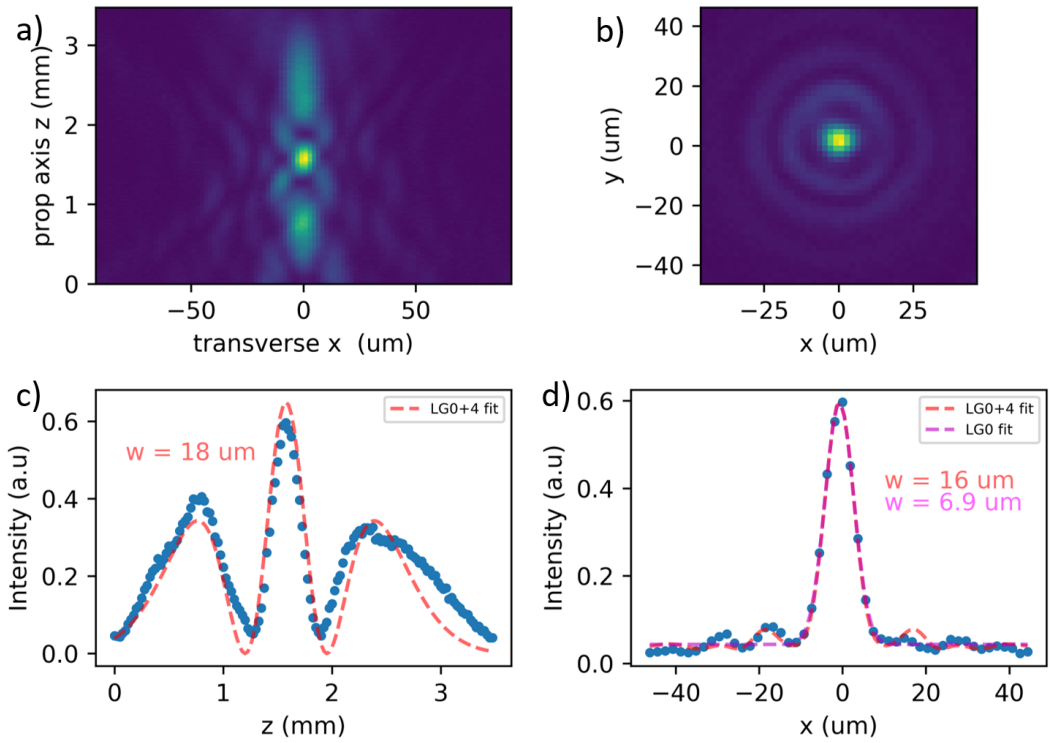

Figure 6.14: Preliminary results of LG mode superposition generated by the SLM for $p = 0+4$ superposition. (a-d) Measured intensity profiles in (a) $x-z$ plane with $y = 0$, (b) $x-y$ plane at the focus position, (c) line cut (blue dots) of (a) along z axis with $x = 0$, (d) line cut (blue dots) of (b) along x axis with $y = 0$. Here the red dashed curves correspond to the model fit from paraxial solutions of $p = 0+4$ with the waist $w = 18$ μm from fitting along z and $w = 16$ μm from fitting along x axis. The dashed pink curve in (d) represents a Gaussian beam $p = 0$ fit, with the fitted effective waist $w = 6.9$ μm. Image courtesy of Jean-Baptiste Béguin .

Fig. 6.13 (b) shows numerical results for a Gaussian source field $\vec{E}_{\rm s}$ input to a SLM to create the field $\vec{E}_{\rm i}$ leaving the SLM. $\vec{E}_{\rm i}$ is then focused by an ideal thin spherical lens and propagated to the focal plane at $z = 0$ by way of the Fresnel-Kirchhoff scalar diffraction integral. The resulting intensity distributions in the focal plane are plotted in Fig. 6.13(c,d) (red solid) for comparison with the ideal $\vec{E}_{\rm i} = \vec{E}_0$ (gray solid) and ideal $\vec{E}_{\rm i} = \vec{E}_\Sigma$ (black dashed). These results are encouraging for our efforts to experimentally generate tightly focused radial LG superpositions.

With the design principles presented above, Fig. 6.14 shows an example of the preliminary experimental results that demonstrated the axial reduction of superposed LG modes. Here, the specific combination we consider is $p = 0+4$ and the intensity profile in space is measured by scanning the position of the camera (with pixel size

$\simeq 2\ \mu$m) along z axis. As shown in Fig. 6.14 (a) in $x-z$ plane and (c) for a line cut along z axis, the measured axial profile (blue dots) matches very well the theoretical predictions (dashed red curves). Further experiment for tightly focused LG beams with high NA objectives is a work under progress.

6.6 Focal volume reduction beyond Laguerre-Gauss beams

The general problem

In this section, we investigate the possibility to further reduce the focal volume further beyond the results within Laguerre-Gauss beams. Generally, the point spread function generated from an objective can be interpreted as an interference phenomena as shown in the Fig. 6.15 for both the radial (a) and axial (b) directions. Four different types are identified as shown in Fig. 6.15. By engineering the wavefront amplitude A and phase Ψ, we can reduce the size of the a focal spot specific for either the radial or the axial direction. However, as shown in Ref. [163], there is a fundamental limitation for the product of radial and axial spot size and it is generally impossible for both radial and axial takes the minimum.

To get the minimum spot size along z, we recall that in the superposition of LG mode, the smallest dimension $z_{\Sigma,\min}$ is achieved by the superposition of the maximum index $p_{\max}$ LG beam with the 'zero' spatial frequency plane wave (Eq. 6.8). This interference from the maximum and the minimum Gouy phase gradient near the focus generates a minimum spot size along axial direction. By following the same logic, the smallest dimension $z_{NA,\min}$ for a finite aperture objective with numerical aperture NA can be generated by the superposition of maximum phase gradient with the smallest phase gradient. To understand what is the maximum and minimum phase gradient for a finite aperture objective, we approach this problem by studying the Gouy phase within the Debye-Wolf integral method.

Apodization and the Gouy phase

To get the phase gradient focused by a finite aperture objective, we separate the input field $E_{\text{inc}}(\theta)$ in the pupil aperture into a series of concentric annuluses with width $\delta\theta$. We call these concentric annuluses as 'partial waves'. As $\delta\theta \to 0$, we get

$$E_{\text{inc}}(\theta) = \int_0^{\theta_{\max}} E_{\text{inc}}(\theta')\delta(\theta'-\theta)\, d\theta'. \tag{6.51}$$

That is the input field can be viewed as a summation of infinite 'partial waves' $\delta(\theta'-\theta)$ with amplitude $E_{\text{inc}}(\theta')d\theta'$. Equivalently, by defining $t \equiv \cos\theta$, we

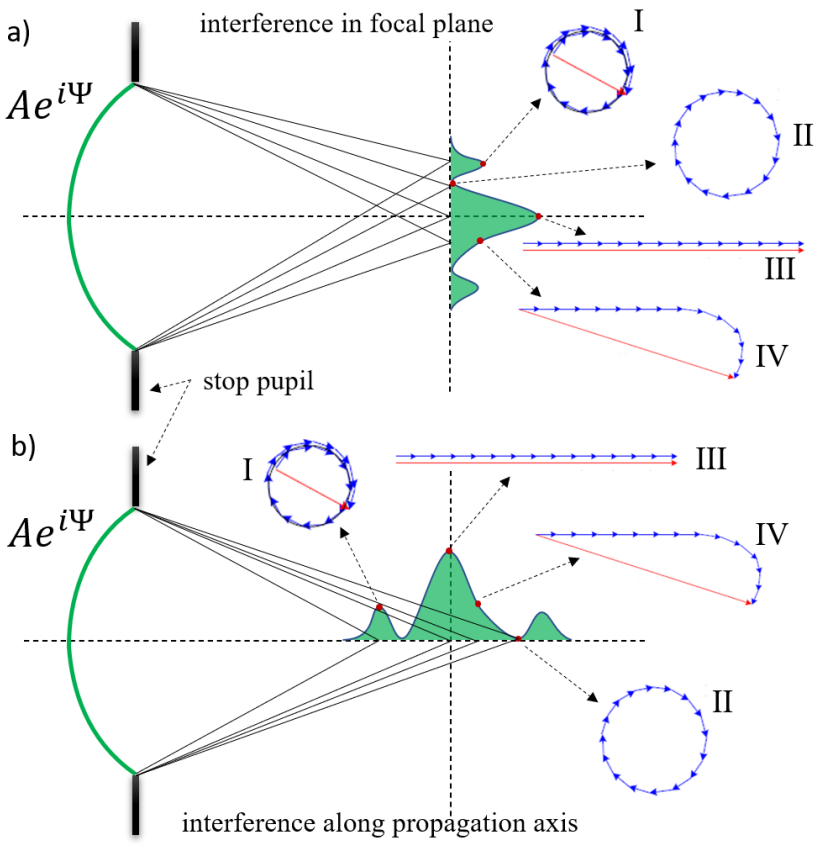

Figure 6.15: Interpretation of the point spread function as an interference phenomena. (a) Interference on the focal plane. (b) Interference along the propagation axis. Four different interference types are illustrated with summation of phasors as (I) local intensity maximum (side lope peak) when a half circle is formed (II) intensity minimum as completely destructive interference (III) Intensity maximum as completely constructive interference (IV) side of peak as reduced constructive interference.

rewrite Eq. 6.51 as

$$E_{\text{inc}}(t) = \int_{\cos\theta_{max}}^{1} E_{\text{inc}}(t')\delta(t'-t)\,dt'. \tag{6.52}$$

Next, we would like to calculate the Gouy phase from the 'partial wave' $\delta(t-t_0)$ for $t_0 \in [\cos\theta_{\max}, 1]$. Replacing $E_{\text{inc}}(t)$ with $\delta(t-t_0)$ in Eq. 6.42, we get

$$\begin{aligned}\mathbf{E}(\rho=0,\varphi=0,z) &= -\frac{ikfe^{-ikf}}{2}\sqrt{\frac{n_1}{n_2}}\int_{\cos\theta_{max}}^{1}\delta(t-t_0)e^{ikzt}(1+t)\sqrt{t}\,dt \\ &= -\frac{ikfe^{-ikf}}{2}\sqrt{\frac{n_1}{n_2}}e^{ikzt_0}(1+t_0)\sqrt{t_0}.\end{aligned} \tag{6.53}$$

We recall the definition of the Gouy phase for a focusing beam is (Eq. 6.3)

$$\psi_G \equiv kz - \mathrm{Arg}(\mathbf{E}(\rho = 0, \varphi = 0, z)). \tag{6.54}$$

We get the Gouy phase for the 'partial wave' $\delta(t - t_0)$ as

$$\psi_G(t_0) = kz(1 - t_0). \tag{6.55}$$

As $\psi_G(t_0)$ is a linear function of t_0, we can calculate the maximum and minimum phase gradient as

$$\psi_{G,\max}(t_0 = \cos\theta_{\max}) = kz(1 - \cos\theta_{\max}), \tag{6.56}$$

$$\psi_{G,\min}(t_0 = 1) = 0. \tag{6.57}$$

Physically, the maximum phase gradient corresponds to an extremely thin annulus (mathematically speaking, a circle) on the edge of the input aperture. This apodization is very common in the generation of Bessel beams [54]. The minimum phase gradient corresponds to extremely small annulus (mathematically speaking, a dot) at the center of the pupil. The Gouy phase for apodization makes sense as for a small filling ratio input beam, the focal field has very large Rayleigh range and thus negligible Gouy phase gradient.

As we can see in the LG beam superposition case, the superposition of two waves with largest phase gradient contrast will produce the smallest spot size along z axis. Here combining the two limits ('circle' and 'dot') should give us the smallest spot size along z axis. As illustrated in Fig. 6.16 (a, b), the apodization shape of this input consists a dot and circle and we name this mode as CD profile. As an example, the input field can be take the form

$$E_{\mathrm{inc}}(t) = \frac{1}{(1+t)\sqrt{t}}(\delta(t - \cos\theta_{\max})) + \delta(t - 1))). \tag{6.58}$$

Inserting this into Eq. 6.42, we get the electric field near focus to be

$$\mathbf{E}(\rho = 0, \varphi = 0, z) \propto \left(e^{ikz} + e^{ikz\cos\theta_{\max}}\right), \tag{6.59}$$

and the intensity is:

$$I(\rho = 0, \varphi = 0, z) \propto \cos^2\left[\frac{1}{2}kz(1 - \cos\theta_{\max})\right]. \tag{6.60}$$

The first intensity minimum z_1 is at:

$$z_{1,\mathrm{CD}} = \frac{\lambda}{2(1 - \cos\theta_{max})}. \tag{6.61}$$

As a comparison, the first minimum position under uniform illumination (the diffraction limited spot size) is:

$$\boxed{z_{1,\mathrm{diff}} = \frac{2\lambda}{\mathrm{NA}^2} = \frac{2\lambda}{1-\cos^2\theta_{\max}}}. \tag{6.62}$$

The equation above defines the diffraction limit resolution in the axial direction. Then the ratio to diffraction limit G_A, as defined in Ref. [163] for the CD profile will be:

$$G_A = \frac{1}{4}(1+\cos\theta_{\max}) = \frac{1}{4}(1+\sqrt{1-\mathrm{NA}^2}). \tag{6.63}$$

We notice that the minimum ratio is achieved at $G_{A,\min} = 0.25$ for NA = 1 and the corresponding first intensity minimum is at $z_{1,\mathrm{CD,min}} = \lambda/2$. While if only the 'circle' is presented (as shown in the upper panel in Fig. 6.16 (a), this will generate the Bessel beams), the first intensity minimum is at $z_1 = \lambda$ and $G_A = 0.5$ [163] for NA = 1. For our objectives with NA = 0.7, we calculate the first intensity minimum for the CD profile to be $z_{1,\mathrm{CD,min}} \approx 1.75\lambda$ while the diffraction limit $z_{1,\mathrm{diff}} \approx 4.08\lambda$ and $G_A \approx 0.43$.

However, as we can see in Fig. 6.16, the intensity by focusing a CD profile is oscillatory near the focus with many trap sites along z. As one example, we calculate the CD profile in free-space (c) and aligned to the APCW structure (d) as shown in Fig. 6.16

$$E_{\mathrm{inc}}(t) = \frac{1}{\sqrt{2}}(\exp\Big(-s^2(t-\cos\theta_{\max})^2\Big) + \exp\Big(-s^2(t-1)^2\Big), \tag{6.64}$$

with $s \equiv 1/f_0\mathrm{NA}$ as defined before, $f_0 = 0.05$ and NA = 0.7. For our Mitutoyo NA = 0.7 objective with entrance pupil diameter $\simeq$ 5 mm, a filling ratio $f_0 = 0.05$ corresponds to a Gaussian beam of waist $\simeq$ 125 μm. This small waist on the pupil can be generated by focusing a lens on the entrance pupil. Fig. 6.17 (b) shows a potential way of generating this CD profile input by using a flattened axicon, as compared to the method for conventional Bessel beams in (a).

For the applications, the oscillatory intensity near the focus generated by the CD profile input can be useful in the Structured Illumination Microscopy (SIM) [76, 190]. For applications to trapping atoms, this can be used to generate an array of trap sites along the propagation direction. Together with the usage of AODs to make arrays in the transverse direction (as discussed in Chapter 5), this allows generation of 3D lattice sites with single objective, which is robust against phase fluctuations. Also, the tight confinement along the propagation axis could be used to improve the

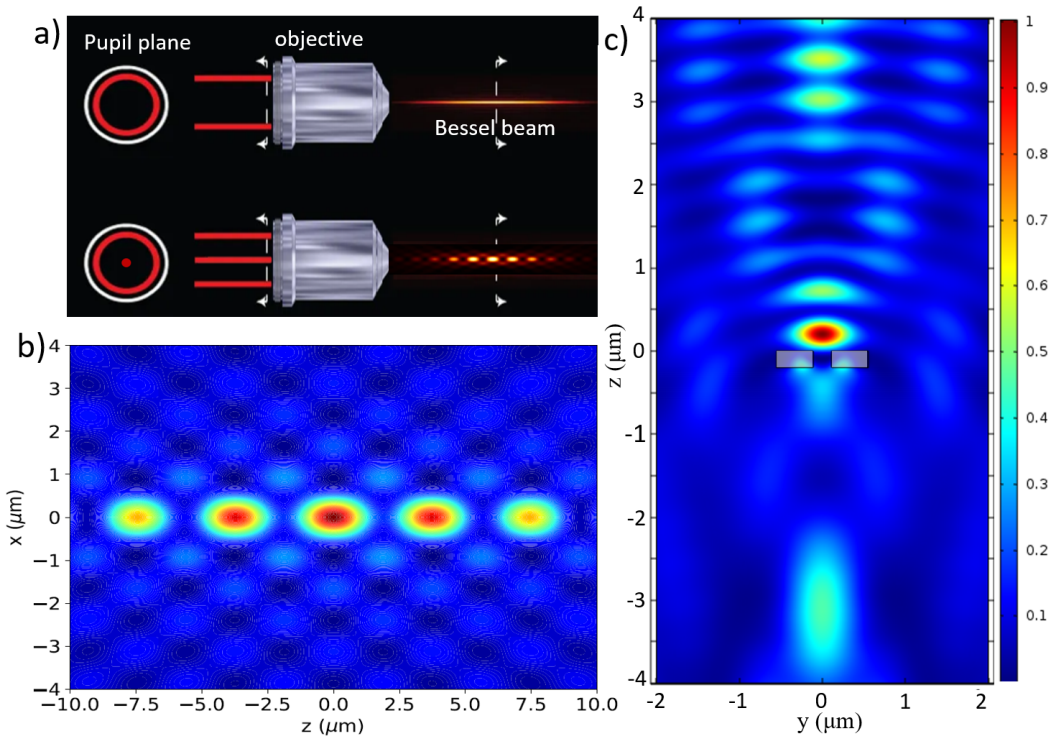

Figure 6.16: (a) *upper panel*: the input profile for generating Bessel beams, view from the pupil plane (left) and from the side (right). *lower panel*: the 'circle-dot' (CD) input profile, view from the pupil plane (left) and from the side (right). As illustrated at the output of objective, the interference of Gouy phase will generate oscillatory intensity profile near the focus. (b) Free-space intensity with CD profile input, the result is calculated from the Debye-Wolf integral for input field E_{inc} defined in Eq. 6.64 with $f_0 = 0.05$ and $NA = 0.7$ (c) COMSOL®[45] simulation of the CD profile input on APCW with parameters same as in (b)

ground state cooling along the axial direction as the cooling rate is proportional to ω_z. One can start with a single atom in the optical tweezer and then adiabatically switch to the CD profile input for efficient ground state cooling.

Note that the oscillatory behavior of CD profile can be also suppressed by adding more 'partial waves', similar to the case of LG beam superpositions. As a special case, we consider the continuum summation of 'partial waves' as

$$E_{\text{inc}}(t) = \left((1+t)\sqrt{t}\right)^{-1}. \tag{6.65}$$

Note that this distribution does not correspond to a uniform incident field E_{inc}, but actually a uniform far-field electric $\mathbf{E}_\infty = 1$. Physically, this represents a uniform amplitude converging spherical wave. With this uniform amplitude converging

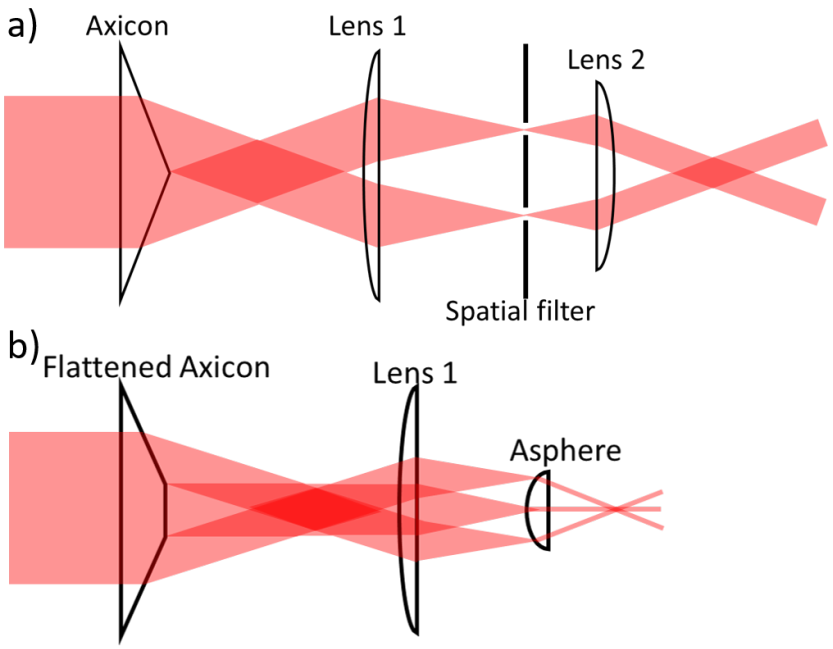

Figure 6.17: (a) Illustration of generating Bessel beams with axicon. (b) Illustration of generating CD profile input with flattened axicon.

spherical wave, the focal field becomes a summation of phasors with equal amplitudes (as we did for the constructive LG beam superpositions), namely

$$\mathbf{E}(\rho = 0, \varphi = 0, z) \propto \int_{\cos\theta_{max}}^{1} e^{ikzt}\, dt = \frac{1}{ikz}\left(e^{ikz} - e^{ikz\cos\theta_{\max}}\right). \tag{6.66}$$

The intensity in the continuum superposition case is given as:

$$I(\rho = 0, \varphi = 0, z) \propto \mathrm{sinc}^2\left[\frac{1}{2}kz(1 - \cos\theta_{\max})\right]. \tag{6.67}$$

The first minimum is at:

$$z_1 = \frac{\lambda}{1 - \cos\theta_{max}}. \tag{6.68}$$

For NA = 0.7, we calculate the first intensity minimum at $z_1 = 3.50\lambda$. It worth pointing out that LG beam '0+2+4' superposition with same NA = 0.7 and a filling ratio $f_0 = 0.35$, the first minimum is at $z_1 = 3.02\lambda$.

6.7 Application to atom transport to nanophotonic devices

In Chapter 4, we have shown that the side-transfer technique can achieve a high efficiency transfer of atom arrays from free-space to 1D and 2D nanophotonic

structures. There, we have implicitly assumed the distance between the edge of 2D nanostructures to the target positions on 2D nanostructure is close, with distance less than 100 μm, given the constraint of field of view of the objective. However, for general devices such as large photonic crystal slabs or devices with unetched substrates, the condition we assume above is not fulfilled and side-transfer technique might not be applicable to these complex nanostructures. As we shown before in Fig. 6.3 and Fig. 6.9, the axial reduction from the superposed LG beams can lead to reduction the reflection fringes. Thus, it is expected the axial reduction can be applied to improve the transfer efficiency for transporting atoms normally to the dielectric surface.

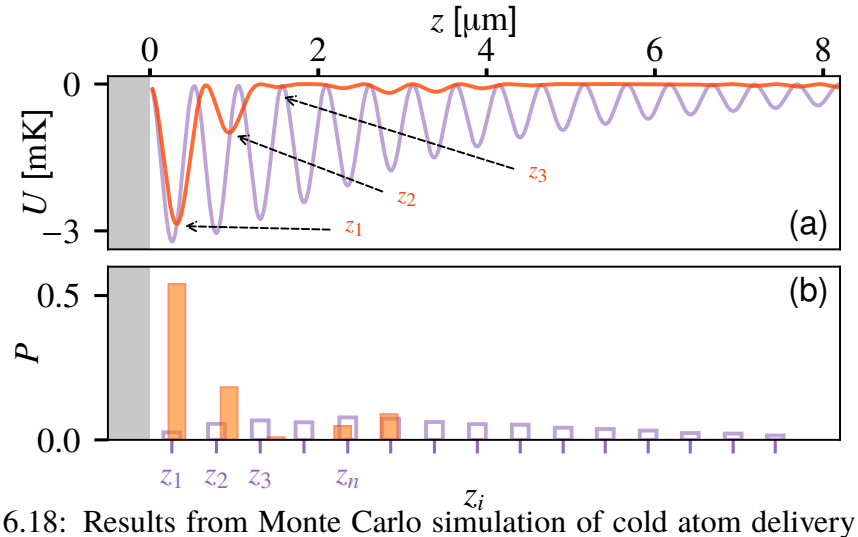

Figure 6.18: Results from Monte Carlo simulation of cold atom delivery close to a semi-infinite planar surface with an amplitude reflection coefficient $r = -0.8$. (a) Optical potentials $U(0, 0, z)$ for optical tweezers formed from the $p = 0$ Gauss mode (violet) and '0 + 2 + 4' superposition (red), respectively, as in Fig. 1(d) for focus at $z = 0$. (b) The final probabilities $P(z_i)$ for delivery of atoms to optical traps centered at positions z_i. Atoms are initially loaded into an optical tweezer of depth $U_0 = 1$ mK at focal distance $z_{initial} = 600\,\mu$m from the surface and initial temperature of 100 µK. The focal plane of the optical tweezer is then scanned from $z_{initial}$ to $z_{final} = 0\,\mu$m.

To verify that atoms can indeed be efficiently delivered to reflective traps near dielectric surfaces, we performed Monte Carlo simulations of atom trajectories by moving the tweezer's focus position from far away ($z = 600\,\mu$m) to the surface ($z = 0\,\mu$m, as shown in Fig. 6.18(a)) for amplitude reflection coefficient $r = -0.8$. In the Monte Carlo simulation of atom transport from free space tweezers to near surface traps, the atom sample is initialized from a sample of temperature 100 µK in 1 mK trap depth with position $\simeq 600\,\mu$m away from the surface. The tweezer

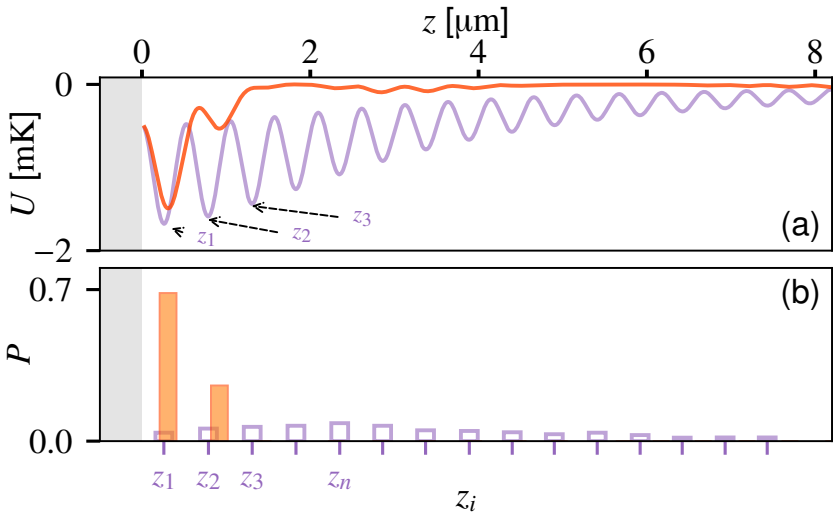

Figure 6.19: Results from a Monte Carlo simulation of cold atom delivery close to a semi-infinite planar surface with an amplitude reflection coefficient $r = -0.3$. (a) Optical potentials $U(0, 0, z)$ for optical tweezers formed from the $p = 0$ Gauss mode (violet) and '$0 + 2 + 4$' superposition (red), respectively, for focus at $z = 0$. (b) The final probabilities $P(z_i)$ for delivery of atoms to optical traps centered at positions z_i. Atoms are initially loaded into an optical tweezer of depth $U_0 = 1$ mK at focal distance $z_{initial} = 600\,\mu$m from the surface and initial temperature of $100\,\mu$K. The focal plane of the optical tweezer is then scanned from $z_{initial}$ to $z_{final} = 0\,\mu$m.

focus is then accelerated with acceleration $a = 1\,\mathrm{m\,s^{-2}}$ towards the surface for 20 ms and then moves at constant velocity for 10 ms before decelerating with acceleration $a = -1\,\mathrm{m\,s^{-2}}$ to stop at the surface ($z = 0\,\mu$m). We then extracted probabilities for single atoms being delivered and trapped in near surface traps as shown in Fig. 6.18(b). The specific choice of reflection coefficient $r = -0.8$ is based on full numerical simulations of wavelength-scale tweezer reflection from the nanoscale surface of an APCW as presented in [86] for tweezer polarization parallel to the long axis of the APCW.

As shown in Fig. 6.18(b), the trap formed by the '$0 + 2 + 4$' superposition (orange histogram) leads to large enhancement in delivery efficiencies into near surface traps (z_1, z_2...) as compared to the very small probability of delivery for the conventional trap formed by $p = 0$ Gauss beam (violet histogram). The probability of delivering an atom into the z_1 trap with '$0+2+4$' superposition is $P_\Sigma(z_1) \simeq 0.55$ as compared to $P_0(z_1) \simeq 0.03$ with $p = 0$ Gauss beam.

To demonstrate the robustness of our scheme, we also simulated the atom transport with reflection coefficient $r = -0.3$. The choice of this reflectivity is based on

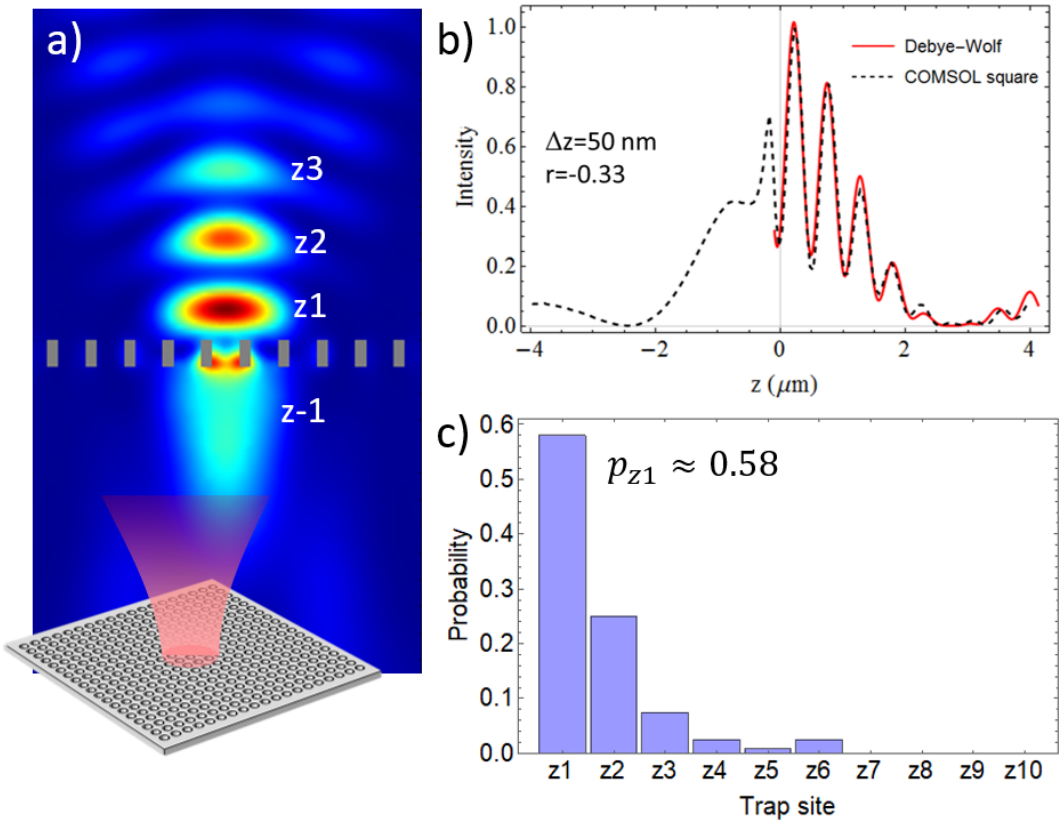

Figure 6.20: (a) The COMSOL®[45] simulated field of LG '0+2+4' superposition reflecting from the squared lattice slab described in Chapter 3. (b) Fitting of the COMSOL®[45] simulated field (dashed line) with the Debye-Wolf evaluated field reflecting from a planar surface (red solid line). (c) The transfer probabilities into different trap sites evaluated from a 3D trajectory simulation using Debye-Wolf method evaluated field reflecting from a planar surface with reflection coefficient $r = -0.33$ as fitted from (b).

fitting of reflection fringes from the APCW with polarization perpendicular to the waveguide. Fig. 6.19(a) shows the final frame for traps near the surface. As shown in Fig. 6.19(b), atoms are mostly delivered into the first two traps near the surface (z_1 and z_2). The probability of atom being delivered to z1 trap is 68.4%.

We stress that Fig. 6.18 and Fig. 6.19 are based upon a one-dimensional model of reflection and transport and hence provides only a qualitative guide. A 3D trajectory simulation with the vector field is also calculated, as shown in Fig. 6.20 (c). As COMSOL®[45] simulation 3D field with a large travel range requires a huge amount of computation time, here we approximate the 3D field scattered from a 2D square lattice described in Chapter 3 by the field evaluated from Debye-Wolf integral method. The COMSOL®[45] simulated field profile is shown in Fig. 6.20 (a) and

the fitting of the COMSOL®[45] field (dashed line) with the Debye-Wolf method evaluated field reflecting from a planar surface (red solid line) is shown in Fig. 6.20 (b). The fitted parameter $r = -0.33$ is consistent with the reflection coefficient from bulk material with refractive index $n = 2$ with surface at $z = -50nm$. The transfer probability into different trap sites evaluated from a 3D trajectory simulation using Debye-Wolf method evaluated field reflecting from a planar surface with reflection coefficient $r = -0.33$ as fitted from (b). The transfer probabilities into different trap sites are evaluated from a 3D Monte-Carlo trajectory simulation using approximated field evaluated from Debye-Wolf method. The result is summarized in Fig. 6.20 with the probability into the first trap site z_1 to be 0.58. The slightly lower transfer probability in to the z_1 trap as compared to previous paraxial results ($p \approx 0.68$) is a result due to the presence of relative significant trap sites z_2 and z_3.

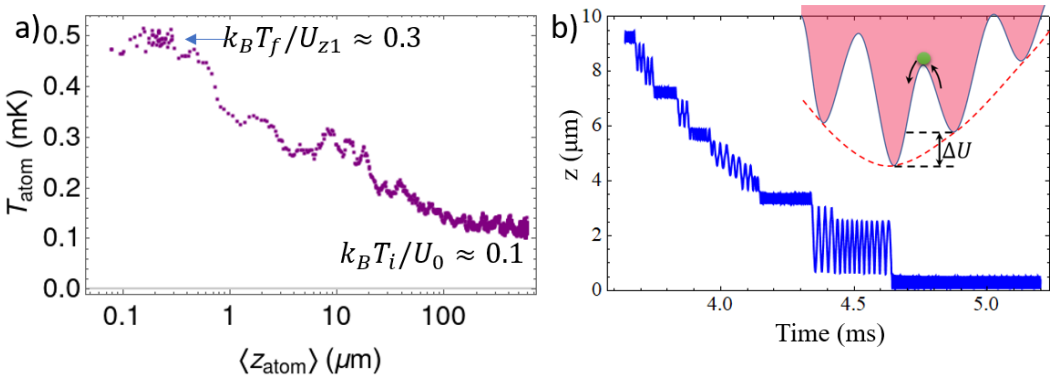

Figure 6.21: (a) Averaged atom temperature during transport as a function of atom mean position along z axis. Temperature is evaluated from the 3D trajectory simulation with vector field from Debye-Wolf integral method. (b) An example of typical trajectories from the trajectory simulation. The 'steps' here correspond to atom trapped in one specific 'pancake' and the 'jumps' correspond to atom left the 'pancake' and hopped into another 'pancake'. *Inset*: Atom transfer from one site to the neighbor site. A kinetic energy $E_k = |\Delta U|$ is obtained during the transfer. $|\Delta U|$ is related to the envelope of the profile (red dashed line).

The higher probability for lower reflectivity can be qualitatively understood from the heating process during the transport. Fig. 6.21 (a) shows the extracted atom temperature as a function of atom average position (along z) during the transport where the atom are heated up from the initial atom temperature $k_B T_i/U_0 = 0.1$ to the final atom temperature $k_B T_f/U_{z1} \approx 0.3$ when atom are delivered to the z_1 trap. An example of the typical trajectories from the trajectory simulation is shown in Fig. 6.21 (b), with the x axis being the simulation time and y axis being the position

in z. Here, the trajectory shows features of 'steps' (flattened z position) and 'jumps' (sudden change in z position). The 'steps' here correspond to atom trapped in one specific 'pancake' and the 'jumps' correspond to atom left the 'pancake' and hopped into another 'pancake', as illustrated in Fig. 6.21 (b). This 'hopping' behavior can lead to heating of atom temperature and the mechanism has already been described detail in the setting of 2D photonic crystal slabs in Chapter 4.

Beyond the results shown above, improvements have been found by including atom cooling in the simulations at various stages of the transport, as well as applying blue-detuned guided-mode (GM) beams as atoms arrive near the surface to overcome loss due to surface forces such as the Casimir-Polder potential. Another promising but yet to be investigated method is to load atom in the lower half space and then move towards the slab using the z_1 trap. This z_{-1} trap delivery method can get rid of the heating due to hopping from different trap sites and thus should be able to achieve nearly 100% delivery efficiency to the lower surface of 2D slabs. More numerical investigation of this method is still under progress.

6.8 Summary

In conclusion, we have shown that coherent superpositions of radial LG beams can lead to tightly focused optical tweezers with reduced volume and increased trapping frequency. A specific application has been presented for the efficient transport of atoms via optical tweezers directly to trap sites near the surface of a reflecting dielectric. We are currently investigating other applications of the rapid variation of the Gouy phase within wavelength-scale focal regions, including phase-contrast microscopy within heterogeneous sample volumes. We are currently investigating other applications of the rapid variation of the Gouy phase within wavelength-scale focal regions, including phase-contrast microscopy within heterogeneous sample volumes.

Chapter 7

COUPLING OF LIGHT AND MECHANICS IN A PHOTONIC CRYSTAL WAVEGUIDE

This chapter describes research in the Caltech QOG whose major goals are to achieve direct, strong, and efficient links between individual photons and phonons, and thereby enable opto-mechanics at the quantum level. Toward this end, experiments harness strong interactions resulting from coupling of single atoms to nanophotonic waveguides. The capabilities to observe and manipulate photon-phonon interactions at the level of individual atoms are being developed. Building on this, strategies are being investigated that would enable full tailoring of interactions between atomic spin, phononic, and photonic degrees of freedom. Such capabilities would enable coherent control of quantum optomechanical phenomena at the many-body level and open new opportunities for quantum information science and technology.

The material presented in this chapter is adapted from a manuscript in preparation. The mechanical mode measurement is led by Jean-Baptiste Béguin and Zhongzhong Qin, with also important contributions from Su-Peng Yu, Alex Burgers and Lucas Peng.

7.1 Introduction

Recent decades have seen tremendous advances in our ability to prepare and control the quantum states of atoms, atom-like systems in the solid state, and optical fields in cavities and free space. However, the outstanding goal of integrating these diverse elements to achieve efficient quantum information processing still faces a number of challenges. One of the most significant is the range of highly dissimilar physical systems (atoms, ions, solid-state defects, quantum dots) that must be integrated to realize elements for logic, memory, and long-range coupling. Each of these systems has unique advantages, but they are disparate in their frequencies, their spatial modes, and the fields to which they couple. For example, the electronic degrees of freedom in atoms and atom-like defects typically respond at optical frequencies, while their spin degrees of freedom, which are suitable for long-term storage of quantum states, respond to microwave or radio frequencies. On the other hand, the transmission of quantum information over long distances at room temperature requires the use of telecom-band photons in single-mode optical fibers.

Mechanical systems have been proposed as a broadly applicable means for overcoming these disparities and transferring quantum states between different degrees of freedom [80, 152, 153]. This is because mechanical systems can be engineered to couple coherently to many different systems and can possess very low damping, particularly when operated at cryogenic temperatures. To date, quantum effects have been observed in mechanical systems coupled to superconducting qubits (via piezoelectric coupling) [138], optical photons [27, 37, 150, 151, 160, 161], and microwave photons [144, 180]. Efficient coupling has also been demonstrated between mechanical oscillators and spins in various solid-state systems, although to date the mechanical components of these devices have operated in the classical regime [8, 85, 112, 127, 141, 159, 179].

In this chapter, I describe my group's nascent efforts to utilize strong coupling of atoms, photons, and phonons in nanophotonic PCWs to create a new generation of capabilities for quantum science and technology. The long-term goal is use optomechanical systems operating in the quantum regime to realize controllable, coherent coupling between isolated, few-state quantum systems. In our case, the system will consist of atoms trapped along a PCW (as discussed in previous chapters) that interact strongly with photons propagating in the guided modes (GMs) of the PCW. The mechanical structure of the PCW in turn supports phonons in its various eigenmodes of motion. While much has been achieved in theory and experiment for strong coupling of atoms and photons in nano-photonics, much less has been achieved (or even investigated) for the coupling of motion and light in the quantum regime for the devices that we have discussed in previous chapters.

As emphasized in previous chapters, a "Grand Challenge" for this work is to achieve the long-standing goal of integrating ultracold atoms with nanophotonic devices. We could then use quantum motion to achieve enhanced nonlinear atom-light interactions with single and multiple atoms. New regimes and novel mechanisms for controlling atoms near dielectric objects and realizing strong atom-photon-phonon coupling could be explored.

The first baby steps of the QOG are documented in this chapter and are 1) to observe and characterize the low frequency, mechanical eigenmodes of an APCW and 2) to develop theoretical models that can be validated in the nontraditional regime in which our system works (i.e., well-localized mechanical modes, but nonlocalized propagating photons both far from and near to the band edges of PCWs).

Although technically challenging, the approach of the QOG benefits from several

advantages when compared to conventional optomechanics, including (a) the extreme region of parameter space that atomic systems occupy (such as low mass and high mechanical Q factors), (b) the exquisite level of control and configurability of atomic systems, and (c) the pre-existing quantum functionality of atoms, including internal states with very long coherence times. It should be noted that many spectacular advances of atomic physics already build upon these features (47, 48). On one hand, experiments with linear arrays of trapped ions achieve coherent control over phonons interacting with the ions' internal states (pseudo spins'). Goals that are very challenging for quantum optomechanics with nano- and micro-scopic masses, such as phonon-mediated entanglement of remote oscillators and single-phonon strong coupling, are routinely implemented with trapped ions. On the other hand, cavity QED with neutral atoms produces strong interactions between single photons and the internal states of single atoms or ensembles, leading to demonstrations of state mapping and atom-photon entanglement.

What is missing thus far, and what motivates the initial steps described in this chapter, is a direct strong link between individual photons and phonons, to enable optomechanics with atoms at the quantum level.

7.2 The alligator photonic crystal waveguide

Fig. 7.1 provides an overview of the APCW utilized in our experiments with details related to device fabrication and characterization provided in Refs. [87, 131, 201, 203]. The photonic crystal itself is formed by external sinusoidal modulation of two parallel nano-beams to create a photonic bandgap for TE modes with polarization predominantly along y in Fig. 7.1a). The TE band edges have frequencies near the D1 and D2 transitions in atomic Cesium (Cs). Calculated and measured dispersion relations for such devices are presented in Ref [87] where good quantitative agreement is found. Here, we focus on coupling of light and motion for TE modes of the APCW. TM modes of the APCW near the TE band edges resemble the guided modes of an unstructured waveguide.

As shown by the SEM image in Fig. 7.1(b), the APCW is connected to single-beam waveguides on both end and thereby freely suspended in the center of a 2 mm wide window in a Silicon chip. Well beyond the field of view in Fig. 7.1b), a series of tethers are attached transversely to the single-beam waveguides along $\pm y$ to anchor the waveguides to two side rails that run parallel to the x axis of the device to provide thermal anchoring and mechanical support, with the coordinate system defined in

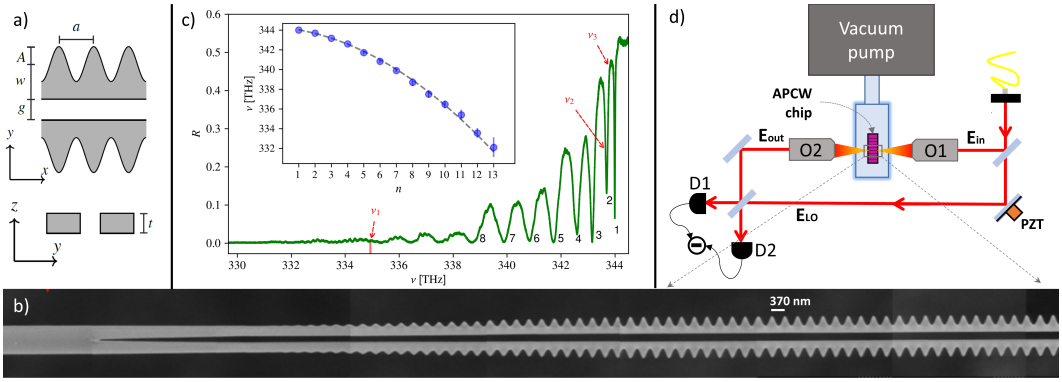

Figure 7.1: Details of the APCW and the setup for our experiments. a) Drawing giving the dimensions of the various components of the APCW in gray. The unit cell spacing $a = 370$nm, the vacuum gap $g = 238$ nm, and the silicon nitride thickness $t = 200$ nm. The outer beams have modulation amplitude $A = 120$ nm and width $w = 280$ nm. b) An SEM image of the left half of the APCW showing (from left to right) a single unstructured rectangular waveguide that splits at a Y-junction into two parallel waveguides each of which is gradually modulated in width to finally match the A, w values of the APCW itself which extends 150 unit cells to the right along x before tapering to a second Y-junction and a uniform rectangular beam. The entire structure is suspended in vacuum by transverse tethers connected to supporting side rails (not shown) [131, 201, 203]. c) Reflection spectrum $R(\nu)$ for the APCW displays a series of low finesse cavity-like resonances for reflections from the input tapers and APCW near the dielectric band edge at 344.3 THz. The inset plots frequencies ν_n for successive cavity resonances $n = 1, 2, \ldots$ near the dielectric band edge. d) Simplified diagram for measurements of mechanical modes of the APCW by way of transmission spectra $T(\nu)$ either by way of direct detection of beam $E_{out}(\nu)$ alone at photodetector D_1 or D_2 or via balanced homodyne detection of the signal beam $E_{out}(\nu)$ combined with the local oscillator beam $E_{LO}(\nu)$ at photodetectors D_1 and D_2.

Fig. 7.1a). Important for our current investigation, the single-beam waveguides and the APCW itself are held in tension with $T \simeq 800$MPa.

Light is coupled into and out of TE guided modes (GMs) of the APCW by a free-space coupling scheme that eliminates optical fibers within the vacuum envelope [refs for our Memorandum and AQT papers]. An example of a reflection spectrum $R(\nu)$ is given Fig. 7.1(c), which is acquired by way of light launched from and recollected by the microscope objective *O1* shown in Fig. 7.1d). Objectives *O1, O2* are mode-matched to the fields to/from the terminating ends of the waveguide resulting in overall throughput efficiency $T \simeq 0.50$ from input objective *O1* through the device with the APCW to output objective *O2* for the experiments described here. The silicon chip itself contains a set of APCWs and is affixed to a small glass

optical table by way of silicate bonding.

7.3 Measurement of modulation spectra

With reference to Fig. 7.1(d), we have recorded spectra of photocurrent fluctuations $\Phi(\nu, f, \theta)$ for light transmitted through an APCW for various probe frequencies ν below the frequency $\nu_{BE} \simeq 344.3$ THZ of the dielectric band edge. Here we employ a balanced homodyne scheme with E_{in} and E_{LO} having identical optical frequencies ν and each absent radio frequency modulation f save that from the APCW. With free-space coupled modes of APCW, homodyne fringe visibility up to ~ 0.95 can be obtained. Measurement results for $\Phi(\nu, f, \theta)$ are displayed in Figures 7.2 and 7.4 for three optical frequencies $\{\nu_1, \nu_2, \nu_3\} = \{334.96, 343.64, 343.78\}$ THz (i.e., wavelengths (895.00, 872.40, 872.04 nm) moving from far below to near the dielectric band edge, as marked by red arrows in Fig. 7.1c. The spectra display a series of narrow peaks and are of increasing complexity as the band edge is approached. All spectra are taken for a weak probe beam $E_{out}(\nu)$ with power $P_{out} \sim 10\mu$W, while $P_{LO} \simeq 500\mu$W. The phase offset θ between E_{in} and E_{LO} is set to maximize the observed spectral peaks whose frequencies f exhibit only small shifts with changes in P_{out}, as illustrated in Fig. 7.3. In vacuum ($\sim 1e-11$ torr) and at room temperature, the quality factor for the lowest peak at $f_1 = 2.4$MHz is $Q \simeq 1 \times 10^5$. While various damping mechanisms operate (reference) this value is compatible with the numerically predicted increase of the intrinsic Q_{int} from the high material pre-stress ($Q_{\text{int}} \simeq 8.4 \times 10^3$ for 200 nm thin SiN beams [192]).

An important feature of the spectra in Fig. 7.2(a) is that peaks beyond f_1 occur at frequencies that are approximately odd harmonics of f_1, with $f_j \simeq j \times f_1$ for $j = 1, 3, 5, \ldots$. By contrast in Fig. 7.2b), the largest peaks double in number with now the presence of *even* harmonics of the fundamental frequency f_1 in addition to the *odd* harmonics from Fig. 7.2(a). As shown by the inset in Fig. 7.2(a), the dispersion relation is approximately linear with frequencies $f_p \simeq p \times f_1$, where $p = 1, 2, 3, \ldots$.

Further understanding emerges if we consider higher accuracy for the frequencies f_p and examine the measured frequency differences $\Delta f = \{f_p - f_1\}$ as in the inset of Fig. 7.2b). Also plotted as the dashed line is the theoretical prediction for the mechanical frequency differences $\Delta \tilde{f} = \{\tilde{f}_p - \tilde{f}_1\}$ of a 1D nanobeam, which is

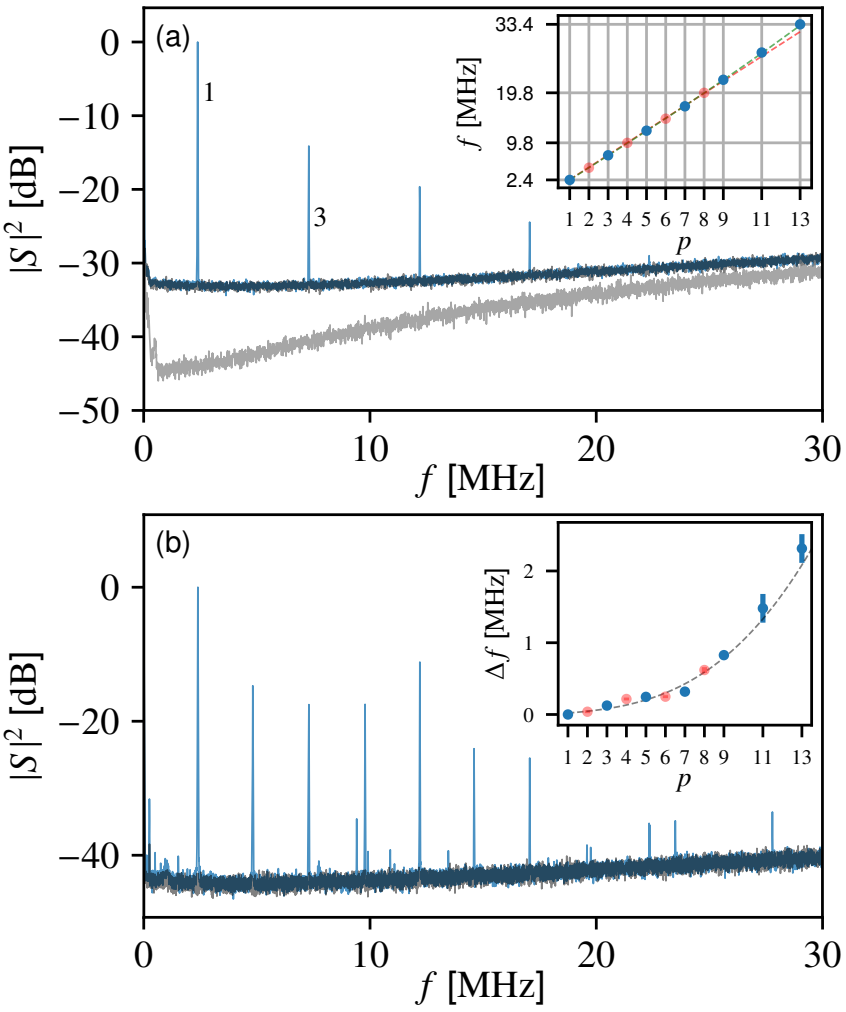

Figure 7.2: Measured vibration spectra with spectrum analyzer at wavelength 895.00 nm (a) and 872.40 nm (b), respectively. Electronic noise floor of the homodyne detector is shown in part (a). Inset in (a) plots the frequencies of odd quasi-harmonics peaks (blue dots) and even quasi-harmonics peaks (red dots) of f_1. Linear fit (dashed red curve) and complete fit of $\tilde{f}_p$ (dashed green curve) are also shown. Inset in (b) plots the measured frequency difference Δf (blue and red dots) and theoretical fit $\Delta \tilde{f}$ (dashed gray curve).

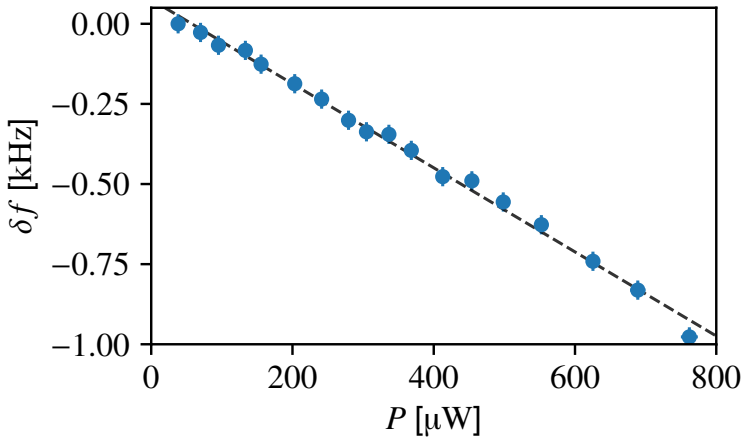

Figure 7.3: Frequency shift δf_1 of the lowest frequency peak at $f_1 = 2.4$MHz in Fig. 7.2a) as a function of transmitted probe power P_{out}. $\delta f_1(P_{out})$ is consistent with thermal expansion (i.e., lengthening) of the APCW due to small optical absorption of probe power.

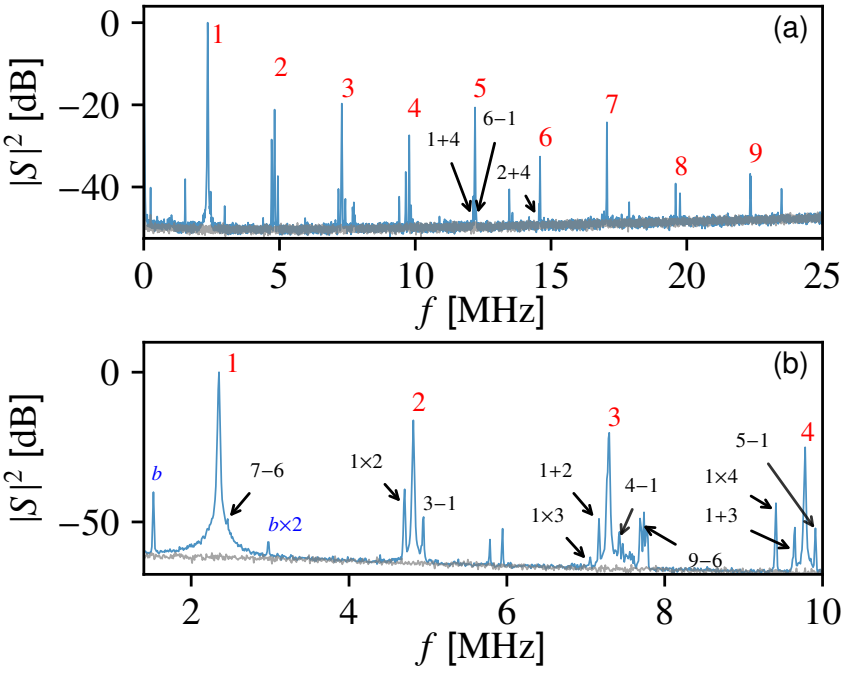

Figure 7.4: Measurement vibration spectrum near band edge 872.04 nm with a span of 25 MHz (a) and 10 MHz (b). Except for the dominant peaks appear in 7.2, pure integer harmonics of f_1, sums and differences of the dominant quasi-harmonics frequency components are also observed. Peak labeled as b is due to unbalanced input laser light noise.

supported at hinged ends. For this model, the mechanical resonances are [84]

$$\tilde{f}_p = \frac{p^2\pi}{2L^2}\sqrt{\frac{EI}{\rho A} + \frac{\sigma L^2}{\rho\pi^2 p^2}}, \tag{7.1}$$

where p is the integer mode index, E is Young's modulus, I the moment of inertia, A the cross sectional beam area, L the beam length, ρ the mass density, and σ is the stress in the beam.

Our APCW and connecting nano-beams are fabricated from SiN with high-tensile stress $\sigma \simeq 800\,\mathrm{MPa}$ [200, 202]. Together with the largely 1D geometry of the APCW (large aspect ratio of transverse to longitudinal dimension), the contribution of the bending term in (7.1) can be neglected for the lowest modes such that $\tilde{f}_p \simeq (p/2L)\sqrt{\sigma/\rho}$, giving rise to a close approximation of the the linear dispersion of a tensioned string as in the inset to Fig. 7.2a). However, upon closer inspection, there is a clear quadratic contribution from the bending term that is evident for higher order modes in the inset to Fig. 7.2b).

In terms of absolute agreement between measured and predicted frequencies for the spectra in Fig. 7.2, from Eq. 7.1 we calculate a fundamental frequency $\tilde{f}_1 = 2.37(30)$ MHz from the total length $L = 180 \times 0.37\,\mu\mathrm{m} + 2 \times 20\,\mu\mathrm{m} = 107(10)\,\mu\mathrm{m}$, the manufacturer's quoted tensile stress $\sigma = 800(50)$ MPa, and the mass density for LPCVD (stoichiometric) silicon nitride [89], $\rho_{\mathrm{SiN}} = 3180\,\mathrm{kg\,m^{-3}}$. For the length L, we consider the 150 unit cells of the actual PCW region, plus the 30 tapered cells on each end, and finally the length from the beginning of the Y-split junction which separates the two corrugated beams. The devices are designed for small stress relaxation from that of the original SiN on Silicon chip [202]. The predicted $\tilde{f}_1$ is close to the measured frequency $f_1 = 2.4$ MHz.

While the frequencies of the largest peaks in Fig. 7.2 are well-described by Eq. 7.1, the complexity of the spectra increases as the band edge is approached with the appearance of many small satellite peaks as in Fig. 7.4 for $\nu_3 = 343.78\,\mathrm{THz}$ (i.e., wavelength $\lambda_3 = 872.04\mathrm{nm}$).

After labeling for clarity the dominant even and odd quasi-harmonics that also appear in Fig. 7.2, we clearly observe a secondary series of pure integer harmonics in Fig. 7.4, such as the second, third and fourth harmonics of the lowest frequency f_1. The majority of the remaining peaks have frequencies which coincide with sums and differences of the main quasi-harmonics frequency components. Other peaks (e.g., at 1.5 MHz) originate from unbalanced input laser light noise.

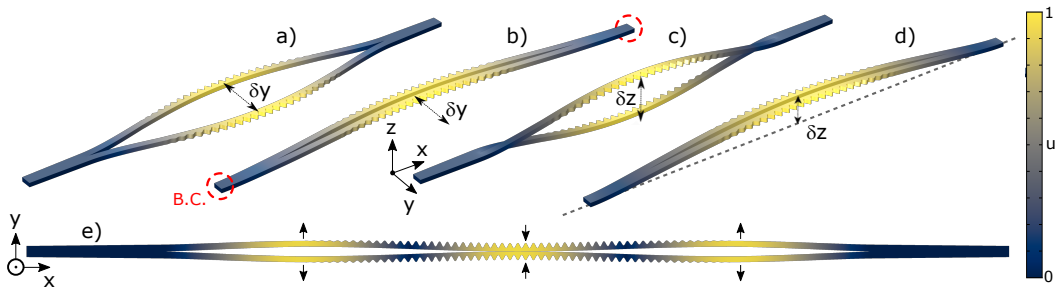

Figure 7.5: Mechanical modes of the APCW structure illustrated with a reduced geometry. Four types of eigenmodes $\psi_1^{y,A}, \psi_1^{y,S}, \psi_1^{z,A}$ and $\psi_1^{z,S}$ are shown in (a)-(d). (e) shows a higher-order mode $\psi_3^{y,A}$ for a longer structure. B.C. means two end-clamped boundary conditions.

7.4 Mechanical modes of the APCW

From measurements as in Figures 7.2 and 7.4 in hand and some understanding of the dispersion relation for the observed mechanical modes of the APCW, we turn next to more detailed characterization by way of numerical simulation. Principal goals are 1) to determine the mechanical eigenfunctions (and not just eigenfrequencies) associated with the observed modulation spectra and 2) to investigate the transduction mechanisms that convert mechanical motion of the various eigenfunctions to modulation of our probe beam. Beyond numerics to find the mechanical eigenmodes, we will present simple models to describe the transduction of mechanical motion to light modulation for various regimes far from and near to a band edge of the APCW. Quantitative numerical evaluation of the opto-mechanical coupling coefficient G_ω for the APCW [36, 102] will be presented in Section 5.

Fig. 7.5 shows the fundamental mechanical modes of the APCW structure obtained via numerical solution to the elastic equations. For clarity, we illustrate with a reduced geometry due to the large aspect ratio of our structure. In Section 5, we evaluate the eigenmodes for our actual full structure. The top panels represent the 3D deformed geometry as prescribed by the displacement vector field associated to each of the mechanical eigenmodes, with an arbitrary choice of mechanical energy. The magnitude of the displacement normalized to its maximum value u is indicated by the colormap.

The design of the relatively long Y-junction arises from the need for efficient (i.e., adiabatic) conversion of the light guided from the single waveguide into the mode of the double-beam photonic crystal. While it does not represent a sharp boundary for the mechanics (please refer to Ref. [200] for details of full suspended structure with an-

choring tethers), it does impose a symmetric termination geometry for both patterned beams. For the choice of effective two end-clamped boundary conditions, the four types of eigenmodes consist of two pairs of symmetric S and antisymmetric A oscillation, one pair with motion predominantly along y, which we denote by $\psi_p^{y,A}, \psi_p^{y,S}$, and the other with motion mostly along z, denoted by $\psi_p^{z,A}, \psi_p^{z,S}$ and labelled by the mode number $p = 1, 2, 3, ...$ For the full structure, the eigenfrequencies for the fundamental $p = 1$ modes are in the ratio $f_1^{y,A}, f_1^{y,S} f_1^{z,A}, f_1^{z,S} = 1, 0.77, 0.98, 0.74$. The bottom panel displays a higher-order anti-symmetric mode with $f_3^{y,A} \sim 3 f_1^{y,A}$ in the x-y plane for a longer structure. While these correspond to the mode families with lowest eigenfrequencies, at higher frequency other types of beam motion with mixed y-z displacement appear. The eigenmodes shown in Fig. 7.5 correspond roughly to those of two weakly coupled nanobeam oscillators. Regarding the accuracy of the choice of boundary condition, we note that the mechanical properties of the differential modes are little impacted by the length of single beam beyond the merging point of the junction.

7.5 Mapping motion to optical modulation

Optical frequencies far from a band edge

A simple model for the transduction of motion of the APCW nano-beams into optical modulation explains some of the key observations from the previous section. First of all, each *mechanical* eigenmode in Fig. 7.5 modifies the band structure of the APCW and thereby the *optical* dispersion relation $\omega(k_x)$ for propagation of a guided mode along x with wave vector k_x relative to the case with no displacements from equilibrium. In our original designs of the APCW, we undertook extensive numerical simulations of the band structure for variations of all the dimensions shown in Fig. 7.1a) Refs. [88, 130, 200]. Guided by these earlier investigations, we deduce that the largest change in band structure with motion arises from variation of the gap width g from displacement δy for the antisymmetric eigenmode $\psi_p^{y,A}$ illustrated in Fig. 7.5 (a).

As suggested by Eq. 7.1, we then consider a $1D$ string model with $\psi_p^{y,A}(x)$ describing y displacement at each point along x, namely $\psi_p^{y,A}(x) = \psi_0 \sin(\beta x)$, with maximum y displacement ψ_0. Here, β is the mechanical wave vector with $\psi^{y,A}(x)$ subject to boundary conditions, which in the simplest case are $\psi^{y,A}(x = 0) = 0 = \psi^{y,A}(L)$ with then eigenvalues $\beta_p = p\pi/L$ for $p = 1, 2, 3, ...$ Again, $\psi_p^{y,A}(x)$ denotes the mechanical eigenmode in Fig. 7.5(a) and represents antisymmetric y displacements of each nanobeam, with one beam of the APCW having displacement

from equilibrium $\pm\delta y/2 = \pm\psi_0/2$ and the opposing beam with phase-coherent displacement $\mp\delta y/2 = \mp\psi_0/2$, leading to an overall variation of the gap width $g \rightarrow g + \psi_0 \rightarrow g \rightarrow g - \psi_0 \rightarrow g$ as described by $\psi_p^{y,A}(x)$ along the x-axis of the APCW. For small y displacements ψ and fixed frequency ω far from the band edge, we can then expand the dispersion relation to find $k_x(\omega, \psi) \simeq k_x(\omega, 0) + \delta k_x(\omega, \psi)$, where $\delta k_x(\omega, \psi) = \xi(\omega) \times \psi$, with $\xi(\omega) = dk_x(\omega)/d\psi$.

Since y displacements vary along x as described by the particular mechanical eigenmode $\psi_p^{y,A}(x)$, δk_x will also vary along x. The differential phase shift due to a mechanical eigenmode for propagation of an optical GM from input to output of the APCW is then given by (in our simple model) $\Phi_p(L) = \int_0^L \delta k_x(\omega, \psi(x))dx = \int_0^L \xi(\omega)\psi_p^{y,A}(x)dx = 2L\xi(\omega)\psi_0/p\pi$ for p odd, and $\Phi_p(L) = 0$ for p even. Here, $\Phi_p(L)$ is the differential phase shift between optical propagation through the APCW with and without mechanical motion (i.e., $\psi_0 \neq 0$ and $\psi_0 = 0$).

Of course, when excited the mechanical mode $\psi_p^{y,A}(x)$ will oscillate at frequency $f_p^{y,A}$, as will the phase shift $\Phi_p(L)$, with $1/f_p^{y,A}$ much larger than the transit time for light propagation through the APCW. Overall, mechanical motion via $\psi_p^{y,A}(x)$ modifies the dispersion relation for an optical GM leading to nonzero phase modulation at frequency f_p for p odd eigenmodes and zero phase modulation for p even modes, precisely as observed in Fig. 7.2(a) far from the band edge.

There remains the question of the 'missing modes'. If indeed the dominant spectral peaks in Fig. 7.2 are associated with the eigenfunctions $\psi_p^{y,A}$, what has become of the other three sets of eigenfunctions $\psi_p^{y,S}, \psi_p^{z,A}, \psi_p^{z,S}$ The answer provided by our simple model of mechanical motion modifying the dispersion relation $k_x(\omega)$ is that $\psi_p^{y,A}$ is unique in producing a large first-order change in $k_x(\omega)$ with displacement.

Fig. 7.5 reveals that only $\psi_p^{y,A}$ has distinct geometries for displacements $\pm\delta y$ (i.e., the two nanobeams are more separated for $+\delta y$ and less separated for $-\delta y$) leading to a much larger calculated transduction factor $\xi_{y,A}(\omega)$ for motion along y than $\xi_{z,A}(\omega)$ for motion along z. Moreover, far from the band edge, the symmetric modes $\psi_p^{y,S}, \psi_p^{z,S}$ have small transduction factors $\xi_{y,S}(\omega), \xi_{zS,}(\omega)$ comparable to those for modes of a single unmodulated nanobeam of the thickness and average width of the APCW.

Optical frequencies near a band edge

Near the band edge of a PCW, the mapping of mechanical motion to modification of an optical probe has a qualitatively distinct origin from that in the previous section

for the dispersive regime of a PCW. For a finite length PCW, there appears a series of optical resonances ν_n with $n = 1, 2, 3...$ as displayed in Fig. 7.1(c). Each optical resonance arises from the condition $\delta k_x(n) = k_{BE} - k_x = n\pi/L$ with $k_{BE} = \pi/a$ at the band edge [88]. The mapping from wave vector $\delta k_x(n)$ to frequency ν_n involves a nonlinear dispersion relation $\delta k_x(\nu)$ near the band edge, which for our devices takes the form

$$\delta k_x(\nu) = \frac{2\pi}{a}\sqrt{\frac{(\nu_{\mathrm{BE2}} - \nu)(\nu_{\mathrm{BE}} - \nu)}{4\zeta^2 - (\nu_{\mathrm{BE2}} - \nu_{\mathrm{BE}})^2}}, \tag{7.2}$$

where ν_{BE} (ν_{BE2}) is the lower (upper) band edge frequency, and ζ is a frequency related to the curvature of the band near the band edge. The frequency for which $\delta k_x = 0$ is defined as the band edge frequency ν_{BE}. Validation of this model by measurement and numerical simulation is provided in Ref. [88].

For our current investigation, we model how displacements of the APCW geometry for the various mechanical eigenmodes illustrated in Fig. 7.5 lead to variation of the parameters in Eq. 7.2. Specifically, since the resonance condition involves only the effective length of the APCW (i.e., $L = (N-1)a$ with the number of unit cells $N \simeq 150$ and lattice constant $a \simeq 370$nm), each optical resonance will be taken to have fixed $\delta k_x(n) = n/(N-1) \times k_{BE}$ with then the associated optical frequency $\nu(n)$ changing due to variation of parameters in Eq. 7.2 driven by displacements from the mechanical eigenmodes.[1]

A mapping of changes in device geometry to changes in band edge frequencies is provided in Ref. [130]. As in the previous subsection, we seek here a qualitative description to understand the complex transduction of mechanical motion to optical modulation in a $3D$ PCW. Quantitative numerical calculations will be described in the next section.

That said, we proceed by way of Table 2.1 and Fig. 2.13 in Ref. [130] to estimate the traditional optomechanical coupling coefficient G_ν for operation at the $n = 1$ optical resonance, ν_1, closest to the dielectric band edge at ν_{BE}. Here, $G_\nu(\nu_1) \equiv y_{zp} \times \frac{d\nu(1)}{dg}$, where we consider change in resonant frequency ν_1 due to variation in gap width

[1] In this regard, operation in the vicinity of an optical resonance near a band edge of a PCW is analogous to more traditional opto-mechanics, with, for example, Fabry-Perot cavities, for which thermally excited mechanical resonances of a cavity mirror can shift the optical resonances of a high-finesse cavity. The result on a circulating optical field can be phase or amplitude modulation, or even more exotic behavior, including parametric instability [reference], which we will shortly discuss for the APCW.

g as in the previous subsection. $y_{zp} = 12\text{fm}$ is the zero-point amplitude along the chosen coordinate y. By way of the dispersion relation Eq. 7.2 and Ref. [130], we find that $\left|\frac{d\nu(1)}{dg}\right| \simeq 0.027\frac{THz}{nm}$, and thus that the optomechanical coupling coefficient $G_\nu(\nu_1) \simeq 320\text{kHz}$, which is to be compared to the value found in the following section for a full $3D$ geometry.

The zero-point motion amplitude of mode p is [121]

$$x_0(p) = \sqrt{\frac{\hbar}{2m_{\text{eff}}\omega_p}},$$

where $\omega_p = 2\pi f_p$ is the mechanical angular frequency. For a 1D string, the effective mass m_{eff} is half the bulk mass $m = \rho_{\text{SiN}}\mathcal{V}$, where the nominal volume of the APCW is $\mathcal{V} \simeq 14.541\,\mu\text{m}^3$. The mass of the APCW is $m \simeq 46.2\,\text{pg}$. For the fundamental mode using the previous frequency f_1, we have $x_0(p = 1) \simeq 12.4\,\text{fm}$. At room temperature $T = 300\,\text{K}$, $\hbar\omega_0 \ll k_B T$, hence the mean thermal phonon number $\bar{n}(\omega_0) \sim 2.6 \times 10^6$. This gives an rms thermal amplitude $\bar{x} \simeq \sqrt{\bar{n}}x_0 = 20.1\,\text{pm}$. The same result is obtained directly from the classical equipartition theorem. The rms amplitude of mode p in thermal equilibrium at temperature T is

$$A_{\text{rms}}(p) = \sqrt{\frac{k_B T}{m_{\text{eff}}\omega_n^2}}, \quad A(p = 1, 300\,\text{K}) \simeq 20.0\,\text{pm}.$$

7.6 Numerical evaluation of the opto-mechanical coupling rate G_ω

In this section, we consider the full APCW structure and evaluate numerically the opto-mechanical coupling rate from the waveguide to the band-edge regions. We first solve for the light field distribution propagating in the structure by launching the TE mode solution of the infinite single nanobeam waveguide section. This also gives the reflection and transmission coefficients of the TE electromagnetic mode at both ends of the structure which is shown on the right axis of Fig. 7.6. We neglect the small imaginary part of the refractive index for SiN as well as losses due to fabrication imperfections. The mechanical eigenmodes are solved for the full structure with clamped ends, taking into account a constant stress distribution which is the steady-state stress field associated to the e-beam written geometry within the sacrificial layer of SiN with initial homogeneous in-plane stress T.

The exact expression for the opto-mechanical coupling rate g due to displacement shifts of the dielectric boundaries within perturbation theory can be found in [104],

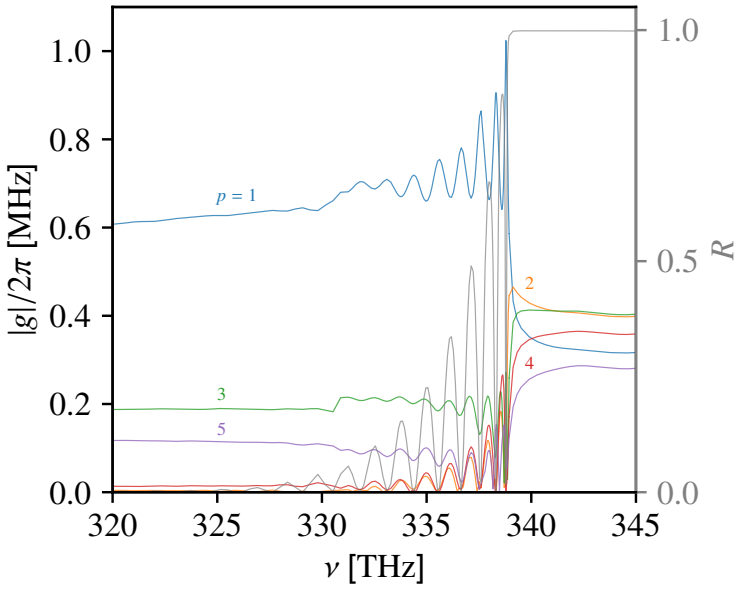

Figure 7.6: Numerically calculated opto-mechanical coupling rate G_ω for eigenmodes from $p = 1$ to $p = 5$ for the family $\psi_p^{y,A}$ as functions of optical frequency. Grey curve shows the reflection spectrum for the TE mode of APCW structure.)

and is

$$g = \frac{d\omega}{d\alpha} x_0, \tag{7.3}$$

which is the product of the mechanical zero-point motion amplitude x_0, and the change in optical mode eigenfrequency due to the dielectric displacement prescribed by the mechanical mode (parametrized by α). The values of the coupling rate g_p are shown in Fig. 7.6 for various eigenmodes p for the family $\psi_p^{y,A}$ as functions of optical frequency. The calculation spans from the waveguide regime far below the TE dielectric band edge, to then approaching the band edge, and finally into the band gap itself.

In contrast to the strains associated with GHz-acoustic modes in our structure for which the phonon wavelength becomes comparable to the optical wavelength, we find the photo-elastic contribution g_{PE} [56] negligible by several orders of magnitude as compared to the dielectric moving boundary contribution for the long-wavelength vibrations under consideration. A measurement of the photo-elastic constant for SiN can be found in [78]. Also, note that $g_{\mathrm{PE}} \propto n^4$, with the ratio of SiN to Si refractive indices $n_{\mathrm{SiN}}/n_{\mathrm{Si}} = 2/3$.

7.7 Conclusion and outlook

We have reported observational data about the motion of an Alligator photonic crystal waveguide and its effects on guided propagating light. The in-plane antisymmetric mode of the two weakly coupled corrugated nanobeam oscillators dominates the coupling to propagating light modes. We have presented a simple model to describe the transduction mechanism as well as numerical simulation of the structure.

The APCW structure was designed in view of combining cold atoms with a room-temperature nano-photonic structure, for which the minimum $Q \cdot f = 6 \times 10^{12}$ Hz product [185] to enter the quantum-mechanical regime would require Q values larger than 2.5×10^6, that is at least x10 than currently observed. The motion of the dielectric is important to consider for combining atom trapping in the vicinity of nano-photonic structures [208]. A simple estimate of heating limited trap lifetime due to trap potential pointing stability can be obtained from the thermal position stability of $\sim 300\,\mathrm{pm}/\sqrt{\mathrm{Hz}}$ at f_1. This corresponds to an energy-doubling time [165] of order 10 ms, at atom trap frequency f_1. Implementing feedback cooling with guided light could alleviate the limitation of operation at room-temperature. The curvature of phonon band can strongly enhanced heating rate for atom trap [90]. We note that due to corrugated pattern for photonic band gap engineering, our structure also possesses phononic band gaps, though in the GHz acoustic domain. Beyond the focus of this article, we can excite selectively the observed mechanical modes with amplitude-modulated guided light at the specific observed frequencies. In fact, we also observe driving of the mechanical resonances with the external optical conveyor belt described in [33]. Further, without light modulation, the APCW is seen to exhibit a bistable behaviour marked with strong self-oscillation (near radian phase modulation amplitude), for continuous guided light power thresholds lower than 100 µW near the band edge. We note that while the q factor values are very modest compared to current records, the very small effective mass allows for a thermo-mechanical force sensitivity limit of $\sqrt{S_{FF}} \simeq 240\,\mathrm{aN}/\sqrt{\mathrm{Hz}}$, only x4 times higher than compared to [185], $S_{FF} = 2m_{\mathrm{eff}} 2\pi f_1 k_B T/Q$. Gravity contributes a force of ~ 1 pN, which when integrated over the long length of the wavelength is equivalent to an effective optical force from guided TE light power of 30 µW. Due to the slow group velocity near the band edge, this value can be lowered by an order of magnitude. Our work suggests further explorations of the mechanical degrees of freedom for atoms coupled to nano-photonic structures.

Chapter 8

CONCLUSIONS AND PERSPECTIVES

The integration of atomic physics and nanophotonics combines the best of two worlds. With atoms as the naturally existing qubits and nanophotonic devices as the engineered interaction medium, new frontiers can be explored for building novel quantum optical circuits for non-conventional quantum optics and exotic quantum many-body physics, as well as potentially serving as a fundamental building block for quantum computation and communication with neutral atoms. While important experimental milestones towards this goal have been reached, a grand challenge for experiments in this new field is the loading and trapping of atomic arrays with high fractional filling near complex nanophotonic structures. In this thesis, we have proposed a novel protocol for atom assembly on nanophotonic structures by integrating optical tweezer arrays and photonic crystal waveguides. This research is inspired by recent exciting progress in free-space atom assembly. However, different from the free-space counterpart, our new proposal should enable subwavelength atom arrays with complex patterns defined by precision nanofabrication. To demonstrate the basic principles behind this new proposal, we have designed and built an advanced apparatus with compact footprint that overcomes several significant experimental barriers in previous experiments. To achieve efficient atom delivery and assembly of arrays for more complex nanostructures, we have proposed a novel direct delivery scheme with optical tweezers by exploiting the rapid spatial variation of the Gouy phase of radial Laguerre-Gauss beams. With reduced dimension in the axial direction, the optical tweezer formed by supposed Laguerre-Gauss beams may find important applications in the communities of general atomic physics and super-resolution imaging. Finally, we have investigated the optomechanical properties of our nanophotonic devices and this information can be further used to evaluate the vibration heating rate to guided mode trapped atoms. The studies presented in this thesis should provide important guidance to future atom-nanophotonic experiments.

BIBLIOGRAPHY

[1] L. Allen, S.M. Barnett, and M.J. Padgett. *Optical Angular Momentum*. Optics and Optoelectronics. Institute of Physics Publishing, Bristol, UK, March 2003. URL http://eprints.gla.ac.uk/65877/.

[2] Wolfgang Alt, Dominik Schrader, Stefan Kuhr, Martin Müller, Victor Gomer, and Dieter Meschede. Single atoms in a standing-wave dipole trap. *Phys. Rev. A*, 67:033403, Mar 2003. doi: 10.1103/PhysRevA.67.033403. URL https://link.aps.org/doi/10.1103/PhysRevA.67.033403.

[3] DJ Alton, NP Stern, Takao Aoki, Hansuek Lee, E Ostby, KJ Vahala, and HJ Kimble. Strong interactions of single atoms and photons near a dielectric boundary. *Nat. Phys.*, 7(2):159, 2011. doi: 10.1038/nphys1837.

[4] Loïc Anderegg, Lawrence W. Cheuk, Yicheng Bao, Sean Burchesky, Wolfgang Ketterle, Kang-Kuen Ni, and John M. Doyle. An optical tweezer array of ultracold molecules. *Science*, 365(6458):1156–1158, 2019. ISSN 0036-8075. doi: 10.1126/science.aax1265. URL https://science.sciencemag.org/content/365/6458/1156.

[5] M. H. Anderson, J. R. Ensher, M. R. Matthews, C. E. Wieman, and E. A. Cornell. Observation of bose-einstein condensation in a dilute atomic vapor. *Science*, 269(5221):198–201, 1995. ISSN 0036-8075. doi: 10.1126/science.269.5221.198. URL https://science.sciencemag.org/content/269/5221/198.

[6] Taro Ando, Yoshiyuki Ohtake, Naoya Matsumoto, Takashi Inoue, and Norihiro Fukuchi. Mode purities of laguerre–gaussian beams generated via complex-amplitudemodulation using phase-only spatial light modulators. *Opt. Lett.*, 34(1):34–36, Jan 2009. doi: 10.1364/OL.34.000034. URL http://ol.osa.org/abstract.cfm?URI=ol-34-1-34.

[7] Takao Aoki, Barak Dayan, E. Wilcut, W. P. Bowen, A. S. Parkins, T. J. Kippenberg, K. J. Vahala, and H. J. Kimble. Observation of strong coupling between one atom and a monolithic microresonator. *Nature*, 443(7112):671, 2006. ISSN 1476-4687. doi: 10.1038/nature05147. URL https://www.nature.com/articles/nature05147.

[8] O. Arcizet, V. Jacques, A. Siria, P. Poncharal, P. Vincent, and S. Seidelin. A single nitrogen-vacancy defect coupled to a nanomechanical oscillator. *Nature Physics*, 7(11):879–883, 2011. doi: 10.1038/nphys2070. URL https://doi.org/10.1038/nphys2070.

[9] J. Arlt and M. J. Padgett. Generation of a beam with a dark focus surrounded by regions of higher intensity: the optical bottle beam. *Opt. Lett.*, 25(4):

191–193, Feb 2000. doi: 10.1364/OL.25.000191. URL http://ol.osa.org/abstract.cfm?URI=ol-25-4-191.

[10] J. Arlt, K. Dholakia, L. Allen, and M. J. Padgett. The production of multiringed laguerre–gaussian modes by computer-generated holograms. *Journal of Modern Optics*, 45(6):1231–1237, 1998. doi: 10.1080/09500349808230913. URL https://doi.org/10.1080/09500349808230913.

[11] A. Asenjo-Garcia, J. D. Hood, D. E. Chang, and H. J. Kimble. Atom-light interactions in quasi-one-dimensional nanostructures: A green's-function perspective. *Phys. Rev. A*, 95:033818, Mar 2017. doi: 10.1103/PhysRevA.95.033818. URL https://link.aps.org/doi/10.1103/PhysRevA.95.033818.

[12] A Asenjo-Garcia, M Moreno-Cardoner, A Albrecht, H J Kimble, and D E Chang. Exponential improvement in photon storage fidelities using subradiance and "selective radiance" in atomic arrays. *Phys. Rev. X*, 7:031024, Aug 2017. doi: 10.1103/PhysRevX.7.031024. URL https://link.aps.org/doi/10.1103/PhysRevX.7.031024.

[13] Arthur Ashkin. *Optical Trapping and Manipulation of Neutral Particles Using Lasers*. WORLD SCIENTIFIC, 2006. doi: 10.1142/4208. URL https://www.worldscientific.com/doi/abs/10.1142/4208.

[14] Mohamed Babiker, David L Andrews, and Vassilis E Lembessis. Atoms in complex twisted light. *Journal of Optics*, 21(1):013001, dec 2018. doi: 10.1088/2040-8986/aaed14. URL https://doi.org/10.1088%2F2040-8986%2Faaed14.

[15] D. Barredo, V. Lienhard, P. Scholl, S. de Léséleuc, T. Boulier, A. Browaeys, and T. Lahaye. Three-dimensional trapping of individual rydberg atoms in ponderomotive bottle beam traps. *Phys. Rev. Lett.*, 124:023201, Jan 2020. doi: 10.1103/PhysRevLett.124.023201. URL https://link.aps.org/doi/10.1103/PhysRevLett.124.023201.

[16] Daniel Barredo, Sylvain de Léséleuc, Vincent Lienhard, Thierry Lahaye, and Antoine Browaeys. An atom-by-atom assembler of defect-free arbitrary two-dimensional atomic arrays. *Science*, 354(6315):1021–1023, 2016. doi: 10.1126/science.aah3778.

[17] Daniel Barredo, Vincent Lienhard, Sylvain de Léséleuc, Thierry Lahaye, and Antoine Browaeys. Synthetic three-dimensional atomic structures assembled atom by atom. *Nature*, 561:79–82, September 2018. doi: 10.1038/s41586-018-0450-2. URL https://doi.org/10.1038/s41586-018-0450-2.

[18] J.-B. Béguin, E. M. Bookjans, S. L. Christensen, H. L. Sørensen, J. H. Müller, E. S. Polzik, and J. Appel. Generation and detection of a sub-poissonian

atom number distribution in a one-dimensional optical lattice. *Phys. Rev. Lett.*, 113:263603, Dec 2014. doi: 10.1103/PhysRevLett.113.263603. URL https://link.aps.org/doi/10.1103/PhysRevLett.113.263603.

[19] J.-B. Béguin, A. P. Burgers, X. Luan, Z. Qin, S. P. Yu, and H. J. Kimble. Advanced apparatus for the integration of nanophotonics and cold atoms. *Optica*, 7(1):1–2, Jan 2020. doi: 10.1364/OPTICA.384408. URL http://www.osapublishing.org/optica/abstract.cfm?URI=optica-7-1-1.

[20] J.-B. Béguin, J. Laurat, X. Luan, A. P. Burgers, Z. Qin, and H. J. Kimble. Reduced volume and reflection for optical tweezers with radial laguerre-gauss beams. *arXiv:2001.11498v2*, 2020.

[21] Hannes Bernien, Sylvain Schwartz, Alexander Keesling, Harry Levine, Ahmed Omran, Hannes Pichler, Soonwon Choi, Alexander S. Zibrov, Manuel Endres, Markus Greiner, Vladan Vuletić, and Mikhail D. Lukin. Probing many-body dynamics on a 51-atom quantum simulator. *Nature*, 551(7682): 579–584, Nov 2017. ISSN 1476-4687. doi: 10.1038/nature24622. URL https://doi.org/10.1038/nature24622.

[22] Tobias Birr, Tim Fischer, Andrey B. Evlyukhin, Urs Zywietz, Boris N. Chichkov, and Carsten Reinhardt. Phase-resolved observation of the gouy phase shift of surface plasmon polaritons. *ACS Photonics*, 4(4):905–908, Apr 2017. doi: 10.1021/acsphotonics.6b00999. URL https://doi.org/10.1021/acsphotonics.6b00999.

[23] Nándor Bokor and Nir Davidson. Toward a spherical spot distribution with 4π focusing of radially polarized light. *Opt. Lett.*, 29(17):1968–1970, Sep 2004. doi: 10.1364/OL.29.001968. URL http://ol.osa.org/abstract.cfm?URI=ol-29-17-1968.

[24] Eliot Bolduc, Nicolas Bent, Enrico Santamato, Ebrahim Karimi, and Robert W. Boyd. Exact solution to simultaneous intensity and phase encryption with a single phase-only hologram. *Opt. Lett.*, 38(18):3546–3549, Sep 2013. doi: 10.1364/OL.38.003546. URL http://ol.osa.org/abstract.cfm?URI=ol-38-18-3546.

[25] Tobias Bothwell, Dhruv Kedar, Eric Oelker, John M Robinson, Sarah L Bromley, Weston L Tew, Jun Ye, and Colin J Kennedy. JILA SrI optical lattice clock with uncertainty of \$2.0 \times 10^{-18}\$. *Metrologia*, 56(6): 065004, oct 2019. doi: 10.1088/1681-7575/ab4089. URL https://doi.org/10.1088%2F1681-7575%2Fab4089.

[26] Robert W. Boyd. Intuitive explanation of the phase anomaly of focused light beams. *J. Opt. Soc. Am.*, 70(7):877–880, Jul 1980. doi: 10.1364/JOSA.70.000877. URL http://www.osapublishing.org/abstract.cfm?URI=josa-70-7-877.

[27] D. W. C. Brooks, T. Botter, S. Schreppler, T. P. Purdy, and D. M. Stamper-Kurn N. Brahms. Non-classical light generated by quantum-noise-driven cavity optomechanics. *Nature*, 488(7412):476–480, 2012. doi: 10.1038/nature11325. URL https://doi.org/10.1038/nature11325.

[28] Antoine Browaeys and Thierry Lahaye. Many-body physics with individually controlled rydberg atoms. *Nature Physics*, 16(2):132–142, Feb 2020. ISSN 1745-2481. doi: 10.1038/s41567-019-0733-z. URL https://doi.org/10.1038/s41567-019-0733-z.

[29] M. O. Brown, T. Thiele, C. Kiehl, T.-W. Hsu, and C. A. Regal. Gray-molasses optical-tweezer loading: Controlling collisions for scaling atom-array assembly. *Phys. Rev. X*, 9:011057, Mar 2019. doi: 10.1103/PhysRevX.9.011057. URL https://link.aps.org/doi/10.1103/PhysRevX.9.011057.

[30] Stefan Yoshi. Buhmann. *Dispersion forces*. Springer, 2012. doi: 10.1007/978-3-642-32484-0.

[31] Stefan Yoshi Buhmann and Dirk-Gunnar Welsch. Dispersion forces in macroscopic quantum electrodynamics. *Progress in Quantum Electronics*, 31(2):51 – 130, 2007. ISSN 0079-6727. doi: https://doi.org/10.1016/j.pquantelec.2007.03.001. URL http://www.sciencedirect.com/science/article/pii/S0079672707000249.

[32] Stefan Yoshi Buhmann, Hassan Safari, Dirk-Gunnar Welsch, and Ho Trung Dung. Microscopic origin of casimir-polder forces. *Open Systems & Information Dynamics*, 13(04):427–436, 2006. doi: 10.1007/s11080-006-9024-0. URL https://doi.org/10.1007/s11080-006-9024-0.

[33] A. P. Burgers, L. S. Peng, J. A. Muniz, A. C. McClung, M. J. Martin, and H. J. Kimble. Clocked atom delivery to a photonic crystal waveguide. *Proceedings of the National Academy of Sciences*, 116(2):456–465, 2019. ISSN 0027-8424. doi: 10.1073/pnas.1817249115. URL https://www.pnas.org/content/116/2/456.

[34] H. B. G. Casimir and D. Polder. The influence of retardation on the london-van der waals forces. *Phys. Rev.*, 73:360–372, Feb 1948. doi: 10.1103/PhysRev.73.360. URL https://link.aps.org/doi/10.1103/PhysRev.73.360.

[35] J. L. Chaloupka, Y. Fisher, T. J. Kessler, and D. D. Meyerhofer. Single-beam, ponderomotive-optical trap for free electrons and neutral atoms. *Opt. Lett.*, 22(13):1021–1023, Jul 1997. doi: 10.1364/OL.22.001021. URL http://ol.osa.org/abstract.cfm?URI=ol-22-13-1021.

[36] Eng Aik Chan, Syed Abdullah Aljunid, Nikolay I. Zheludev, David Wilkowski, and Martial Ducloy. Doppler-free approach to optical pumping dynamics in the 6s1/2−5d5/2 electric quadrupole transition of cesium vapor. *Opt. Lett.*, 41(9):2005–2008, May 2016. doi: 10.1364/OL.41.002005. URL http://ol.osa.org/abstract.cfm?URI=ol-41-9-2005.

[37] J. Chan, T. P. Mayer Alegre, A. H. Safavi-Naeini, J. T. Hill, A. Krause, S. Gröblacher, M. Aspelmeyer, and O. Painter. Laser cooling of a nanomechanical oscillator into its quantum ground state. *Nature*, 478(7367):89–92, 2011. doi: 10.1038/nature10461. URL https://doi.org/10.1038/nature10461.

[38] D E Chang, L Jiang, AV Gorshkov, and HJ Kimble. Cavity qed with atomic mirrors. *New J. Phys.*, 14(6):063003, 2012. doi: 10.1088/1367-2630/14/6/063003.

[39] D E Chang, V Vuletić, and M D Lukin. Quantum nonlinear optics [mdash] photon by photon. *Nat. Photonics*, 8(9):685–694, 2014. doi: 10.1038/nphoton.2014.192.

[40] D. E. Chang, J. S. Douglas, A. González-Tudela, C.-L. Hung, and H. J. Kimble. Colloquium: Quantum matter built from nanoscopic lattices of atoms and photons. *Rev. Mod. Phys.*, 90:031002, Aug 2018. doi: 10.1103/RevModPhys.90.031002. URL https://link.aps.org/doi/10.1103/RevModPhys.90.031002.

[41] K. S. Choi, H. Deng, J. Laurat, and H. J. Kimble. Mapping photonic entanglement into and out of a quantum memory. *Nature*, 452(7183):67–71, Mar 2008. ISSN 1476-4687. doi: 10.1038/nature06670. URL https://doi.org/10.1038/nature06670.

[42] J. Ignacio Cirac and H. Jeff Kimble. Quantum optics, what next? *Nature Photonics*, 11(1):18–20, Jan 2017. ISSN 1749-4893. doi: 10.1038/nphoton.2016.259. URL https://doi.org/10.1038/nphoton.2016.259.

[43] Justin D. Cohen, Seán M. Meenehan, and Oskar Painter. Optical coupling to nanoscale optomechanical cavities for near quantum-limited motion transduction. *Opt. Express*, 21(9):11227–11236, May 2013. doi: 10.1364/OE.21.011227. URL http://www.opticsexpress.org/abstract.cfm?URI=oe-21-9-11227.

[44] Yves Colombe, Tilo Steinmetz, Guilhem Dubois, Felix Linke, David Hunger, and Jakob Reichel. Strong atom–field coupling for bose–einstein condensates in an optical cavity on a chip. *Nature*, 450(7167):272–276, Nov 2007. ISSN 1476-4687. doi: 10.1038/nature06331. URL https://doi.org/10.1038/nature06331.

[45] COMSOL®. COMSOL Multiphysics Reference Manual, version 5.5. www.comsol.com, 2020.

[46] K. L. Corwin, S. J. M. Kuppens, D. Cho, and C. E. Wieman. Spin-polarized atoms in a circularly polarized optical dipole trap. *Phys. Rev. Lett.*, 83:1311–1314, Aug 1999. doi: 10.1103/PhysRevLett.83.1311. URL https://link.aps.org/doi/10.1103/PhysRevLett.83.1311.

[47] Jacob P. Covey, Alp Sipahigil, Szilard Szoke, Neil Sinclair, Manuel Endres, and Oskar Painter. Telecom-band quantum optics with ytterbium atoms and silicon nanophotonics. *Phys. Rev. Applied*, 11:034044, Mar 2019. doi: 10.1103/PhysRevApplied.11.034044. URL https://link.aps.org/doi/10.1103/PhysRevApplied.11.034044.

[48] Jeffrey A. Davis, Don M. Cottrell, Juan Campos, María J. Yzuel, and Ignacio Moreno. Encoding amplitude information onto phase-only filters. *Appl. Opt.*, 38(23):5004–5013, Aug 1999. doi: 10.1364/AO.38.005004. URL http://ao.osa.org/abstract.cfm?URI=ao-38-23-5004.

[49] A. M. Dibos, M. Raha, C. M. Phenicie, and J. D. Thompson. Atomic source of single photons in the telecom band. *Phys. Rev. Lett.*, 120:243601, Jun 2018. doi: 10.1103/PhysRevLett.120.243601. URL https://link.aps.org/doi/10.1103/PhysRevLett.120.243601.

[50] R. H. Dicke. Coherence in spontaneous radiation processes. *Phys. Rev.*, 93: 99–110, Jan 1954. doi: 10.1103/PhysRev.93.99. URL https://link.aps.org/doi/10.1103/PhysRev.93.99.

[51] R. Dorn, S. Quabis, and G. Leuchs. Sharper focus for a radially polarized light beam. *Phys. Rev. Lett.*, 91:233901, Dec 2003. doi: 10.1103/PhysRevLett.91.233901. URL https://link.aps.org/doi/10.1103/PhysRevLett.91.233901.

[52] J. S. Douglas, H. Habibian, C.-L. Hung, A. V. Gorshkov, H. J. Kimble, and D. E. Chang. Quantum many-body models with cold atoms coupled to photonic crystals. *Nature Photonics*, 9:326–331, May 2015. doi: 10.1038/nphoton.2015.57. URL https://doi.org/10.1038/nphoton.2015.57.

[53] L.-M. Duan, M. D. Lukin, J. I. Cirac, and P. Zoller. Long-distance quantum communication with atomic ensembles and linear optics. *Nature*, 414(6862): 413–418, Nov 2001. ISSN 1476-4687. doi: 10.1038/35106500. URL https://doi.org/10.1038/35106500.

[54] J. Durnin, J. J. Miceli, and J. H. Eberly. Diffraction-free beams. *Phys. Rev. Lett.*, 58:1499–1501, Apr 1987. doi: 10.1103/PhysRevLett.58.1499. URL https://link.aps.org/doi/10.1103/PhysRevLett.58.1499.

[55] J. Durnin, J. J. Miceli, and J. H. Eberly. Diffraction-free beams. *Phys. Rev. Lett.*, 58:1499–1501, Apr 1987. doi: 10.1103/PhysRevLett.58.1499. URL https://link.aps.org/doi/10.1103/PhysRevLett.58.1499.

[56] Matt Eichenfield, Jasper Chan, Ryan M. Camacho, Kerry J. Vahala, and Oskar Painter. Optomechanical crystals. *Nature*, 462(7269):78–82, Nov 2009. ISSN 1476-4687. doi: 10.1038/nature08524. URL https://doi.org/10.1038/nature08524.

[57] M Endres, H Bernien, A Keesling, H Levine, E R Anschuetz, A Krajenbrink, C Senko, V Vuletic, M Greiner, and M D Lukin. Atom-by-atom assembly of defect-free one-dimensional cold atom arrays. *Science*, page 3752, 2016. doi: 10.1126/science.aah3752.

[58] R. E. Evans, M. K. Bhaskar, D. D. Sukachev, C. T. Nguyen, A. Sipahigil, M. J. Burek, B. Machielse, G. H. Zhang, A. S. Zibrov, E. Bielejec, H. Park, M. Lončar, and M. D. Lukin. Photon-mediated interactions between quantum emitters in a diamond nanocavity. *Science*, 362(6415): 662–665, 2018. ISSN 0036-8075. doi: 10.1126/science.aau4691. URL https://science.sciencemag.org/content/362/6415/662.

[59] M. Fleischhauer and M. D. Lukin. Quantum memory for photons: Dark-state polaritons. *Phys. Rev. A*, 65:022314, Jan 2002. doi: 10.1103/PhysRevA.65.022314. URL https://link.aps.org/doi/10.1103/PhysRevA.65.022314.

[60] Sonja Franke-Arnold. Optical angular momentum and atoms. *Philosophical Transactions of the Royal Society A: Mathematical, Physical and Engineering Sciences*, 375(2087):20150435, 2017. doi: 10.1098/rsta.2015.0435. URL https://royalsocietypublishing.org/doi/abs/10.1098/rsta.2015.0435.

[61] Harald Friedrich, Georg Jacoby, and Carlo G. Meister. Quantum reflection by casimir–van der waals potential tails. *Phys. Rev. A*, 65:032902, Feb 2002. doi: 10.1103/PhysRevA.65.032902. URL https://link.aps.org/doi/10.1103/PhysRevA.65.032902.

[62] Sebastian Fuchs, Robert Bennett, and Stefan Yoshi Buhmann. Casimir-polder potential of a driven atom. *Phys. Rev. A*, 98:022514, Aug 2018. doi: 10.1103/PhysRevA.98.022514.

[63] Sebastian Fuchs, Robert Bennett, Roman V. Krems, and Stefan Yoshi Buhmann. Nonadditivity of optical and casimir-polder potentials. *Phys. Rev. Lett.*, 121:083603, Aug 2018. doi: 10.1103/PhysRevLett.121.083603. URL https://link.aps.org/doi/10.1103/PhysRevLett.121.083603.

[64] C. W. Gardiner and M. J. Collett. Input and output in damped quantum systems: Quantum stochastic differential equations and the master equation. *Phys. Rev. A*, 31:3761–3774, Jun 1985. doi: 10.1103/PhysRevA.31.3761. URL https://link.aps.org/doi/10.1103/PhysRevA.31.3761.

[65] Crispin Gardiner and Peter Zoller. *The Quantum World of Ultra-Cold Atoms and Light Book I: Foundations of Quantum Optics*. IMPERIAL COLLEGE PRESS, 2014. doi: 10.1142/p941. URL https://www.worldscientific.com/doi/abs/10.1142/p941.

[66] A. Goban, K. S. Choi, D. J. Alton, D. Ding, C. Lacroûte, M. Pototschnig, T. Thiele, N. P. Stern, and H. J. Kimble. Demonstration of a state-insensitive, compensated nanofiber trap. *Phys. Rev. Lett.*, 109:033603, Jul 2012. doi: 10.1103/PhysRevLett.109.033603. URL https://link.aps.org/doi/10.1103/PhysRevLett.109.033603.

[67] A Goban, C-L Hung, S-P Yu, J D Hood, J A Muniz, J H Lee, M J Martin, AC McClung, KS Choi, D E Chang, and H J Kimble. Atom–light interactions in photonic crystals. *Nat. Commun.*, 5:3808, 2014. doi: 10.1038/ncomms4808.

[68] A. Goban, C.-L. Hung, J. D. Hood, S.-P. Yu, J. A. Muniz, O. Painter, and H. J. Kimble. Superradiance for atoms trapped along a photonic crystal waveguide. *Phys. Rev. Lett.*, 115:063601, Aug 2015. doi: 10.1103/PhysRevLett.115.063601. URL https://link.aps.org/doi/10.1103/PhysRevLett.115.063601.

[69] Akihisa Goban. *Strong atom-light interactions along nanosturctures: Transition from free-space to nanophotonic interfaces*. PhD thesis, California Institute of Technology, 2015.

[70] A. González-Tudela and J. I. Cirac. Markovian and non-markovian dynamics of quantum emitters coupled to two-dimensional structured reservoirs. *Phys. Rev. A*, 96:043811, Oct 2017. doi: 10.1103/PhysRevA.96.043811. URL https://link.aps.org/doi/10.1103/PhysRevA.96.043811.

[71] A. González-Tudela, C.-L. Hung, D. E. Chang, J. I. Cirac, and H. J. Kimble. Subwavelength vacuum lattices and atom–atom interactions in two-dimensional photonic crystals. *Nature Photonics*, 9:320–325, May 2015. doi: 10.1038/nphoton.2015.54. URL https://doi.org/10.1038/nphoton.2015.54.

[72] Alejandro González-Tudela and Fernando Galve. Anisotropic quantum emitter interactions in two-dimensional photonic-crystal baths. *ACS Photonics*, 6(1):221–229, 2019. doi: 10.1021/acsphotonics.8b01455. URL https://doi.org/10.1021/acsphotonics.8b01455.

[73] David G. Grier. A revolution in optical manipulation. *Nature*, 424:810–816, August 2003. doi: 10.1038/nature01935. URL https://doi.org/10.1038/nature01935.

[74] T. Gruner and D.-G. Welsch. Quantum-optical input-output relations for dispersive and lossy multilayer dielectric plates. *Phys. Rev. A*, 54:1661–1677, Aug 1996. doi: 10.1103/PhysRevA.54.1661. URL https://link.aps.org/doi/10.1103/PhysRevA.54.1661.

[75] T. Grünzweig, A. Hilliard, M. McGovern, and M. F. Andersen. Near-deterministic preparation of a single atom in an optical microtrap. *Nature Physics*, 6(12):951–954, Dec 2010. ISSN 1745-2481. doi: 10.1038/nphys1778. URL https://doi.org/10.1038/nphys1778.

[76] Mats G. L. Gustafsson, Lin Shao, Peter M. Carlton, C. J. Rachel Wang, Inna N. Golubovskaya, W. Zacheus Cande, David A. Agard, and John W. Sedat. Three-dimensional resolution doubling in wide-field fluorescence microscopy by structured illumination. *Biophysical Journal*, 94(12):4957–4970, Jun 2008. ISSN 0006-3495. doi: 10.1529/biophysj.107.120345. URL https://doi.org/10.1529/biophysj.107.120345.

[77] Dz-Hung Gwo. Ultra precision and reliable bonding method, U.S. Patent 6 284 085, Sep. 2001.

[78] Flavien Gyger, Junqiu Liu, Fan Yang, Jijun He, Arslan S. Raja, Rui Ning Wang, Sunil A. Bhave, Tobias J. Kippenberg, and Luc Thévenaz. Observation of stimulated brillouin scattering in silicon nitride integrated waveguides. *Phys. Rev. Lett.*, 124:013902, Jan 2020. doi: 10.1103/PhysRevLett.124.013902. URL https://link.aps.org/doi/10.1103/PhysRevLett.124.013902.

[79] S Haddadi, D Louhibi, A Hasnaoui, A Harfouche, and K Aït-Ameur. Spatial properties of a diffracted high-order radial laguerre–gauss LGp0beam. *Laser Physics*, 25(12):125002, oct 2015. doi: 10.1088/1054-660x/25/12/125002. URL https://doi.org/10.1088%2F1054-660x%2F25%2F12%2F125002.

[80] K. Hammerer, M. Aspelmeyer, E. S. Polzik, and P. Zoller. Establishing einstein-poldosky-rosen channels between nanomechanics and atomic ensembles. *Physical Review Letters*, 102(2):020501, 2009. doi: 10.1103/physrevlett.102.020501. URL https://doi.org/10.1103/physrevlett.102.020501.

[81] WILLIAM HAPPER. Optical pumping. *Rev. Mod. Phys.*, 44:169–249, Apr 1972. doi: 10.1103/RevModPhys.44.169. URL https://link.aps.org/doi/10.1103/RevModPhys.44.169.

[82] Serge Haroche and Daniel Kleppner. Cavity quantum electrodynamics. *Phys. Today*, 42:24, 1989. doi: 10.1063/1.881201.

[83] Stefan Hell and Ernst H. K. Stelzer. Properties of a 4pi confocal fluorescence microscope. *J. Opt. Soc. Am. A*, 9(12):2159–2166, Dec 1992. doi: 10.1364/JOSAA.9.002159. URL http://josaa.osa.org/abstract.cfm?URI=josaa-9-12-2159.

[84] Fredrik Hocke, Matthias Pernpeintner, Xiaoqing Zhou, Albert Schliesser, Tobias J. Kippenberg, Hans Huebl, and Rudolf Gross. Determination of

effective mechanical properties of a double-layer beam by means of a nano-electromechanical transducer. *Applied Physics Letters*, 105(13):133102, 2014. doi: 10.1063/1.4896785. URL https://doi.org/10.1063/1.4896785.

[85] S. Hong, M. S. Grinolds, P. Maletinsky, R. L. Walsworth, M. D. Lukin, and A. Yacoby. Coherent, mechanical control of a single electronic spin. *Nano Letters*, 12(8):3920–3924, 2012. doi: 10.1021/nl300775c. URL https://doi.org/10.1021/nl300775c.

[86] J D Hood, A Goban, A Asenjo-Garcia, M Lu, S-P Yu, D E Chang, and H J Kimble. Atom–atom interactions around the band edge of a photonic crystal waveguide. *Proc. Natl. Acad. Sci. U.S.A.*, 113(38):10507–10512, 2016. doi: 10.1073/pnas.1603788113.

[87] J D Hood, A Goban, A Asenjo-Garcia, M Lu, S-P Yu, D E Chang, and H J Kimble. Atom–atom interactions around the band edge of a photonic crystal waveguide. *Proc. Natl. Acad. Sci. U.S.A.*, 113(38):10507–10512, 2016. doi: 10.1073/pnas.1603788113.

[88] Jonathan David Hood Hood. *Atom-light interactions in an photonic crystal waveguide*. PhD thesis, California Institute of Technology, 2016.

[89] Hugh. *Handbook of chemical vapor deposition (CVD) : principles, technology, and applications*. Elsevier, 1999.

[90] Daniel Hümmer, Philipp Schneeweiss, Arno Rauschenbeutel, and Oriol Romero-Isart. Heating in nanophotonic traps for cold atoms. *Phys. Rev. X*, 9:041034, Nov 2019. doi: 10.1103/PhysRevX.9.041034. URL https://link.aps.org/doi/10.1103/PhysRevX.9.041034.

[91] Matthew T. Hummon, Songbai Kang, Douglas G. Bopp, Qing Li, Daron A. Westly, Sangsik Kim, Connor Fredrick, Scott A. Diddams, Kartik Srinivasan, Vladimir Aksyuk, and John E. Kitching. Photonic chip for laser stabilization to an atomic vapor with 10−11 instability. *Optica*, 5(4):443–449, April 2018. doi: 10.1364/OPTICA.5.000443. URL http://www.osapublishing.org/optica/abstract.cfm?URI=optica-5-4-443.

[92] C-L Hung, S M Meenehan, D E Chang, O Painter, and H J Kimble. Trapped atoms in one-dimensional photonic crystals. *New Journal of Physics*, 15(8):083026, aug 2013. doi: 10.1088/1367-2630/15/8/083026. URL https://doi.org/10.1088%2F1367-2630%2F15%2F8%2F083026.

[93] C.-L. Hung, Alejandro González-Tudela, J. Ignacio Cirac, and H. J. Kimble. Quantum spin dynamics with pairwise-tunable, long-range interactions. *Proceedings of the National Academy of Sciences*, 113(34):E4946–E4955, 2016. ISSN 0027-8424. doi: 10.1073/pnas.1603777113. URL https://www.pnas.org/content/113/34/E4946.

[94] Nicholas R Hutzler, Lee R Liu, Yichao Yu, and Kang-Kuen Ni. Eliminating light shifts for single atom trapping. *New Journal of Physics*, 19(2):023007, feb 2017. doi: 10.1088/1367-2630/aa5a3b. URL https://doi.org/10.1088%2F1367-2630%2Faa5a3b.

[95] Optotune Inc. Optotune inc. https://www.optotune.com/products/focus-tunable-lenses, 2020. [Online; accessed 06-April-2020].

[96] Starna Inc. Starna cells inc. http://www.starnacells.com/, 2020. [Online; accessed 06-Jan-2020].

[97] L. Isenhower, W. Williams, A. Dally, and M. Saffman. Atom trapping in an interferometrically generated bottle beam trap. *Opt. Lett.*, 34(8):1159–1161, Apr 2009. doi: 10.1364/OL.34.001159. URL http://ol.osa.org/abstract.cfm?URI=ol-34-8-1159.

[98] John David Jackson. *Classical electrodynamics*. Wiley, New York, NY, 3rd ed. edition, 1999. ISBN 9780471309321. URL http://cdsweb.cern.ch/record/490457.

[99] John D. Joannopoulos, Steven G. Johnson, Joshua N. Winn, and Robert D. Meade. *Photonic Crystals: Molding the Flow of Light (Second Edition)*. Princeton University Press, 2 edition, 2008. ISBN 0691124566. URL http://www.amazon.com/Photonic-Crystals-Molding-Light-Second/dp/0691124566%3FSubscriptionId%3D13CT5CVB80YFWJEPWS02%26tag%3Dws%26linkCode%3Dxm2%26camp%3D2025%26creative%3D165953%26creativeASIN%3D0691124566.

[100] Sajeev John. Strong localization of photons in certain disordered dielectric superlattices. *Physical Review Letters*, 58(23):2486–2489, 1987. doi: 10.1103/PhysRevLett.58.2486. URL https://link.aps.org/doi/10.1103/PhysRevLett.58.2486.

[101] Sajeev John and Jian Wang. Quantum electrodynamics near a photonic band gap: Photon bound states and dressed atoms. *Phys. Rev. Lett.*, 64:2418–2421, May 1990. doi: 10.1103/PhysRevLett.64.2418. URL https://link.aps.org/doi/10.1103/PhysRevLett.64.2418.

[102] Steven G. Johnson and J. D. Joannopoulos. Block-iterative frequency-domain methods for maxwell's equations in a planewave basis. *Opt. Express*, 8 (3):173–190, Jan 2001. doi: 10.1364/OE.8.000173. URL http://www.opticsexpress.org/abstract.cfm?URI=oe-8-3-173.

[103] Steven G. Johnson and J. D. Joannopoulos. Block-iterative frequency-domain methods for maxwell's equations in a planewave basis. *Opt. Express*, 8 (3):173–190, 2001. URL http://www.opticsexpress.org/abstract.cfm?URI=OPEX-8-3-173.

[104] Steven G. Johnson, M. Ibanescu, M. A. Skorobogatiy, O. Weisberg, J. D. Joannopoulos, and Y. Fink. Perturbation theory for maxwell's equations with shifting material boundaries. *Phys. Rev. E*, 65:066611, Jun 2002. doi: 10.1103/PhysRevE.65.066611. URL https://link.aps.org/doi/10.1103/PhysRevE.65.066611.

[105] A. M. Kaufman, B. J. Lester, and C. A. Regal. Cooling a single atom in an optical tweezer to its quantum ground state. *Phys. Rev. X*, 2:041014, Nov 2012. doi: 10.1103/PhysRevX.2.041014. URL https://link.aps.org/doi/10.1103/PhysRevX.2.041014.

[106] A. M. Kaufman, B. J. Lester, C. M. Reynolds, M. L. Wall, M. Foss-Feig, K. R. A. Hazzard, A. M. Rey, and C. A. Regal. Two-particle quantum interference in tunnel-coupled optical tweezers. *Science*, 345(6194):306–309, 2014. ISSN 0036-8075, 1095-9203. doi: 10.1126/science.1250057. URL https://science.sciencemag.org/content/345/6194/306.

[107] Hyosub Kim, Woojun Lee, Han-gyeol Lee, Hanlae Jo, Yunheung Song, and Jaewook Ahn. In situ single-atom array synthesis using dynamic holographic optical tweezers. *Nature Communications*, 7(1):13317, Oct 2016. ISSN 2041-1723. doi: 10.1038/ncomms13317. URL https://doi.org/10.1038/ncomms13317.

[108] May E. Kim, Tzu-Han Chang, Brian M. Fields, Cheng-An Chen, and Chen-Lung Hung. Trapping single atoms on a nanophotonic circuit with configurable tweezer lattices. *Nature Communications*, 10(1):1647, 2019. ISSN 2041-1723. doi: 10.1038/s41467-019-09635-7.

[109] H. J. Kimble. Strong interactions of single atoms and photons in cavity QED. *Physica Scripta*, T76(1):127, 1998. doi: 10.1238/physica.topical.076a00127. URL https://doi.org/10.1238%2Fphysica.topical.076a00127.

[110] H. J. Kimble. The quantum internet. *Nature*, 453(7198):1023–1030, 2008. ISSN 1476-4687. doi: 10.1038/nature07127. URL https://doi.org/10.1038/nature07127.

[111] Charles Kittel. *Introduction to Solid State Physics*. Wiley, 2004.

[112] S. Kolkowitz, A. C. Bleszynski Jayich, Q. P. Unterreithmeier, S. D. Bennett, P. Rabl, J. G. E. Harris, and M. D. Lukin. Coherent sensing of a mechanical resonator with a single-spin qubit. *Science*, 335(6076):1603–1606, 2012. doi: 10.1126/science.1216821. URL https://doi.org/10.1126/science.1216821.

[113] Hideo Kosaka, Takayuki Kawashima, Akihisa Tomita, Masaya Notomi, Toshiaki Tamamura, Takashi Sato, and Shojiro Kawakami. Self-collimating phenomena in photonic crystals. *Applied Physics Letters*, 74(9):1212–1214, 1999. doi: 10.1063/1.123502. URL https://doi.org/10.1063/1.123502.

[114] Takahiro Kuga, Yoshio Torii, Noritsugu Shiokawa, Takuya Hirano, Yukiko Shimizu, and Hiroyuki Sasada. Novel optical trap of atoms with a doughnut beam. *Phys. Rev. Lett.*, 78:4713–4716, Jun 1997. doi: 10.1103/PhysRevLett.78.4713. URL https://link.aps.org/doi/10.1103/PhysRevLett.78.4713.

[115] S. Kuhr, W. Alt, D. Schrader, I. Dotsenko, Y. Miroshnychenko, A. Rauschenbeutel, and D. Meschede. Analysis of dephasing mechanisms in a standing-wave dipole trap. *Phys. Rev. A*, 72:023406, Aug 2005. doi: 10.1103/PhysRevA.72.023406. URL https://link.aps.org/doi/10.1103/PhysRevA.72.023406.

[116] Aishwarya Kumar, Tsung-Yao Wu, Felipe Giraldo, and David S. Weiss. Sorting ultracold atoms in a three-dimensional optical lattice in a realization of maxwell's demon. *Nature*, 561(7721):83–87, Sep 2018. ISSN 1476-4687. doi: 10.1038/s41586-018-0458-7. URL https://doi.org/10.1038/s41586-018-0458-7.

[117] A. Kuzmich, L. Mandel, and N. P. Bigelow. Generation of spin squeezing via continuous quantum nondemolition measurement. *Phys. Rev. Lett.*, 85:1594–1597, Aug 2000. doi: 10.1103/PhysRevLett.85.1594. URL https://link.aps.org/doi/10.1103/PhysRevLett.85.1594.

[118] Fam Le Kien, Philipp Schneeweiss, and Arno Rauschenbeutel. Dynamical polarizability of atoms in arbitrary light fields: general theory and application to cesium. *The European Physical Journal D*, 67(5):92, 2013. ISSN 1434-6079. doi: 10.1140/epjd/e2013-30729-x. URL https://doi.org/10.1140/epjd/e2013-30729-x.

[119] Woojun Lee, Hyosub Kim, and Jaewook Ahn. Three-dimensional rearrangement of single atoms using actively controlled optical microtraps. *Opt. Express*, 24(9):9816–9825, May 2016. doi: 10.1364/OE.24.009816. URL http://www.opticsexpress.org/abstract.cfm?URI=oe-24-9-9816.

[120] Brian J. Lester, Niclas Luick, Adam M. Kaufman, Collin M. Reynolds, and Cindy A. Regal. Rapid production of uniformly filled arrays of neutral atoms. *Phys. Rev. Lett.*, 115:073003, Aug 2015. doi: 10.1103/PhysRevLett.115.073003. URL https://link.aps.org/doi/10.1103/PhysRevLett.115.073003.

[121] Yongzhuo Li, Kaiyu Cui, Xue Feng, Yidong Huang, Zhilei Huang, Fang Liu, and Wei Zhang. Optomechanical crystal nanobeam cavity with high optomechanical coupling rate. *Journal of Optics*, 17(4):045001, 2015. URL http://stacks.iop.org/2040-8986/17/i=4/a=045001.

[122] E.M. Lifshitz. The theory of molecular attractive forces between solids. *Sov. Phys. JETP*, 2:73–83, 1956.

[123] Yanbing Liu and Andrew A. Houck. Quantum electrodynamics near a photonic bandgap. *Nature Physics*, 13(1):48–52, Jan 2017. ISSN 1745-2481. doi: 10.1038/nphys3834. URL https://doi.org/10.1038/nphys3834.

[124] Peter Lodahl, Sahand Mahmoodian, Soren Stobbe, Arno Rauschenbeutel, Philipp Schneeweiss, Jurgen Volz, Hannes Pichler, and Peter Zoller. Chiral quantum optics. *Nature*, 541:473–490, January 2017. doi: 10.1038/nature21037. URL https://doi.org/10.1038/nature21037.

[125] Xingsheng Luan, Jean-Baptiste Béguin, Alex P. Burgers, Zhongzhong Qin, Su-Peng Yu, and Harry J. Kimble. The integration of photonic crystal waveguides with atom arrays in optical tweezers. *Advanced Quantum Technologies*, n/a(n/a):2000008, 2020. doi: 10.1002/qute.202000008. URL https://onlinelibrary.wiley.com/doi/abs/10.1002/qute.202000008.

[126] Lumerical®. Lumerical FDTD Reference Manual. https://www.lumerical.com/products/, 2020.

[127] E. R. MacQuarrie, T. A. Gosavi, N. R. Jungwirth, S. A. Bhave, and G. D. Fuchs. Mechanical spin control of nitrogen-vacancy centers in diamond. *Physical Review Letters*, 111(22):227602, 2013. doi: 10.1103/physrevlett.111.227602. URL https://doi.org/10.1103/physrevlett.111.227602.

[128] V. Mangano, A. A. van Veggel, R. Douglas, J. Faller, A. Grant, J. Hough, and S. Rowan. Determination of the refractive index and thickness of a hydroxide-catalysis bond between fused silica from reflectivity measurements. *Opt. Express*, 25(4):3196–3213, Feb 2017. doi: 10.1364/OE.25.003196. URL http://www.opticsexpress.org/abstract.cfm?URI=oe-25-4-3196.

[129] Alexander P. McCauley, Alejandro W. Rodriguez, John D. Joannopoulos, and Steven G. Johnson. Casimir forces in the time domain: Applications. *Phys. Rev. A*, 81:012119, Jan 2010. doi: 10.1103/PhysRevA.81.012119. URL https://link.aps.org/doi/10.1103/PhysRevA.81.012119.

[130] Andrew Corby McClung. *Photonic Crystal Waveguides for Integration into an Atomic Physics Experiment*. PhD thesis, California Institute of Technology, 2017.

[131] Andrew Corby McClung. *Photonic Crystal Waveguides for Integration into an Atomic Physics Experiment*. PhD thesis, California Institute of Technology, 2017.

[132] Y. Meng, A. Dareau, P. Schneeweiss, and A. Rauschenbeutel. Near-ground-state cooling of atoms optically trapped 300 nm away from a hot surface. *Phys. Rev. X*, 8:031054, Sep 2018. doi: 10.1103/PhysRevX.8.031054. URL https://link.aps.org/doi/10.1103/PhysRevX.8.031054.

[133] Harold J. Metcalf and Peter van der Straten. *Laser Cooling and Trapping*. Springer-Verlag, New York, 1999.

[134] Mohammad Mirhosseini, Eunjong Kim, Xueyue Zhang, Alp Sipahigil, Paul B. Dieterle, Andrew J. Keller, Ana Asenjo-Garcia, Darrick E. Chang, and Oskar Painter. Cavity quantum electrodynamics with atom-like mirrors. *Nature*, 569(7758):692–697, 2019. ISSN 1476-4687. doi: 10.1038/s41586-019-1196-1. URL https://doi.org/10.1038/s41586-019-1196-1.

[135] Kali P. Nayak, Jie Wang, and Jameesh Keloth. Real-time observation of single atoms trapped and interfaced to a nanofiber cavity. *Phys. Rev. Lett.*, 123: 213602, Nov 2019. doi: 10.1103/PhysRevLett.123.213602. URL https://link.aps.org/doi/10.1103/PhysRevLett.123.213602.

[136] M. Notomi, K. Yamada, A. Shinya, J. Takahashi, C. Takahashi, and I. Yokohama. Extremely large group-velocity dispersion of line-defect waveguides in photonic crystal slabs. *Phys. Rev. Lett.*, 87:253902, Nov 2001. doi: 10.1103/PhysRevLett.87.253902. URL https://link.aps.org/doi/10.1103/PhysRevLett.87.253902.

[137] Lukas Novotny and Bert Hecht. *Principles of Nano-Optics*. Cambridge University Press, 2006. doi: 10.1017/CBO9780511813535.

[138] A. D. O'Connell, M. Hofheinz, M. Ansmann, R. C. Bialczak, M. Lenander, Erik Lucero, M. Neeley, D. Sank, H. Wang, M. Weides, J. Wenner, J. M. Martinis, and A. N. Cleland. Quantum ground state and single-phonon control of a mechanical resonator. *Nature*, 464(7289):697–703, 2010. doi: 10.1038/nature08967. URL https://doi.org/10.1038/nature08967.

[139] Daniel Ohl de Mello, Dominik Schäffner, Jan Werkmann, Tilman Preuschoff, Lars Kohfahl, Malte Schlosser, and Gerhard Birkl. Defect-free assembly of 2d clusters of more than 100 single-atom quantum systems. *Phys. Rev. Lett.*, 122:203601, May 2019. doi: 10.1103/PhysRevLett.122.203601. URL https://link.aps.org/doi/10.1103/PhysRevLett.122.203601.

[140] Ardavan F. Oskooi, David Roundy, Mihai Ibanescu, Peter Bermel, J.D. Joannopoulos, and Steven G. Johnson. Meep: A flexible free-software package for electromagnetic simulations by the fdtd method. *Computer Physics Communications*, 181(3):687 – 702, 2010. ISSN 0010-4655. doi: https://doi.org/10.1016/j.cpc.2009.11.008. URL http://www.sciencedirect.com/science/article/pii/S001046550900383X.

[141] P. Ovartchaiyapong, K. W. Lee, B. A. Myers, and A. C. B. Jayich. Dynamic strain-mediated coupling of a single diamond spin to a mechanical resonator. *Nature Communications*, 5(1):4429, 2014. doi: 10.1038/ncomms5429. URL https://doi.org/10.1038/ncomms5429.

[142] Roee Ozeri, Lev Khaykovich, and Nir Davidson. Long spin relaxation times in a single-beam blue-detuned optical trap. *Phys. Rev. A*, 59:R1750–R1753, Mar 1999. doi: 10.1103/PhysRevA.59.R1750. URL https://link.aps.org/doi/10.1103/PhysRevA.59.R1750.

[143] Miles Padgett and Richard Bowman. Tweezers with a twist. *Nature Photonics*, 5(6):343–348, 2011. ISSN 1749-4893. doi: 10.1038/nphoton.2011.81. URL https://doi.org/10.1038/nphoton.2011.81.

[144] T. A. Palomaki, J. D. Teufel, R. W. Simmonds, and K. W. Lehnert. Entangling mechanical motion with microwave fields. *Science*, 342(6159):710–713, 2013. doi: 10.1126/science.1244563. URL https://doi.org/10.1126/science.1244563.

[145] V. Paulisch, M. Perarnau-Llobet, A. González-Tudela, and J. I. Cirac. Quantum metrology with one-dimensional superradiant photonic states. *Phys. Rev. A*, 99:043807, Apr 2019. doi: 10.1103/PhysRevA.99.043807. URL https://link.aps.org/doi/10.1103/PhysRevA.99.043807.

[146] Lucas Sky Peng. *Clocked Atom Delivery to a Photonic CrystalWaveguide: Simulations and Experiments*. PhD thesis, California Institute of Technology, 5 2019.

[147] J. Perczel, J. Borregaard, D. E. Chang, S. F. Yelin, and M. D. Lukin. Topological quantum optics using atom-like emitter arrays coupled to photonic crystals. *Phys. Rev. Lett.*, 124:083603, Feb 2020. doi: 10.1103/PhysRevLett.124.083603. URL https://link.aps.org/doi/10.1103/PhysRevLett.124.083603.

[148] Nathalie Picqué and Theodor W. Hänsch. Frequency comb spectroscopy. *Nature Photonics*, 13:146–157, March 2019. doi: 10.1038/s41566-018-0347-5. URL https://doi.org/10.1038/s41566-018-0347-5.

[149] E. M. Purcell. Proceedings of the american physical society. *Phys. Rev.*, 69: 674–674, Jun 1946. doi: 10.1103/PhysRev.69.674. URL https://link.aps.org/doi/10.1103/PhysRev.69.674.

[150] T. P. Purdy, R. W. Peterson, and C. A. Regal. Observation of radiation pressure shot noise on a macroscopic object. *Science*, 339(6121):801–804, 2013. doi: 10.1126/science.1231282. URL https://doi.org/10.1126/science.1231282.

[151] T. P. Purdy, P.-L. Yu, R. W. Peterson, N. S. Kampel, and C. A. Regal. Strong optomechanical squeezing of light. *Physical Review X*, 3(3):031012, 2013. doi: 10.1103/physrevx.3.031012. URL https://doi.org/10.1103/physrevx.3.031012.

[152] P. Rabl, P. Cappellaro, M. V. Gurudev Dutt, L. Jiang, J. R. Maze, and M. D. Lukin. Strong magnetic coupling between an electronic spin qubit and a mechanical resonator. *Physical Review B*, 79(4):041302, 2009. doi: 10.1103/physrevb.79.041302. URL https://doi.org/10.1103/physrevb.79.041302.

[153] P. Rabl, S. J. Kolkowitz, F. H. L. Koppens, J. G. E. Harris, P. Zoller, and M. D. Lukin. A quantum spin transducer based on nanoelectromechanical resonator arrays. *Nature Physics*, 6(8):602–608, 2010. doi: 10.1038/nphys1679. URL https://doi.org/10.1038/nphys1679.

[154] Andreas Reiserer and Gerhard Rempe. Cavity-based quantum networks with single atoms and optical photons. *Rev. Mod. Phys.*, 87:1379–1418, Dec 2015. doi: 10.1103/RevModPhys.87.1379. URL https://link.aps.org/doi/10.1103/RevModPhys.87.1379.

[155] Gerhard Rempe, Herbert Walther, and Norbert Klein. Observation of quantum collapse and revival in a one-atom maser. *Physical Review Letters*, 58(4):353–356, 1987. doi: 10.1103/PhysRevLett.58.353. URL https://link.aps.org/doi/10.1103/PhysRevLett.58.353.

[156] B. Richards, E. Wolf, and Dennis Gabor. Electromagnetic diffraction in optical systems, ii. structure of the image field in an aplanatic system. *Proceedings of the Royal Society of London. Series A. Mathematical and Physical Sciences*, 253(1274):358–379, 1959. doi: 10.1098/rspa.1959.0200. URL https://royalsocietypublishing.org/doi/abs/10.1098/rspa.1959.0200.

[157] Ralf Ritter, Nico Gruhler, Helge Dobbertin, Harald Kübler, Stefan Scheel, Wolfram Pernice, Tilman Pfau, and Robert Löw. Coupling thermal atomic vapor to slot waveguides. *Phys. Rev. X*, 8(2):021032, 2018. doi: 10.1103/PhysRevX.8.021032.

[158] Alejandro W. Rodriguez, Alexander P. McCauley, John D. Joannopoulos, and Steven G. Johnson. Casimir forces in the time domain: Theory. *Phys. Rev. A*, 80:012115, Jul 2009. doi: 10.1103/PhysRevA.80.012115. URL https://link.aps.org/doi/10.1103/PhysRevA.80.012115.

[159] D. Rugar, R. Budakian, H. J. Mamin, and B. W. Chui. Single spin detection by magnetic resonance force microscopy. *Nature*, 430(6997):329–332, 2004. doi: 10.1038/nature02658. URL https://doi.org/10.1038/nature02658.

[160] A. H. Safavi-Naeini, J. Chan, J. T. Hill, T. P. M. Alegre, A. Krause, and O. Painter. Observation of quantum motion of a nanomechanical resonator. *Physical Review Letters*, 108(3):033602, 2012. doi: 10.1103/physrevlett.108.033602. URL https://doi.org/10.1103/physrevlett.108.033602.

[161] A. H. Safavi-Naeini, S. Gröblacher, J. T. Hill, J. Chan, M. Aspelmeyer, and Oskar Painter. Squeezed light from a silicon micromechanical resonator. *Nature*, 500(7461):185–189, 2013. doi: 10.1038/nature12307. URL https://doi.org/10.1038/nature12307.

[162] K. Sakoda. *Optical Properties of Photonic Crystals*. Springer Berlin Heidelberg, 2004. doi: 10.1007/b138376.

[163] Tasso R. M. Sales. Smallest focal spot. *Phys. Rev. Lett.*, 81:3844–3847, Nov 1998. doi: 10.1103/PhysRevLett.81.3844. URL https://link.aps.org/doi/10.1103/PhysRevLett.81.3844.

[164] Polnop Samutpraphoot, Tamara Dordević, Paloma L. Ocola, Hannes Bernien, Crystal Senko, Vladan Vuletić, and Mikhail D. Lukin. Strong coupling of two individually controlled atoms via a nanophotonic cavity. *Phys. Rev. Lett.*, 124:063602, Feb 2020. doi: 10.1103/PhysRevLett.124.063602. URL https://link.aps.org/doi/10.1103/PhysRevLett.124.063602.

[165] T. A. Savard, K. M. O'Hara, and J. E. Thomas. Laser-noise-induced heating in far-off resonance optical traps. *Phys. Rev. A*, 56:R1095–R1098, Aug 1997. doi: 10.1103/PhysRevA.56.R1095. URL https://link.aps.org/doi/10.1103/PhysRevA.56.R1095.

[166] M Schlosser, J Kruse, C Gierl, S Teichmann, S Tichelmann, and G Birkl. Fast transport, atom sample splitting and single-atom qubit supply in two-dimensional arrays of optical microtraps. *New Journal of Physics*, 14(12): 123034, dec 2012. doi: 10.1088/1367-2630/14/12/123034. URL https://doi.org/10.1088%2F1367-2630%2F14%2F12%2F123034.

[167] N. Schlosser, G. Reymond, I. Protsenko, and P. Grangier. Sub-poissonian loading of single atoms in a microscopic dipole trap. *Nature*, 411:1024–1027, Jun 2001. doi: 10.1038/35082512. URL https://doi.org/10.1038/35082512.

[168] N. Schlosser, G. Reymond, and P. Grangier. Collisional blockade in microscopic optical dipole traps. *Phys. Rev. Lett.*, 89:023005, Jun 2002. doi: 10.1103/PhysRevLett.89.023005. URL https://link.aps.org/doi/10.1103/PhysRevLett.89.023005.

[169] Fujio Shimizu. Specular reflection of very slow metastable neon atoms from a solid surface. *Phys. Rev. Lett.*, 86:987–990, Feb 2001. doi: 10.1103/PhysRevLett.86.987. URL https://link.aps.org/doi/10.1103/PhysRevLett.86.987.

[170] A. E. Siegman. *Lasers*. Oxford University Press, 1986.

[171] Juan Andres Muniz Silva. *Nanoscopic atomic lattices with light-mediated interactions*. PhD thesis, California Institute of Technology, 5 2017.

[172] A. Sipahigil, R. E. Evans, D. D. Sukachev, M. J. Burek, J. Borregaard, M. K. Bhaskar, C. T. Nguyen, J. L. Pacheco, H. A. Atikian, C. Meuwly, R. M. Camacho, F. Jelezko, E. Bielejec, H. Park, M. Lončar, and M. D. Lukin. An integrated diamond nanophotonics platform for quantum-optical networks. *Science*, 354(6314):847–850, 2016. ISSN 0036-8075. doi: 10.1126/science.aah6875. URL https://science.sciencemag.org/content/354/6314/847.

[173] D A Steck. Cesium d line data. . URL http://george.ph.utexas.edu/~dsteck/alkalidata/cesiumnumbers.pdf.

[174] D A Steck. *Quantum and Atom optics*. . URL http://atomoptics-nas.uoregon.edu/~dsteck/teaching/quantum-optics/.

[175] NP Stern, DJ Alton, and HJ Kimble. Simulations of atomic trajectories near a dielectric surface. *New J. Phys.*, 13(8):085004, 2011. doi: 10.1088/1367-2630/13/8/085004.

[176] Ole Steuernagel, Eric Yao, Kevin O'Holleran, and Miles Padgett. Observation of gouy-phase-induced transversal intensity changes in focused beams. *Journal of Modern Optics*, 52:2713–2721, 12 2005. doi: 10.1080/09500340500347121.

[177] Yasuzi Suzaki and Atsushi Tachibana. Measurement of the μm sized radius of gaussian laser beam using the scanning knife-edge. *Appl. Opt.*, 14(12):2809–2810, Dec 1975. doi: 10.1364/AO.14.002809. URL http://ao.osa.org/abstract.cfm?URI=ao-14-12-2809.

[178] Eduardo Sánchez-Burillo, Alejandro González-Tudela, and Carlos Gonzalez-Ballestero. Theory of waveguide-qed with moving emitters, 2020.

[179] J. Teissier, A. Barfuss, P. Appel, E. Neu, and P. Maletinsky. Strain coupling of a nitrogen-vacancy center spin to a diamond mechanical oscillator. *Physical Review Letters*, 113(2):020503, 2014. doi: 10.1103/physrevlett.113.020503. URL https://doi.org/10.1103/physrevlett.113.020503.

[180] J. D. Teufel, T. Donner, Dale Li, J. W. Harlow, M. S. Allman, K. Cicak, A. J. Sirois, J. D. Whittaker, K. W. Lehnert, and R. W. Simmonds. Sideband cooling of micromechanical motion to the quantum ground state. *Nature*, 475(7356):359–363, 2011. doi: 10.1038/nature10261. URL https://doi.org/10.1038/nature10261.

[181] J. D. Thompson, T. G. Tiecke, A. S. Zibrov, V. Vuletić, and M. D. Lukin. Coherence and raman sideband cooling of a single atom in an optical tweezer. *Phys. Rev. Lett.*, 110:133001, Mar 2013. doi: 10.1103/PhysRevLett.110.133001. URL https://link.aps.org/doi/10.1103/PhysRevLett.110.133001.

[182] J D Thompson, TG Tiecke, N P de Leon, J Feist, AV Akimov, M Gullans, A S Zibrov, V Vuletić, and M D Lukin. Coupling a single trapped atom to a nanoscale optical cavity. *Science*, 340(6137):1202–1205, 2013. doi: 10.1126/science.1237125.

[183] R. J. Thompson, G. Rempe, and H. J. Kimble. Observation of normal-mode splitting for an atom in an optical cavity. *Physical Review Letters*, 68(8):1132–1135, 1992. doi: 10.1103/PhysRevLett.68.1132. URL https://link.aps.org/doi/10.1103/PhysRevLett.68.1132.

[184] TG Tiecke, Jeffrey Douglas Thompson, Nathalie Pulmones de Leon, LR Liu, Vladan Vuletić, and Mikhail D Lukin. Nanophotonic quantum phase switch with a single atom. *Nature*, 508(7495):241, 2014. doi: 10.1038/nature13188.

[185] Y. Tsaturyan, A. Barg, E. S. Polzik, and A. Schliesser. Ultracoherent nanomechanical resonators via soft clamping and dissipation dilution. *Nature Nanotechnology*, 12(8):776–783, 2017. doi: 10.1038/nnano.2017.101. URL https://doi.org/10.1038/nnano.2017.101.

[186] C. Tuchendler, A. M. Lance, A. Browaeys, Y. R. P. Sortais, and P. Grangier. Energy distribution and cooling of a single atom in an optical tweezer. *Phys. Rev. A*, 78:033425, Sep 2008. doi: 10.1103/PhysRevA.78.033425. URL https://link.aps.org/doi/10.1103/PhysRevA.78.033425.

[187] Kerry J. Vahala. Optical microcavities. *Nature*, 424(6950):839–846, Aug 2003. ISSN 1476-4687. doi: 10.1038/nature01939. URL https://doi.org/10.1038/nature01939.

[188] S. J. van Enk and H. J. Kimble. Strongly focused light beams interacting with single atoms in free space. *Physical Review A*, 63(2):023809, 2001. doi: 10.1103/PhysRevA.63.023809. URL https://link.aps.org/doi/10.1103/PhysRevA.63.023809.

[189] Anna-Maria A. van Veggel and Christian J. Killow. Hydroxide catalysis bonding for astronomical instruments. *Advanced Optical Technologies*, 3(3):293–307, Jun 2014. doi: 10.1515/aot-2014-0022. URL https://doi.org/10.1515/aot-2014-0022.

[190] J Vangindertael, R Camacho, W Sempels, H Mizuno, P Dedecker, and K P F Janssen. An introduction to optical super-resolution microscopy for the adventurous biologist. *Methods and Applications in Fluorescence*, 6(2):022003, mar 2018. doi: 10.1088/2050-6120/aaae0c. URL https://doi.org/10.1088%2F2050-6120%2Faaae0c.

[191] E Vetsch, D Reitz, G Sagué, R Schmidt, ST Dawkins, and A Rauschenbeutel. Optical interface created by laser-cooled atoms trapped in the evanescent field surrounding an optical nanofiber. *Phys. Rev. Lett.*, 104(20):203603, 2010. doi: 10.1103/PhysRevLett.104.203603.

[192] L. G. Villanueva and S. Schmid. Evidence of surface loss as ubiquitous limiting damping mechanism in sin micro- and nanomechanical resonators. *Physical Review Letters*, 113(22):227201, 2014. doi: 10.1103/physrevlett.113.227201. URL https://doi.org/10.1103/physrevlett.113.227201.

[193] Haifeng Wang, Luping Shi, Boris Lukyanchuk, Colin Sheppard, and Chong Tow Chong. Creation of a needle of longitudinally polarized light in vacuum using binary optics. *Nature Photonics*, 2(8):501–505, 2008. ISSN 1749-4893. doi: 10.1038/nphoton.2008.127. URL https://doi.org/10.1038/nphoton.2008.127.

[194] Andrew I. Whiting, Ayman F. Abouraddy, Bahaa E. A. Saleh, Malvin C. Teich, and John T. Fourkas. Polarization-assisted transverse and axial optical superresolution. *Opt. Express*, 11(15):1714–1723, Jul 2003. doi: 10.1364/OE.11.001714. URL http://www.opticsexpress.org/abstract.cfm?URI=oe-11-15-1714.

[195] Paweł Woźniak, Peter Banzer, Frédéric Bouchard, Ebrahim Karimi, Gerd Leuchs, and Robert W. Boyd. Tighter spots of light with superposed orbital-angular-momentum beams. *Phys. Rev. A*, 94:021803, Aug 2016. doi: 10.1103/PhysRevA.94.021803. URL https://link.aps.org/doi/10.1103/PhysRevA.94.021803.

[196] Peng Xu, Xiaodong He, Jin Wang, and Mingsheng Zhan. Trapping a single atom in a blue detuned optical bottle beam trap. *Opt. Lett.*, 35(13):2164–2166, Jul 2010. doi: 10.1364/OL.35.002164. URL http://ol.osa.org/abstract.cfm?URI=ol-35-13-2164.

[197] Eli Yablonovitch. Inhibited spontaneous emission in solid-state physics and electronics. *Physical Review Letters*, 58(20):2059–2062, 1987. doi: 10.1103/PhysRevLett.58.2059. URL https://link.aps.org/doi/10.1103/PhysRevLett.58.2059.

[198] Takayuki Yamamoto, Masaya Notomi, Hideaki Taniyama, Eiichi Kuramochi, Yutaka Yoshikawa, Yoshio Torii, and Takahiro Kuga. Design of a high-q air-slot cavity based on a width-modulated line-defect in a photonic crystal slab. *Opt. Express*, 16(18):13809–13817, Sep 2008. doi: 10.1364/OE.16.013809. URL http://www.opticsexpress.org/abstract.cfm?URI=oe-16-18-13809.

[199] Jun Ye, H. J. Kimble, and Hidetoshi Katori. Quantum state engineering and precision metrology using state-insensitive light traps. *Science*, 320(5884):1734–1738, 2008. ISSN 0036-8075. doi: 10.1126/science.1148259. URL https://science.sciencemag.org/content/320/5884/1734.

[200] S.-P. Yu, J. D. Hood, J. A. Muniz, M. J. Martin, Richard Norte, C.-L. Hung, Seán M. Meenehan, Justin D. Cohen, Oskar Painter, and H. J. Kimble. Nanowire photonic crystal waveguides for single-atom trapping and strong

light-matter interactions. *Applied Physics Letters*, 104(11):111103, 2014. doi: 10.1063/1.4868975. URL https://doi.org/10.1063/1.4868975.

[201] S-P Yu, JD Hood, JA Muniz, MJ Martin, R Norte, C-L Hung, S M Meenehan, J D Cohen, O Painter, and HJ Kimble. Nanowire photonic crystal waveguides for single-atom trapping and strong light-matter interactions. *Appl. Phys. Lett.*, 104(11):111103, 2014. doi: 10.1063/1.4868975.

[202] Su Peng Yu. *Nano-Photonic Platform for Atom-Light Interaction*. PhD thesis, California Institute of Technology, 5 2017.

[203] Su-Peng Yu. *Nano-Photonic Platform for Atom-Light Interaction*. PhD thesis, California Institute of Technology, 2017.

[204] Su-Peng Yu, Juan A. Muniz, Chen-Lung Hung, and H. J. Kimble. Two-dimensional photonic crystals for engineering atom–light interactions. *Proceedings of the National Academy of Sciences*, 116(26):12743–12751, 2019. ISSN 0027-8424. doi: 10.1073/pnas.1822110116. URL https://www.pnas.org/content/116/26/12743.

[205] Qiwen Zhan. Cylindrical vector beams: from mathematical concepts to applications. *Adv. Opt. Photon.*, 1(1):1–57, Jan 2009. doi: 10.1364/AOP.1.000001. URL http://aop.osa.org/abstract.cfm?URI=aop-1-1-1.

[206] Tian Zhong, Jonathan M. Kindem, Evan Miyazono, and Andrei Faraon. Nanophotonic coherent light–matter interfaces based on rare-earth-doped crystals. *Nature Communications*, 6(1):8206, Sep 2015. ISSN 2041-1723. doi: 10.1038/ncomms9206. URL https://doi.org/10.1038/ncomms9206.

[207] Tian Zhong, Jonathan M. Kindem, John G. Bartholomew, Jake Rochman, Ioana Craiciu, Varun Verma, Sae Woo Nam, Francesco Marsili, Matthew D. Shaw, Andrew D. Beyer, and Andrei Faraon. Optically addressing single rare-earth ions in a nanophotonic cavity. *Phys. Rev. Lett.*, 121:183603, Oct 2018. doi: 10.1103/PhysRevLett.121.183603. URL https://link.aps.org/doi/10.1103/PhysRevLett.121.183603.

[208] Hashem Zoubi and Klemens Hammerer. Optomechanical multimode hamiltonian for nanophotonic waveguides. *Phys. Rev. A*, 94:053827, Nov 2016. doi: 10.1103/PhysRevA.94.053827. URL https://link.aps.org/doi/10.1103/PhysRevA.94.053827.